

Measurement of Second-Order Coherence in the Microlaser

by

Abdulaziz M. Aljalal

M. Sc. Physics

King Fahd University of Petroleum and Minerals, 1991

Submitted to the Department of Physics
in partial fulfillment of the requirements for the degree of

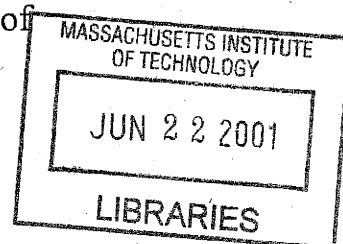
Doctor of Philosophy

at the

MASSACHUSETTS INSTITUTE OF TECHNOLOGY

JUNE 2001

© Massachusetts Institute of Technology 2001, All right reserved



ARCHIVES

Author: _____

A handwritten signature in black ink, circled in red, which appears to read "Abdulaziz M. Aljalal".

Department of Physics
May 7, 2001

Certified by: _____

A handwritten signature in black ink that reads "Michael S. Feld".

Michael S. Feld
Professor of Physics
Thesis Supervisor

Accepted by: _____

A handwritten signature in black ink that reads "Thomas J. Greytak".

Thomas J. Greytak
Professor, Associate Department Head for Education

Measurement of Second-Order Coherence in the Microlaser

by

Abdulaziz M. Aljalal

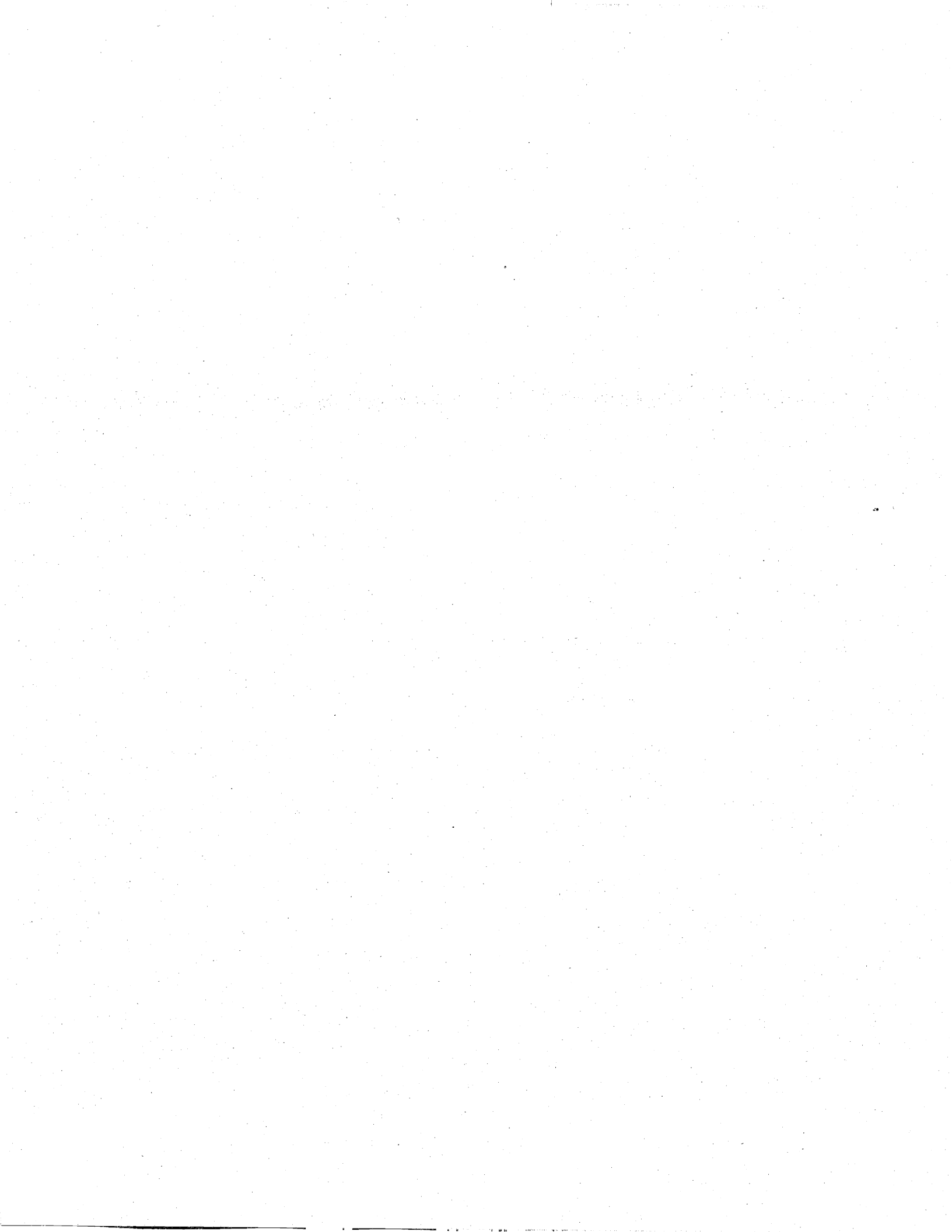
Submitted to the Department of Physics
on May 2001, in partial fulfillment of the
requirements for the degree of
Doctor of Philosophy

Abstract

We study the output and the degree of the second-order coherence function for a microlaser in which the average number of atoms inside the cavity mode is larger than one. Two configurations of the microlaser are explored. In the standing-wave configuration, the atom-cavity coupling strength has a large variation depending on where an atom is injected in the cavity standing-wave mode. On the other hand, for the traveling-wave configuration, the atom-cavity coupling is constant along the cavity mode axis. The difference between the behavior of the microlaser for these two configurations can be attributed to the difference between their gain curves. The experimental results from our many-atom microlaser agree well with the predictions of the single-atom microlaser theory. This is anticipated because the average time an atom spends in the cavity mode is much smaller than the lifetime of a photon in the cavity mode.

As byproduct of this research, two experimental techniques are developed: a new velocity selection scheme for the barium atomic beam and a new simple multi-stop time-to-digital converter (MSTDC). Using two dye lasers, a narrow velocity ground-state barium atomic beam is prepared. It has a velocity width of about 10% and a height of more than 50% of the original effusive atomic beam. The design of the MSTDC is based on a fast first-in-first-out (FIFO) memory. The implemented version provides stop times for any photons separated by more than 20 nsec and its range can be varied from 5 μ sec to 0.66 msec.

Thesis Supervisor: Michael S. Feld
Title: Professor



Acknowledgments

Many people have contributed to the success of this work and I shall forever be in their debts. The role they played may or may not be known to them. My advisor, Professor Michael S. Feld, support and encouragement were valuable. He is a great educator and researcher. Comments of Professor Wolfgang Ketterle and Professor Rainer Weiss on this thesis were very much valuable. Thanks are due to Dr. Ramachandra Dasari for his kindness and precious advices. Professor Kyungwon An taught me a lot of useful experimental and computational techniques. My officemate and lab mate, Chis Fang-Yen, has many contributions to this work. Dr. Chung-Chieh Yu optimism and handwork helped especially at the last stage of this experiment. I am also thankful to Changhuei Yung, Alan Heins, Bryndol Snoes and all who contributed to this work.

I would like to thank King Fahd University of Petroleum and Minerals for supporting me financially for many years and the National Science Foundation for supporting this research.

I am so grateful to my mother, my wife and the rest of my family for their unlimited support and great patience while I was conducting this research.

Contents

1 Introduction	9
1.1- Background	9
1.2- What is a microlaser?	10
1.3- Contributions of the present work.....	12
1.4- Thesis outline	13
1.5- References	14
2 Theory	15
2.1- Properties of the degree of the second-order coherence function.....	16
2.2- Photon number distribution for single-atom microlaser.....	20
2.3- The degree of second-order coherence function for single-atom microlaser	28
2.4- Nonuniform coupling and nonuniform interaction time in single-atom microlaser	30
2.5- Many-atom effects in single-atom microlaser theory	39
2.5.1- Quantum trajectory simulation code.....	42
2.6- Rate-equation model	48
2.7- Pumping Process	55
2.8- References	65
3 Experimental Setup	67
3.1- Overview	67
3.2- Barium atomic beam	68
3.3- Ti:sapphire laser	74

3.3.1- Lamb dip method.....	75
3.3.2- FM Spectroscopy.....	77
3.4- Cavity	81
3.5- Cavity locking	90
3.6- $g^{(2)}(\tau)$ apparatus	95
3.7- Controlling and data-collecting software.....	103
3.8- References	107
4 Velocity Selection of Barium Atomic Beam	109
4.1- Two-laser velocity selection scheme	110
4.1.1- Pumping stage predictions.....	113
4.1.2- Repumping stage predictions.....	116
4.2- Experiment	121
4.2.1- Pumping stage.....	121
4.2.2- Finding 583 nm Resonance	124
4.2.3- Repumping stage	126
4.3- Laser long-term drift stabilization:	131
4.4- References	136
5 Multi-Stop Time-to-Digital Converter.....	138
5.1- Introduction	138
5.2- MSTDC overview	142
5.3- MSTDC details.....	143
5.3.1- Clock.....	144
5.3.2- Synchronizer.....	145
5.3.3- Counters.....	148
5.3.4- Smart switch	151
5.3.5- FIFO memory	154
5.3.6- Synchronization.....	157

5.4- NIM to TTL.....	158
5.5- Interface card.....	159
5.6- MSTDC Tests.....	164
5.7- References	166
6 Results	168
6.1- Pumping process	168
6.2- Atomic number and photon number calibration	171
6.3- Microlaser average number of photons measurements.....	178
6.4- The degree of the second-order coherence	183
7 Conclusions and future improvements	191
A Calculations of P_n and $g^{(2)}(\tau)$	193
B Controlling and data collecting program.....	203
C PCB boards for the MSDTDC	225

Chapter

1 Introduction

1.1- Background

In 1930, Weisskopf and Wigner [1] showed that spontaneous emission process of an excited atom may be understood as a result of the coupling of this atom to the infinite quantized modes of the free space. The coupling strength is inversely proportional to the square root of the mode volume. By preventing this atom to couple to these modes or by making the volume of some of these mode very small the free-space spontaneous emission rate of the atom can be altered. The first experimental observation of enhanced spontaneous emission was observed in 1946 by Purcell [2] for an atom inside a conducting cavity mode whose dimensions are comparable to the transition wavelength.

An experimental interest in this field was revived by the availability of high-Q single mode microwave cavities and long-lived Rydberg atoms [3]. Enhanced spontaneous emission was observed in 1983[4] and inhibited spontaneous emission was observed in 1985[5]. It did not take a long period of time to observe these very interesting behaviors in the optical regime. In 1987, large enhancements and suppressions of spontaneous emission as well as cavity-enhanced radiative level shifts were observed in degenerate confocal and concentric cavities [6,7] and suppression in spontaneous decay was observed in a cavity made of two parallel plane mirrors separated by a very small distance[8].

The spontaneous emission process into a cavity mode can be made reversible if the cavity can store the emitted photon for sufficient long time that the atom can reabsorb the emitted photon. This reversible process is called vacuum Rabi oscillation and it is similar to the oscillation experienced by an atom placed in an intense laser field.

The first theoretical work on a two-level atom placed into a single mode cavity was performed by Jaynes and Cummings [9] in 1963. This very interesting ideal quantum mechanical system had remained a theoretical model until the arrival of low-loss microwave cavities combined with long-lived Rydberg atoms. In 1985, the first maser action with a single atom was realized [10]. This new maser was named the micromaser and it has been extensively studied theoretically and experimentally. Unlike conventional masers, the maser action in the micromaser is initiated by the reversible spontaneous emission into one single cavity mode.

The availability of mirrors with exceptional high reflectivity makes it possible to observe some physical phenomena related to vacuum Rabi oscillation in the optical region of the spectrum. In 1994, the first laser akin to the micromaser was demonstrated in our lab[11,12]. Experiments performed in the optical region have an advantage over those in the microwave region, namely, individual optical photons emitted from the cavity can be detected directly. In the micromaser, the photon statistics can not be measured directly but it is inferred from the state of atoms after they have traversed the microwave cavity[13, 14].

1.2- What is a microlaser?

In the microlaser, two-level atoms are injected randomly into a cavity mode at a rate $R=1/T$ where T is the average time between two successive atoms. Before the atoms enter the cavity mode they are excited from the ground state into the excited state by a pump laser beam (See Figure 1). The probability for an excited atom to emit a photon into the cavity mode is given by

$$P = \sin^2(\sqrt{n+1}g_0 t_{int}), \quad (1)$$

where n is the number of photons inside the cavity mode, t_{int} is the interaction time between the atom, and the cavity mode and g_0 is the atom-cavity coupling constant which is given by

$$g_0 = \frac{\mu}{\hbar} \sqrt{\frac{2\pi\hbar\omega}{V}} \quad (2)$$

Here μ is the dipole moment matrix element between the ground state and the excited state, \hbar is the Planck constant, ω is the angular frequency of the laser transition, and V is the volume of the cavity mode.

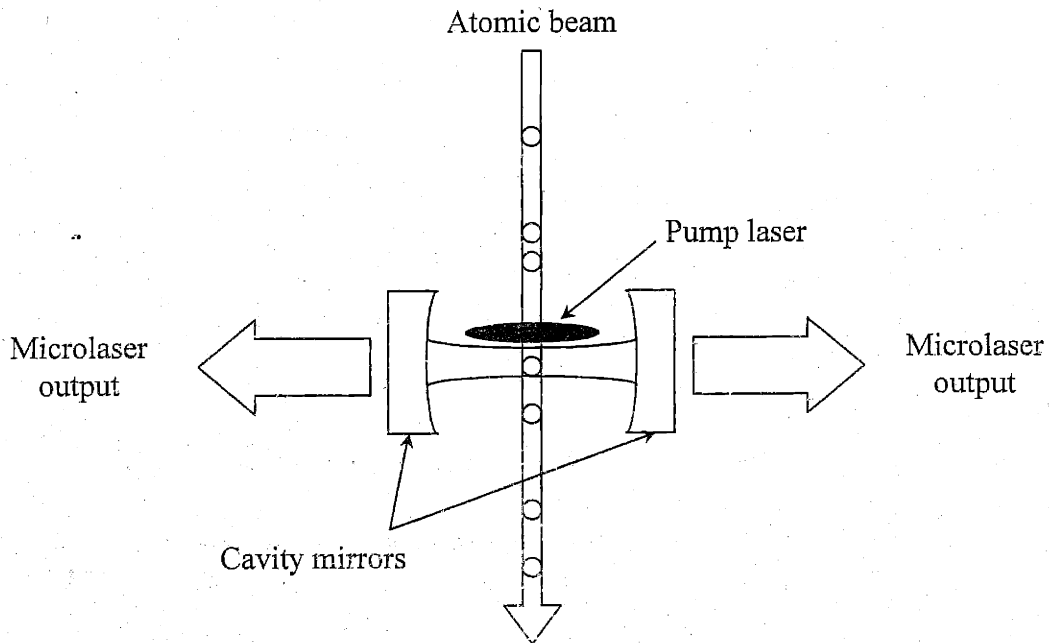


Figure 1. A schematic diagram of the microlaser.

When an excited atom is injected into an empty cavity mode, its probability to emit a photon into the cavity mode is $\sin^2(g_0 t_{\text{int}})$. Once a photon is emitted by an atom, it is stored in the cavity for long enough time that some of the following atoms see it in the mode and consequently their probabilities to emit photons are modified by the presence of the photon in the cavity mode. The steady state is reached when the rate of photons emitted by the atoms into the cavity mode is equal to the rate at which photons escape from the cavity mirrors.

The microlaser possesses many novel properties that make it a very attractive system to study. Those properties are alien to conventional lasers. For example, the width of photon

number distributions in conventional lasers can not be narrower than that of a Poisson distribution. In the microlaser, there are large ranges of operation in which its photon number distribution is much narrower than a Poisson distribution. This is a clear signature of nonclassical light. Moreover, while the output of conventional lasers above threshold increases with the amount of the gain medium, there are regions of operation in which the output of the microlaser is almost independent of the amount of the gain medium. This behavior is called the photon-number stabilization. In addition, the microlaser may exhibit abrupt jumps in its output which only can be predicted by the quantum mechanical theory.

In an idealized microlaser, the average number of atoms inside the cavity mode $\langle N \rangle$ is assumed to be much smaller than one. This makes it possible to obtain an analytical solution, using quantum theory, for the photon number distribution inside the cavity as a function of $\langle N \rangle$. One interesting feature of our microlaser is that its threshold occurs for $\langle N \rangle$ larger than one. This provides us with an opportunity to explore the effect of many atoms on the performance of the microlaser. This effect has not been studied experimentally before and as we will show in the next chapter all numerical simulations of this effect are limited.

1.3- Contributions of the present work

We have studied the output of the microlaser as a function of the number of atoms in the cavity mode for two microlaser configurations, namely, the standing-wave and the traveling-wave configurations. The average number of atoms in the cavity mode is larger than one. We have found that there is a good agreement between our many-atom microlaser and the predictions of the single-atom microlaser theory.

Furthermore, we have studied the degree of the second-order coherence function $g^{(2)}(\tau)$ of the two microlaser configurations. In the micromaser, where a single photon is not detectable, $g^{(2)}(\tau)$, if not impossible, is very difficult to deduce. Here, also, the single-atom microlaser theory agrees well with our experimental results.

In addition, we have developed a new laser-based velocity selection scheme to prepare a very narrow velocity distribution of a ground-state barium atomic beam. Our scheme may be applicable to other kind of atoms.

Also, we have designed and built a new multi-stop time-to-digital converter which has been used to measure the $g^{(2)}(\tau)$ function.

1.4- Thesis outline

In the next chapter, we present the theories behind our work. In the same chapter, we define the degree of the second-order coherence and discuss its properties. In addition, we present some simulations regarding pumping atoms adiabatically to the excited state. In chapter three, we describe our experimental setup. Velocity selection scheme for barium atomic beam is explored in Chapter 4 and the multi-stop time-to-digital converter is detailed in Chapter 5. Finally, in Chapter 6 and 7, we present our results and discuss further improvements that may reveal sub-Poisson statistics of the microlaser.

1.5- References

- [1] V. S. Weisskopf and E. Wigner. *Z. Phys.* **63**, 54 (1930)
- [2] E. M. Purcell. *Phys. Rev.* **69**, 681 (1946).
- [3] D. Kleppner, *Phys. Rev. Lett.* **47**,233 (1981).
- [4] P. Goy, J. M. Raimond, M. Gross and S. Haroche, *Phys. Rev. Lett.* **50**, 1903(1983)
- [5] R. G. Hulet, E. S. Hilfer and D kleppner, *Phys. Rev. Lett.* **55**, 2137(1985).
- [6] D. J. Heinzen, J. J. Childs, J. E. Thompson and M. S. Feld., *Phys. Rev. Lett.* **58**, 1320 (1987).
- [7] D. J. Heinzen and M. S. Feld., *Phys. Rev. Lett.* **59**, 2623 (1987).
- [8] W. Jhe, A. Anderson, E. A. Hinds, D. Meschede, L. Moi and S. Haroche, *Phys. Rev. Lett.* **58**, 666(1987)
- [9] E. T. Jaynes and F. W. Cummings, *Proc. IEEE* **51**, 89 (1963).
- [10] D. Meschede, H. Walther and G. Muller, *Phys. Rev. Lett.* **54**, 551(1985).
- [11] K. An, J. J. Child, R. R. Dasari and M. S. Feld, *Phys. Rev. Lett.* **73**, 3357(1994).
- [12] K. An. Ph.D. Thesis, Massachusetts Institute of technology, May 1995.
- [13] G. Rempe and H. Walther, *Phys. Rev. Lett.* **58**, 353(1987).
- [14] G. Rempe, F. Schmidt-Kaler, H. Walther, *Phys. Rev. Lett.* **64**, 2783(1990).

Chapter

2 Theory

At the beginning of this chapter, we discuss the definition of the degree of second-order coherence function and some of its general properties. Next, we describe how to calculate the $g^{(2)}(\tau)$ function as well as the photon-number distribution for the microlaser using three different methods, namely, the quantum single-atom microlaser theory, the rate-equation model and the quantum trajectory simulation. The advantage of the single-atom microlaser theory is its ability to provide us with an analytical solution from which we learn a lot about the microlaser behavior, especially the way it scales with different experimental parameters. One assumption of the single-atom microlaser theory is that there is at most one atom in the cavity mode at any time. This is not the case in our microlaser. We dedicate Sections 2, 3 and 4 to discuss the single-atom microlaser theory. For an idealized microlaser, Section 2 presents the photon-number distribution calculation and Section 3 describes the $g^{(2)}(\tau)$ function calculation. In Section 4, the results obtained in Sections 2 and 3 are expanded to include a more realistic microlaser model in which atoms are allowed to have velocity distribution and the atom-cavity coupling is permitted to be non-uniform. In Section 5, the quantum trajectory simulation helps us to study the effect of many atoms on our microlaser performance and helps us to reach the following fascinating result: for our experimental parameters, the single-atom microlaser theory formula is applicable to our many-atom microlaser. The rate equation model is discussed in Section 6. Although this model is an approximate one, it provides us with a valuable simple physical picture of our microlaser.

Finally, in the last section, we describe an adiabatic process by which the atoms in our microlaser are inverted before they enter the cavity mode. We show that, for an atomic beam with wide velocity distribution, it is preferable to invert atoms adiabatically, since this process can be made effective and almost velocity independent

2.1- Properties of the degree of the second-order coherence function

The degree of the second-order coherence function, $g^{(2)}(\tau)$, is a key tool in this thesis. For this reason, some important general properties of the $g^{(2)}(\tau)$ function will be presented before any theoretical studies of the microlaser itself.

Since the first experiment conducted by Hanbury Brown and Twiss [1] in 1957, the intensity-intensity correlation measurement has become an indispensable tool to characterize light sources. The $g^{(2)}(\tau)$ function is a normalized intensity-intensity correlation function. It is normalized such that its value is one for an uncorrelated light beam, such as a conventional laser beam operated well above threshold. Its value at $\tau=0$, $g^{(2)}(0)$, is proportional to the width of the photon number distribution of the light source. Its functional shape is strongly related to the dynamics by which light is generated. Unlike the degree of first-order coherence, $g^{(1)}(\tau)$, which is a normalized field-field correlation function and which cannot be used to demonstrate any nonclassical behavior of light, $g^{(2)}(\tau)$ is used to reveal two features of nonclassical light. $g^{(2)}(0) < 1$ indicates sub-Poisson statistics of light source and a positive slope of $g^{(2)}(\tau)$ at $\tau = 0$ indicates antibunched light. Furthermore, because of the way $g^{(2)}(\tau)$ is normalized, its shape, as explained below, is preserved even when low efficient detectors are used.

Quantum mechanically, $g^{(2)}(\tau)$ is defined as

$$g^{(2)}(\tau) = \frac{\langle \mathcal{T} : n(t)n(t+\tau) \rangle}{\langle n \rangle^2} = \frac{\langle a^\dagger(t)a^\dagger(t+\tau)a(t+\tau)a(t) \rangle}{\langle a^\dagger a \rangle^2}, \quad (1)$$

where \mathcal{T} is the time ordering symbol, which rearranges creation operators in forward time order and annihilation operators in backward time order. The pair of colons surrounding an operator is used as a normal ordering symbol, which rearranges operators such that any creation operator is to the left of any annihilation operator. This ordering is a natural consequence of the absorption

process by which photons are detected.[2] The quantity $n \equiv a^\dagger a$ is the photon-number operator for the field inside the cavity mode. Since the annihilation operator for the field inside the cavity, a , is related to the annihilation operator for the field outside the cavity, a_{out} , by $a_{\text{out}} = \sqrt{\Gamma_c} a$, the intensity operator $I \equiv a_{\text{out}}^\dagger a_{\text{out}}$ can be used in Eq. (1) instead of photon-number operator. Here Γ_c is the cavity damping rate.[3]

From Eq. (1), $g^{(2)}(0)$ is given by

$$g^{(2)}(0) = \frac{\langle a^\dagger a^\dagger a a \rangle}{\langle n \rangle^2} = \frac{\langle n^2 \rangle - \langle n \rangle^2}{\langle n \rangle^2} = \frac{Q}{\langle n \rangle} + 1, \quad (2)$$

where the commutation relation $a^\dagger a = a a^\dagger - 1$ is used. The Q parameter is a normalized variance defined as follows[4]

$$Q \equiv \frac{\langle (n - \langle n \rangle)^2 \rangle}{\langle n \rangle} - 1 = \frac{\langle n^2 \rangle - \langle n \rangle^2}{\langle n \rangle} - 1. \quad (3)$$

For a Poisson distribution, $\langle n^2 \rangle - \langle n \rangle^2 = \langle n \rangle$, and $Q = 0$. From Eq. (2), $g^{(2)}(0) = 1$ signifies a photon-number distribution with a width equal to that of a Poisson distribution. $g^{(2)}(0) > 1$ indicates that the photon-number distribution is wider than that of a Poisson distribution, and this distribution is called a super-Poisson distribution. $g^{(2)}(0) < 1$ implies that the distribution is narrower than a Poisson distribution and for this reason it is called a sub-Poisson distribution (See Figure 1).

$g^{(2)}(0) < 1$ can not occur when light is treated as a classical field. For classical field E , Eq. (2) becomes

$$g_c^{(2)}(0) = \frac{\langle E^* E^* E E \rangle}{\langle E^* E \rangle^2} = \frac{\langle I^2 \rangle}{\langle I \rangle^2}. \quad (4)$$

Here the subscript c indicates classical field and the intensity $I \equiv E^*E$. Cauchy's inequality states that for two real variables A and B, $2AB \leq A^2 + B^2$. Applying this inequality to Eq. (4), it can be shown that $g_c^{(2)}(0) \geq 1$. The main difference between the quantum mechanical treatment and the classical treatment is the term $\langle n \rangle$ in the numerator of Eq. (2). Quantum mechanically, the act of measurement can interfere with the measured system and a measurement of number n of photons itself reduces the photon number by 1, so that the second measurement finds only n-1 photons.[5]

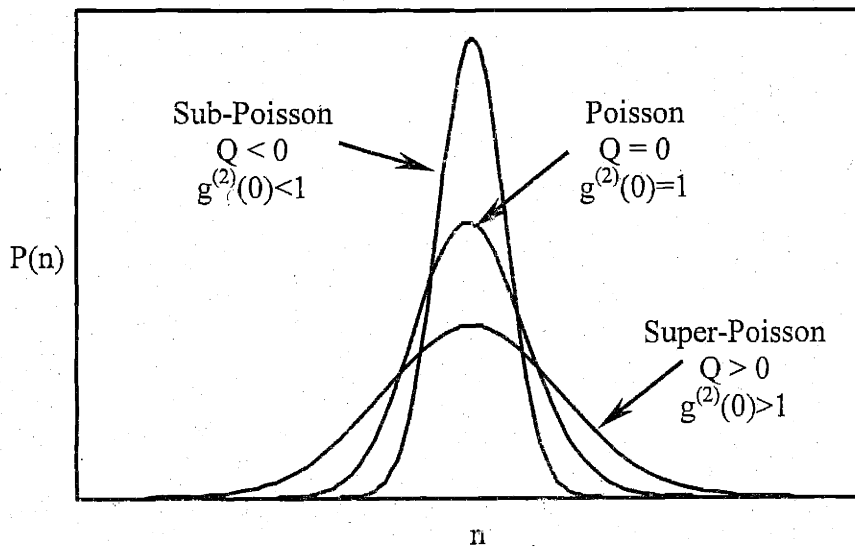


Figure 1. $g^{(2)}(0)$ or Q parameter indicate the width of a photon-number distribution relative to a Poisson distribution.

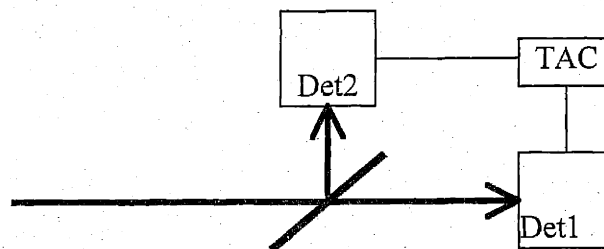


Figure 2. Two-detector $g^{(2)}(\tau)$ measurement configuration.

Using Cauchy's inequality, the slope of the degree of second-order coherence function at $\tau = 0$ for classical field is either negative or equal to zero, and it can not be positive [6].

$$\frac{d}{d\tau} g_c^{(2)}(\tau = 0) \leq 0. \quad (5)$$

Negative slopes indicate that successive photons are more likely to arrive at the same time or very close together than further apart. This is simply a manifestation of intensity fluctuations. The arrival of a high intensity fluctuation at the detector produces closely spaced photon counts, while a low intensity fluctuation produces low count rates. This behavior is referred to as photon bunching. When $g^{(2)}(\tau) = 1$, as is the case of a conventional laser operated well above threshold, the arrival of photons is completely random. For nonclassical light the slope of $g^{(2)}(\tau)$ at $\tau = 0$ can be positive. This kind of light is said to be antibunched, and the arrival of photons is spaced out in time. The antibunched behavior cannot be predicted by the classical theory of light.

Why is $g^{(2)}(\tau)$ insensitive to detector efficiency? Suppose we measure $g^{(2)}(\tau)$ using a beam splitter and a two-detector configuration as shown in Figure 2. A photon detected by detector 1 starts a time to digital converter (TAC), which then records the time of detecting subsequent photons by detector 2 within some time range T_R . Then TAC stops until a photon is detected by detector 1. The histogram built from the arrival times on detector 2 is equal to the conditional probability of detecting a photon by detector 2 at time $t = \tau$ within Δt_2 given that a photon is detected by detector 1 at time $t = 0$. Here Δt_2 is the width of the histogram bin.

The joint probability of detecting a photon a time $t = 0$ within Δt_1 and another photon at $t = \tau$ within Δt_2 is given by[7]

$$P_2(t_1 = 0; t_2 = \tau) \Delta t_1 \Delta t_2 = \eta_1 \eta_2 \langle \mathcal{T} : I(0)I(\tau) : \rangle. \quad (6)$$

Here η_i is the quantum efficiency of detector i . $I(0)$ and $I(\tau)$ are photon intensity operators. The conditional probability of detecting a photon by detector 2 at time $t = \tau$ within Δt_2 given that a

photon is detected by detector 1 at time $t = 0$ is simply obtained by dividing Eq.(6) by the probability of detecting a photon at time $t = 0$ by detector 1 within Δt_1

$$P_c(t_2 = \tau | t_1 = 0) \Delta t_2 = \frac{P_2(t_1 = 0; t_2 = \tau) \Delta t_1 \Delta t_2}{P_1(t_1 = 0) \Delta t_1} = \frac{\eta_1 \eta_2 \langle \mathcal{T} : I(0)I(\tau) \rangle}{\eta_2 \langle I \rangle}. \quad (7)$$

For τ much larger than correlation time of the light, t_c , detecting a photon by detector 1 is completely uncorrelated to detecting another photon by detector 2, and the joint probability in Eq. (6) can be written as the product of single-fold probability density for detecting a photon by each detector.

$$P_2(t_1 = 0; t_2 = \tau \gg t_c) \Delta t_1 \Delta t_2 = P_1(t_1 = 0) \Delta t_1 P_2(t_2 = \tau) \Delta t_2 = \eta_1 \langle I \rangle \Delta t_1 \eta_2 \langle I \rangle \Delta t_2, \quad (8)$$

thus for $\tau \gg t_c$, the conditional probability in Eq. (7) becomes the probability density of detecting a photon at time $t = \tau$ by detector 2. So when our histogram is normalized by dividing it by the counts on the bins for which $\tau \gg t_c$, we obtain

$$\frac{P_c(t_2 = \tau | t_1 = 0) \Delta t_2}{P_c(t_2 \gg t_c | t_1 = 0) \Delta t_2} = \frac{P_2(t_1 = 0; t_2 = \tau) \Delta t_1 \Delta t_2}{P_1(t_1 = 0) \Delta t_1 P_2(t_2 = \tau) \Delta t_2} = \frac{\eta_1 \eta_2 \langle \mathcal{T} : I(0)I(\tau) \rangle}{\eta_1 \eta_2 \langle I \rangle \langle I \rangle} \equiv g^2(\tau). \quad (9)$$

The efficiencies of the two detectors cancel out and $g^{(2)}(\tau)$ is independent of the detector efficiencies.

2.2- Photon number distribution for single-atom microlaser

What is an ideal microlaser? In an ideal microlaser, monovelocity two-level atoms are injected randomly into a single-mode cavity. The atoms are assumed to be perfectly excited before they enter the cavity mode. The excited level is assumed to be a long-lived level such that no spontaneous decay occurs during atom-cavity interaction time. In addition, the cavity is assumed to couple uniformly with atoms; no standing-wave nature of the cavity mode is

considered. To derive the photon number distribution two important conditions are assumed. First, the atoms are injected at a very low rate such that at most one atom can be in the cavity mode at any time. Thus, we do not need to consider more than one atom interacting with the field at the same time. Second, the atom-cavity interaction time is assumed to be much smaller than the lifetime of photons in the cavity, so that the relaxation of the cavity field mode can be ignored while an atom is inside the cavity. Since the output of the microlaser is in the optical regime, thermal photons can be ignored. This is one difference between the microlaser and the micromaser (in which thermal photons are significant except at very low temperatures).

Several authors have studied theoretically the photon number distribution inside the microlaser cavity. Here, I will follow the derivation of Filipowicz [8].

The approach used to find the photon statistics in this ideal microlaser is as follows. When an atom enters the cavity, the coupled field-atom density operator is evolved according to the Jaynes-Cummings Hamiltonian. During the interaction time between the atom and the cavity mode t_{int} , photons are not allowed to escape from the cavity. While there are no atoms inside the cavity mode, the photon field decays exponentially at a rate Γ_c . Since the time between two successive atoms is random with average value T , we need to average the field density operator over the exponential distribution $\frac{1}{T} e^{-t/T}$.

The Jaynes-Cummings Hamiltonian for a two-level atom interacting with a single mode is given by

$$H = \frac{\hbar\omega_0}{2} S_3 + \hbar\omega a^\dagger a + \hbar g(S_+ a + S_- a^\dagger), \quad (10)$$

where ω_0 is the frequency difference between the two atomic level, ω is the frequency of the cavity field mode, g is the electric dipole coupling constant, a and a^\dagger are the annihilation and creation operators and S_3 and S_\pm are the Pauli spin operators.

Let us assume that at time t_i , the i^{th} atom enters the cavity mode which has a field described by the field density operator $\rho_f(t_i)$. At this time, the combined atom-field system is described by a density operator $\rho(t_i)$, which is a tensor product of the field density operator $\rho_f(t_i)$ and the initial atomic density operator. At the end of the interaction time between the atom and the cavity mode, the combined density operator $\rho(t)$ evolves to

$$\rho(t_i + t_{\text{int}}) = U(t_{\text{int}})\rho(t_i)U^\dagger(t_{\text{int}}), \quad (11)$$

where the time development operator $U(t_{\text{int}})$ is given by

$$U(t_{\text{int}}) = e^{-iHt/\hbar}. \quad (12)$$

The field operator at time $t_i + t_{\text{int}}$ is obtained by taking the trace of the operator in Eq. (12) over the atomic variables:

$$\rho_f(t_i + t_{\text{int}}) = \langle a | \rho(t_i + t_{\text{int}}) | a \rangle + \langle b | \rho(t_i + t_{\text{int}}) | b \rangle \equiv F(t_{\text{int}})\rho_f(t_i), \quad (13)$$

where $|a\rangle$ and $|b\rangle$ are the atomic excited and ground states, respectively. During the interaction, the field density matrix in the number state representation $\langle n | \rho_f | n' \rangle$ will remain diagonal if the initial field density matrix at time t_i is diagonal and the atoms are injected perfectly inverted. The diagonal element of the field density operator $p_n \equiv \langle n | \rho_f | n \rangle$ can be found from Eq. (13), after lengthy algebra, to be

$$p_n(t_i + t_{\text{int}}) = (1 - \beta_{n+1})p_n(t_i) + \beta_n p_{n-1}(t_i). \quad (14)$$

Here

$$\beta_n = \frac{n}{(\Delta/2g)^2 + n} \sin^2(gt_{\text{int}} \sqrt{(\Delta/2g)^2 + n}) \quad (15)$$

and Δ is atom-cavity detuning $\Delta \equiv \omega - \omega_0$.

When there are no atoms inside the cavity mode, the field density operator is governed by the standard master equation of a damped harmonic oscillator:

$$\dot{\rho}_f = \frac{\Gamma_c}{2} (2a\rho_f a^\dagger - a^\dagger a \rho_f - \rho_f a^\dagger a) \equiv L\rho_f. \quad (16)$$

During field decay, its density operator remains diagonal and this leads to

$$\dot{p}_n = \Gamma_c ((n+1)p_{n+1} - np_n). \quad (17)$$

Using Eq. (13) and Eq. (14), the field density operator at time t_i , just before the i^{th} atom is injected, can be related formally to that just before the injection of the next atom, at time t_{i+1} , by

$$\rho_f(t_{i+1}) = \exp(LT_i)F(t_{\text{int}})\rho_f(t_i), \quad (18)$$

where $T_i = t_{i+1} - t_i - t_{\text{int}} \approx t_{i+1} - t_i$. If we start with zero photons in the cavity, which is diagonal at the number state representation, the density matrix obtained from successive iterations of Eq. (9) will be also diagonal.

Since the time between successive atoms T_i is random, we need to average Eq. (18) over this random variable

$$\langle \rho_f(t_{i+1}) \rangle = \langle \exp(LT_i)F(t_{\text{int}})\rho_f(t_i) \rangle. \quad (19)$$

Since $\rho_f(t_i)$ depends only on atoms injected before t_i , it depends only on T_j where $j = 0, 1, \dots, i-1$ and it is statistically independent of T_i . Thus the average, on the right hand side of Eq. (19), can be found simply by factorizing the terms:

$$\langle \rho_f(t_{i+1}) \rangle = \langle \exp(LT_i) \rangle F(t_{int}) \langle \rho_f(t_i) \rangle. \quad (20)$$

$$\text{Using } \langle \exp(LT_i) \rangle = \frac{1}{T} \int_0^{\infty} \exp(LT_i) \exp(-\frac{T_i}{T}) dT_i = \frac{1}{1-LT}, \quad (21)$$

Eq. (20) becomes

$$(1-LT) \langle \rho_f(t_{i+1}) \rangle = F(t_{int}) \langle \rho_f(t_i) \rangle. \quad (22)$$

Here T is the average time between the arrival of two successive atoms. After a number of successive iterations of Eq. (22), a steady state is obtained. This steady state may not be a "true" steady state; but it is a steady state of the return map of Eq. (22) in which the field repeats at a precise time when a new atom is injected into the cavity. Therefore, at steady state, we can set

$\langle \rho_f(t_{i+1}) \rangle = \langle \rho_f(t_i) \rangle \equiv \bar{\rho}_{f,st}$ and Eq. (22) becomes

$$(1-LT) \bar{\rho}_{f,st} = F(t_{int}) \bar{\rho}_{f,st}. \quad (23)$$

Using Eq. (14) and Eq.(17), Eq.(23) can be rewritten in terms of the occupation number

$$\bar{p}_n \equiv \langle n | \bar{\rho}_{f,st} | n \rangle$$

$$\bar{p}_n - TT_c ((n+1)\bar{p}_{n+1} - n\bar{p}_n) = (1-\beta_{n+1})\bar{p}_n + \beta_n \bar{p}_{n-1}. \quad (24)$$

This can be rearranged to

$$\frac{1}{T}\beta_n\bar{p}_{n-1} - \Gamma_c n\bar{p}_n = \frac{1}{T}\beta_{n+1}\bar{p}_n - \Gamma_c(n+1)\bar{p}_{n+1}. \quad (25)$$

These four terms represent the rate of growth and loss of \bar{p}_n . The first term represents the growth of \bar{p}_n due to emission from photon level $n-1$ to n , while the third term represents loss due to emission from level n to level $n+1$. The second and the fourth terms represent loss and growth due to cavity decay from levels $n+1$ and n , respectively.

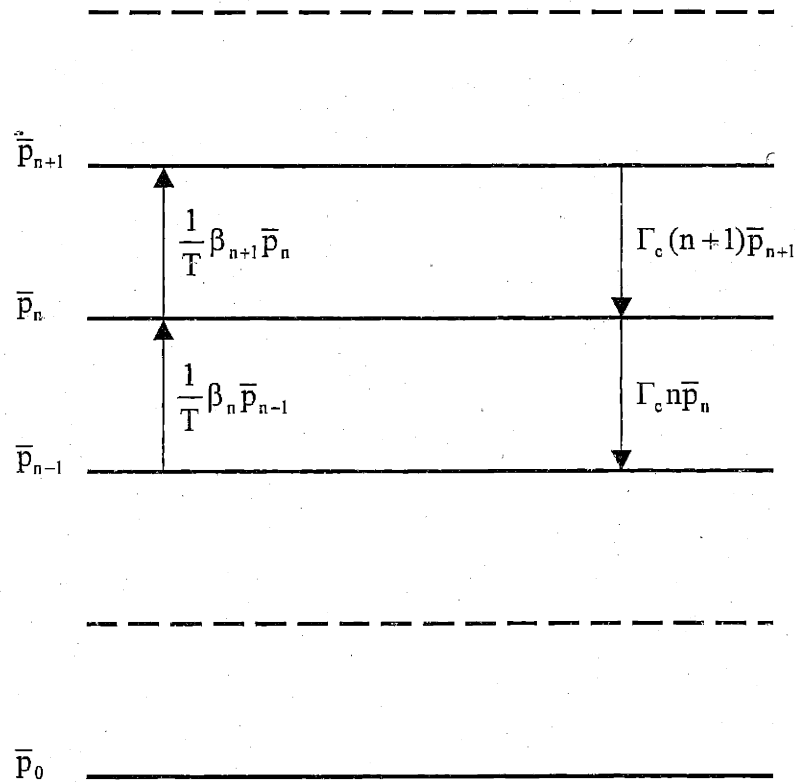


Figure 3. Photon energy-level diagram depicting the rate of growth and loss of \bar{p}_n produced by the atomic transitions and the cavity loss process.

If we define $S_n \equiv \frac{1}{T}\beta_n\bar{p}_{n-1} - \Gamma_c n\bar{p}_n$, then Eq. (25) becomes

$$S_n = S_{n+1}. \quad (26)$$

To be able to normalize the field density matrix, $\bar{\rho}_n$ should go to zero faster than $1/n$ for $n \rightarrow \infty$. Therefore, for $n \rightarrow \infty$, $S_n \rightarrow 0$. Using this fact and Eq. (26), S_n should be 0 for any n . This leads to

$$\bar{\rho}_n = \frac{1}{T\Gamma_c} \frac{\beta_n}{n} \bar{\rho}_{n-1}, \quad (27)$$

or

$$\bar{\rho}_n = \bar{\rho}_0 \prod_{k=1}^{n-1} \frac{\beta_k}{k T\Gamma_c}, \quad (28)$$

where $\bar{\rho}_0$ is found from normalizing the photon-number distribution.

Lugiato, Scully and Walther [9] have pointed out that a similar result can be obtained by applying the standard quantum laser theory where at any time the density operator of the microlaser is affected by the gain and loss in the system according to

$$\frac{\partial}{\partial t} \bar{\rho}_f = \frac{1}{T} \delta \bar{\rho}_{t_{\text{int}}} + L \bar{\rho}_f, \quad (29)$$

where $1/T$ is the injection rate and $\delta \bar{\rho}_{t_{\text{int}}}$ is the change in $\bar{\rho}_f$ due to one atom interacting for a time t_{int} . The interaction between an atom and the laser field is interrupted by spontaneous emission in conventional lasers while it is interrupted by an atom exiting the cavity mode in the microlaser.

In the photon-number representation the diagonal element of $\bar{\rho}_f$ of Eq. (29) can be written as

$$\frac{d}{dt} \bar{p}_n = -\frac{1}{T} \beta_{n+1} \bar{p}_n + \frac{1}{T} \beta_n \bar{p}_{n-1} - \Gamma_c n \bar{p}_n + \Gamma_c (n+1) \bar{p}_{n+1}. \quad (30)$$

This, for steady state, is the same equation as Eq. (25).

Appendix A lists a code written in Mathematica to calculate the average number of photons inside the cavity mode $\langle n \rangle$, which is given by

$$\langle n \rangle = \sum_{i=0}^{\infty} i \bar{p}_i \quad (31)$$

and Q parameter (See Eq (3) for definition). Figure 4 shows $\langle n \rangle$ and Q for typical experimental parameters for our microlaser. We ignore the effect of many atoms in this calculation. Above the first threshold, the photon number of the microlaser is stabilized and the Q parameter becomes less than zero. This means that the photon distribution becomes narrower than that of a Poisson distribution, which is a signature of nonclassical light. In addition, very sharp jumps are predicted to occur. These features are alien to conventional lasers.

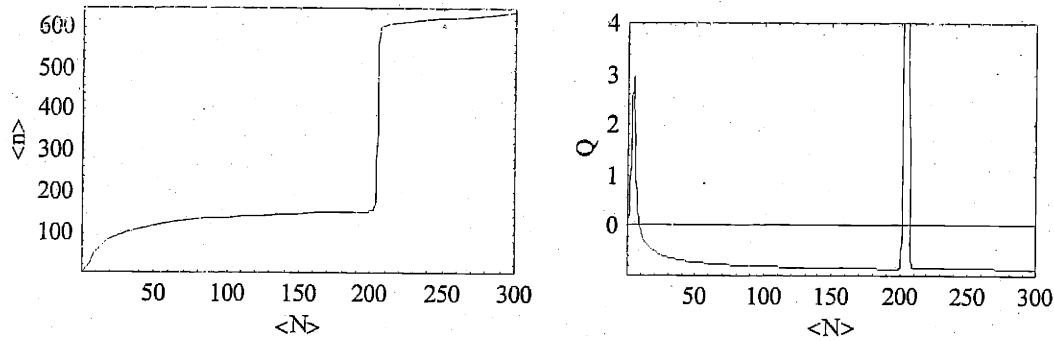


Figure 4. Calculation of average number of photons inside the cavity $\langle n \rangle$ and the Q parameter as a function of average number of atoms inside the cavity for finesse of 1 million and atomic velocity of 360 m./sec . Here many atom effects are ignored.

2.3- The degree of second-order coherence function for single-atom microlaser

T. Quang [10], as well as S. Kumar and G. Agarwal [11], have studied the $g^{(2)}(\tau)$ function of the microlaser. Here, T. Quang's derivation of $g^{(2)}(\tau)$ will be presented. Eq.(1) defines the $g^{(2)}(\tau)$ to be

$$g^{(2)}(\tau) = \frac{\langle a^\dagger(t)a^\dagger(t+\tau)a(t+\tau)a(t) \rangle}{\langle a^\dagger a \rangle^2} \quad (1)$$

Using the time development operator of the combined field-atom system, $\bar{U}(\tau)$, the photon-number operator $a^\dagger(\tau+t)a(\tau+t)$ can be written in terms of that at $\tau = 0$ as in

$$a^\dagger(t+\tau)a(t+\tau) = \bar{U}^\dagger(\tau)a^\dagger(t)a(t)\bar{U}(\tau). \quad (32)$$

Now, the two-time photon number correlation can be written as

$$\begin{aligned} \langle a^\dagger(t)a^\dagger(t+\tau)a(t+\tau)a(t) \rangle &= \text{Tr}_{f,a} [a^\dagger(t)\bar{U}^\dagger(\tau)a^\dagger(t)a(t)\bar{U}(\tau)a(t)\bar{\rho}(t)] \\ &= \text{Tr}_{f,a} [a^\dagger(t)a(t)\bar{U}(\tau)a(t)\bar{\rho}(t)a^\dagger(t)\bar{U}^\dagger(\tau)] \\ &= \text{Tr}_f [a^\dagger(t)a(t)\bar{\bar{\rho}}(t)], \end{aligned} \quad (33)$$

where the subscript in trace operator $\text{Tr}_{f,a}$ referees to field and atom respectively, $\bar{\rho}(t)$ is the density operator of the combined atom-filed system and

$$\bar{\bar{\rho}}(\tau) \equiv \text{Tr}_a [\bar{U}(\tau)a(t)\bar{\rho}(t)a^\dagger(t)\bar{U}^\dagger(\tau)]. \quad (34)$$

The microlaser statistical behavior is that of a Markov process. The statistical properties of any operator $O(t)$ describing the microlaser for time $t > t_0$, requires only the knowledge of the

value of $O(t)$ at $t = t_0$ and behavior of $O(t)$ before $t = t_0$ is irrelevant. It can be shown that for the a Markov process, given Eq. (34), $\bar{\rho}(\tau)$ satisfy similar equations of motion as that of density operator $\bar{\rho}_f(t) = \text{Tr}_a \bar{\rho}(t)$, Eq. (29).[12] The initial condition for $\bar{\rho}(\tau)$ is

$$\bar{\rho}(0) \equiv a(t)\bar{\rho}(t)a^\dagger(t). \quad (35)$$

For steady state, the two-time photon number correlation $\langle a^\dagger(t)a^\dagger(t+\tau)a(t+\tau)a(t) \rangle$ is independent of t , so for steady state t will be replaced with $t = 0$.

$$\begin{aligned} \langle a^\dagger(0)a^\dagger(\tau)a(\tau)a(0) \rangle &= \sum_{n,k} \langle n|a^\dagger(0)a(0)|k \rangle \langle k|\bar{\rho}(\tau)|n \rangle \\ &= \sum_n n \langle n|\bar{\rho}(\tau)|n \rangle = \sum_n n \bar{p}_n(\tau), \end{aligned} \quad (36)$$

where $\bar{p}_n(\tau)$ satisfy Eq. (30) but with the initial conditions

$$\bar{p}_n(0) = \langle n|a(0)\bar{\rho}(0)a^\dagger(0)|n \rangle = (n+1)\bar{p}_{n+1}. \quad (37)$$

The steady state two-time photon-number correlation has similar time behavior as that of the evolution of the average number of photons $\langle n \rangle$ of the microlaser when the microlaser is disturbed from its steady state such that at initial time $p_n \rightarrow (n+1)p_{n+1}$.

Using Eqs. (1), (36) and (37), $g^{(2)}(0)$ can be related to the Q parameter of the photon-number distribution as in

$$g^{(2)}(0) = \frac{\sum_n n(n+1)\bar{p}_{n+1}}{\langle n \rangle^2} \equiv \frac{\langle n^2 \rangle - \langle n \rangle}{\langle n \rangle^2} = \frac{Q}{\langle n \rangle} + 1. \quad (38)$$

See Eq (3) for definition and significance of the Q parameter.

To calculate $g^{(2)}(\tau)$, we need to solve many coupled equations, Eq. (30). The number of equations depends on the size of steady state photon distribution and can be as large as 100 equations. Appendix A lists a program written in Mathematica, which finds the eigenvalues, and eigenvectors of these coupled equations and matches the initial conditions to calculate $\bar{\bar{p}}_n(\tau)$.

2.4- Nonuniform coupling and nonuniform interaction time in single-atom microlaser

Nonuniformity in the atom-cavity coupling constant and nonuniformity in the interaction time between atoms and the cavity mode can be included in the formalism of the single-atom microlaser. For a single atom, the coupling constant varies in strength as the atom passes through the cavity Gaussian mode. Different atoms may experience different average atom-cavity coupling depending on where they are injected. In addition, the interaction time of atoms with the cavity mode is a function of the speed of atoms as well as where they are injected with respect to the cavity mode.

Due to the Gaussian nature of the cavity mode, an atom passing through the cavity mode experiences time-dependent atom-cavity coupling $g(t)$ given by

$$g(t) = g_0 e^{-\frac{v^2 + y^2}{w^2}}, \quad (39)$$

where g_0 is the coupling strength on the axis of the cavity mode, v is the speed of the atom, w is the cavity mode waist and y is the y coordinate (See Figure 5). How can this variation be included in the single-atom microlaser?

Using the Schrödinger equation, it can be shown that if the Hamiltonian is a function of time then the time development operator $U(t)$ becomes

$$U(t) = e^{-i \int_0^t H(t') dt' / \hbar}, \quad (40)$$

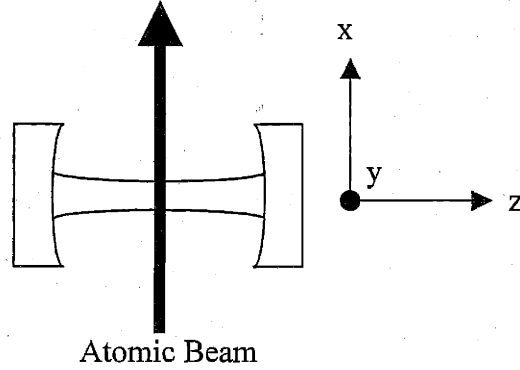


Figure 5. Top view of the microlaser cavity along with the coordinate convention.

where $U(t_1) = 0$. In deriving Eq. (14), the atom-cavity coupling is assumed to be zero except in the cavity mode where it has a constant value. The atom-cavity coupling has a top-hat shape and this enables us to write the time development operator as in Eq. (12). In the case of a Gaussian mode, we need to do the integration in Eq. (40) while the atom is in the cavity mode. The Gaussian mode has no definite boundaries so we will carry the integration from $-\infty$ to ∞ .

$$\int_{-\infty}^{\infty} g(t') dt' = g_0 \int_{-\infty}^{\infty} e^{-\frac{v(t'^2+y^2)}{w^2}} dt' = g_0 e^{-\left(\frac{y}{w}\right)^2} \frac{\sqrt{\pi w}}{v}. \quad (41)$$

This is equivalent to a top-hat mode with a width of $\sqrt{\pi}w$. So to accommodate for the Gaussian mode shape along the x-axis, we need to replace t_{int} in Eq. (15) with

$$t_{\text{int}} = \frac{\sqrt{\pi w}}{v} \quad (42)$$

Nonuniformity between different atoms can be included in the microlaser formalism based on the same principle that enables us to account for different time separation between two consecutive atoms [8]. Since the injection process is completely random, there is no correlation between atoms and when we average Eq. (9) over these nonuniformities, we can factorize the average as follows

$$\langle \rho_f(t_{i+1}) \rangle = \langle \exp(LT_i) F(t_{int}) \rangle \langle \rho_f(t_i) \rangle. \quad (43)$$

This leads to a formula similar to Eq. (28) for the photon occupation number \bar{p}_n and similar to Eq. (36) for the two-time photon number correlation $\langle a^\dagger(t) a^\dagger(t+\tau) a(t+\tau) a(t) \rangle$ with the following modification

$$\frac{\beta_k}{T} \rightarrow \left\langle \frac{\beta_k}{T} \right\rangle. \quad (44)$$

When atoms are sent perpendicular to the cavity axis, atoms interact with the standing-wave cavity mode and the nonuniform-coupling constant is given by

$$g = g_0 e^{-\frac{v^2+y^2}{w^2}} \sin\left(\frac{2\pi}{\lambda} z\right), \quad (45)$$

where λ is the laser wavelength. For standing-wave interaction and monovelocity atoms, Eq. (44) becomes

$$\left\langle \frac{\beta_k}{T} \right\rangle = \frac{1}{\lambda} \int_0^\lambda \frac{1}{T} \sin^2\left(\sqrt{k} g_0 \sin\left(\frac{2\pi}{\lambda} z\right) \frac{\sqrt{\pi} w}{v}\right) dz = \frac{1}{T} \frac{1}{2} \left(1 - J_0\left(2\sqrt{k} g_0 \frac{\sqrt{\pi} w}{v}\right)\right) \quad (46)$$

Here the cavity is assumed to be in resonance with atomic transition and the Gaussian nature of the mode along the y-axis is ignored. J_0 is the Bessel function of the first kind of order zero.

For an effusive atomic beam, the velocity distribution of the atomic flux is given by [13]

$$Fl(v) = v \frac{4 \langle N \rangle v^2}{\sqrt{\pi} v_0^3} e^{-\left(\frac{v}{v_0}\right)^2}, \quad (47)$$

where v_0 is the most probable velocity in the atomic velocity distribution density and $\langle N \rangle$ is the average number of atoms in the cavity mode. To incorporate the velocity distribution in the microlaser theory, we need to replace the flux of the monovelocity atomic beam, $1/T$, with that of Eq. (47). So, for resonance standing-wave interaction with an effusive atomic beam and a top-hat coupling along the y -axis, Eq. (44) becomes

$$\left\langle \frac{\beta_k}{T} \right\rangle = \int_0^\infty v \frac{4 \langle N \rangle v^2}{\sqrt{\pi} v_0^3} e^{-\left(\frac{v}{v_0}\right)^2} \frac{1}{2} \left(1 - J_0\left(2\sqrt{k}g_0 \frac{\sqrt{\pi}w}{v}\right)\right) dv. \quad (48)$$

If, in addition, the Gaussian nature of the mode along the y -axis is considered and a slit of height Δy centered at the cavity axis ($y=0$) is used to allow just those atoms injected within its height to interact with cavity mode, Eq. (44) becomes

$$\left\langle \frac{\beta_k}{T} \right\rangle = \frac{1}{\Delta y} \int_{-\frac{\Delta y}{2}}^{\frac{\Delta y}{2}} \int_0^\infty v \frac{4 \langle N \rangle v^2}{\sqrt{\pi} v_0^3} e^{-\left(\frac{v}{v_0}\right)^2} \frac{1}{2} \left(1 - J_0\left(2\sqrt{k}g_0 e^{-\left(\frac{y}{w}\right)^2} \frac{\sqrt{\pi}w}{v}\right)\right) dv dy. \quad (49)$$

Nonuniform coupling and nonuniform interaction time are sources of randomness in our system. With enough randomness introduced to an ideal microlaser, microlaser behavior approaches that of an ordinary laser [8]. Figure 6 shows that the Rabi oscillation in the term

$\frac{1}{\langle N \rangle} \left\langle \frac{\beta_n}{T} \right\rangle$ is washed out as more sources of randomness are introduced to the system. It will

be shown using the rate-equation model that the term $\frac{1}{\langle N \rangle} \left\langle \frac{\beta_n}{T} \right\rangle$ corresponds to gain per atom when there are $n+1$ photons in the cavity mode. A well-defined Rabi oscillation is obtained for

monovelocity and uniform coupling. When the standing wave nature of the cavity is considered, Eq. (46), the depth of oscillation becomes smaller but it does not vanish. For large n , the gain per atom approaches one half of its maximum value for the ideal microlaser. The oscillation almost vanishes when, in addition, an effusive atomic beam is used. A further reduction in oscillation happens when the Gaussian nature of the cavity mode along the y -axis is considered, Eq. (49). Here we consider the central part of the Gaussian mode limited by a slit of width $25 \mu\text{m}$. The oscillation disappears completely for very wide slit.

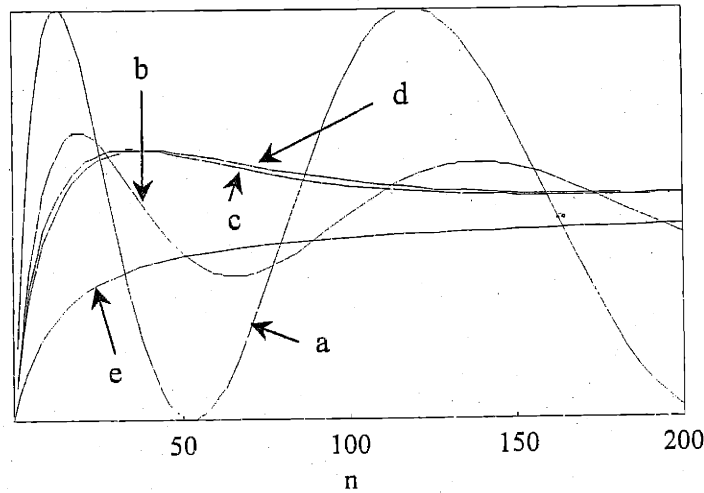


Figure 6. $\frac{1}{\langle N \rangle} \left\langle \frac{\beta_n}{T} \right\rangle$ for standing-wave configuration. (a) Monovelocity and uniform coupling along z axis and y axis (see Figure 5 for axes convention). (b) Monovelocity, standing-wave coupling along z -axis and uniform coupling along y -axis. (c) Effusive atomic beam, standing-wave coupling along z -axis and uniform coupling along y -axis. (d) Effusive atomic beam, standing-wave coupling along z -axis and Gaussian coupling along y -axis narrow slit (slit width = $25 \mu\text{m}$). (e) Same as (d) but with very wide slit. Case (e) is normalized such that for very large n its value is one-half of the maximum value of case (a). Here the most probable velocity is 370 m/sec ; finesse is 1 million; cavity mode is $42 \mu\text{m}$ and maximum coupling strength is g_0 .

By tilting the atomic beam with respect to the cavity axis, due to Doppler shift, atoms can be made to interact only with one of the two traveling waves that make up the standing wave. In this case, atom-cavity coupling does not have any variation due to the standing wave nature of

the cavity mode. If the cavity is tuned such that it is in resonance with atoms having the most probable velocity v_0 , then the frequency shift as a function of atomic velocity is given by

$$\Delta = 2\pi \frac{v - v_0}{\lambda} \sin(\theta), \quad (50)$$

where θ is the angle by which the atomic beam is tilted from perpendicular position.

The minimum tilt angle that makes atoms, with the most probable velocity, interact only with one traveling wave can be estimated roughly by requiring that the Doppler shift due to the tilt is larger than the transit time broadening. The transit time broadening for an atom with speed $v_0 = 370$ m/sec and cavity mode waist $w = 40 \mu\text{m}$ is roughly given by [14]

$$\Delta f = 2 \frac{v_0}{w} \frac{\sqrt{2 \ln 2}}{2\pi} \approx 3 \text{ MHz}. \quad (51)$$

Therefore, the minimum tilt angle is approximately

$$\theta \approx \sin^{-1} \left(\frac{\lambda}{v_0} \Delta f \right) = 4 \text{ mrad}. \quad (52)$$

For traveling-wave interaction with an effusive atomic beam injected through a slit of height Δy , Eq.(44) becomes

$$\left\langle \frac{\beta_k}{T} \right\rangle = \frac{1}{\Delta y} \int_{-\frac{\Delta y}{2}}^{\frac{\Delta y}{2}} \int_0^\infty v \frac{4 \langle N \rangle v^2}{\sqrt{\pi} v_0^3} e^{-\left(\frac{v}{v_0}\right)^2} \frac{k(2g_{t0} e^{-\left(\frac{y}{w}\right)^2})^2}{\left(2\pi \frac{v - v_0}{\lambda} \sin(\theta)\right)^2 + k(2g_{0t} e^{-\left(\frac{y}{w}\right)^2})^2} \times \sin^2 \left(\frac{\sqrt{\pi} w}{v} \frac{1}{2} \sqrt{\left(2\pi \frac{v - v_0}{\lambda} \sin(\theta)\right)^2 + (2g_{0t} e^{-\left(\frac{y}{w}\right)^2})^2 k} \right) dv dy, \quad (53)$$

where g_{0t} is atom-cavity coupling for traveling wave case. It can be shown that $g_{0t} = g_0/2$. For standing-wave interaction, the electric field operator E_z is the sum of the electric field operator E_{z+} for the traveling wave moving in the positive z direction and the electric field operator E_{z-} for the traveling wave moving in the negative z direction. But E_z is given by [15, 16]

$$E_z = g_0(ae^{-i\omega t} + a^\dagger e^{+i\omega t}) \cos(kz) = g_0(ae^{-i\omega t} + a^\dagger e^{+i\omega t}) \frac{e^{+ikz} + e^{-ikz}}{2}. \quad (54)$$

After collecting terms, E_z becomes

$$E_z = \frac{g_0}{2}(ae^{-i(kz+\omega t)} + a^\dagger e^{+i(kz+\omega t)}) + \frac{g_0}{2}(ae^{-i(-kz+\omega t)} + a^\dagger e^{+i(-kz+\omega t)}) = E_{z+} + E_{z-}. \quad (55)$$

Figure 7 shows the effect of velocity distribution and Gaussian coupling along the y -direction on the oscillation of gain-per-atom term in the traveling-wave configuration. Two factors contribute to the larger oscillation in Figure 7 case (c) compared to the similar case for standing-wave configuration, Figure 6 case (d), namely, the uniform coupling constant along the z -axis and the velocity selectivity provided by the tilted cavity. These two cases are shown on a similar plot in Figure 8. Because of the larger coupling constant, the standing-wave case has larger gain per atom for small n . This makes the threshold in standing-wave case to occur, as a function of the average number of atoms in the cavity, before that in the traveling-wave-case. In addition, at the beginning, the curvature in the gain-per-atom curve for the standing-wave case is larger. This influences, as will be shown later, the intensity correlation time and makes it smaller at the threshold than that of the traveling-wave case.

We have checked the assertion that the field density operator can be factorized as in Eq. (43) by comparing the result that follows from this assertion with a result obtained differently by using our quantum trajectory simulation (QTS) code (the QTS code is discussed in the next section). Both methods give similar results. Figure 9 shows the results for $\langle n \rangle$ versus $\langle N \rangle$, photon occupation number \bar{p}_n and $g^{(2)}(\tau)$ for an effusive atomic beam.

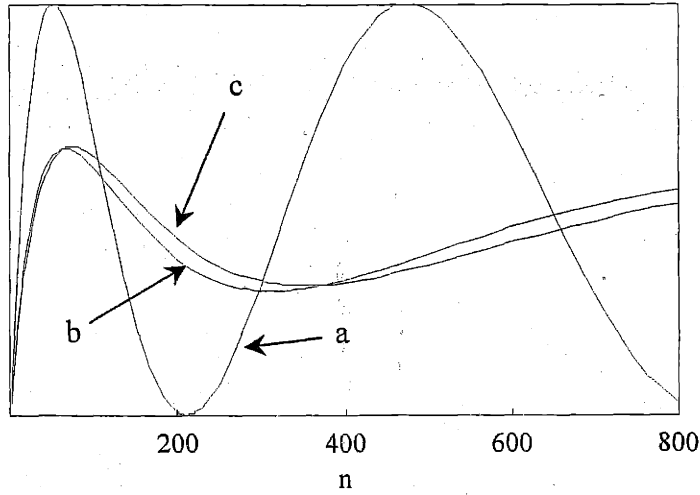


Figure 7. $\frac{1}{\langle N \rangle} \left\langle \frac{\beta_n}{T} \right\rangle$ for traveling-wave configuration. (a) Monovelocity and uniform coupling along y axis (See Figure 5 for axes convention). (b) Effusive atomic beam and uniform coupling along y-axis. (c) Effusive atomic beam and Gaussian coupling along y-axis narrow slit (slit width = 25 μm). Same parameters as in Figure 6 are used except coupling constant = $g_0/2$ and the tilt angle = 10 mrad.

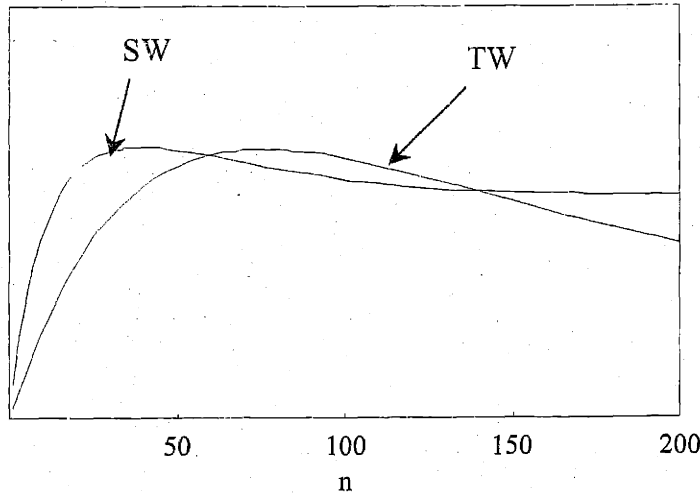


Figure 8. Comparison between $\frac{1}{\langle N \rangle} \left\langle \frac{\beta_n}{T} \right\rangle$ term for traveling-wave configuration (Figure 7 case (c)) and standing wave configurations Figure 6 case (d).

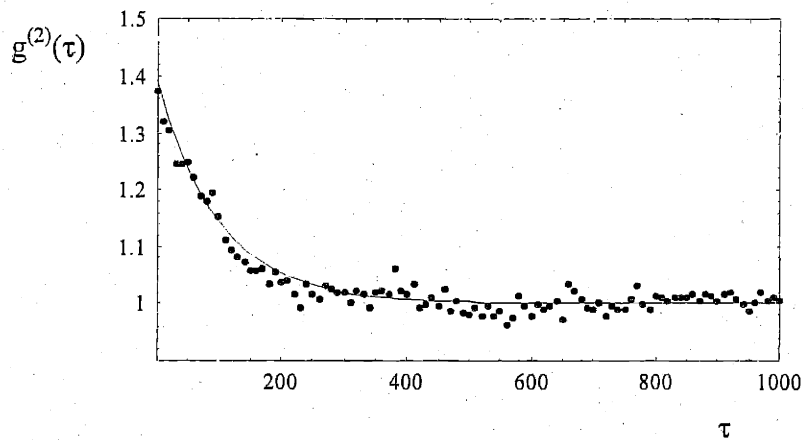
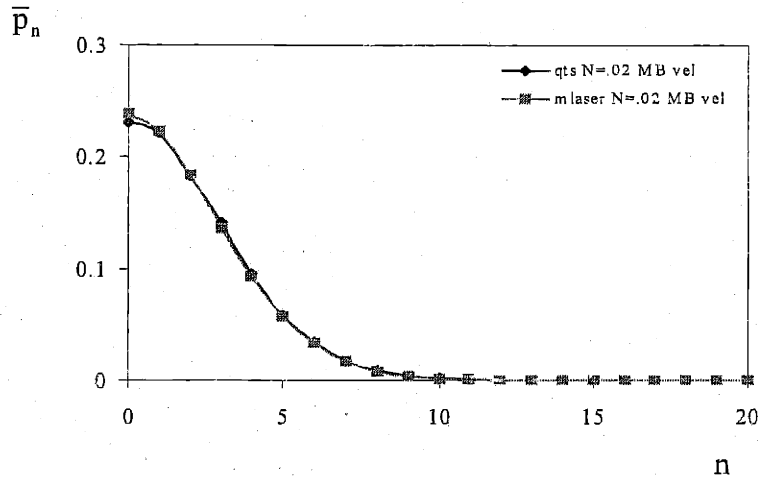
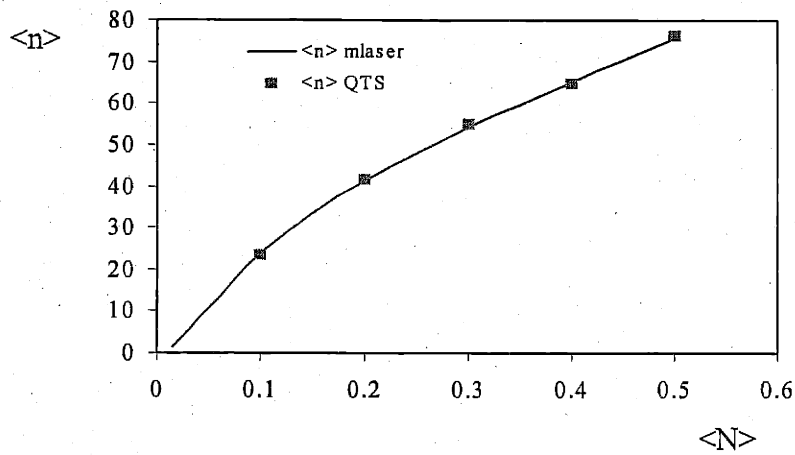


Figure 9. Comparison between microlaser theory and QTS when an effusive beam is used. Here the most probable velocity is 400 m/sec and the finesse is 50 million..

2.5- Many-atom effects in single-atom microlaser theory

A number of authors [17, 18, 19] have investigated numerically the effect of many atoms interacting at the same time with the cavity mode on the photon statistics of the microlaser. These studies find that the effect is small for the case where the interaction time between one atom and the cavity mode, t_{int} , is much smaller than the lifetime of a photon in the cavity, $1/\Gamma_c$, or $t_{\text{int}} \Gamma_c \ll 1$. This is the case for our system. In our system t_{int} for the most probable velocity is about 0.2 μsec and $1/\Gamma_c$ is about 1.2 μsec ($t_{\text{int}} \Gamma_c \sim 0.17$).

D'Ariano et al. [17] study a microlaser in which monovelocity clusters of atoms are injected into the cavity mode. Each cluster of atoms is treated as a point-like object with respect to the cavity length. It is assumed that, when a cluster of atoms leaves the cavity mode, another cluster is immediately injected into the cavity mode. So there is only one cluster of atoms at the cavity mode at all times. The number of atoms in different clusters is not the same but varies according to a Poisson distribution with an average number of N_{ave} . This model approaches the single-atom microlaser when $N_{\text{ave}} \rightarrow 0$, $t_{\text{int}} \rightarrow 0$ while keeping the injection rate, $N_{\text{ave}}/t_{\text{int}}$, fixed. The quantum trajectory method is used to evaluate the steady state solution of the average and the normalized standard deviation of the photon number distribution inside the cavity mode. N_{ave} is varied to up to 100 atoms and it is found that this model deviates from the ideal single-atom microlaser theory only when $t_{\text{int}} \Gamma_c \geq 1$.

Using this model of clustered atoms makes it possible for a large number of atoms to be incorporated in the quantum trajectory simulation. Without this trick, this simulation would be impossible to conduct with more than about ten atoms in the cavity mode. Although it is not a realistic model, it is a reasonable one for getting an educated guess of the many-atom effect on the microlaser behavior especially when $t_{\text{int}} \Gamma_c \ll 1$. Since for the case $t_{\text{int}} \Gamma_c \sim 1$, the field decays appreciably before a new cluster is injected into the cavity mode, the way atoms are clustered together may have a big influence on distorting the outcome of this model away from a realistic microlaser output [18].

Elk [18] uses another model to study the many-atom effect in the microlaser. In his model, individual atoms are injected regularly into the cavity mode. The time between any two successive atoms is adjusted such that at the same time an atom leaves the cavity, another atom enters the cavity. The master equation approach is used to find, for at most 5 atoms in the cavity mode, the steady state solution of the average, $\langle n \rangle$, and the normalized standard deviation, Q , of the photon number distribution inside the cavity. The problem is solved exactly for $N = 1$ and 2 atoms but it is solved approximately, by using subspace diagonalization, for $N = 3, 4$ and 5

atoms. $t_{\text{int}} \Gamma_c$ is varied to up to 0.5. In the range of pump parameter $\Theta \equiv g t_{\text{int}} \sqrt{\frac{N}{\Gamma_c t_{\text{int}}}} < 5$, $\langle n \rangle$ is in good agreement with that obtained from the single-atom microlaser theory. For $\Theta < 2$, Q is also in good agreement with the single-atom microlaser theory but for $2 < \Theta < 5$, Q deviates, linearly as a function of N and Θ , slightly from single-atom microlaser theory predictions. Some of this deviation in this range is attributed to the regular injection of atoms into the cavity.

Fang-Yen et al[19] study the many-atom effect using a realistic injection model: individual excited atoms are injected randomly into the cavity mode. The quantum trajectory simulation (QTS), which is briefly described at the end of this section in a separate subsection, is used to study up to 7 atoms on average in the cavity mode. Similar results as in reference [18] are reached but now with a realistic microlaser model. Figure 10 shows calculations of the average number of photon inside the cavity $\langle n \rangle$ as a function of the pump parameter

$\Theta \equiv g t_{\text{int}} \sqrt{\frac{\langle N \rangle}{\Gamma_c t_{\text{int}}}}$ using the single-atom microlaser theory and the QTS. Both methods are in

good agreement with each other over the pump parameter range shown in the figure. In our study of the many-atom effect, we use the fact that the microlaser theory produces the same photon number distribution for different values of $\langle N \rangle$ as long as we keep $\langle N \rangle / \Gamma_c$ or equivalently $\langle N \rangle F$ constant (See Eq. (28) and Eq. (70)). Figure 11 compares the single-atom microlaser theory and the QTS calculations of the Q -parameter. For $\Theta < 2$ both methods agree with each other. In our experimental studies of the microlaser, Θ is always less than 2. For $2 < \Theta < 5$, the deviations of QTS predictions become larger for larger $\langle N \rangle$. These deviations are the consequence of the following fact: since we fix the ratio $\langle N \rangle / \Gamma_c$, larger $\langle N \rangle$ means larger t_{int}

Γ_c . We would like to emphasize that it is possible to have $\langle N \rangle \gg 1$ and small deviations in Q in the range Θ between 2 and 5 when $t_{\text{int}}\Gamma_c \ll 1$.

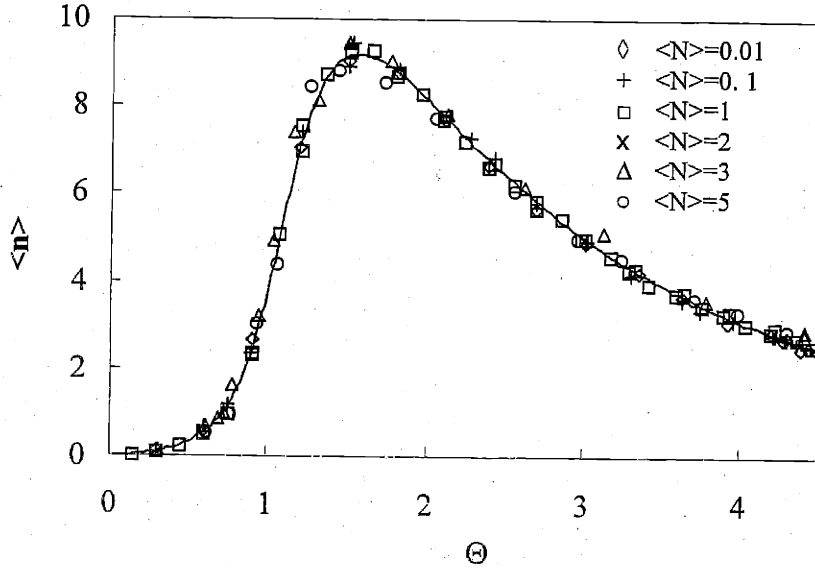


Figure 10. Comparison between the microlaser theory (solid line) and the QTS using different average number of atoms in the cavity mode $\langle N \rangle$. Here the product of the finesse and $\langle N \rangle$ is kept constant. $F\langle N \rangle = 8$ and $t_{\text{int}}\Gamma_c = 0.1 \langle N \rangle$.

The reason that the many-atom effect is small for the case $t_{\text{int}}\Gamma_c \ll 1$ is that during the lifetime of a photon, many atoms are injected at random in the cavity mode. The time one single atom has to coherently evolve with the photon and other atoms is comparatively small. Thus, any coherence between atoms is washed out. On the other hand, for $t_{\text{int}}\Gamma_c \sim 1$, a single atom has a long time to evolve coherently with other atoms during the lifetime of a photon. The decoherence process caused by the random injection of atoms is relatively small and the many-atom effect is expected to influence the photon-number distribution in this case.

It is interesting to notice that even in the derivation of the microlaser photon-number distribution, Eq. (28), Filipowicz [8] assumes that $t_{\text{int}}\Gamma_c \ll 1$. In this case, cavity decay is very small and it can be ignored while a single atom interacts with the cavity mode; the field-atom density matrix can be evolved coherently according the Jaynes-Cummings Hamiltonian.

It remains an interesting problem to investigate experimentally and to develop an analytical theory or a simple model to account for the many-atom effect in the microlaser as a function of $t_{\text{int}}\Gamma_c$.

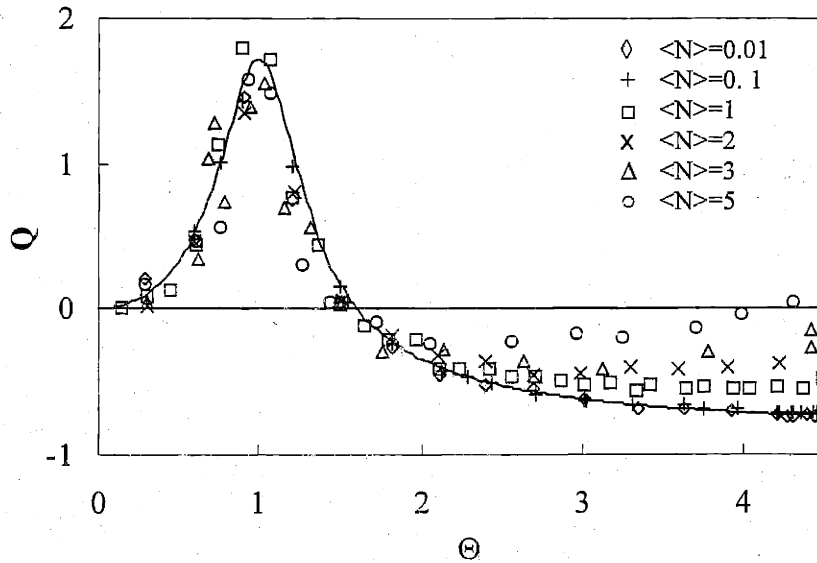


Figure 11. Comparison between the microlaser theory (solid line) and the QTS using different average number of atoms in the cavity mode $\langle N \rangle$. Here the product of the finesse and $\langle N \rangle$ is kept constant. $F\langle N \rangle = 8$ and $t_{\text{int}}\Gamma_c = 0.1 \langle N \rangle$.

2.5.1- Quantum trajectory simulation code

Quantum trajectory simulation (QTS) is a very powerful tool to analyze incoherent processes and many-atom effect in the microlaser. In this work, QTS is used to demonstrate two important facts. First, QTS is used to support the assertion that nonuniform coupling and nonuniform interaction time can be incorporated in the microlaser theory by averaging over the gain term in the microlaser as in Eq. (44) (See Figure 9). Also it is used to show that the many-atom-effect is small for the case $t_{\text{int}}\Gamma_c \ll 1$. Here a brief description of this simulation is given. More details can be found in [20,21,22].

The basic idea of the QTS is the following. For very short times, dt 's, the wave function of the microlaser is evolved coherently according to the Schrödinger equation with all incoherent processes ignored. dt should be very small compared to any incoherent process. After each coherent evolution of the wave function, the incoherent processes are examined and the wave function and the Hamiltonian are adjusted according to the result of this examination.

The Hermitian part of the microlaser Hamiltonian, which is responsible for the coherent evolution process, is given by

$$H = \hbar \sum_{j=1}^N \frac{\omega_{0,j}}{2} S_{3,j} + \hbar \omega a^\dagger a + \hbar \sum_{j=1}^N g_j (S_{+,j} a + S_{-,j} a^\dagger) + \hbar \sum_{j=1}^N \frac{\Omega_{0,j}}{2} (S_{+,j} + S_{-,j}). \quad (56)$$

Here $\omega_{0,j}$ is the atomic transition angular frequency for the j^{th} atom, ω is the angular frequency of the cavity field mode, g_j is the coupling constant between the cavity field and the j^{th} atom. a and a^\dagger are the annihilation and creation operators. $S_{3,j}$ and $S_{\pm,j}$ are the Pauli spin operators for the j^{th} atom. $\Omega_{0,j}$ is the Rabi frequency due to the pump field. The last term is ignored when the pumping process is not simulated.

The incoherent processes, which are examined at the end of each dt , are the following: a new atom enters the cavity mode; an atom leaves the cavity mode; an atom spontaneously decays to the ground state or the metastable state and finally a photon escapes from the cavity mirrors.

At the time the first atom enters an empty cavity mode, the wave function of the system becomes

$$|\Psi\rangle = (a_g |g\rangle + a_e |e\rangle)(|0\rangle + 0|1\rangle + 0|2\rangle + \dots + 0|n\rangle + \dots 0|n_{\text{max}} - 1\rangle), \quad (57)$$

where a_g and a_e are the probability amplitudes that the atom is in the ground state or the excited state respectively and $|n\rangle$ is the photon number state n . n_{max} is the maximum number of photons allowed in the simulation. In general, at the time of a new atom arrival to the microlaser, the combined new wave function of the system $|\Psi\rangle_{\text{new}}$ is simply the product of the wave function

describing the new atom and the wave function describing the microlaser just before the entry of this atom $|\Psi\rangle_{old}$,

$$|\Psi\rangle_{new} = (a_g |g\rangle + a_e |e\rangle)|\Psi\rangle_{old}. \quad (58)$$

For N atoms in the cavity mode, the number of terms in $|\Psi\rangle$ is given by $n_{max}2^N$. For example, for maximum allowable number of atoms 20 (the average number should be much smaller than 20) and $n_{max} = 100$, the size of memory needed for the terms in $|\Psi\rangle$ is about 1.7 GigaByte. Here we use a double variable for the real and imaginary part of each term. The double variable in typical C compiler needs 8 Bytes. In addition to this huge memory consumption, the time the computer processor needs to manipulate this huge number of variables becomes too long.

The arrival of atoms into the cavity mode is a random process with the average time between two successive atoms given by T . Suppose an atom arrives at $t = 0$. The probability that the next atom arrive at time between t and $t + dt$ is given by $T^{-1}e^{-\frac{t}{T}} dt$, and the probability that it arrives between $t = 0$ and t is given by

$$P_a = 1 - e^{-\frac{t}{T}}. \quad (59)$$

The arrival time of the next atom can be found by generating a random number between 0 and 1, r_a and equating it to P_a . [23] Thus, the arrival time of the next atom is given

$$t = T \ln\left(\frac{1}{1 - P_a}\right). \quad (60)$$

For a monovelocity atomic beam, the average time between two successive atoms T is simply given by

$$T = \frac{\langle N \rangle \sqrt{\pi w}}{v}, \quad (61)$$

where $\langle N \rangle$ is the average number of atoms in the cavity mode, and w is the cavity mode waist. The simulation is started by injecting the first atom at time zero and finding the arrival time of the second atom from Eq. (61). When the second atom arrives, the arrival time of the third atom is found and so on.

If the atoms have a normalized velocity distribution $f(v)$, T may be found by subdividing the velocity distribution into many velocity groups of width Δv . In each group $f(v)$ is almost constant, and T is given

$$T(v) = \frac{f(v) \Delta v \langle N \rangle \sqrt{\pi w}}{v}. \quad (62)$$

In finding the arrival times, each group is treated as an independent monovelocity beam. The arrival time of the first atom in each velocity group is found by Eq.(60) and Eq. (62). The arrival time of next atom in any velocity group is updated when an atom belonging to that group arrives.

What happens when an atom exits the microlaser? The exiting atom is no longer interacting with the field and its component may be separated. Half of the terms in the original wave function have the state of the exiting atom in the ground state and the other half have its state in the exciting state. Which half should be used to construct the new wave function? This depends on whether the exiting atom leaves the microlaser in the ground state or the excited state. This is determined by generating a random number, r_{exit} , between 0 and 1 and comparing it with the probability for the exiting atom to be in the ground state p_g . p_g is simply given by the sum of the squares of probability amplitudes in the terms in the original wave function in which the exiting atom is in the ground state. If $r_{\text{exit}} < p_g$, then the atom exits in the ground state and the new wave function is constructed from the terms in the original wave function in which the exiting atom is in the ground state. The new wave function should be renormalized.

If an atom decays to the metastable state, it will no longer be interacting with the cavity field. For this reason, this atom is treated in a similar way as an atom existing the microlaser in the excited state. An atom does not decay to the metastable state unless it is in the excited state. An atom undergoes a decay to the metastable state if its probability to decay to the metastable state is larger or equal to a random number generated between 0 and 1.

To determine whether a photon has decayed during dt , the probability for a photon to escape from the cavity mirrors $P_p = \Gamma_c dt \langle \Psi | a^\dagger a | \Psi \rangle$ is compared to a random number r_p generated between 0 and 1. If $r_p \leq P_p$, then a photon has decayed during dt and the new wave function becomes

$$|\Psi\rangle_{\text{new}} = a |\Psi\rangle_{\text{old}} \quad (63)$$

Here a is the annihilation operator. On the other hand, if $r_p > P_p$, then no photon has decayed during dt . The fact that no photon has decayed is a valuable piece of information, which tells us that the chance of having no photons in our particular sample is more likely than the average value and the number of photons is lower than the average value. This should be reflected in the wave function and the new wave function is given by

$$|\Psi\rangle_{\text{new}} = \left(1 - \frac{\Gamma_c dt}{2} a^\dagger a\right) |\Psi\rangle_{\text{old}} \quad (64)$$

Both wave functions, Eq. (63) and Eq. (64), should be renormalized. The following simple example might help in understanding why we need to adjust the wave function when no photon is detected during dt . Let us consider the following initial wave function which has an equal superposition of the zero-photon state and the one-photon state.

$$|\Psi\rangle_{\text{example}} = \frac{1}{\sqrt{2}} |0\rangle + \frac{1}{\sqrt{2}} |1\rangle \quad (65)$$

This wave function tells us that if we have many identical cavities, which are prepared identically such that the state of each cavity is given by the above wave function, then half of these cavities will have no photon inside them and the other half will contain one photon inside each cavity. Suppose we select a sample of these cavities and we want to test whether it has no photon or one photon inside it. If we wait for a very long time compared to the lifetime of a photon inside the cavity and we are not able to observe any photon, then we can say with almost absolute certainty that there is no photon inside this particular sample. This is why we need to adjust the amplitudes of the wave function as in Eq (64) every time, during dt , we observe no photon. After normalizing Eq (64), the magnitude of the zero-photon state increases and the magnitude of non-zero-photon state decreases.

Spontaneous emission to the ground state is treated in a similar way as the cavity decay. The probability for the j^{th} atom to decay to the ground state, which is given by $P_s = \Gamma_a dt \langle \Psi | S_{+,j} S_{-,j} | \Psi \rangle$ is compared to a random number, r_s , generated between 0 and 1. Here Γ_a is the spontaneous emission rate to the ground state. If $r_s \leq P_s$ then the atom has decayed to the ground state and the new unnormalized wave function is given by

$$|\Psi\rangle_{\text{new}} = S_{-,j} |\Psi\rangle_{\text{old}} \quad (66)$$

If $r_s > P_s$ then the atom has not decayed to the ground state and the new un-normalized wave function is given by

$$|\Psi\rangle_{\text{new}} = \left(1 - \frac{\Gamma_a dt}{2} S_{+,j} S_{-,j}\right) |\Psi\rangle_{\text{old}} \quad (67)$$

Figure 12 shows a flow diagram of the QTS program. The program is asked to inject a predetermined number of atoms, `tot_atom_count`. Typically `tot_atom_count` is about 30,000 atoms. If the time t is larger than the arrival time of the next atom, `next_entry_time`, a new atom is injected into the microlaser. Here the `next_entry_time` of the next atom and the properties of the new atom are calculated. The following properties are calculated: atom exit time, atom excitation status and atom cavity coupling. In addition, the actual number of atoms in the cavity

N_{atom} as well as the wave function space are updated. If there are atoms in the microlaser, then the wave function is coherently evolved for dt and the time is updated. Then spontaneous decay to ground state and to the metastable state (D state) and atom exiting the microlaser are treated. If the cavity is empty, $N_{\text{atom}} = 0$ and $n_{\text{mean}} = 0$, the time is updated to the arrival time of the next atom. Otherwise, the photon decay is examined and the photon number distribution is calculated. Different interesting quantities are not recorded except after some time T_2 . T_2 is chosen such that the microlaser reaches a steady state.

2.6- Rate-equation model

A physical picture that describes, in a simple terms, the microlaser can be obtained from a simplified model based on the rate-equation. This model gives good predictions for the average number of photons inside the cavity as well as the intensity correlation time obtained from the $g^{(2)}(\tau)$ measurements.

The rate equation for our microlaser is obtained by equating the rate of change of the average number of photons inside the cavity to the difference between rate of gain and rate of loss. This can be written as

$$\frac{d}{dt} \langle n \rangle = \text{rate of gain} - \Gamma_c \langle n \rangle. \quad (68)$$

Here $\Gamma_c \langle n \rangle$ is the rate of loss due to cavity damping. For an ideal case, where we have a uniform coupling and monovelocity fully inverted atoms injected into the cavity mode at a rate $1/T$, the rate of gain is given by

$$\text{rate of gain} = \frac{1}{T} \sin^2(\sqrt{\langle n \rangle + 1} g t_{\text{int}}), \quad (69)$$

where T is the average time between two successive atoms, and is given by

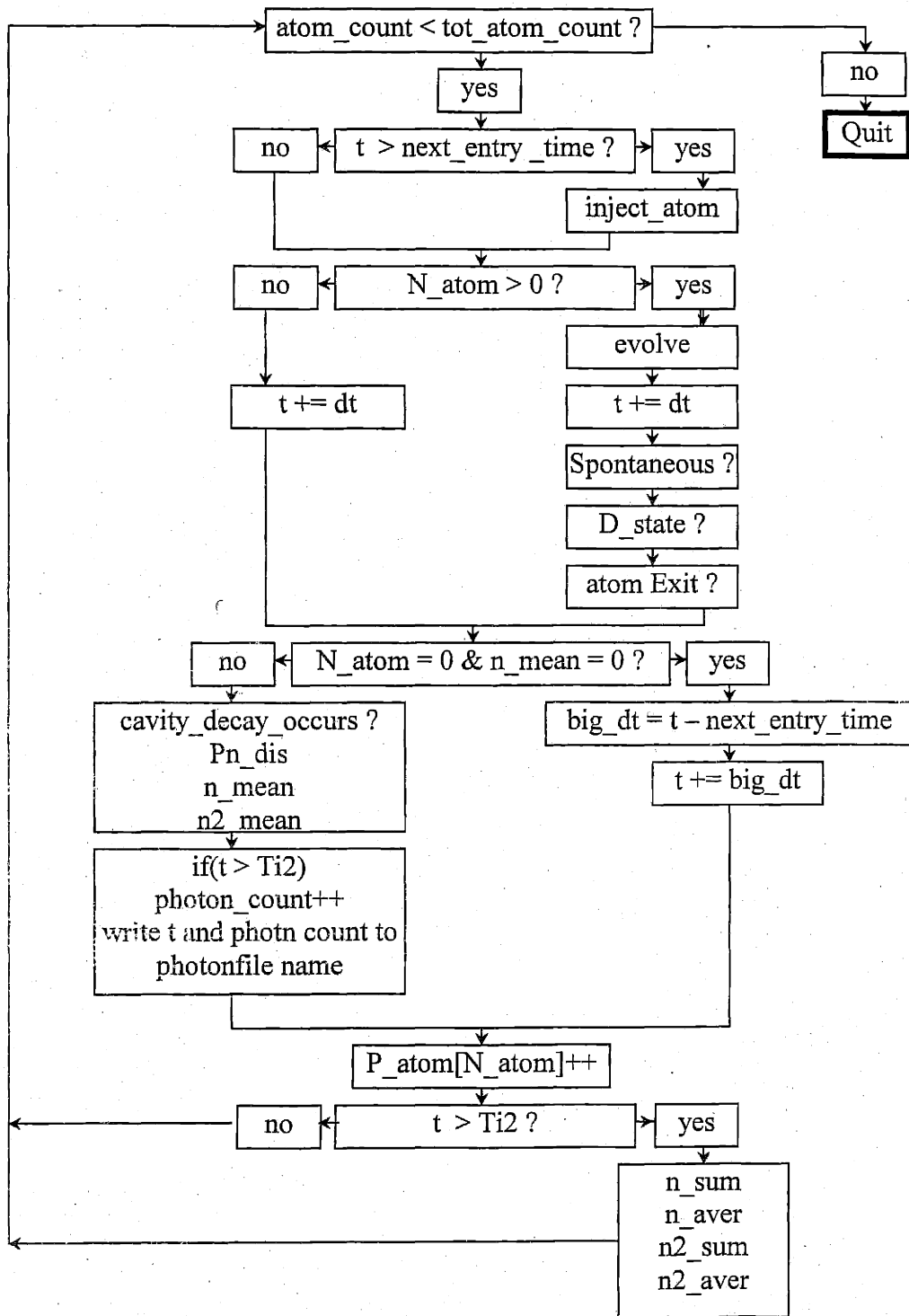


Figure 12. A flow diagram of the quantum trajectory simulation code.

$$T = \frac{t_{\text{int}}}{\langle N \rangle}, \quad (70)$$

where $\langle N \rangle$ is the average number of atoms inside the cavity mode.

For nonuniform coupling or for velocity distribution, the rate of gain can be obtained by averaging over coupling or velocity distribution as shown previously. Here we will use Eq. (69) to demonstrate the suitability of rate-equation model. By dividing Eq. (68) by average number of atoms inside the cavity mode, we obtain the rate of change per $\langle N \rangle$ as follows

$$\frac{1}{\langle N \rangle} \frac{d}{dt} \langle n \rangle = \frac{1}{t_{\text{int}}} \sin^2(\sqrt{\langle n \rangle + 1} g t_{\text{int}}) - \frac{\Gamma_c}{\langle N \rangle} \langle n \rangle. \quad (71)$$

For the steady state case, Eq. (71) becomes

$$0 = \frac{1}{t_{\text{int}}} \sin^2(\sqrt{\langle n \rangle + 1} g t_{\text{int}}) - \frac{\Gamma_c}{\langle N \rangle} \langle n \rangle. \quad (72)$$

This equation can be obtained from the microlaser equation for the photon occupation number:

$$\bar{p}_n = \frac{1}{T\Gamma_c} \frac{\beta_n}{n} \bar{p}_{n-1}. \quad (27)$$

The average number of photons usually occurs near the peak of the photon number distribution. This is especially true when $\langle n \rangle \gg 1$ for which the photon number distribution is almost symmetric. The peak of the photon number distribution in Eq. (27) can be found by assuming n to be a continuous variable and by setting $\bar{p}_n = \bar{p}_{n-1}$. This leads to

$$1 = \frac{1}{T\Gamma_c} \frac{\beta_{\langle n \rangle}}{\langle n \rangle}. \quad (73)$$

This is the same as Eq. (72) when $\sqrt{\langle n \rangle + 1}$ is replaced by $\sqrt{\langle n \rangle}$ in Eq. (72). We thus expect the rate equation to give an accurate prediction for $\langle n \rangle \gg 1$.

Eq. (72) can be solved graphically as shown in Figure 13. The gain-per-atom curve is independent of the number of atoms in the cavity $\langle N \rangle$. When $\langle N \rangle$ is very small, the loss-per-atom line has a very large slope and it is almost vertical. As $\langle N \rangle$ increases, the slope decreases. For small number of $\langle N \rangle$, there is only one solution while for bigger $\langle N \rangle$ there are a number of solutions. The rate equation is able to predict stable and unstable solutions. Suppose a fluctuation in the system occurs which makes the number of photons inside the cavity $\langle n \rangle$ slightly different from the steady-state value. A solution is stable if, according to Eq. (71), $\langle n \rangle$ is brought back to the steady state value. For example, consider solution 1 in Figure 13. When a fluctuation makes $\langle n \rangle$ larger than the steady-state value, the gain-per-atom term becomes smaller than the loss-per-atom term and their difference in Eq. (71) becomes negative. This means that $\langle n \rangle$ decreases as a function of time and is brought back to the steady state value. On the other hand, for solution 2 in Figure 13, when a fluctuation makes $\langle n \rangle$ larger than the steady-state value, the gain-per-atom term becomes larger than the loss-per-atom term and their difference in Eq. (71) becomes positive. This implies that $\langle n \rangle$ is pushed away from the steady-state value and thus solution 2 is not stable.

Figure 14 shows solutions from the microlaser theory (Eq. (31) zero detuning) and the rate equation for $\langle n \rangle$ versus $\langle N \rangle$ (Eq. (72)). The parameters used here are almost the same as our experimental values. The agreement is excellent except at the beginning. However, the rate equation model cannot predict the position of the sharp jump, which is anticipated by microlaser theory to occur around $\langle N \rangle \approx 210$ for the parameters used here.

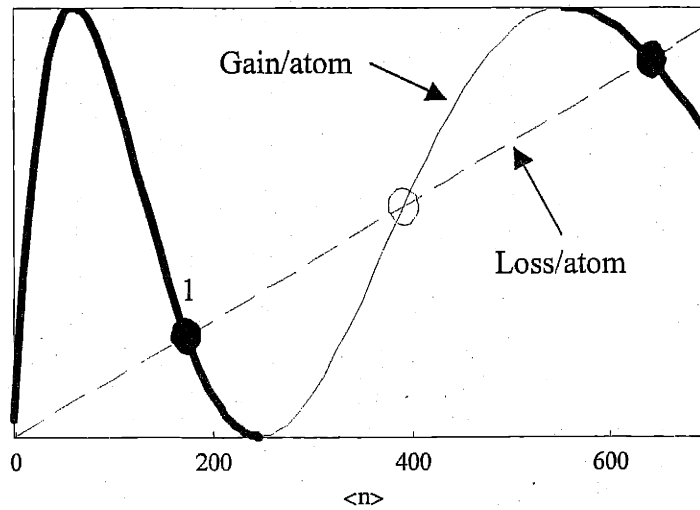


Figure 13. Graphical solution of Eq. (72). Thick curve regions indicates stable solution ranges. Circle indicates possible solutions. This plot is generated using finesse = 1 million, velocity = 400 m/sec, cavity length = 1 mm, cavity mode waist = 42 μm , traveling wave coupling and $\langle N \rangle = 120$.

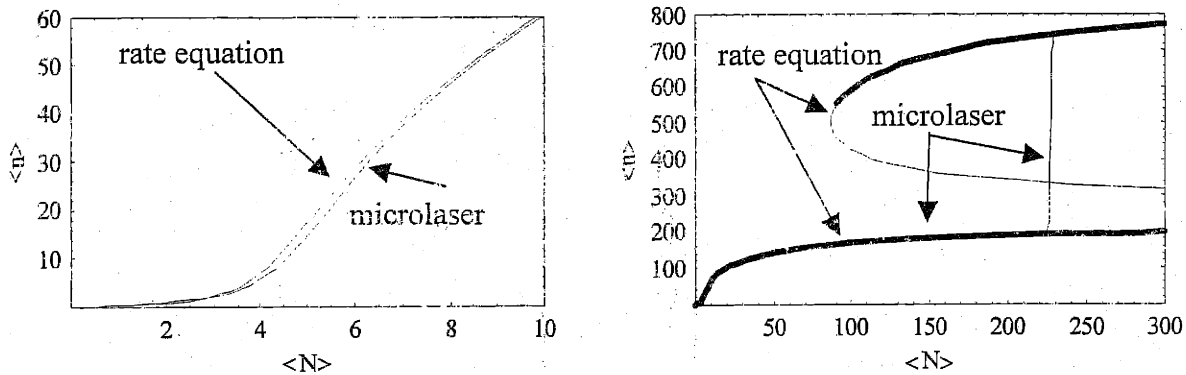


Figure 14. Microlaser theory and rate equation theory prediction for average number of photon as a function of average number of atoms $\langle N \rangle$. Thick curve regions indicates stable solution ranges of the rate equation. While the rate equation model predicts multi-value solutions of $\langle n \rangle$ as a function of $\langle N \rangle$, the microlaser theory predicts a single-value solution with a sharp jump between different rate-equation solutions. This plot is generated using same parameters as in Figure 13.

We can use Eq. (71) to model the dynamics of our system approximately. We show that $g^{(2)}(\tau)$ reflects the average response of the system when it is disturbed slightly from the steady-state. Our system spends most of its time at or near the steady state solution of Eq. (68). Let us assume at time $t = 0$, a small disturbance occurs causing the number of photons inside the cavity

to change from the steady state value n_{ss} to $n_{ss} + \delta n$. We mean by small disturbance that the disturbance in photon number δn is of order of $\sqrt{n_{ss}}$. Then according to Eq. (68), the number of photons inside the cavity evolves as follows:

$$n(t) = n_{ss} + \delta n f(t), \quad (74)$$

where $f(t=0) = 1$ and $f(t \rightarrow \infty) = 0$. $g^{(2)}(\tau)$ is given by (See Eq. (1))

$$g^{(2)}(\tau) = \frac{\langle n(\tau)n(0) \rangle}{n_{ss}^2} = \frac{\langle (n_{ss} + \delta n f(\tau))(n_{ss} + \delta n) \rangle}{n_{ss}^2}. \quad (75)$$

Expanding the numerator, this equation leads to

$$g^{(2)}(\tau) = \frac{\langle (n_{ss}^2 + n_{ss} \delta n + \delta n n_{ss} f(\tau) + \delta n \delta n f(\tau)) \rangle}{n_{ss}^2} = \frac{n_{ss}^2 + \langle \delta n \delta n f(\tau) \rangle}{n_{ss}^2}, \quad (76)$$

where we use the fact that the average of these disturbances is zero, $\langle \delta n \rangle = 0$. Since for a small disturbance, $f(t)$ is depends weakly on the disturbance amplitude, we can take $f(\tau)$ out of the average in the previous equation. This leads to

$$g^{(2)}(\tau) = 1 + (g^{(2)}(0) - 1)f(\tau), \quad (77)$$

where $g^{(2)}(0) = 1 + \frac{\langle \delta n \delta n \rangle}{n_{ss}^2}$ is used. Eq. (77) shows that the temporal behavior of $g^{(2)}(\tau)$ is related to average temporal behavior of the equation of motion of the system, Eq. (71), when it is disturbed slightly from the steady state values.

For our experimental parameters $g^{(2)}(\tau)$ decays to one exponentially. This is not in general the case. But, sticking to our experimental boundaries, we define the intensity correlation time t_c as the time over which the exponential part of $g^{(2)}(\tau)$ decays by $1/e$. The

length of the intensity correlation time tells us how fast our system responds to disturbances caused by a fluctuation in number of atoms or number of photons in the cavity mode. To put it in another way, t_c tells us how long our system remembers fluctuations. Figure 15 compares the intensity correlation time obtained by the microlaser theory (Eq. (1), Eq. (36) and Eq. (15) with $\Delta=0$) and by the rate equation model using Eq. (71) and Eq. (77). Here t_c is obtained by fitting an exponential decaying function to $g^{(2)}(\tau)$ obtained from the microlaser theory or the solution of Eq. (71) for initial disturbance of $\delta n = 1$. The change in t_c obtained from Eq. (71) by using initial disturbance δn within $\sqrt{n_{ss}}$ is less than 10% of that obtained for $\delta n = 1$.

An analytical form for t_c obtained from rate equation model can be obtained by linearizing Eq. (71). We know from numerical studies of this equation that it has an exponential decaying solution for our experimental parameters. The intensity correlation time t_c is obtained from the slope of Eq. (71) solution at $t=0$:

$$t_c = -\frac{1}{\text{slope at } t = 0}. \quad (78)$$

For a very small deviation Eq. (71) becomes

$$\frac{d}{dt} \delta n = \left(\frac{g}{2} \frac{\langle N \rangle}{\sqrt{\langle n \rangle + 1}} \sin(2\sqrt{\langle n \rangle + 1}gt_{int}) - \Gamma_c \right) \delta n,$$

or

$$t_c = \frac{1}{\Gamma_c \left(1 - \frac{g}{2\Gamma_c} \frac{\langle N \rangle}{\sqrt{\langle n \rangle + 1}} \sin(2\sqrt{\langle n \rangle + 1}gt_{int}) \right)}. \quad (79)$$

Eq(79) is also shown in Figure 15. There is a good agreement between Eq. (79) and solution obtained by fitting the solution of Eq.(71) with initial disturbance of $\delta n = 1$. The size of t_c is

inversely proportional to the difference between the slope of loss line and the slope of gain curve..

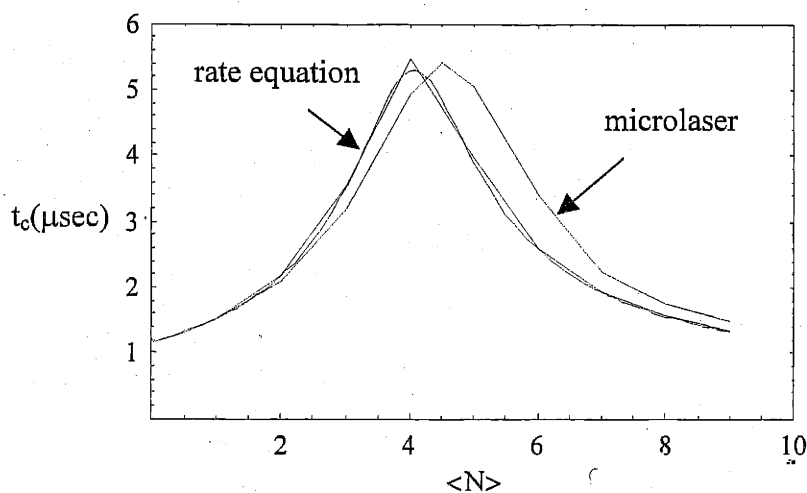


Figure 15. Microlaser theory and rate equation theory prediction for intensity correlation time as a function of average number of atoms $\langle N \rangle$. This plot is generated using finesse = 1 million, velocity = 400 m/sec and traveling wave coupling. For rate equation, two curves are shown. One curve is obtained by using an initial disturbance of $\delta n = 1$ and the other curve is obtained by using Eq. (79).

2.7- Pumping Process

Before barium atoms enter the microlaser cavity mode, they are pumped from the ground state to the excited state by a Ti:sapphire laser beam (See Figure 1 in Chapter 1). The atoms can be inverted by a constant-frequency-shift inversion process (π -pulse excitation is a special case) or by an adiabatic inversion process. As it is shown below, the constant-frequency-shift inversion process depends on the atomic velocity as well as on the laser pump intensity. This is not optimum for an atomic beam with a wide velocity distribution. Only atoms with a specific velocity satisfy the π -pulse condition and all other atoms are partially inverted. In this section, we show that in our experimental geometry, in the population inversion process, adiabatic inversion can occur, and can invert the atoms effectively and independently of their velocities.

When a two-level atom is sent through the waist of a Gaussian laser beam (See Figure 17), which is in resonance with atomic transition, the probability that the atom is pumped from the ground state to the excited state is given by [24]

$$P_e = \sin^2\left(\frac{\Omega_0}{2}t\right). \quad (80)$$

Here Ω_0 is the Rabi frequency and t is the interaction time between the atom and the laser beam which is given by

$$t = \frac{\sqrt{\pi}w_p}{v}, \quad (81)$$

where w_p is the waist of the laser beam and v is the atomic velocity.

The problem with this method is that the pumping process is velocity dependent. As shown in Figure 16, if an effusive atomic beam is used and the intensity of the laser beam is adjusted such that atoms with the most probable velocity are pumped fully to the excited state, then there will be a large fraction of atoms left in ground state because of their velocities. About 30% of the atoms are left in the ground state.

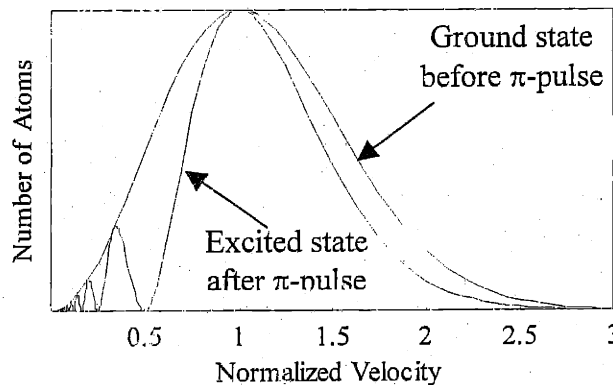


Figure 16. Excitation efficiency for an effusive atomic beam crossing the waist of a Gaussian beam. The intensity of the laser is adjusted such that atoms with most probable velocity is fully inverted.

In our experiments to monitor the pumping process (See Section 6.1), we find that the inversion of the microlaser transition is greater than that predicted by π -pulse excitation and does not exhibit the expected features. The observed behavior can be better described by adiabatic inversion.

What happens when atoms are not sent exactly through the beam waist but slightly away from the beam waist as shown in Figure 17? Due to Doppler shift, atoms experience frequency shift as they traverse the diverging pumping beam. This frequency chirp, under appropriate conditions, causes atoms to be adiabatically inverted. Before showing numerical simulations of this process, it will be shown below that this frequency shift, to a good approximation, is linear with the distance from the pump axis. For simplicity, we consider only the case where the atomic beam is perpendicular to the laser axis.

The phase front of a Gaussian beam $\Phi(x, y)$, which is depicted in Figure 17, is given by [25]

$$\Phi(x, y) = -ky + \tan^{-1}\left(\frac{y}{y_0}\right) - \frac{kx^2}{2R(y)}, \quad (82)$$

where $k \equiv \frac{2\pi}{\lambda}$, $y_0 \equiv \frac{\pi w_p^2}{\lambda}$ is the Rayleigh range or the waist length and $R(y) \equiv y\left(1 + \frac{y_0^2}{y^2}\right)$ is

radius of curvature. Here λ is the laser wavelength. The angle θ between the axis of the Gaussian beam and a vector normal to the phase front at point (x, y) can be found from

$$\theta = \tan^{-1}\left(\frac{dy}{dx}\right), \quad (83)$$

where dy/dx can be found by setting $\Phi(x, y)$ in Eq. (82) to a constant

$$\theta = \tan^{-1} \left(\frac{|y|}{-(y^2 + y_0^2) + \frac{y_0}{k} + \frac{x^2}{2} \frac{y^2 - y_0^2}{y^2 + y_0^2}} x \right). \quad (84)$$

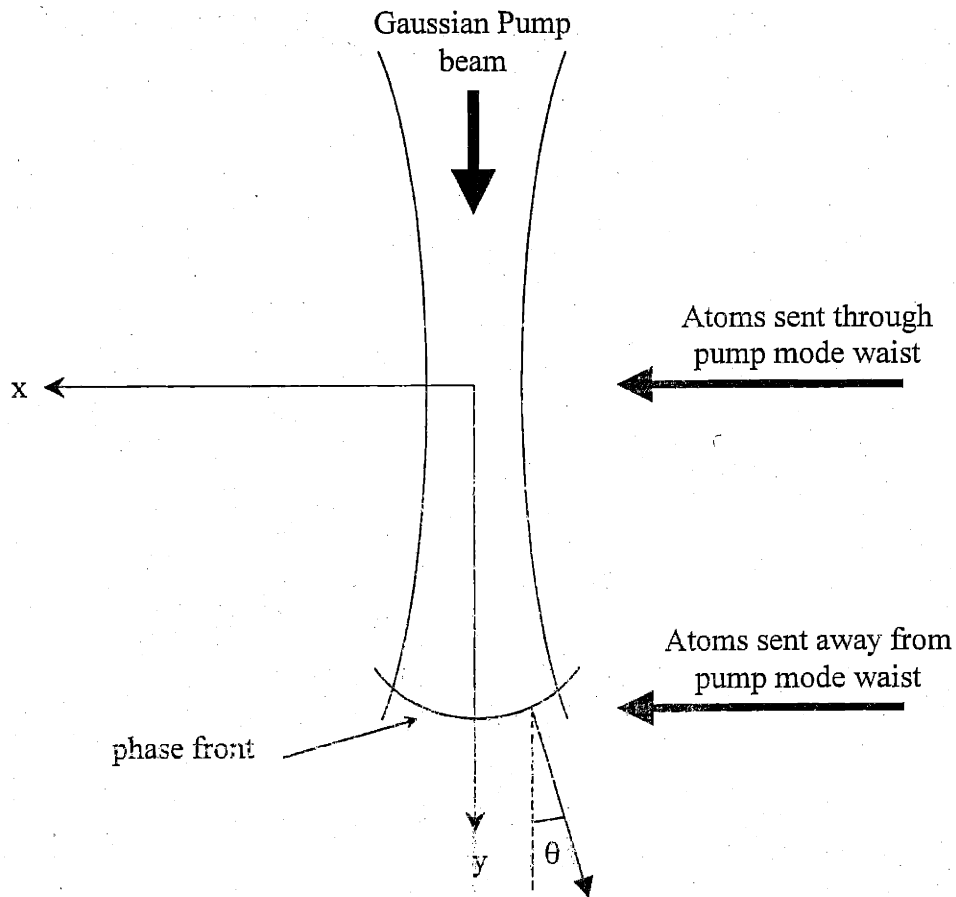


Figure 17. Pump laser beam. For simplicity, we consider only the case where the atomic beam is perpendicular to the laser axis.

The sign of the angle is chosen such that it is positive when the x-component of the vector normal to the phase front is opposite to the direction of the atomic beam velocity vector. This complicated formula can be simplified for our laser pump beam. We want to study the behavior of the angle θ as a function of the distance x from the beam axis near $y \geq y_0$. The mode waist of the laser beam is typically $w_p \approx 30 \mu\text{m}$ which implies that $k \gg y_0$. Also, for $y \geq y_0$, $x \ll y$ in regions where the electrical field has significant value. Eq. (84) becomes

$$\theta \approx -\frac{|y|}{y^2 + y_0^2} x. \quad (85)$$

Figure 18 compares the exact solution of θ , Eq. (84), and the approximate solution Eq. (85), for $y = y_0$ as a function the distance from beam axis. $w(y)$ is the radius of the beam at y which defined as the distance from the Gaussian beam axis at which the intensity falls to e^{-2} of that on the axis. $w(y)$ is given by $w(y) = w_p \sqrt{1 + \left(\frac{y}{y_0}\right)^2}$. As the right plot of Figure 18 shows, the agreement between them are excellent in regions where the electrical field has an appreciable magnitude.

If the pump laser is assumed in resonance with atoms crossing its waist, then an atom traversing the pump laser beam at y will have the following Doppler shift

$$\Delta_d = 2\pi \frac{v}{\lambda} \sin(\theta) \approx -2\pi \frac{v}{\lambda} \frac{|y|}{y^2 + y_0^2} x. \quad (86)$$

The excited level of the microlaser transition, level $6p^3P_1$, may decay back to the ground state or to a metastable state. The decay rate to the ground state is $\Gamma_g = 2\pi \cdot 50k \text{ sec}^{-1}$ and to the metastable state is $\Gamma_m = 2\pi \cdot 70k \text{ sec}^{-1}$. The optical Bloch equations describing pumping barium atoms from ground state to the excited $6p^3P_1$ by a laser beam are given by [26]

$$\dot{\rho}_{ee}(t) = -\frac{\Omega_0(t)}{2} R_2(t) - (\Gamma_g + \Gamma_m) \rho_{ee}(t), \quad (87-a)$$

$$\dot{\rho}_{gg}(t) = +\frac{\Omega_0(t)}{2} R_2(t) - \Gamma_g \rho_{ee}(t), \quad (87-b)$$

$$\dot{\rho}_{mm}(t) = \Gamma_m \rho_{ee}(t), \quad (87-c)$$

$$\dot{R}_2(t) = \Delta R_1(t) + \Omega_0(t) (\rho_{ee}(t) - \rho_{gg}(t)) - \frac{\Gamma_g}{2} R_2(t), \quad (87-d)$$

$$\dot{R}_1(t) = -\Delta R_2(t) - \frac{\Gamma_g}{2} R_1(t), \quad (87-e)$$

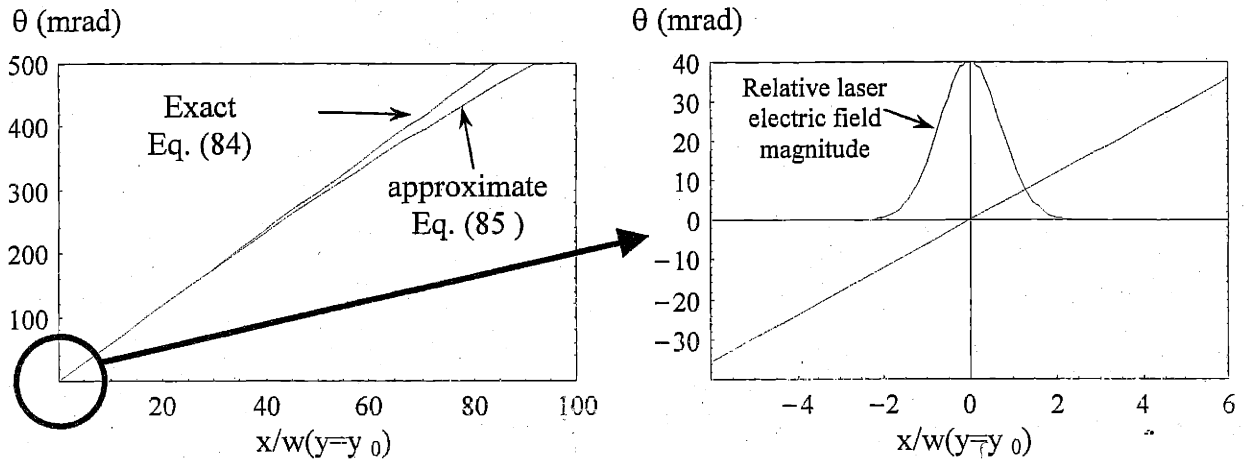


Figure 18. Left plot compares the exact solution Eq. (84) and the approximate solution Eq. (85) of θ for $y=y_0$ as a function the distance from beam axis, x . Right plot shows the relative magnitude of the electric field of the Gaussian beam along with the change in the angle θ .

where ρ_{ee} , ρ_{mm} and ρ_{gg} are the population probability of the excited state, metastable state and the ground state respectively. $R_1 \equiv (\rho_{eg} + \rho_{ge})$ and $R_2 \equiv i(\rho_{ge} - \rho_{eg})$. ρ_{eg} and ρ_{ge} are the density matrix elements between the ground state and the excited states. Δ is the atomic-laser detuning, which is given by

$$\Delta \equiv \omega_l + \Delta_d - \omega_a, \quad (88)$$

where ω_l is the laser angular frequency and ω_a is the atomic transition angular frequency. The on-resonance Rabi frequency $\Omega_0(t)$ is given by

$$\Omega_0(t) = \Omega_0 e^{-\frac{vt}{w(y)}} = \sqrt{\frac{i}{2i_s}} \Gamma_g e^{-\frac{vt}{w(y)}}, \quad (89)$$

Where Ω_0 and i are the Rabi frequency and the laser intensity at the axis of the Gaussian laser beam. The saturation intensity of the atomic transition i_s is given by

$$i_s = \frac{\pi h c}{3 \lambda^3} \Gamma_g = 13 \mu\text{W} / \text{cm}^2. \quad (90)$$

Here $\lambda = 791 \text{ nm}$ is the wavelength of the atomic transition.

Figure 19 shows simulation results for the ground state population ρ_{gg} as a function of laser pump intensity and Figure 20 shows it as a function of atomic velocity. When the distance from the pump beam waist becomes larger, the large variation in ρ_{gg} as a function of the laser intensity or atomic velocity disappears. It is preferable to send the atomic beam slightly away from the pump waist because it is more efficient and insensitive to the laser intensity drift.

The following geometrical picture may help in visualization the difference between the adiabatic inversion process and the ordinary pumping process in which atom-laser frequency shift is kept constant. For simplicity let us ignore the damping processes in Eq. (87). This is a fairly good assumption in our case where typical damping time is about $1 \mu\text{sec}$ and typical transit time is about $0.2 \mu\text{sec}$. Eq. (87) becomes [27]

$$\frac{d}{dt} \vec{\rho} = \vec{\Omega} \times \vec{\rho}, \quad (91)$$

where $\vec{\rho} \equiv (R_1, R_2, \rho_{ee} - \rho_{gg})$ and $\vec{\Omega} \equiv (-\Omega_0(t), 0, \Delta)$. This equation says that vector $\vec{\rho}$ precesses around vector $\vec{\Omega}$ at a rate given by $|\vec{\Omega}|$. Initially, atoms are in the ground state. So $\vec{\rho}$ is pointing down along the negative z-axis direction.

For the constant-frequency-shift inversion process, the direction of $\vec{\Omega}$ is fixed. Maximum pumping occurs when $\Delta = 0$. In this case $\vec{\Omega}$ points along x-axis and $\vec{\rho}$ rotates in y-z

plane. The angle of rotation depends on the area under the pulse seen by atoms as they cross the laser beam and the inversion is given by

$$\text{inversion} \equiv \rho_{ee} - \rho_{gg} = -\cos\left(\int_{-\infty}^{\infty} \Omega_0 e^{-\left(\frac{vt}{w}\right)^2} dt\right) = -\cos\left(\Omega_0 \frac{\sqrt{\pi w}}{v}\right). \quad (92)$$

The final rotation angle of $\vec{\rho}$ can be any angle depending on the intensity of the laser beam. This is depicted in Figure 21 by the partial circle in the y - z plane for the case $y = 0$, $v = 370$ m/sec and $i = 2 i_0$. Here, i_0 is the laser intensity at which atoms going through the pump waist experience a π -pulse.

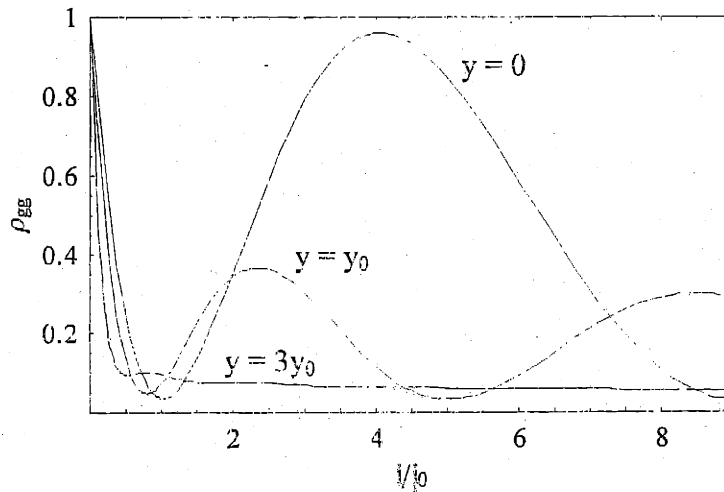


Figure 19. The ground state population ρ_{gg} as a function of laser pump intensity for atomic beams sent at different distances from the pump beam waist. Here atoms have mono-velocity of 370 m/sec. i_0 is the laser intensity at which atoms going through the pump waist experience a π -pulse.

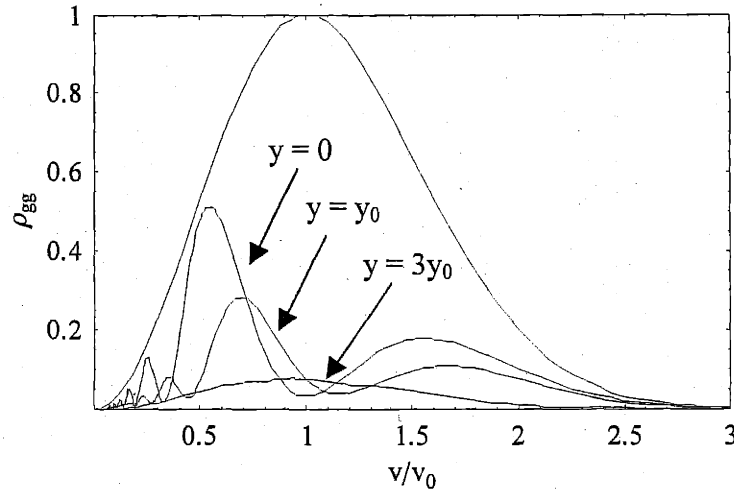


Figure 20. The ground state population ρ_{gg} as a function of atomic velocity for atomic beams sent at different distances from the pump beam waist. The most probable velocity v_0 is 370 m/sec. For $y = 0$ and $y = y_0$, i is set to i_0 where ρ_{gg} is minimum near v_0 while for $y = 3y_0$ $i = 2i_0$ is used.

In an adiabatic inversion process, $\bar{\rho}$ approximately follows $\bar{\Omega}$. This happens when the direction of $\bar{\Omega}$ changes at a rate much slower than the rate at which $\bar{\rho}$ precesses around $\bar{\Omega}$. The condition for this to happen can be found as follows. At a region where the laser beam intensity has an appreciable effect on the atoms, $i \geq 2i_s$, the direction of $\bar{\Omega}$ should move from the negative z-axis direction to the positive z-axis direction. $\bar{\Omega}$ approximately points along z-axis when its z-component, Δ , is much larger than its x-component, Ω_0 . At $i \approx 2i_s$, $\Omega_0 \approx \Gamma_g$. Let this occur when $x \approx w(y)$ then

$$|\Delta_d(x=w)| = \left| 2\pi \frac{v}{\lambda} \frac{y}{y^2 + y_0^2} w \right| \gg \Gamma_g. \quad (93)$$

During the time T_{int} over which $i \geq 2i_s$, $\bar{\Omega}$ changes its direction roughly by π . The rate at which $\bar{\Omega}$ rotates, is roughly π/T_{int} . This rate should be much slower than the precession frequency of $\bar{\rho}$ around $\bar{\Omega}$ which is given by $|\dot{\bar{\rho}}| \approx \Omega_0$:

$$\frac{\pi}{T_{\text{int}}} \approx \frac{\pi}{2w} \approx \frac{v}{w} \ll \Omega_0 \quad (94)$$

Figure 21 shows numerical solutions of Eq. (90) for $y = 3 y_0$, $v = 370$ m/sec and $i = 2 i_0$. For a laser mode waist of $30 \mu\text{m}$, $w(3 y_0) = 95 \mu\text{m}$, $v/w(3 y_0) = 4 \times 10^6 \text{ sec}^{-1}$, $\Omega_0 = 10 \times 10^6 \text{ sec}^{-1}$ and $\Delta_d(x = w) = 23 \times 10^6 \text{ sec}^{-1}$. The tip of $\bar{\rho}$ lies near the plane in which $\bar{\Omega}$ is moving. When the conditions Eq. (92) and Eq. (93) are satisfied, the final position $\bar{\rho}$ is near the positive z-axis, and atoms are almost on the excited state irrespective of their velocities or the intensity of the laser beam.

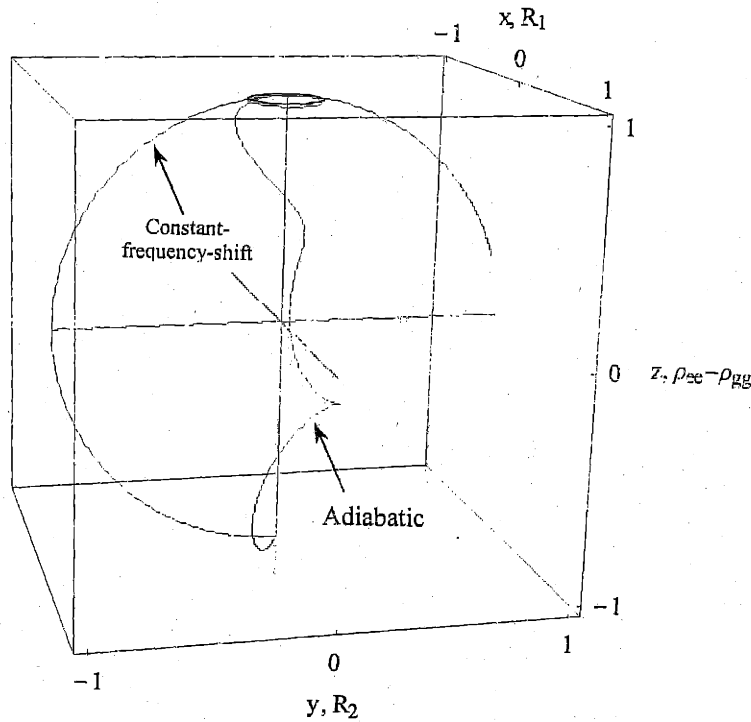


Figure 21. Comparison between adiabatic inversion process ($y = 3 y_0$) and constant-frequency-shift inversion process ($y = 0$ and $\Delta = 0$). This plot is a numerical simulation of Eq. (90) for $v = 340$ m/sec and $i = 2 i_0$.

2.8- References

- [1] E. Hanbury Brown and R. Q. Twiss, *Nature* **177**, 27 (1957).
- [2] L. Mandel and E. Wolf, *Optical Coherence and Quantum Optics* (Cambridge University Press, New York, 1995), p.487 and p. 578.
- [3] D. F. Walls and G. J. Milburn, *Quantum Optics*(Springer, New York, 1995), p. 124.
- [4] L. Mandel and E. Wolf, *Optical Coherence and Quantum Optics* (Cambridge University Press, New York, 1995), p.487 and p. 627.
- [5] R. Loudon, *The Quantum Theory of Light*(The Clarendon Press, Oxford, 1983) p. 220.
- [6] R. Loudon, *The Quantum Theory of Light*(The Clarendon Press, Oxford, 1983) p. 107.
- [7] L. Mandel and E. Wolf, *Optical Coherence and Quantum Optics* (Cambridge University Press, New York, 1995), p.487 and p. 706.
- [8] P. Filipowicz, J. Javanaine, and P. Meystre, *Phys. Rev. A* **34**, 3077 (1986).
- [9] L. A. Lugiato, M. O. Scully and H. Walther, *Phys. Rev. A* **36**, 740 (1987).
- [10] T. Quang , *Phys. Rev. A* **46**, 682 (1992).
- [11] S.A. Kumar and G. S. Agarwal , *Phys. Rev. A* **50**, 680 (1994).
- [12] C. W. Gardiner, *Handbook of Stochastic Methods*(Springer, Heidelberg, 1985), p.402.
- [13] N. F. Ramsey, *Molecular Beams*(The Clarendon Press, Oxford, 1985) p. 20.
- [14] Wolfgang Demtroeder, *Laser Spectroscopy Basic concept and Instrumentation*, p. 85, 2nd Edition, Springer 1998.
- [15] M. Sargent III, M. O. Scully, and W. E. Lamb, Jr. *Laser Physics* (Addison-Wesley, Reading, MA, 1974), p. 224.
- [16] R. Loudon, *The Quantum Theory of Light*(The Clarendon Press, Oxford, 1983) p. 135.
- [17] G. M. D'Ariano, N. Sterpi and A. Zucchetti, *Phys Rev. Lett.* **74**, 900(1995).
- [18] M. Elk, *Phys. Rev. A* **54**, 4351(1996).
- [19] C. Fang-Yen, A. Aljalal, C. Yu, R. R. Dasari and M. S. Feld, to be published
- [20] J. Dalibard, Y. Custin and K. Molmer, *Phys. Rev. Lett.* **68**, 580 (1992).
- [21] L. Tan and H. J. Carlmichael, *Phys. Rev. A* **46**, R6801 (1992).
- [22] C. Yang, Bachelor Thesis, Massachusetts Institute of Technology, 1995).

-
- [23] S. Lerman, Problem Solving and computation for scientists and engineers (Prentice-Hall, Inc., Englewood Cliffs,1993) p. 416.
- [24] Wolfgang Demtroeder, Laser Spectroscopy Basic concept and Instrumentation, p. 36, 2nd Edition, Springer 1998.
- [25] A. Yariv, Quantum Electronic(John Wiley and Sons, New York, 1975, 2nd Edition) p.110.
- [26] C. Cohen-Tannoudji, J. Dupont-Roc and G. Grynberg, Atom-Photon Interaction (John wiley and Sons, Inc. , 1992) p359
- [27] L. Allen and J. H. Eberly,(Dover Publications, Inc., New York, 1987) p.72.

Chapter

3 Experimental Setup

3.1- Overview

To be able to measure the degree of the second order coherence of the microlaser, we have made several necessary improvements on the original microlaser setup. First, we have built a very stable oven, which produces a stable atomic beam. Second, we have improved the cavity-locking scheme by improving its duty cycle as well as elongating the data collection period. Third, we have made the coupling between atom and cavity mode more uniform by using a very thin slit in front of the cavity mode and using traveling wave interaction. Fourth, we also have developed a new design for a multi-stop time-to-digital converter. This device is discussed in detail in another separate chapter.

We also have developed a new velocity selection scheme for the barium atom. The resulting atomic beam has about 10% of the width and more than 50 % of the height of the original effusive atomic beam. Although this scheme is useful in producing more uniform atom-cavity interaction time and a more efficient nonadiabatic inversion pumping process, we do not use this scheme in our present measurements. The reason is that the resulting flux of the atomic beam is too low and the microlaser is barely lasing. A new atomic oven design with a higher flux or a cavity with a higher finesse are needed to make this elegant scheme useful for our microlaser. This velocity scheme is discussed in a separate chapter.*

Figure 1 shows an overview of our experimental setup. Heating a piece of barium metal in the oven produces an effusive atomic beam. Two dye lasers select a narrow velocity group of ground state barium atoms (not used in present measurements). A very narrow slit forces the

* Recently, we have developed a supersonic atomic beam that has a huge flux and a narrow velocity distribution.

barium atoms to go through the middle of the Gaussian cavity mode. A CDD camera is used to align the slit with respect to the cavity mode as well as to measure the atomic density in the cavity mode. Before atoms enter the cavity mode, they are pumped by a Ti sapphire laser into the microlaser excited state. The Ti sapphire laser is locked to the atomic transition using a lamp-dip technique in a vapor cell. Our cavity mirrors are glued to a piezoelectric cylinder, which controls their separation. A probe beam from the stabilized Ti:sapphire laser is used to lock the cavity with respect to the barium atomic transition. Three acousto-optic modulators are used to alternate between cavity locking mode and microlaser output mode. In cavity locking mode, the probe beam is sent to a photodiode and the signal from the photodiode is used to control the voltage on the piezoelectric cylinder. In the laser output mode, the microlaser output is sent to the start and stop detectors of the second order coherence setup. The degree of the second order coherence is built up using the multi-stop time-to-digital converter (MSTDC). A computer is used to collect data from the MSTDC as well as to control the locking AOMs.

Our experimental setup is described in detail in the following sections.

3.2- Barium atomic beam

Figure 2 shows a level diagram for the ^{138}Ba atomic levels relevant to the microlaser. The microlaser transition is between the ground state $6s^2\ ^1S_0$ and the $6p\ ^3P_1$ state. The wavelength of this transition is 791.1 nm and the width is 50 kHz. The excited state $6p\ ^3P_1$ decays primarily to the ground state and two metastable states with a branching ratio of 0.43:0.41:0.16. The lifetime of the excited state is 1.3 μsec . A keeper field, about 5 Gauss, is used so that only the sublevels $m=0 \leftrightarrow m=0$ transition is used in the microlaser. For the sublevels $m = \pm 1$ in the $6p\ ^3P_1$ state the shift is 2.1 MHz per Gauss.

The microlaser transition is too weak to be used in any density measurement of our atomic beam. Instead, the resonance transition $6s^2\ ^1S_0 \leftrightarrow 6s6p\ ^1P_1$ is used. This transition has a wavelength of 553.5 nm and width of 18.9 MHz. The upper state has a lifetime of 8.4 nsec and decays mainly to the ground state and two metastable states with a branching ratio of

0.9966:0.0025:0.0009. On average a barium atom decays to the metastable states after about 293 excitations to the upper state.[1]

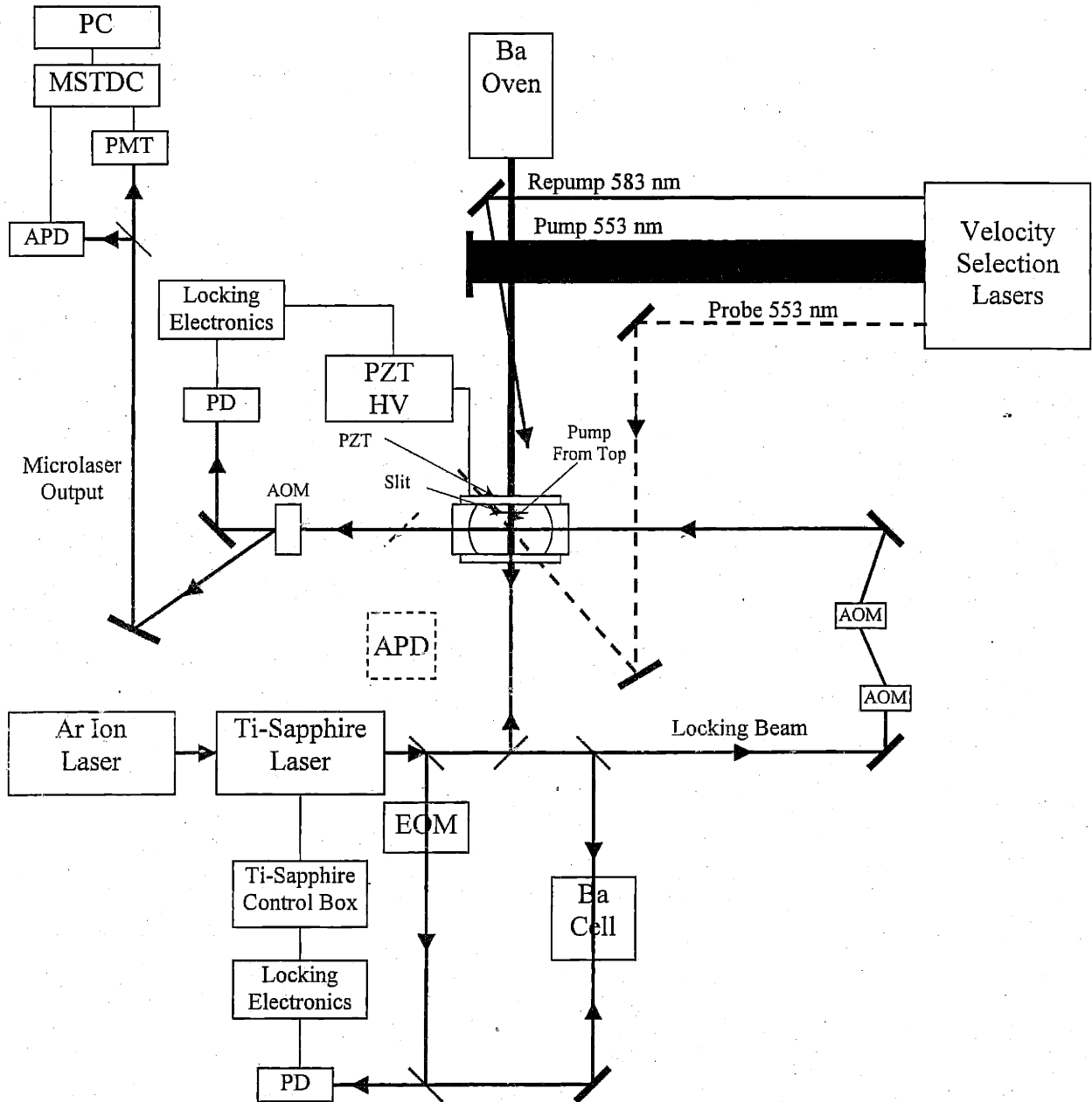


Figure 1. Overview of experimental setup. Dashed lines indicates that the component is not used during data collection but is used for diagnostic purposes.

Our atomic beam is produced effusively by heating up a natural barium metal to about 900⁰ C. The natural abundance of the ¹³⁸Ba isotope is about 72%. The energy levels of the ¹³⁸Ba isotope are well separated from that of other isotopes.

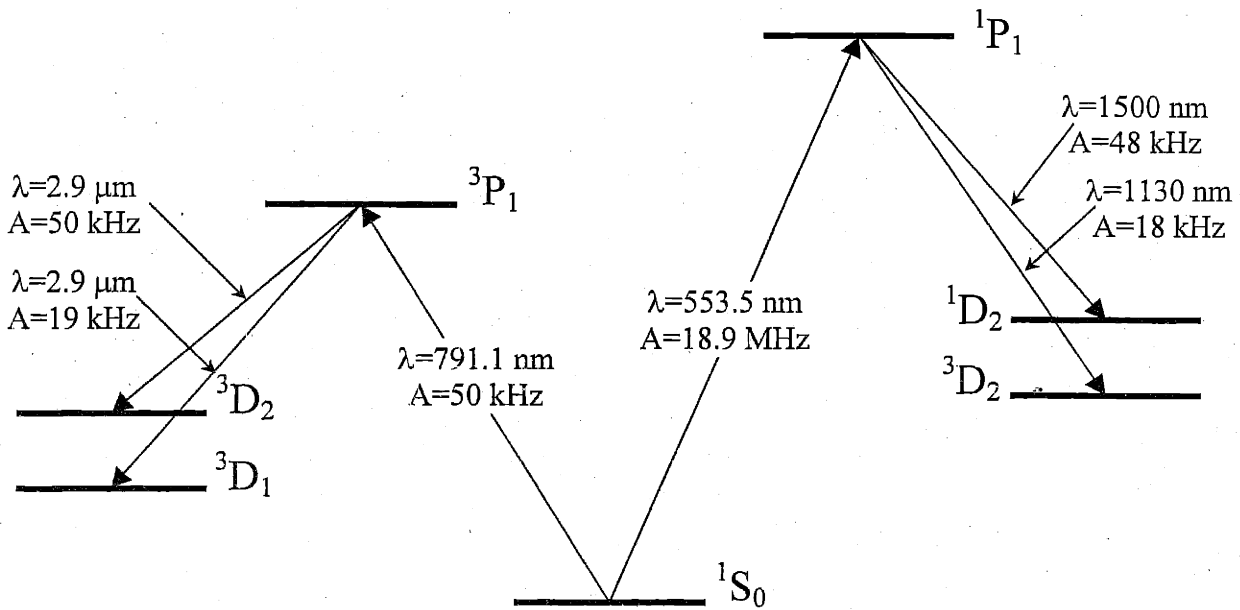


Figure 2. Relevant ¹³⁸Ba atomic levels used in the microlaser.

Figure 3 shows a schematic diagram for the atomic oven. The oven is made from Inconel alloy 600 which has a melting point of 1400⁰ C and resists oxidization up to 1175⁰ C when heated up in air. Three pairs of heaters are used (Mellen model Clam Shell Heaters 12C-205). The oven is cooled at both ends with copper blocks cooled by running cold water. Each pair of heaters is controlled separately by a temperature controller from Omega Model DP25. The temperature stability of the oven is less than 1⁰ C. Inside the oven a separator is used to separate liquid barium from the oven nozzle, which is made out of nickel (nickel is eroded by liquid barium at very high temperatures.) The nozzle is made out nickel because it has much better conductivity than Inconel alloy. To avoid nozzle clogging, the nozzle is kept about 100⁰ C hotter than the rest of the oven.

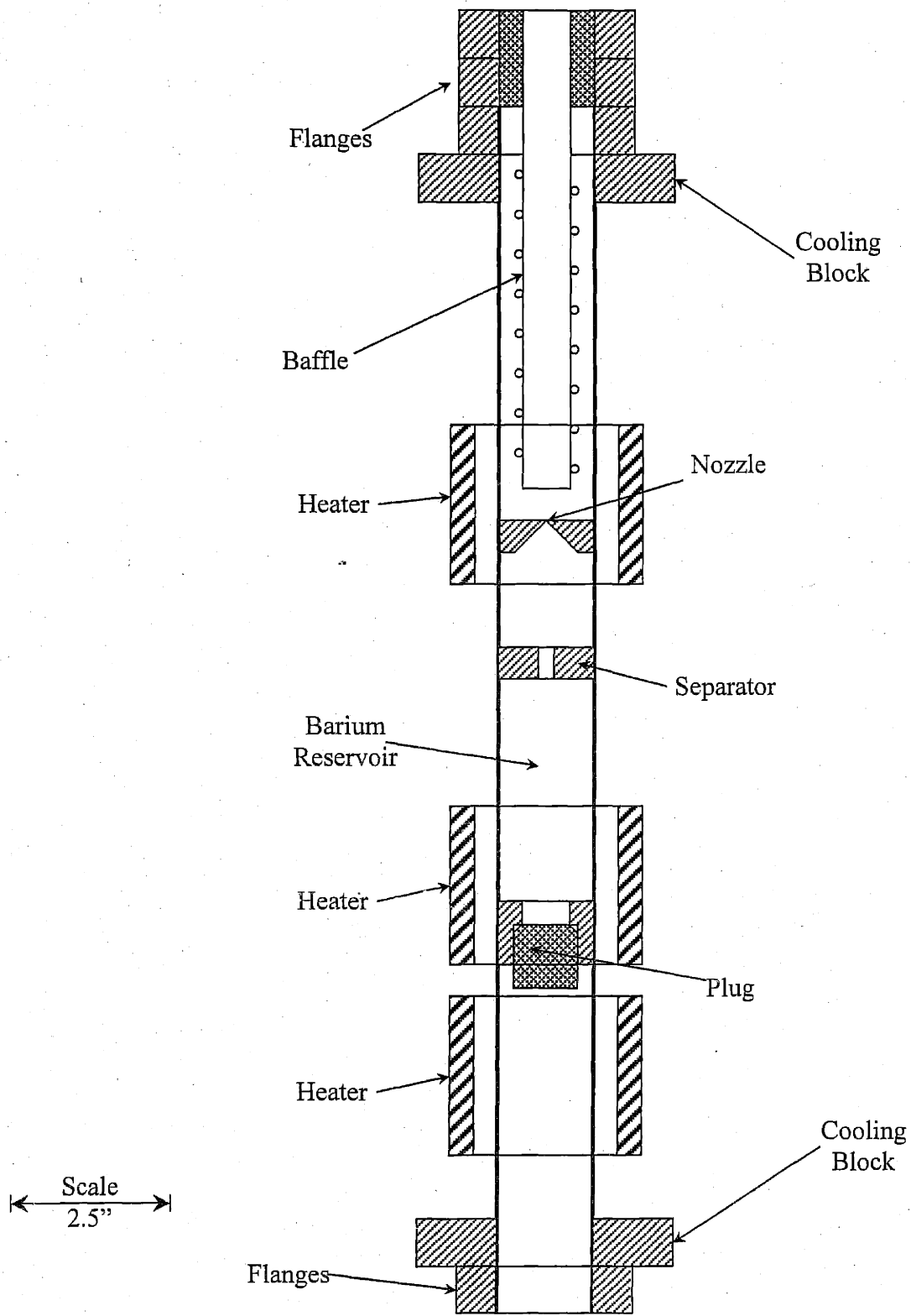


Figure 3. Schematic diagram of the atomic oven.

In front of the nozzle, a cooled baffle is used to trap barium atoms that are emitted at large angles. The baffle prevents these atoms from scattering back to the atomic beam and forming an unwanted atomic cloud in front of the nozzle. Such a cloud would make the nozzle aperture effectively much larger than the actual size and would degrade the quality of the effusive atomic beam in two ways. First, it would reduce the flux of atoms that are going in straight paths from the nozzle to the cavity. Second, atoms scattered with large angles with respect to the nozzle-cavity direction, might end up in the cavity mode. These atoms have large Doppler shifts. Thus they may not be pumped effectively and their contribution to the microlaser output is difficult to predict. The baffle is made out of a copper tube which is cooled by cold water. The tube has a diameter of 0.75" and length of 7.5". The tube is placed about 0.25" away from the nozzle.

At temperatures above 900⁰ C, the lifetime of the oven is not limited by the amount of barium that can be stored in it but by a crack that develops over time in the middle of the oven and by gradual nozzle clogging.

Typical pressure in the chamber is in the range of 10^{-7} mtorr, which is accomplished with a diffusion pump. More details about the vacuum system in our chamber can be found in [2].

The atomic beam shape is defined by the nozzle aperture and a narrow slit in front of the cavity mode. The diameter of the nozzle aperture is 1 mm and it is about 1 m away from the cavity mode. The slit is about 5 mm in front of the cavity mode. It is 500 μ m long and 25 μ m wide. Thus the atomic beam has divergence of 1mm/1 m = 1 mrad. For atoms with the most probable velocity $v_0 = 370$ m/sec, this divergence corresponds to a Doppler shift of less than 0.47 MHz. This is much smaller than the transit time broadening caused by crossing the pump laser beam or the cavity mode, which is larger than 3 MHz.

Before introducing the trapping baffle, another aperture is used to prevent most of the scattered atoms from ending up in the cavity mode. This aperture has a diameter of 2 mm and it is located about 40 cm from the cavity mode. By comparing the density of atoms in the cavity with and without this aperture, one can find the ratio of bad atoms. For high temperatures, this

ratio is as large as 50%. With a cooled baffle in front of the nozzle, the difference between the density of atoms in the cavity mode with and without the 2-mm aperture is less than 5%. This aperture is used during our measurements.

To allow a large number of atoms into the cavity mode, the slit is made long along the cavity mode axis. Also, to minimize the coupling nonuniformity due to the Gaussian mode nature normal to the atomic beam direction, the slit is made thin. (See Figure 4.) The cavity mode waist is about 42 μm and the slit width is 25 μm . This makes the coupling variation about 8% ($1 - e^{-\frac{12.5^2}{42^2}} = .08$).

A motorized rotational micro-stage is used to control the rotation of the slit with respect to the cavity axis and two linear micro stages are used to move the slit in a plane perpendicular to the atomic beam direction.

To align the slit, a 553-nm laser beam is sent along the cavity axis and is mode-matched with the 791 nm Ti:sapphire probe beam. The probe beam can be aligned precisely along the cavity mode by maximizing the cavity transmission of the $\text{TEM}_{0,0}$ mode. By observing the 553-nm fluorescence from the atomic beam on the CDD camera (model Roper Scientific model ss-C400-G1), the position of the slit with respect to the cavity mode can be found. Final slit alignment is accomplished by maximizing the microlaser output.

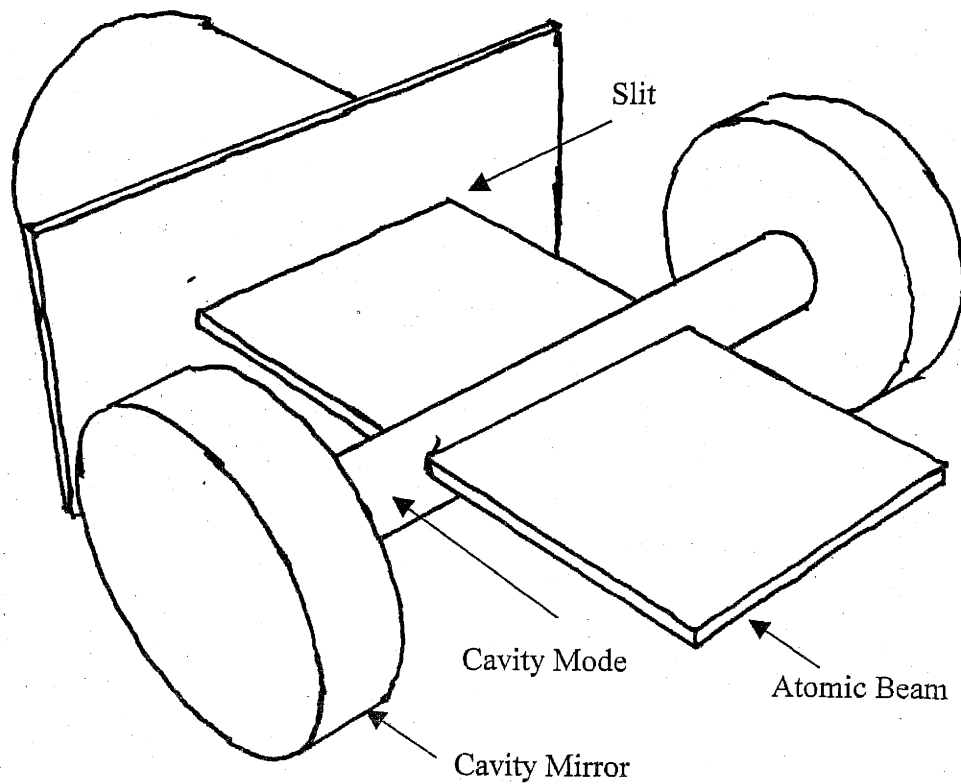


Figure 4. Thin Slit in front of the cavity mode.

3.3- Ti:sapphire laser

In the experiment, a Ti:sapphire laser is used to accomplish three tasks. It pumps atoms from the ground state to the 3P_1 excited state before they enter the cavity mode; it is used in locking the microlaser cavity relative to the microlaser transition; and it is used in measuring the finesse of the microlaser cavity. We tune the Ti:sapphire laser to 791 nm, the wavelength of the barium $^1S_0 - ^3P_1$ transition.

We use a commercial Ti:sapphire ring laser from Coherent model 899-21. It is pumped by a 10 W laser beam from an Ar-ion laser. Our Ar-ion laser is Coherent model Innova 300C. The Ti:sapphire laser has a temperature-stabilized external cavity to which the laser can be

locked. When the laser is locked to its external cavity, it has jitter of about 1 MHz and long-time drift of about 100 MHz/hour.

To use the Ti:sapphire laser in our experiment, we need to eliminate its long-term drift as well as to reduce its jitter. The stringent requirement on the laser jitter is set by the microlaser cavity linewidth, which is about 200 kHz. To be able to lock the microlaser cavity to the laser, its linewidth should be less than 200 kHz. Because of time-transit broadening, the requirement on the laser linewidth set by pumping atoms to the 3P_1 excited state is more relaxed. Since the pump beam mode waist is about 35 μm , the transit-time broadening for atoms with the most probable velocity is given by [3]

$$\Delta f = 2 \frac{v}{w} \frac{\sqrt{2 \ln 2}}{2\pi} = 2 \frac{370}{35 \times 10^{-6}} \frac{\sqrt{2 \ln 2}}{2\pi} = 4 \text{ MHz}, \quad (1).$$

where Δf is full-width at half-maximum of the transit-time broadened line, v is the atomic velocity, and w is the pump beam mode waist. This is much larger than the natural line width of the $^1S_0 - ^3P_1$ transition, which is only 50 kHz.

We eliminate long-term drifts as well as reduce the laser line width to about 50 kHz by locking the laser directly to the $^1S_0 - ^3P_1$ transition. We combine the Lamb dip method with frequency modulation (FM) spectroscopy to obtain the necessary error signal for the laser negative feedback loop. In the following two subsections, the implementation of the Lamb dip method and the FM spectroscopy to lock the Ti:sapphire laser are discussed.

3.3.1- Lamb dip method

The Lamb dip method is used to reveal Doppler-free atomic spectral lines. Due to atomic velocity distribution in a vapor cell, a Doppler-broadened absorption profile is observed when a probe laser beam is sent through the vapor cell and the probe laser frequency is scanned around an atomic transition frequency. In the optical regime, the width of this Doppler-broadened

profile is much larger than typical widths of atomic transition lines. If a pump laser beam that has the same frequency as the probe laser is sent through the vapor cell in a propagating direction counter to the probe beam, the absorption profile of the probe will be the Doppler-broadened profile, with a sharp dip at the middle where atoms have an almost zero velocity component along the probe beam direction. The width of this dip is the width of homogeneously broadened atomic lines. This dip is called the Lamb dip and it occurs because the pump and the probe interact with the same atoms; the pump excites some atoms to an excited state and makes them unable to absorb the probe beam. An atom that has a velocity component along the probe direction v_z is in resonance with the probe when the probe frequency is $\omega_{\text{probe}} = \omega_0 + kv_z$, and it is in resonance with the pump when the frequency is $\omega_{\text{pump}} = \omega_0 - kv_z$, where ω_0 is the angular frequency of the atomic transition and $k = 2\pi/\lambda$. λ is the laser wavelength. Since $\omega_{\text{probe}} = \omega_{\text{pump}}$, this atom interacts at the same time with both the pump and the probe beams only when $v_z \approx 0$.

The pump and probe beams should be well collimated and aligned so that the only homogeneous linewidth of the transition contributes to the linewidth of the Lamb dip. The natural linewidth of an atomic transition may be homogeneously broadened by collision or laser powers.

Our barium vapor cell is made of stainless steel tube with a glass window at each end. The tube has a diameter of $\frac{3}{4}$ " and length of about 12". The central part of the tube, about 2" long, is surrounded by a non-contact cylindrical heater. The heater nichrome wires are twisted so as to reduce any stray magnetic field inside the cell. barium inside the cell is heated to about 520°C . At this temperature, the absorption of the probe by the $^1\text{S}_0 - ^3\text{P}_1$ transition is about 60%. Typical probe intensity is about 5 mW/cm^2 and typical pump intensity is 20 mW/cm^2 . This produces a power broadening of about $\sqrt{1 + I/I_s}\Gamma_a \approx 2\text{MHz}$, where $I_s = 0.013\text{ mW/cm}^2$ is the saturation intensity of the $^1\text{S}_0 - ^3\text{P}_1$ transition and $\Gamma_a = 50\text{ kHz}$ is the natural linewidth of the transition. Vapor pressure inside the cell is a few millitorrs. This leads to collision broadening of about 10 kHz , which is much smaller than the power broadening. Figure 5 shows a typical Lamb dip signal.

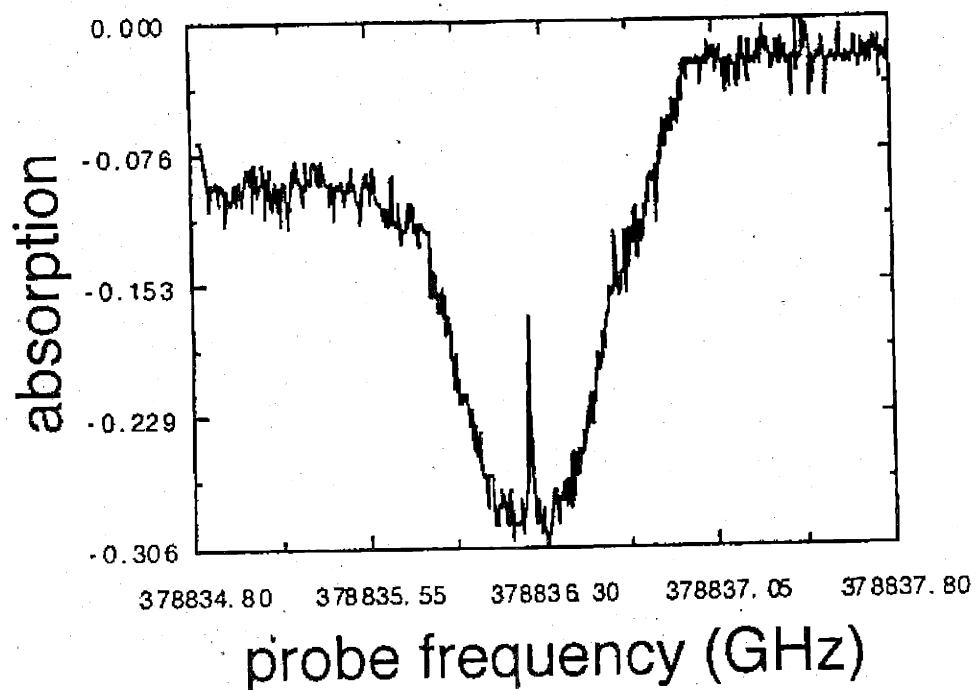


Figure 5. A typical Lamb dip signal of the $^1S_0 - ^3P_1$ transition[2].

3.3.2- FM Spectroscopy

Frequency modulation spectroscopy is a sensitive spectroscopy method used to extract tiny atomic absorption lines. It works as follows: a laser beam is sent through an atomic sample. The frequency of this laser beam is sinusoidally modulated. The amplitude of the modulation is much smaller than the linewidth of the absorption line. The signal of the transmitted laser beam is detected by a detector with response time much faster than the modulation frequency. The signal of the detector is multiplied by a signal, called the local oscillator, which is usually obtained from the same source that modulates the laser frequency. The average of this multiplication is recorded. If the phase between the signal from the transmitted beam and the local oscillator is correct, the recorded result will be proportional to the derivative of the absorption profile, as shown below. For this reason, FM spectroscopy is also sometime called derivative spectroscopy [4].

We use FM spectroscopy here not because we want to extract a very small absorption line but because we want to obtain the derivative of the absorption line profile so we can use the zero crossing point to lock our Ti:sapphire laser to the $^1S_0 - ^3P_1$ transition.

The transmission intensity of a laser beam through our vapor cell I_t is given by

$$I_t(\omega) = I_0 e^{-l\alpha(\omega)}, \quad (2)$$

where I_0 is the transmitted laser intensity when laser frequency is very far from the atomic transition, l is the interaction length of the laser beam and the vapor cell and $\alpha(\omega)$ is the absorption coefficient. In our situation $\alpha(\omega)$ has Lorentzian profile given by

$$\alpha(\omega) = \alpha_0 \frac{1}{1 + \left(\frac{\omega - \omega_0}{\Gamma_s/2}\right)^2}, \quad (3)$$

where ω_0 is the central atomic transition frequency, α_0 is the absorption coefficient at $\omega = \omega_0$ and Γ_s is FWHM of the homogeneously broadened atomic transition. Since we choose the vapor cell length l such that $\alpha_0 \ll 1$, Eq. (2) can be approximated to

$$I_t(\omega) \approx I_0 (1 - l\alpha(\omega)). \quad (4)$$

We sinusoidally modulate the laser frequency ω_L such that the resulting frequency is given by

$$\omega = \omega_L + \omega_m \cos(\Omega t), \quad (5)$$

where the modulation amplitude ω_m is much smaller than the width of the absorption linewidth Γ_s . The transmission intensity now becomes

$$I_t(\omega_L) \approx I_0(1 - I(\alpha(\omega_L + \omega_m \cos(\Omega t)))) = I_0(1 - I\alpha_0 \frac{1}{1 + (\frac{\omega_L - \omega_0 - \omega_m \cos(\Omega t)}{\Gamma_s/2})^2}). \quad (6)$$

For $\omega_m \ll \Gamma_s$, we can expand I_t around ω_L to get

$$I_t(\omega_L) \approx I_0(1 - I(\alpha(\omega_L) + \omega_m \cos(\Omega t) \frac{d}{d\omega_L} \alpha(\omega_L))). \quad (7)$$

When this signal is multiplied by $\cos(\Omega t)$ and averaged over one modulation period, only the third term survives, and the resulting signal is proportional to derivative of the absorption coefficient.

To incorporate FM spectroscopy to the Lamb dip method, the probe laser beam is sinusoidally modulated at frequency Ω while the pump beam is left without modulation. The signal from the FM spectroscopy setup has more than one zero-crossing point. The main zero-crossing point, which we use for locking, occurs at $\omega_L = \omega_0$, and two other occur at $\omega_L = \omega_0 \pm \Omega/2$. When we consider the spectrum of the modulated laser beam, the origin of these extra two zero-crossing points can be understood. If a laser beam is modulated at frequency Ω , its frequency spectrum will have, in addition to the main peak at ω_L , sidebands at $\pm n\Omega$, where n is an integer. The biggest sidebands, which are much smaller than the main peak, occur at $\pm \Omega$. Because of these side bands, an atom with non-zero velocity v_z along the probe, can interact at the same time with the pump beam and a sideband of the probe beam. $\omega_{\text{pump}} = \omega_0 - kv_z$ while $\omega_{\text{probe}} \pm \Omega = \omega_0 + kv_z$. This leads to $\omega_{\text{probe}} \pm \Omega = -\omega_{\text{pump}}$, or $\omega_L = \omega_{\text{probe}} = \omega_{\text{pump}} = \pm \Omega/2$.

We modulate our probe beam with an electro-optic modulator EOM from the Inrad model 651-254. This EOM is driven by a function generator from the Stanford Research model DS-3100 at frequency 24.600 MHz. A silicon photodiode from EG&G model FND100 is used to detect the transmitted probe beam. It is biased at -90 V and it has a rise time of 2 nsec across 50Ω load resistor. The voltage across the 50Ω load resistor is fed directly into the RF input of a balanced mixer where it is mixed with the local oscillator signal. Our balanced mixer

is from Vari-L model CM-4. The signal on the IF (intermediate frequency) output of the balanced mixer represents the DC average value of the product of the RF signal and the local oscillator. The phase between the local oscillator and the FM signal and the local oscillator is roughly determined by the choosing an appropriate coaxial cable between the function generator and the RF port of the mixer. At 25 MHz, a length of 8 m produces about a 2π phase difference. Fine adjustment of the phase is accomplished by tuning the frequency of the function generator to produce the deepest line slope at the main zero-crossing point. Figure 6 shows the output of IF output of the balanced mixer after amplification, while the Ti:sapphire laser is scanned around the $^1S_0 - ^3P_1$ transition. This zero-crossing straight line provides us with the necessary error signal for locking and stabilizing the Ti:sapphire laser around to the atomic transition.

We amplify the signal for the IF output of the balanced mixer such that it is compatible with the error signal from the laser reference cavity. We use a switch to choose between the error signal from the laser external reference cavity or from our locking setup. This enables us to lock the laser independently either to its external reference cavity or to the atomic transition.

We can determine the stability of our laser from the slope of the straight line in Figure 6 and the size of the error signal fed back to the laser when the laser is locked. The slope of the line is about 10 kHz/mV. The error signal has two components, one is regular at 660 Hz and the other is random: the size of the regular component is about 15 mV, which corresponds to 150 kHz, whose origin is the mechanical resonance of the galvo-driven tipping plate in the Ti:sapphire laser head; The size of the random component is about 5 mV RMS, which corresponds to 50 kHz. The size of the regular component of the error signal is slightly smaller than the microlaser cavity linewidth, which is about 200 kHz. Since we are able to lock the cavity to the stabilized laser, we put no effort into eliminating the regular component in the error signal.

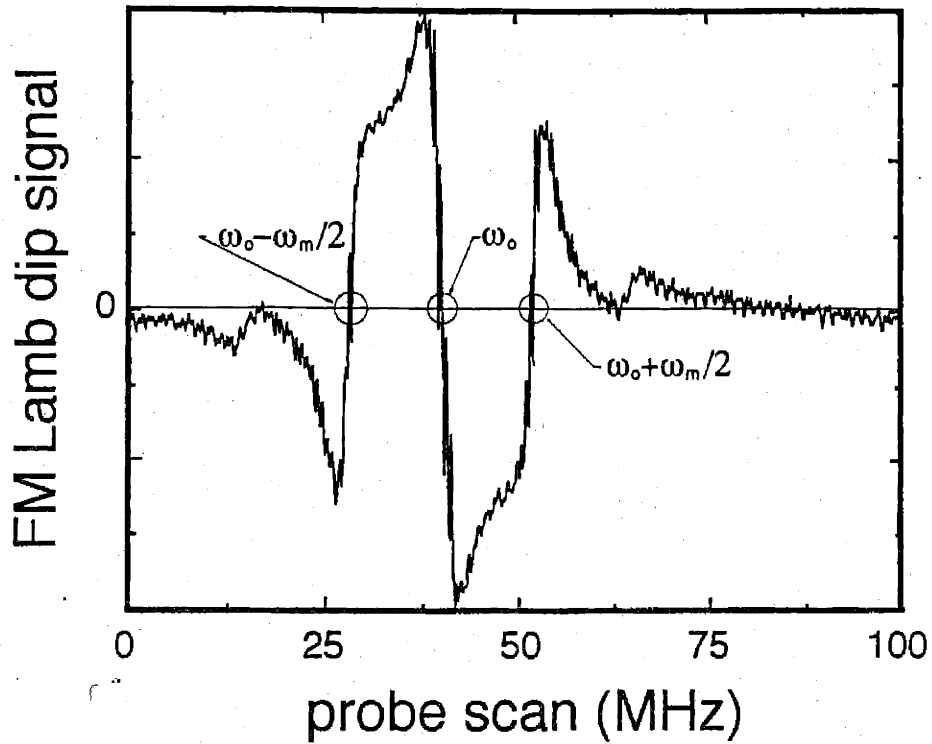


Figure 6. A typical FM lamb-dip signal. The laser is locked using the central zero crossing point[2].

3.4- Cavity

Our cavity is a single-mode resonator. We choose the distance between the cavity mirrors to be much smaller than their radius of curvature. The distance between the mirrors is $L \approx 1$ mm while their radius of curvature is $r_0 = 10$ cm. Thus, the mode waist of the middle of the cavity, w_0 , is given by

$$w_0 \approx \left(\frac{r_0 L \lambda^2}{2\pi^2} \right)^{\frac{1}{4}} = 42 \mu\text{m}, \quad (8)$$

where $\lambda = 791$ nm is the wavelength of the laser transition. The interaction time between atoms and the cavity mode is given by

$$t_{\text{int}} = \frac{\sqrt{\pi} w_0}{v} \quad (9)$$

Here v is the atomic velocity and $\sqrt{\pi} w_0$ is used as the interaction distance with the Gaussian profile. This distance is the width of a top-hat intensity profile, which has an area similar to the Gaussian profile. A top-hat profile is a profile which has a constant intensity over a specific region of the space and zero intensity elsewhere. For an atom with the most probable velocity ($v \approx 370$ m/sec) the interaction time is about $0.2 \mu\text{sec}$. The Raleigh length z_0 , which is given by

$$z_0 = \frac{\pi w_0^2}{\lambda} = 7 \text{ mm}, \quad (10)$$

is much larger than the distance between the cavity mirrors. Therefore, the spot size of the mode at the surface of the mirrors is almost equal to the mode waist at the middle of the cavity and the shape of the mode is almost cylindrical. The volume of the mode V_s for a standing wave inside the cavity is given by

$$V_s = \int_{-L/2}^{L/2} dz \sin^2(kz) \int_0^{2\pi} d\theta \int_0^\infty r dr e^{-2\left(\frac{r}{w_0}\right)^2} = \frac{\pi}{4} L w_0^2, \quad (11)$$

where z is assumed to be along the cavity axis and $k = 2\pi/\lambda$. Thus the atom-cavity coupling is given by

$$g_0 = \frac{\mu}{\hbar} \sqrt{\frac{2\pi\hbar\omega}{V}} = 0.33 \text{ MHz}, \quad (12)$$

where μ is the dipole moment matrix element of the laser transition, \hbar is the Planck constant, ω is the angular frequency of the laser transition, and V is the volume of the mode.

Our cavity mirrors are made by Research Electro Optic, Inc. The fused silica mirror substrate is first polished such that its RMS roughness is in sub angstrom range. Then the substrate is coated, using an ion beam, with 45 dielectric layers, each of which has an optical thickness of a quarter wave. These 45 dielectric layers are built out of two types of dielectric layers stacked in alternating order. One type of layer is made of silicon dioxide (SiO_2), which has a higher index of refraction ($n=2.1$) than the other type which is made of tantalum pentoxide (Ta_2O_5) $n=1.48$. The mirror substrate has a diameter of 4 mm and a height of 8 mm. Its uncoated end is wedged at a 4-degree angle to the normal angle so that reflections from this end do not interfere with the coated surface when the cavity is aligned. The mirrors are inserted and glued to stainless steel holders. (See Figure 9.) Each mirror holder has three symmetrically protruded edges. To eliminate any stress-related birefringence, these edges are machined such that they just touch the mirror substrate without exerting any stress on the substrate. A torr-seal epoxy is applied in the hollow space between the substrate and the holder.

A detailed characterization of these mirrors was accomplished in our lab [5]. The transmission T , absorption A , and scattering S of these mirrors were measured to be about 0.5 parts per million (ppm), 0.3 ppm and 2.7 ppm, respectively, while the finesse of the cavity is measured routinely using the ring-down technique.

The finesse of a cavity, F , is defined as the ratio between its free spectral range FSR and the full width at half maximum of its transmission peak $\Delta\nu_t$:

$$F = \frac{FSR}{\Delta\nu_t}. \quad (13)$$

Thus, the finesse is a measure of the resolving power of the cavity. The free spectral range of a cavity is defined as the frequency difference between two successive axial transmission modes, and is given by $c/2L$. The lifetime of a photon inside the cavity mode T_c is

$$T_c = \frac{1}{2\pi\Delta\nu_t}. \quad (14)$$

The finesse can be rewritten as

$$F = \pi \frac{T_c}{L/c}. \quad (15)$$

We can understand F/π as the number of times a photon travels the cavity length during one cavity lifetime T_c , or we can understand it as the number of reflections a photon suffer during T_c . F can be related to the reflectivity R of the cavity mirrors [6] by

$$F = \pi \frac{\sqrt{R}}{1-R} \approx \pi \frac{1}{1-R} \quad (16)$$

Here, R is the geometric average of the both mirrors reflectivity R_1 and R_2 , $R = \sqrt{R_1 R_2}$ and it is assumed to be very close to one.

To determine the cavity finesse experimentally, according to Eq. (15), we need to measure the cavity length as well as the cavity decay time.

We do not determine the cavity length by measuring its FSR directly for the following technical reason. A voltage ramp of 130 V obtained from a Tektronics 555 oscilloscope is used to scan the cavity. This corresponds to a scan range of about 60 GHz. This is much smaller than the FSR of the cavity, which is about 150 GHz. Instead, the length of the cavity is determined by measuring the spacing between two successive transverse cavity modes, which are separated by roughly 6 GHz. A DC offset voltage is added, if needed, to the ramp voltage to bring a longitudinal mode within the ramp voltage range.

Higher transverse modes can be excited if the cavity mirrors are not well aligned with each other or the probe laser beam does not exactly match the cavity $TEM_{0,0}$ mode. We believe that the cavity mirrors are well aligned with each other and they are axially symmetric for the following two reasons. First, when a He-Ne laser is sent through the cavity, concentric ring

patterns can be observed in the transmission and reflection from the cavity. Second, if the cavity mirrors are symmetric, $TEM_{n,m}$ modes with $n + m = k$ should be degenerate with $TEM_{k,0}$. We find the frequency difference among the $TEM_{n,m}$ modes with $n + m = k$, if any, is much smaller than 1MHz. The excitation of the higher transverse modes can be attributed to improper coupling of the probe laser beam with the cavity.

In our cavity where the curvature of its mirrors r_0 is much larger than the separation between the mirrors L , the transverse modes are separated by

$$\Delta\nu_{tr} = \frac{c}{2\pi\sqrt{\frac{Lr_0}{2}}}, \text{ Where } r_0 \gg L. \quad (17)$$

Figure 7 shows a typical transmission of a Ti:sapphire laser beam through our cavity. The spacing between $TEM_{0,0}$ and $TEM_{1,0}$ is 6.6 GHz and this corresponds to cavity length of 1.05 mm. The frequency axis is calibrated by changing the frequency of the Ti:sapphire laser by a known amount and observing the change of the positions of the peaks on the oscilloscope.

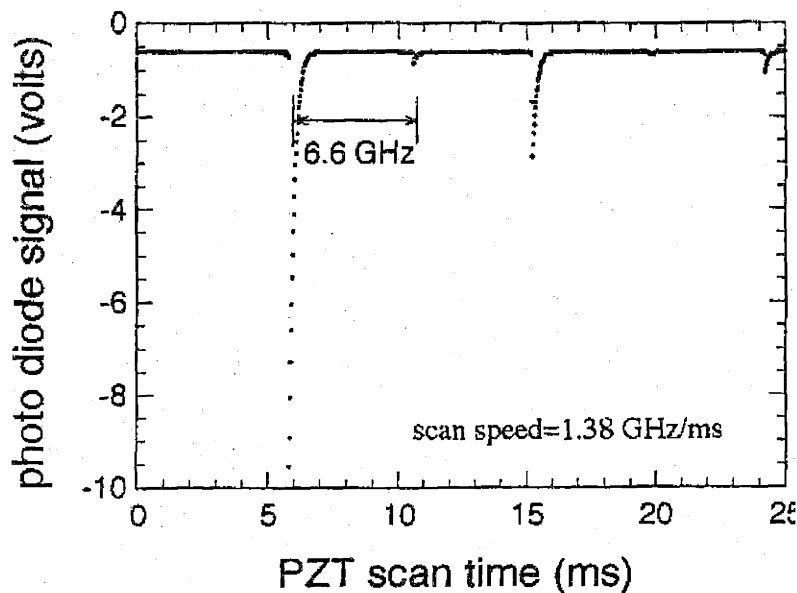


Figure 7. Transmitted Ti:sapphire laser beam through the cavity. From left, these peaks correspond to $TEM_{0,0}$, $TEM_{1,0}$, $TEM_{2,0}$, $TEM_{3,0}$, and $TEM_{4,0}$ [2].

The decay time of the cavity can be measured in either frequency or time domains. In the frequency domain, a laser is sent through the cavity, the cavity is scanned and the full width at half maximum of the transmission peak $\Delta\nu_t$ is measured. The decay time of the cavity is determined from Eq. (14). This method is more accurate when the line width of the cavity transmission is much larger than the line width of the laser. This is not the case in our system, where the cavity line width is about 200 kHz and the Ti:sapphire laser line width is about 50 kHz. Therefore, we resort to a more accurate way to determine the cavity decay time by measuring it directly by the ring-down technique.

The basic idea of the ring-down technique is to fill the cavity mode with radiation and then to observe the decay of transmitted radiation as a function of time. One method to accomplish this is to send a laser beam through the cavity; let the cavity drift slowly to resonance; when a certain transmission level is reached, the laser is switched off quickly, for example by an AOM; and the exponential decay of the transmitted light is measured [7]. We use another method to accomplish the same effect [2]. Our method does not involve a switching device nor does it involve a triggering electronics. It is much simpler. In our method, we exploit the fact that when the cavity is scanned very fast, it becomes in resonance with the laser for a very short time compared to the lifetime of the cavity. During this short time, some radiation builds up in the cavity. This radiation slowly decays while the cavity is out of resonance and almost no laser beam is allowed through the cavity.

Figure 8 shows a typical transmission from our cavity when it is scanned at 14.5 GHz/msec. Typical line width of the transition is about 200 kHz, which corresponds to a scan time of about 14 nsec. This is much smaller than typical lifetime of the cavity, which is about 1 μ sec. Current from an EG&G photodiode model number FND-100 is converted to voltage by a 220 Ω resistor. This small resistor value is chosen to reduce the effective RC of the circuit to about 30 nsec, a value much smaller than the decay time of the cavity. The voltage on the 220 Ω resistor is recorded by a Lecroy 9310M digital oscilloscope and then it is transferred to a computer. The decay time of the cavity is obtained by fitting the curve to an exponential function.

In Figure 8, at the beginning of the cavity decay, small modulations in the transmission can be observed. This modulation is attributed to the interference between the intra-cavity field which builds up during resonance and the Ti:sapphire field. During decay, the intra-cavity field acquires a frequency shift due to the Doppler shift caused by the moving mirrors. Because of finite transmission of the cavity mirrors, the Ti:sapphire laser field always leaks inside the cavity even if the cavity is not in resonance with the laser. The interference between these two fields, which have different frequencies, causes the modulation in the cavity transmission. This modulation becomes more pronounced for slow cavity scan speed [2].

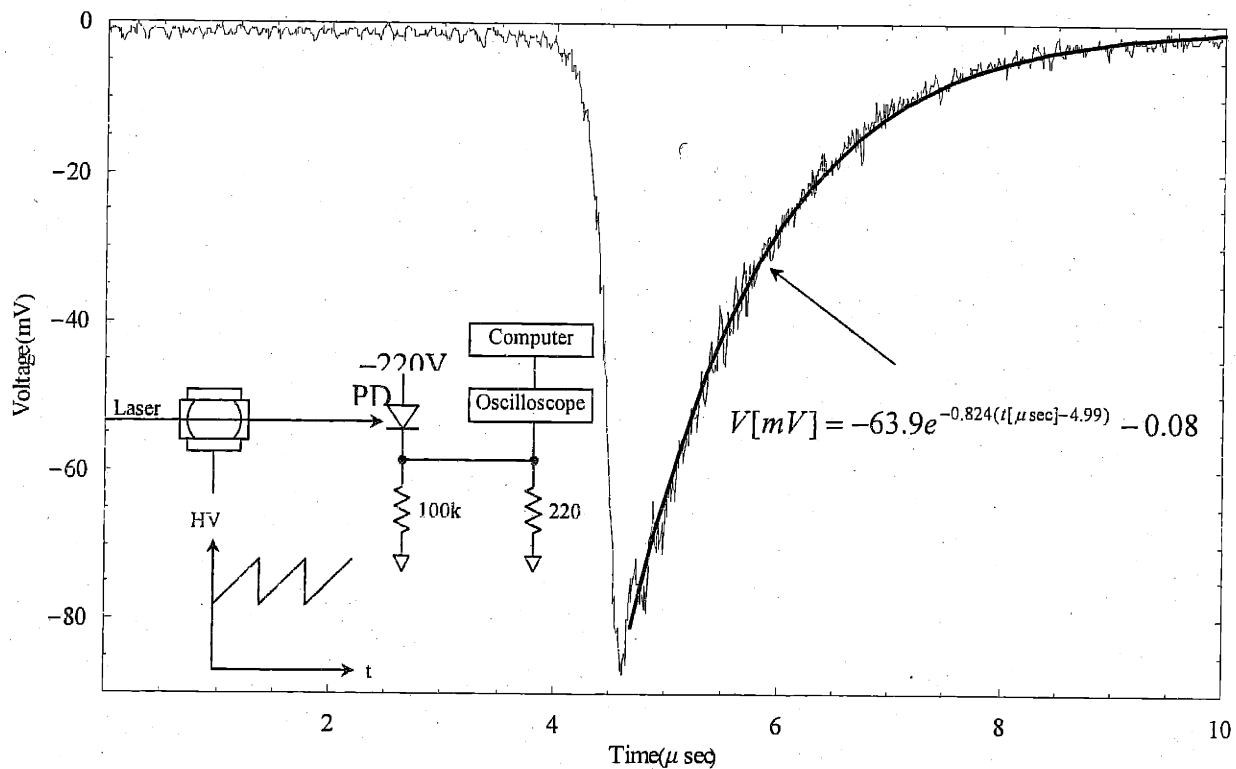


Figure 8. Typical transmission from our cavity when scanned at 14.5 GHz/msec. The insert shows a block diagram for measuring this transmission.

Our PZT is a tube from Vernitron type PZT-5A. Its height is $\frac{3}{4}$ " , its inner diameter is also $\frac{3}{4}$ " and its wall thickness is $\frac{1}{8}$ ". In the middle of the tube, there are four holes to allow free passage of the atomic beam as well as the pump beam. On each end of the PZT tube, a mirror holder is inserted to about $\frac{1}{3}$ of the PZT length and it is glued there by torr-seal epoxy glue.

About 1/3 at the middle of the PZT tube is free from glue and it is used to control the distance between the cavity mirrors. A special mount is used to align and hold the mirror holders while the epoxy is hardening overnight. Transmission of the He-Ne laser is used to align the cavity mirrors. When the mirrors are aligned, a concentric pattern is observed in the transmission of the He-Ne laser beam through the cavity.

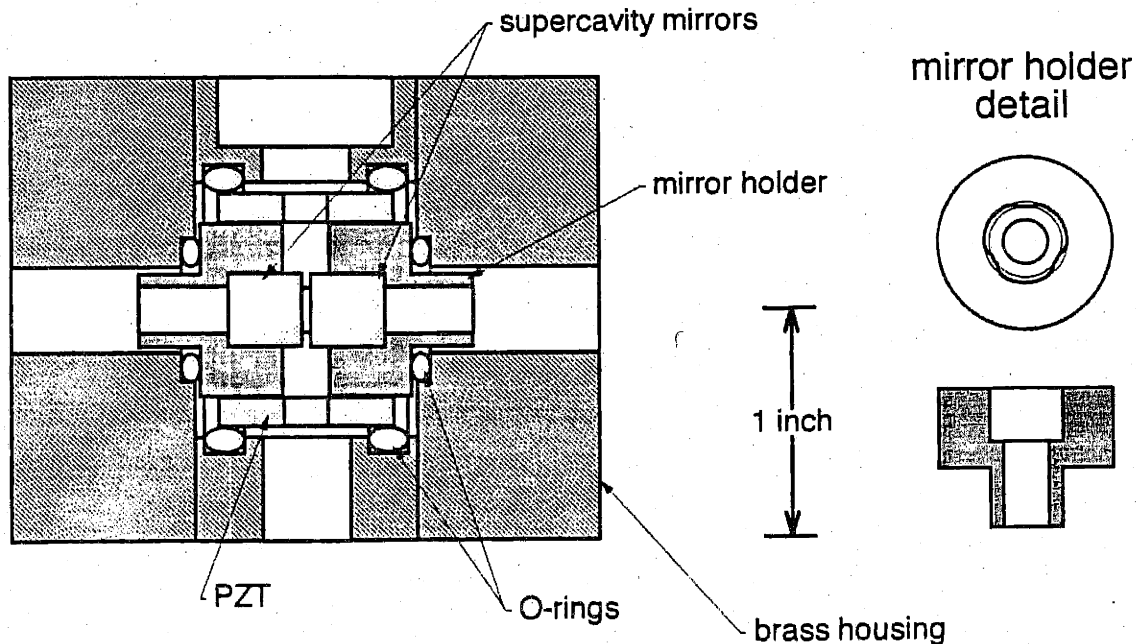


Figure 9. Schematic diagram of the cavity in its brass housing. Four O-rings are used to isolate the cavity from external mechanical vibrations[2].

Three isolation mechanisms are used to isolate the cavity from external mechanical vibrations. Four Viton O-rings are used to suspend the cavity assembly inside a heavy brass enclosure. As shown in Figure 9, two O-rings hold the PZT tube while the two other O-rings hold the mirror holders. Second, as shown in Figure 10, two 1/4" thick Teflon spacers isolate the brass enclosure from the two 1" supporting aluminum plates. Third, three Teflon screws are used to mount supporting aluminum plates to the inner wall of the vacuum chamber. One way to check the cavity stability is by using a probe laser beam from the stabilized Ti:sapphire laser. The probe beam is coupled with the $TEM_{0,0}$ mode of the cavity. The cavity is scanned repeatedly. If the distance between the two mirrors is not stable enough, the position of the transmission peak through the cavity will move from one point to another on the oscilloscope.

We verify that the stability of the distance between cavity mirrors is better than a frequency excursion of 50 kHz. We are limited in our estimation by the stability of the probe laser, which is about 50 kHz.

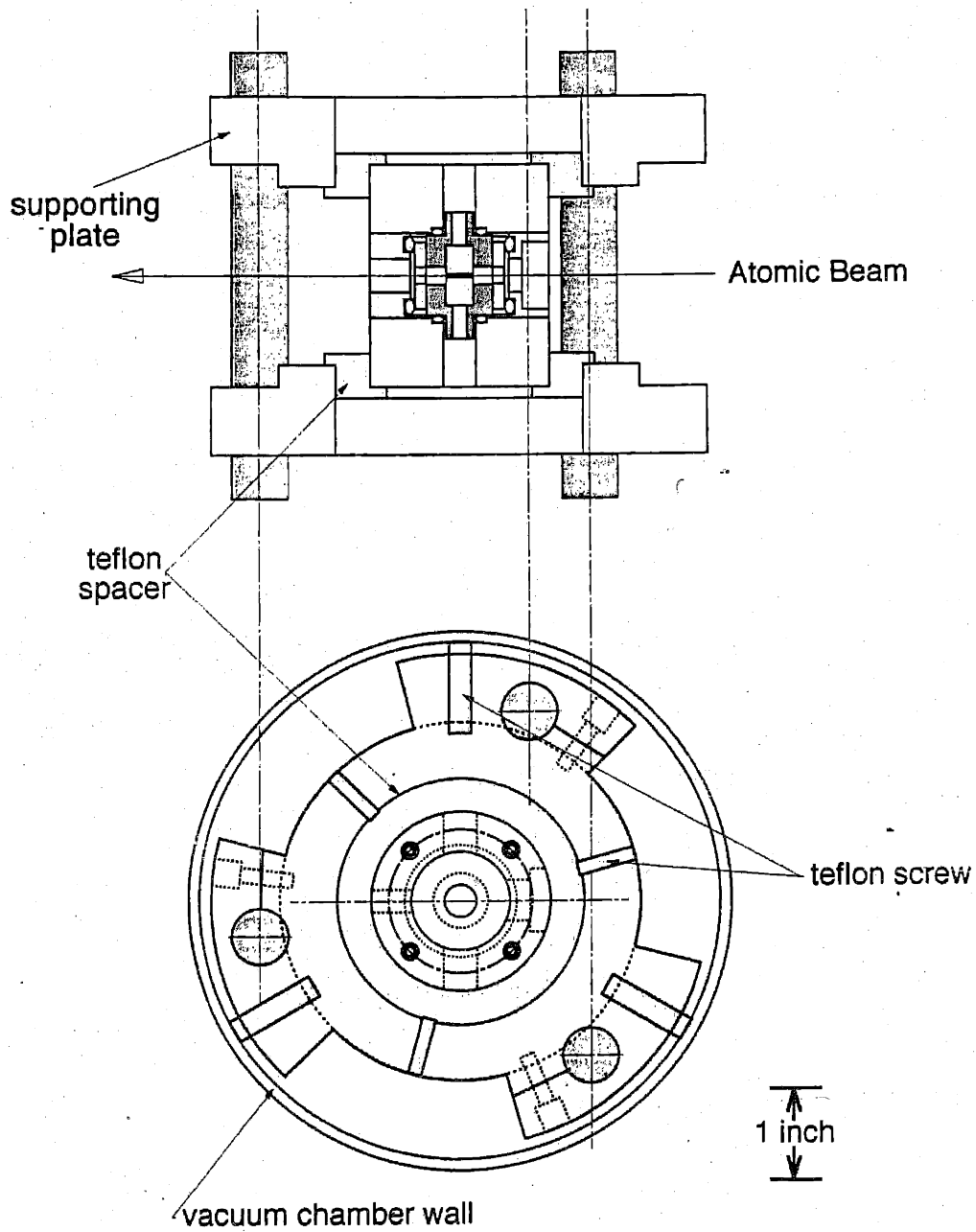


Figure 10. Schematic diagram of the cavity mounted in the vacuum chamber. In addition to the four O-rings, Teflon spacer and Teflon screws are used to isolate the cavity from mechanical vibrations[2].

3.5- Cavity locking

The distance between the microlaser cavity mirrors is stabilized by applying an appropriate voltage to the cavity PZT. This PZT voltage is determined by eliminating the difference between two voltage sources. One voltage source is obtained from detecting the transmission of a Ti:sapphire laser beam through the cavity. This source level changes as a function of the distance between cavity mirrors. The other source is a fixed DC source the level of which is adjusted to correspond to a point on the side of the cavity transmission spectrum. The cavity line width is about 200 kHz and the Ti:sapphire laser line width is about $\Delta f = 50$ kHz. The distance between the cavity mirrors is fixed within a distance Δl that corresponds to the line width of Ti:sapphire laser. Δl is given by

$$\Delta l = \frac{\Delta f \lambda}{c} l = \frac{50 \times 10^3 \times 791 \times 10^{-9}}{3 \times 10^8} 1 \times 10^{-3} = 0.1 \mu m, \quad (18)$$

where λ is the wavelength of the laser beam, l is the distance between the cavity mirrors and c is the speed of light. This distance does not refer to the thermal motion of individual atoms but instead to the collective motion of atoms on the surface of the two mirrors.

As in Figure 1, three acoustic-optic modulators (AOMs) are used to switch between the cavity locking mode and the microlaser output mode. When the two AOMs before the cavity (AOMs B) are switched off, no locking laser beam is allowed into the cavity and the output of the microlaser is directed to the APD and PMT by switching on the AOM after the cavity (AOM A). On the other hand, when the AOMs B are on, the AOM A is switched off so that the transmitted locking beam is channeled only to the photodiode (PD), the locking detector, and the APD and PMT are protected from this relatively high-intensity transmitted beam.

All the drivers of the AOMs are digital and they are switched off and on by a TTL signal from the computer. The two AOMs B are switched simultaneously. The frequency of the locking laser beam is up-shifted by one of the AOMs B and down-shifted by the other such that

the locking laser beam is in resonance with barium atoms in the atomic beam. For the standing-wave configuration, the frequency is down-shifted and up-shifted equally, while for the traveling-wave configuration, the difference in the frequency is made equal to the Doppler shift caused by the tilted atomic beam. Typically, this difference is about 6 MHz.

Our AOMs are Isomet model number 1206C. Their typical deflection efficiency is about 80%. One of the AOMs B is driven by an AOM driver Model 223A-1. This driver has a fixed Radio Frequency (RF) output of 110 MHz with stability of less than 3 kHz. It can switch the RF power off and on typically within 5 nsec and the ratio between the on and off power is 40 dB. Each of the other two AOMs is driven by a driver Model B323B. The frequency of this driver can be varied from 82 MHz to 138 MHz by changing a tuning voltage from 4V to 17V (4MHz/V). This means that noise of magnitude 12 mV in the tuning voltage power supply introduces a jitter in the laser frequency of a magnitude equal to its line width of 50 kHz. The B323B driver has residual FM noise typically less than 10 kHz. Similar to the 223A-1 driver, the B323B driver can switch its RF power off and on within 5 nsec with a ratio between the on and off power of 40 dB.

Figure 12 shows a circuit diagram of the cavity locking electronics. The transmitted locking Ti:sapphire laser beam from the AOM A is detected by a photodiode EG&G model number FND-100. A bias voltage of about -220V is applied to this PD. A differential amplifier compares the amplified signal from this PD with a reference voltage. To follow the drift of the PZT, a fraction of the signal from the differential amplifier is integrated by an integrator. The output of the integrator is applied to one terminal of the PZT while a DC voltage is applied to the other terminal. The DC voltage can be as high as 700V. Floating the voltage on the PZT enables us to add a small voltage from the locking circuit to this high DC voltage while keeping both the DC power supply and the locking circuit referenced to the ground.

When the locking beam is switched off during the microlaser output mode, it is necessary to stop the integrator. Otherwise, the integrator integrates the large signal on the differential amplifier caused by an absence of the signal on the PD and consequently causing the cavity to drift quickly from the resonance. Without stopping the integrator, the cavity can be locked but

the period for switching the locking beam off and on is short, typically 500 μsec , among which about 125 μsec the locking beam is switched off. This is about 25% efficiency for obtaining the microlaser output. An analogue switch DG401 from Intersil is used to stop the integrator. When this switch is on, the inverting input of the integrator Op Amp is grounded, and the integration is stopped. This switch is controlled by a TTL signal from the computer. The switch is on when high TTL logic is applied to the logic input of DG401. With this switch, the efficiency for obtaining the microlaser output can be as high as 90%, with switching off and on periods of a couple of hundred milliseconds.

In the experiment, we use a period of about 400 milliseconds with the cavity locked half of the time. The reason for locking the cavity 50% of the time instead of 10% of time is to minimize the effect of a small misalignment caused by the temperature of the AOMs B crystals. Since 1.2 W of RF is applied to an AOM to switch it on, the crystal heats up and it needs a couple of seconds to reach its steady-state temperature. This causes the angle of the deflected beam to change until steady state temperature is reached. This variation in the angle of the deflected beam is so small that in typical applications of AOMs, it is not noticeable but in our case where the transmission through the cavity is so sensitive to the alignment, this effect is detectable. Usually, the cavity-locking beam is aligned with the cavity when the AOMs B are switched on for some time and they reach the steady state. We notice that as we decrease the ratio of the time the cavity is locked during a switching on and off period, the transmission through the cavity becomes smaller. Locking the cavity for 50% of the time gives us a reasonable transmission as well as reasonable duty cycle. The typical cavity-locking beam power is about 10 μW .

During 200 msec of microlaser output mode, the cavity typically drifts roughly 200 kHz. This is much smaller than the microlaser gain bandwidth, which is limited by transit-time broadening across the 42 μm cavity mode waist. The transit-time full-width at half-maximum Δf is given roughly by [8]

$$\Delta f = 2 \frac{v}{w} \frac{\sqrt{2 \ln 2}}{2\pi} = 2 \frac{370}{42 \times 10^{-6}} \frac{\sqrt{2 \ln 2}}{2\pi} = 3 \text{ MHz}, \quad (19).$$

where v is the atomic velocity and w is the cavity mode waist.

A manual switch is used to discharge the integrator capacitor when the output of the CA3140 Op Amp reaches its limits. The CA3140 Op Amp output saturating limits are about +15V and -15V. The time the Op Amp needs to reach its limits depends on the drift rate of the cavity. Typically, the cavity drifts 1 MHz per sec. Since about 0.35 V is needed to shift the transmission of the cavity by 50 MHz, about 35 minutes are needed to saturate the output of the Op Amp.

A switch after the integrator is used to switch between cavity-locking and cavity-scanning modes. The procedure to lock the cavity is as follows. First, the cavity-scanning mode is chosen. This forces the integrator capacitor to be discharged. The HV DC power supply is adjusted so that the cavity transmission resonance is brought within the scanning range, which is at most 0.7 V. A locking point on the cavity transmission spectrum is chosen by adjusting the reference voltage level. Then the cavity-locking mode is chosen. At this moment, the signal on the locking detector does not correspond to the locking point but the integrator drifts the cavity towards the locking point until the signal on the detector corresponds to the locking point and the cavity is locked there.

Figure 11 shows the output of the photo multiplier tube (PMT) during the cavity-locking mode. During the unlock cycle, the output of the microlaser is detected. The stability of the microlaser output demonstrates that the cavity drift is much smaller than the microlaser gain bandwidth. When the microlaser is switched off, for example by blocking the atomic beam, the PMT signal drops to the background level, which is about 6 k counts/ sec (0.06 V on Figure 11). The background level is mainly caused by the scattering of the pump laser beam into the cavity mode. The leakage of the locking probe from the AOMs B, which are off, is much smaller than the background level. During the lock cycle, some of the locking probe leaks through the AOM A to the PMT.

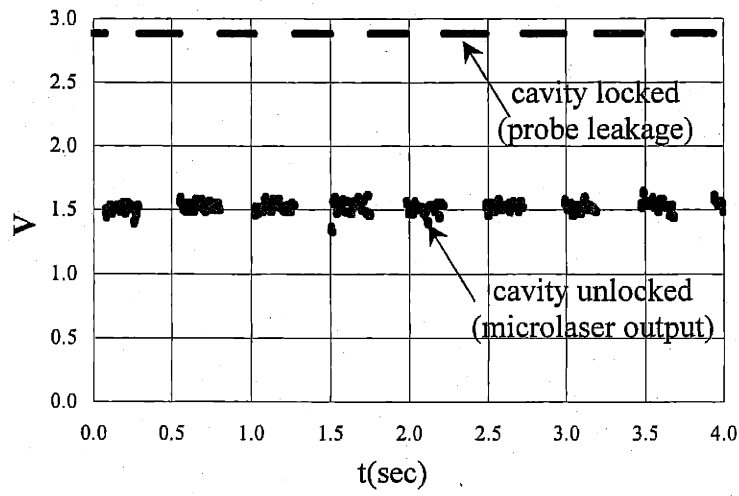


Figure 11. PMT Signal during cavity-locking mode.

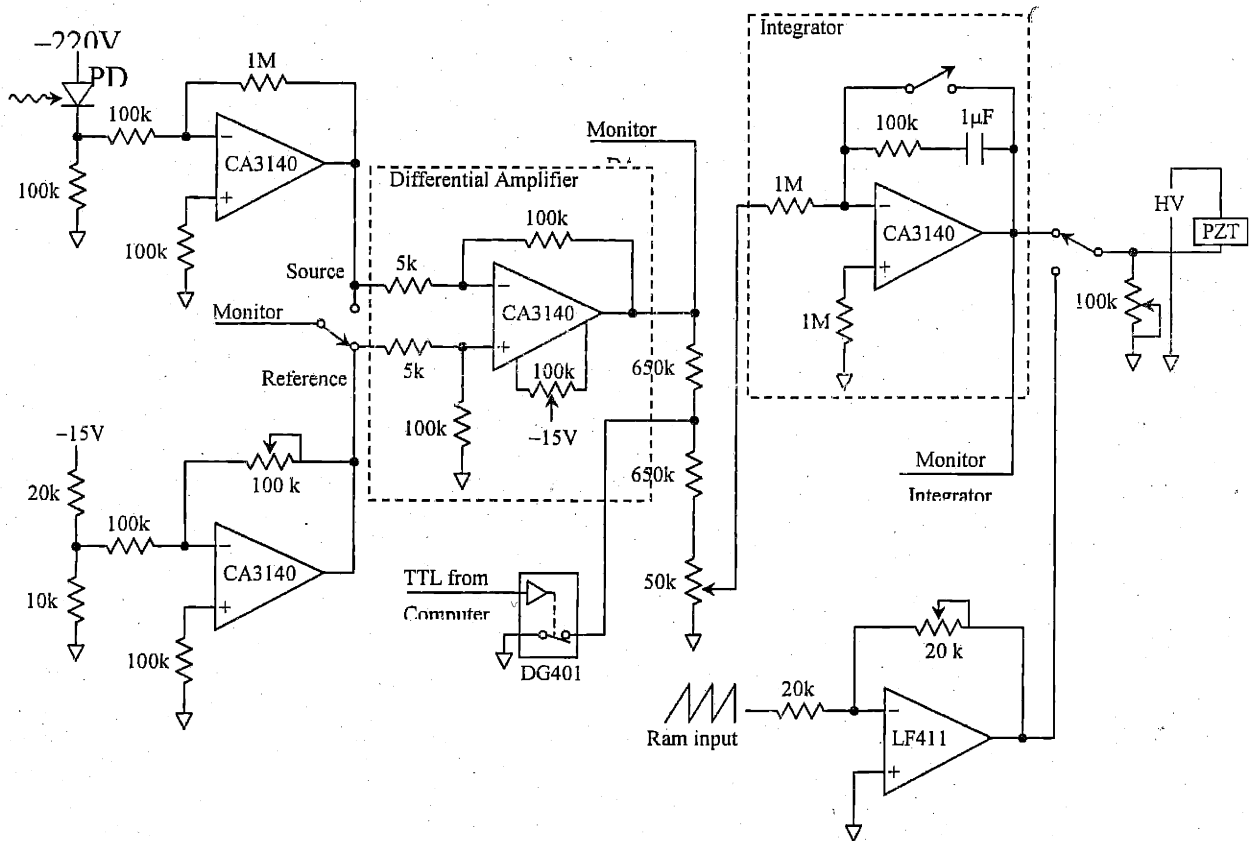


Figure 12. Circuit diagram of the cavity-locking electronics.

3.6- $g^{(2)}(\tau)$ apparatus

Figure 13 shows the $g^{(2)}(\tau)$ apparatus. A beam splitter splits a beam from our microlaser into two beams. The first beam is directed into a start detector and the other is sent to a stop detector. Signals from the stop detector are converted into NIM signals by a preamplifier/discriminator and a constant fraction discriminator (CFD). These NIM signals are delayed and then duplicated by a second CFD. One copy of these signals are converted into TTL signals and used in the stop port of a multi-stop time-to-digital converter (MSTDC), which is discussed in detail in Chapter 5. The second copy is used for monitoring purposes and is sent to a counter whose analog output is connected to a digital scope. The CFD after the start detector is used to convert the start detector pulses into NIM pulses as well as to duplicate them. A copy of these NIM pulses is converted into TTL signals and then sent to the start port of the MSTDC. The other copy is used to monitor the count rate on the start detector.

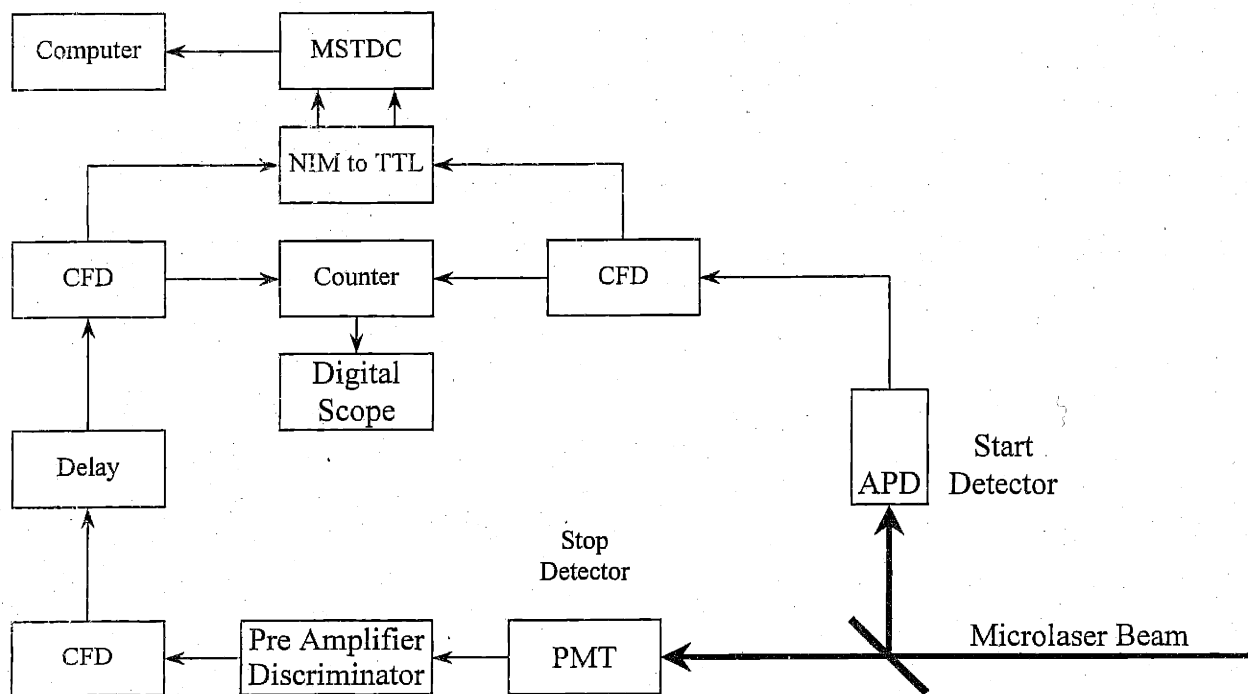


Figure 13. Block diagram of the $g^{(2)}(\tau)$ electronics.

The beam splitter directs 15% of the microlaser beam into the start detector and 85% into the stop detector. We use an avalanche photo diode (APD) as the start detector and a PMT as the stop detector. At a wavelength of 791 nm, the APD has much higher quantum efficiency than the PMT. Unlike the PMT, the APD is not damaged easily by high light intensities. On the other hand, without active quenching, the APD saturates at much lower count rates than the PMT. Also, the APD active area is much smaller than that of the PMT. This makes the alignment of the microlaser beam with the APD much more sensitive.

Our APD is from PerkinElmer model C30902S-TC. It is mounted on a thermoelectric cooler which cools it down to about -20°C . At this temperature, its dark count rate is about 300 counts/sec. Its effective area has a diameter of 0.5 mm. It is operated at a reverse bias voltage of 167V which is 10V above its breakdown voltage. Above the breakdown voltage, the avalanche process can occur and a single photon can be detected.

As Figure 14 shows, pulses from our APD have relatively narrow height distribution. Any discriminator level between -25 mV and -200 mV does not eliminate real photon counts. In the experiment, we use a discriminator level of -50 mV. Figure 15 shows a typical pulse from the APD. One of the four independent channels of a Stanford TC455 CFD is used as a discriminator for the APD signals. The CFD is very fast; its pulse pair resolving time is less than 5 nsec. When triggered, the CFD produces three simultaneous NIM-standard negative logic signals. On 50 Ω loads, the "high" level of the NIM signals is typically -1.0 V. The width of the output pulses is adjusted to be 36 nsec. This makes the MSTDC more efficient, as discussed in Chapter 5. One of the outputs of the CFD is converted to TTL signals by the NIM-to-TTL circuit. The TTL signal is used to start the MSTDC. Another output is used to monitor the count rate of the APD. It is connected to a Stanford Research Systems SR400 counter. The analogue output of the counter is sent to a LeCroy 9310M digital oscilloscope where it is monitored in real time. The third output of the CFD is not used.

Unlike the PMT, the saturation count rate in the APD is not limited by the pulse width but it is limited by the recharging time of the PN junction capacitance. The saturation count of

the APD is measured to be about 300 k counts/sec[2], which is much lower than the saturation count rate when no recharging time is involved.

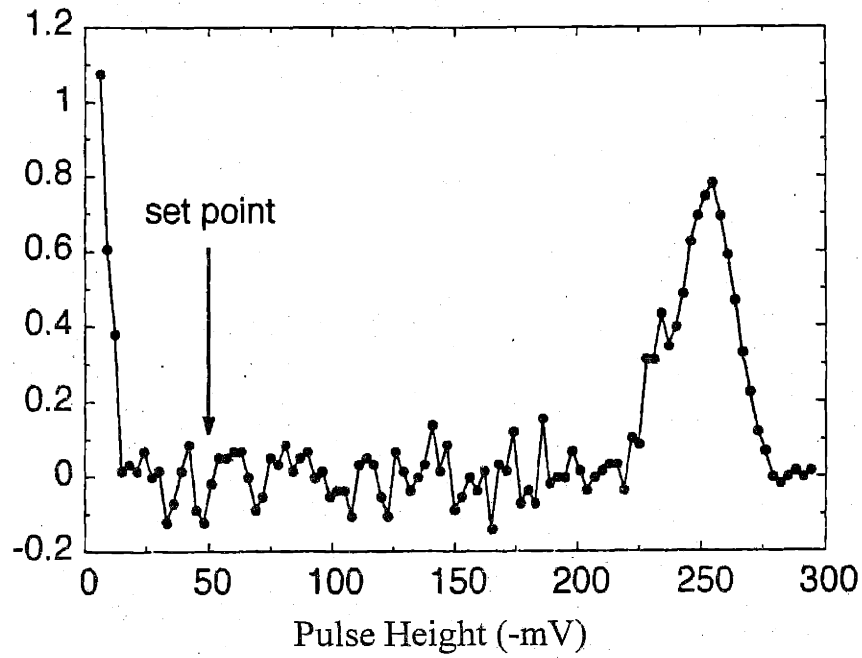


Figure 14. Pulse height distribution of the APD[2].

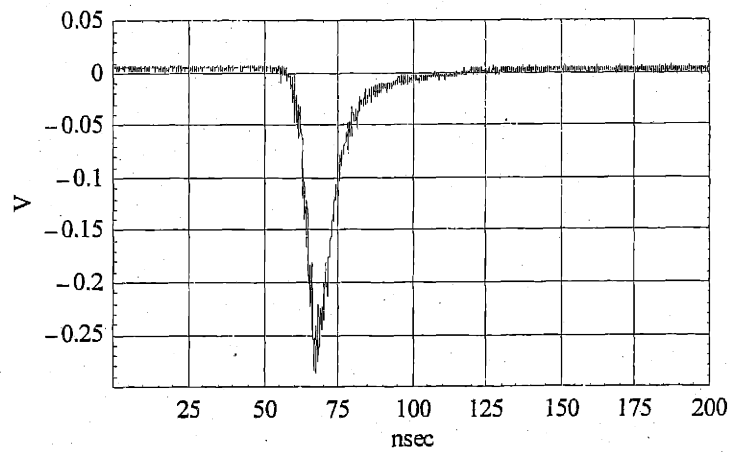


Figure 15. A typical pulse from the APD.

An APD is equivalent to an RC circuit with a switch as shown in Figure 16. Before any photon detection, the switch is open and the voltage across the capacitor is the bias voltage. When a photon falls on the PN junction, it provides an avalanche of electrons and current flows through the APD or, equivalently, the switch in the equivalent circuit is closed. When the current flows through the current-limiting load resistor R_L ($R_L=R_1+ R_2$), the voltage across it increases. Since the power supply provides constant voltage, the bias voltage across the PN junction drops below the breakdown voltage and the switch opens again. Avalanche current flows through the circuit only for about 20 nsec as Figure 15 shows. The bottleneck occurs in the recharging process. The capacitance needs recharging to the reverse bias voltage in order to detect another photon efficiently. The time constant for the recharging process is given by the time constant of the equivalent RC circuit: $R_L C_{int}$. To have a very small constant time, R_L should be as small as possible. But R_L cannot be made arbitrarily small for the following reason. If the current through the APD reaches $50 \mu\text{A}$ and the voltage across it does not drop below the breakdown voltage, the current through it is sustained for ever. To have pulses,

$$50\mu\text{A} > \frac{\Delta V}{R_L}, \quad (20)$$

where $\Delta V \equiv V_R - V_{BR}$ is the difference between the reverse bias voltage V_R and the breakdown voltage V_{BR} . $I_{Latch} = 50 \mu\text{A}$ is called the latching current. As shown in Figure 17, the probability of initiating an avalanche process is proportional to ΔV . But making ΔV large requires larger R_L . Thus the value of R_L is a compromise between higher counting efficiency and lower recharging time. Here we choose $\Delta V = 10 \text{ V}$, which gives us 0.4 probability of a free electron in the PN junction initiating an avalanche process. According to Eq. (20), R_L should be larger than $200 \text{ k}\Omega$. We choose R_L to be slightly larger than $200 \text{ k}\Omega$. This makes $R_L C_{iny}$ roughly $0.3 \mu\text{sec}$. A circuit with a current-limiting load resistor is called a passive-quenching circuit.

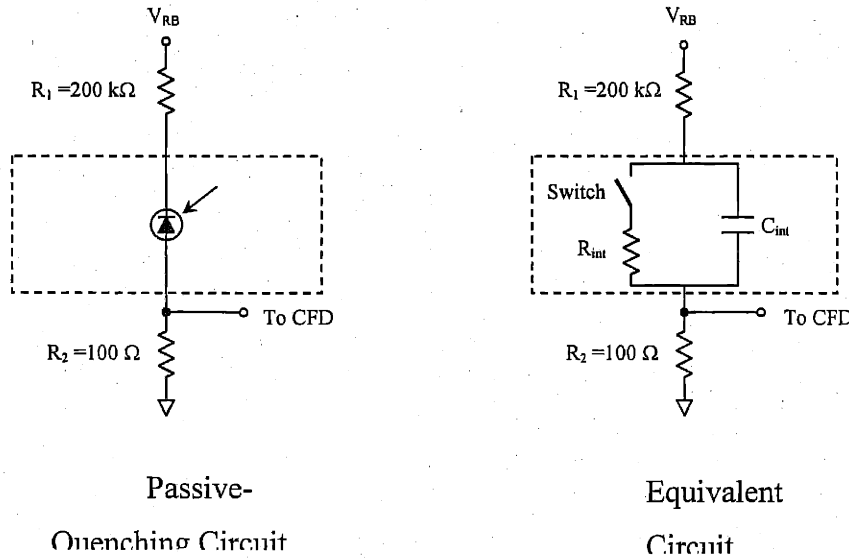


Figure 16. An APD is equivalent to an RC circuit with a switch.

An active-quenching circuit can be used to overcome the limitation on the recharging time imposed by a large R_L . With these circuits, the saturation count rate can be easily improved by an order of magnitude. One way of implementing active-quenching is by shorting R_L for a very short time after the pulse is detected. Typically few nsec are needed to recharge the capacitor through a very low resistor. For more detail on active quenching, see for example [9] and [10]. In the current experiment, we use a passive-quenching circuit. For this reason, we keep the count rate on the APD during the $g^{(2)}(\tau)$ measurement well below the saturation intensity, typically less than 30 k count/sec. Higher count rate on the APD do not help much in reducing the collection time in our $g^{(2)}(\tau)$ measurements. The APD is the start detector and the limitation on how fast to start is determined, for a very high count rate, by the range of the $g^{(2)}(\tau)$. Typically the range of 20 μsec is used and count rates higher than $1/20\mu\text{sec}=50$ k count/sec do not buy us much in terms of reducing the $g^{(2)}(\tau)$ collection time.

The total efficiency for detecting a single photon by an APD depends on two factors. The first factor is the probability of producing a photoelectron when a photon falls on the PN junction. This is by definition the quantum efficiency of the APD. As Figure 17 shows, it is quite high at 791 nm, about 0.8. The second factor is the probability of creating an avalanche pulse when a photoelectron sweeps through the PN junction. This depends on the bias voltage,

as Figure 18 illustrates. Thus for $\Delta V = 10 \text{ V}$, the efficiency for detecting a photon is given by $0.8 \cdot 0.4 = 0.32$. This is confirmed experimentally by [2].

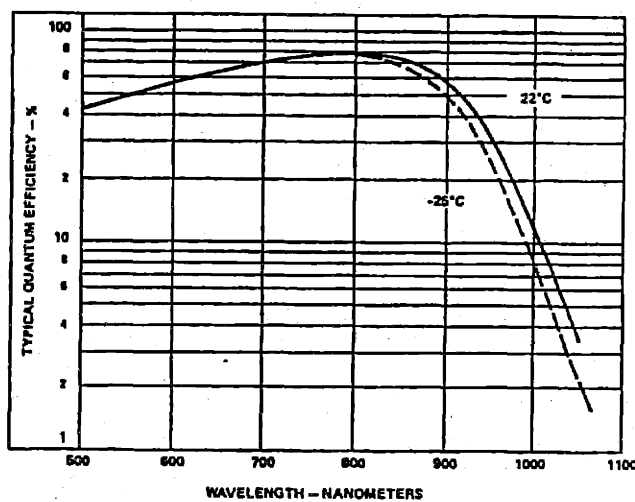


Figure 17. Typical quantum efficiency of the APD as a function of wavelength.[11]

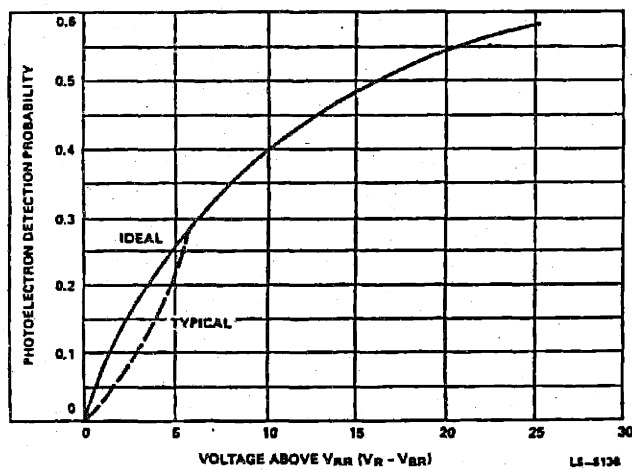


Figure 18. Photoelectron detection probability of the APD as a function of voltage above V_{BR} . [11]

Our PMT is Hamamatsu model R943-2. It is cooled by a thermoelectric cooler (Pacific Instruments model 3470) to less than -20°C . At this temperature, it has dark counts of about 20 count/sec. It has an effective area of $10\text{ mm} \times 10\text{ mm}$. A high voltage of -1500V is used to bias the PMT. At this bias voltage, the rise time of the PMT signal is about 3 nsec. Figure 19 shows a typical signal from our PMT.

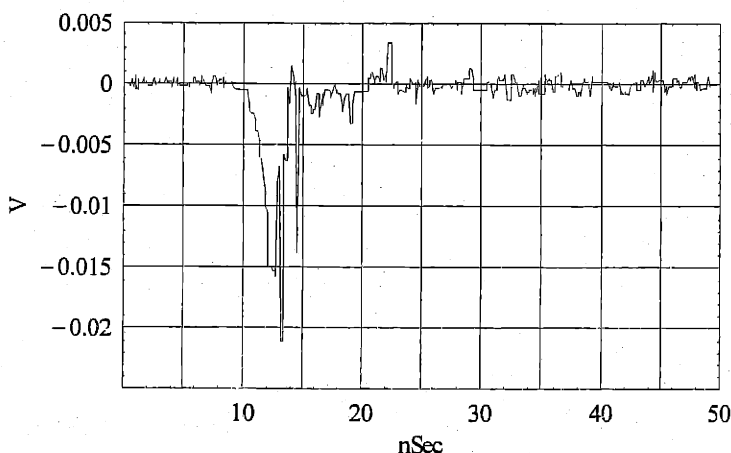


Figure 19. A typical signal from the PMT.

The PMT signal is amplified and discriminated by a built-in amplifier/discriminator unit in the Pacific cooling housing. The amplifier model 3470/2A50 provides a fixed $\times 100$ voltage gain. The level of the discriminator 3470/AD6 is set just above the electronic noise of the amplifier. The discriminator has two simultaneous outputs: one is TTL and the other is NIM. When the PMT is completely blocked, its count rate is about 20 count/sec. R943-02 has an excellent pulse height distribution. The dark count has much smaller amplitudes than photon signals. Typical pulse height distribution and quantum efficiency curve are shown in Figure 20. The quantum efficiency of the PMT at 791 nm is typically 12%.

The NIM output of the discriminator is sent to a channel of the CFD. Using a Canberra Delay and Gate Generator (DGG) model 410A, the output of the CFD is delayed by about 1.1 μsec . The purpose of this delay is to move the zero of the $g^{(2)}(\tau)$ function to a higher bin number. This helps in identifying the bin that corresponds to $\tau = 0$. The DGG has a dead time of 100 nsec plus the delay period. This dead time makes the reading on the monitor counter

smaller than the actual count rates on the PMT. The count rates of the PMT appear to saturate. Using calibrated density filters, the saturation count rate of the PMT and the DGG is measured to be 0.86×10^6 cps. The actual count rates of the PMT n_{det} can be recovered from the counter reading n_{count} by the following relation,

$$n_{det} = \frac{n_{count}}{1 - \frac{n_{count}}{0.86 \times 10^6}} \quad (21)$$

Typically our count rates are less than 100 k cps and the above equation produces a correction of less than $\sim 10\%$. For very high count rates, the dead time in the DGG becomes a problem. A better solution, which introduces no dead time, is to use a very long 50- Ω coaxial cable to introduce the delay. For a RG174/U coaxial cable, 1 m corresponds to a 5-nsec delay. This improves the saturation count rates by about an order of magnitude. The delayed signal is sent through another channel of the CFD. As in the case of the APD, one output of the CFD is converted to TLL and used as the stop input for the MSTDC and the other output is connected to the SR400 counter to monitor the count rates on the PMT in real time.

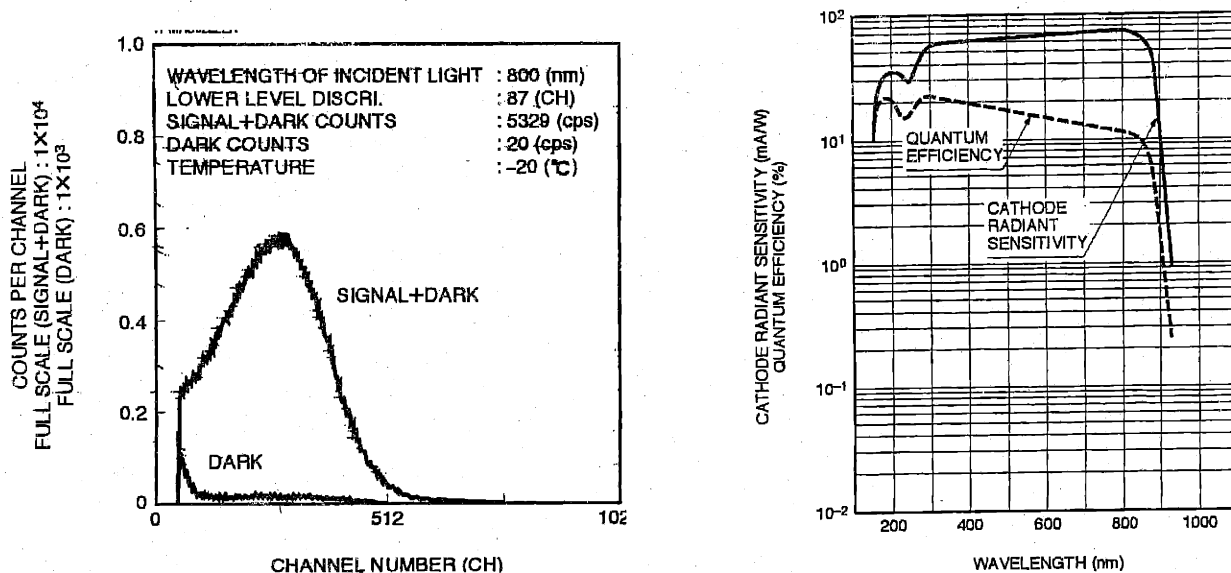


Figure 20. Typical pulse height distribution and quantum efficiency of the R943-02 PMT.

3.7- Controlling and data-collecting software

Figure 21 shows a flow diagram of the program used to control various parts of the experiment and to collect data. A complete list of the program is given in Appendix B.

When the program is executed, a menu pops up so that different experimental parameters can be chosen. Some of these parameters are variables used in the programs; others are just experimental parameters saved with the file and have nothing to do with the program variables, for example, oven temperatures. The program variables that are chosen in the menu are the following: time to lock the cavity (T_l), time to write to the FIFO memory (T_w), time between switching on and off various parts (T_b), total collection time, range of the MSTDC and AOMs configuration. The time is measured in units of $2 \mu\text{sec}$, which is the time the computer need to reads two bytes from the FIFO memory.

Three of the four AOMs configurations are used for testing and aligning purposes. These configurations are the following: AOMs before cavity (AOMs B) are always off and AOM after the cavity (AOM A) is always on; AOMs B are always off and AOM A are always on; and all AOMs are on. Data collection is done with the fourth AOM configuration, alternate, during which AOMs B and AOM A are switched on and off alternatively.

Before collecting any data, the cavity needs to be locked. A hardware switch is used to tell the program whether it needs only to lock the cavity and not to collect any data or it needs to lock the cavity as well as to collect data. This switch is called the stop acquisition bit. When the stop acquisition bit is low, the program only locks the cavity.

A binary variable clock is used to enable the program to track time spent in collecting data. During data collection, the clock variable is set to high. The data collection process can be stopped any time by switching the stop acquisition bit to low. When the stop acquisition bit is switched high again, data collection is resumed as if it were not interrupted.

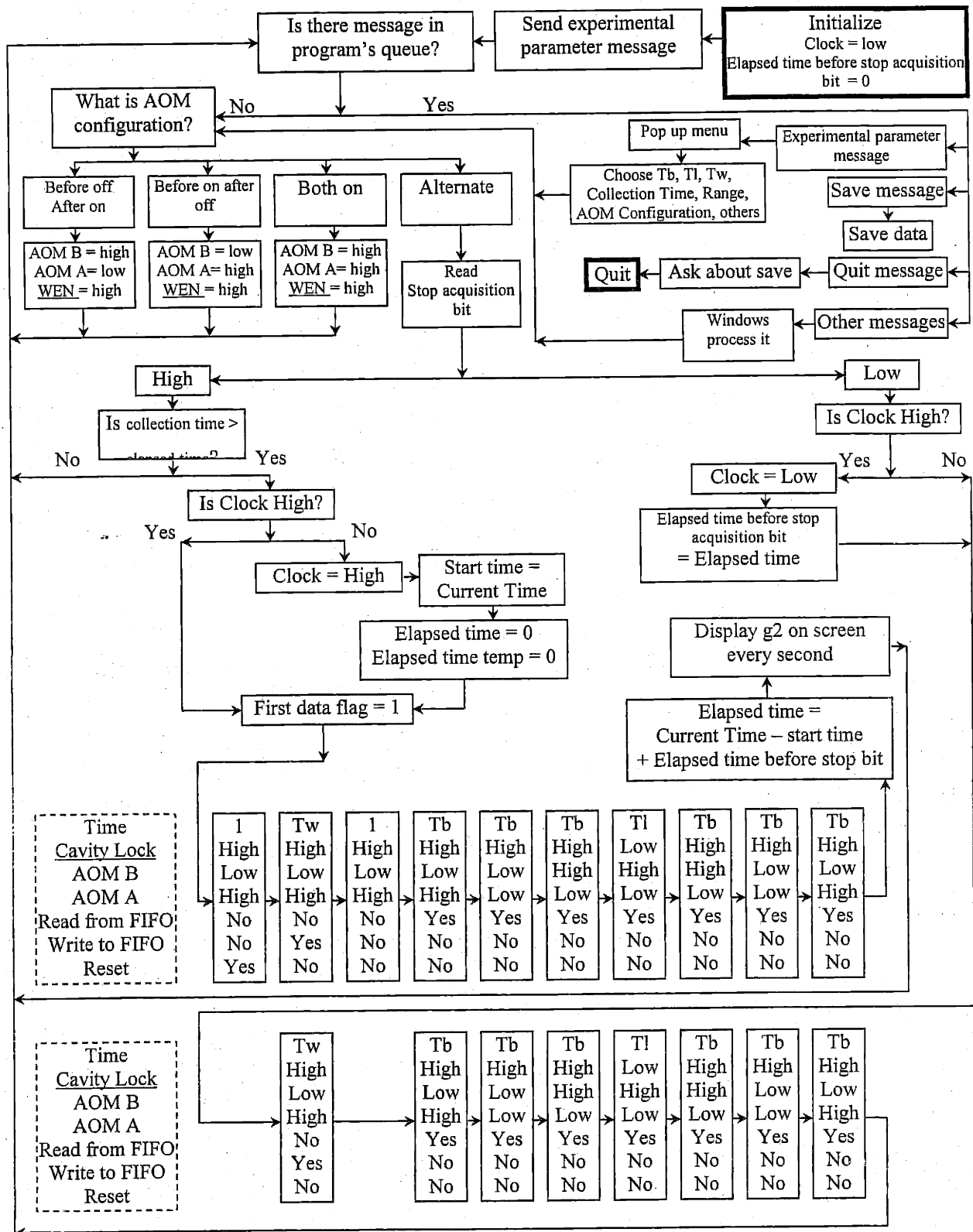


Figure 21. Flow diagram of the controlling and data-collecting program.

At the beginning of each data collection cycle(see Figure 22) the FIFO memory is reset. Then during T_w , typically 0.2 sec, data is written to the FIFO memory and during the reset of the cycle, typically 0.2 sec, the computer reads from the FIFO memory to its memory. Small time intervals T_b , typically 0.1 msec, are used to separate switching on and off various components. These are used so that everything is settled down before switching other components. This is especially important to protect the detectors from a relatively high-intensity locking beam.

Data points written at the beginning of T_w may not start at the beginning of the MSTDC range and data written at the end of T_w may not end at the end of the MSTDC range. So usually, we need to ignore the first data points before the first end-of-the-range flag and the last data points after the last end-of-the-range flag. The end-of-the-range flag is a data point written to the FIFO memory each time the MSTDC reaches its range. For example, if the range is chosen to be 20.48 μ sec (2^{10} 20 nsec), the end-of-the-range flag will be 2^{10} . Figure 23 shows the flow diagram of the iRead_FIFO function. When this function is called, it searches for the first end-of-the-range flag and it ignores any data point before this flag. Then it stores data points into array elements until it finds the next end-of-the-range flag. At this point it sorts the stored data points into their corresponding bins in the $g^{(2)}(\tau)$ function bins and then resets the array elements and array index to zero. This process is repeated until all data are read. Data at the end, which are not bounded by the end-of-the-range flag, are ignored. The array size chosen is much larger than the maximum expected photon number in one range. When the FIFO is empty, the computer reads zeros from it. This may cause the array to be filled with spurious zeros and may cause computer memory error. For this reason, the array index is reset whenever the array is full.

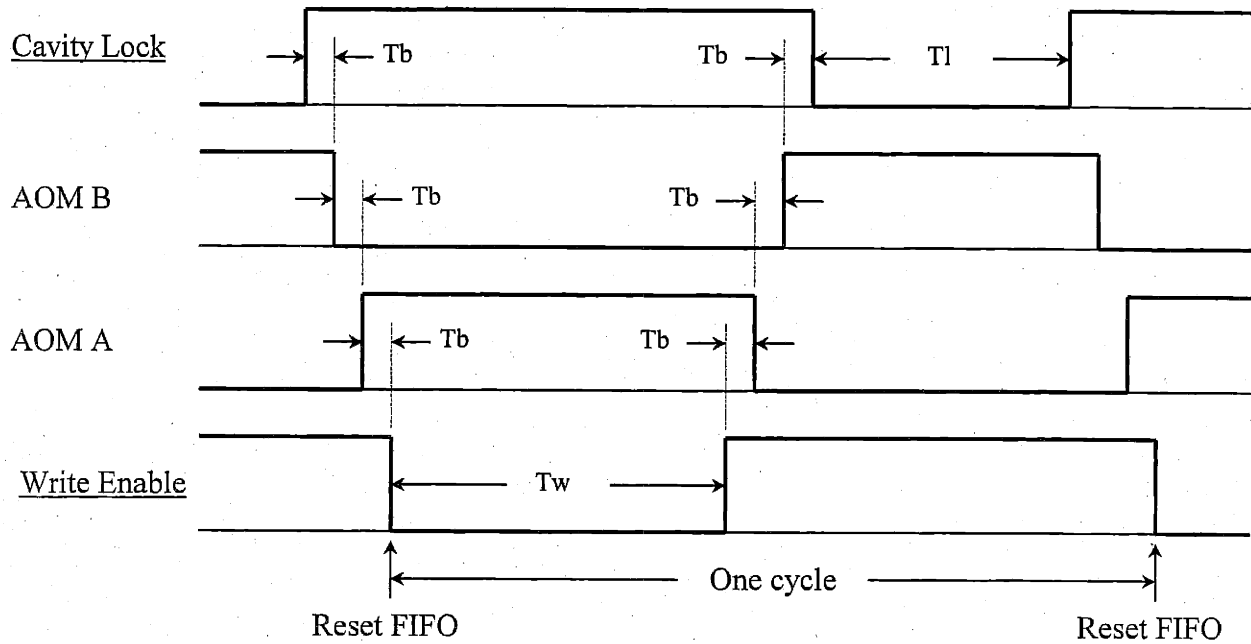


Figure 22. Timing for signals controlling the cavity locking circuit, the acousto-optic modulators, writing, and resetting the FIFO memory. Under line indicates inverse logic.

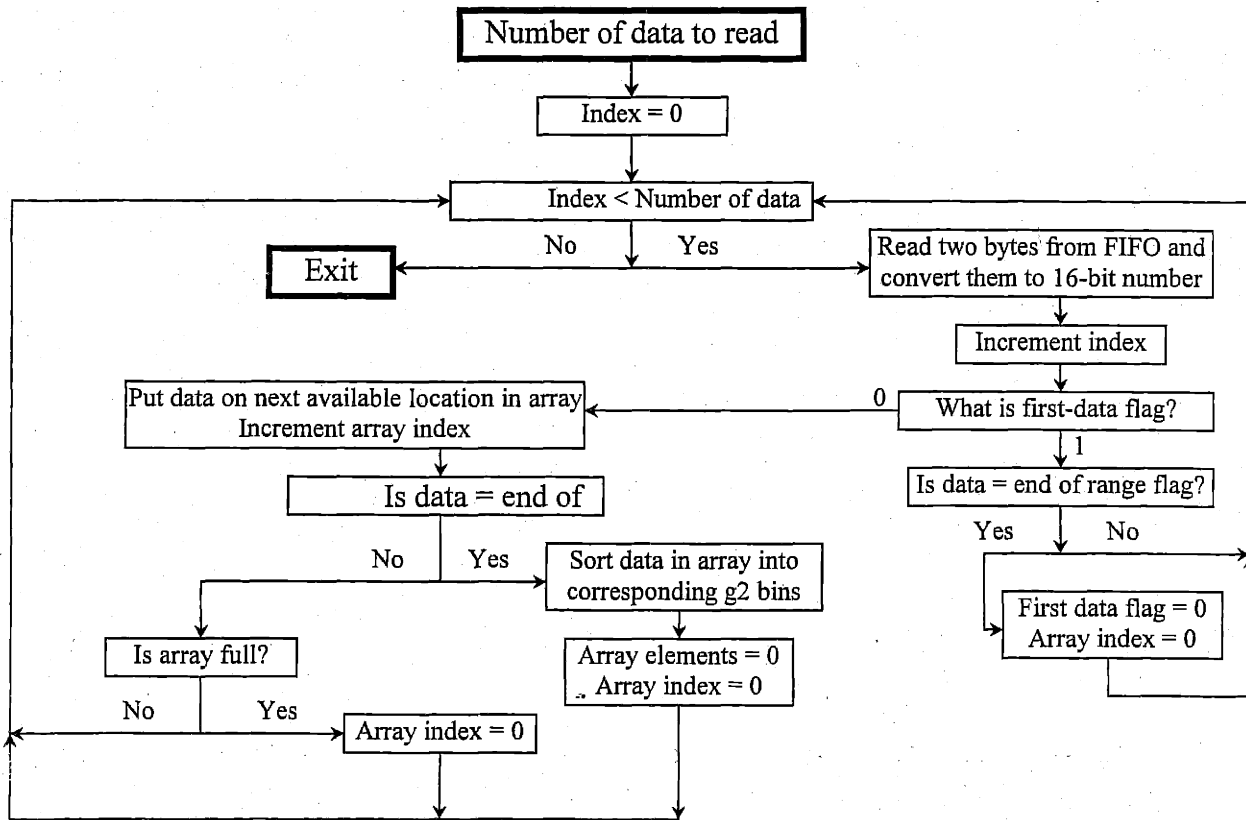


Figure 23. Flow Diagram of the iRead_FIFO function that reads data from FIFO memory to the computer memory.

3.8- References

[1] S. Niggli and M. Huber, Phys. Rev. A **35** 2908(1987).

[2] K. An, Ph.D. Thesis, Massachusetts Institute of Technology, May 1995

[3] Wolfgang Demtroeder, Laser Spectroscopy Basic concept and Instrumentation, p. 85, 2nd Edition, Springer 1998.

[4] Wolfgang Demtroeder, Laser Spectroscopy Basic concept and Instrumentation, p. 372, 2nd Edition, Springer 1998

[5] B. Sones, M. Sc., Massachusetts Institute of Technology, May 1997.

[6] A. Siegman, Lasers, p.436, University Science books 1986.

[7] G. Rempe, R. J. Thompson and H. J. Kimble, Opt. Lett. **17**,363 (1992).

-
- [8] Wolfgang Demtroeder, *Laser Spectroscopy Basic concept and Instrumentation*, p. 85, 2nd Edition, Springer 1998.
- [9] W. Ghioni, S. Cova,, F. Zappa, and C. Samori, *Rev. Sci. Instrum.* **67**, 3440 (1996).
- [10] E. Overbeck, C. Sinn, I. Flammer and J. Ricka, *Rev. Sci. Instrum.* **69**, 3515 (1998).
- [11] Silicon Avalanche Photodiodes C30902S data sheet, RCA Inc., ElectroOptics.

Chapter

4 Velocity Selection of Barium Atomic Beam

In the microlaser, it is desirable to have an atomic beam with a narrow velocity distribution for the following reason: a narrow velocity distribution guarantees that all atoms to have almost similar atom-cavity interaction time. This makes our microlaser closer to the ideal microlaser model(See Section 2.2). In addition, if we want to study, in a control way, the effect of partially inverted atoms on the performance of the microlaser, it is easier to use the constant-frequency-shift inversion process (See Section 2.7) with a narrow-velocity atomic beam.

In what follows, we describe how we prepare a barium atomic beam with a velocity spread of about 10% of that of the effusive atomic beam distribution.

A barium atom does not have a closed two-level system. For this reason, it is impossible to use just one laser to do the velocity selection, for example, by deflection the atoms by an orthogonal laser beam[1] or by slowing the atoms down by counter-propagating laser beams [2]. Instead, the drawback of this open two-level system in barium is exploited and a new scheme for preparing a narrow velocity distribution of barium atomic beam has been developed. This new scheme is based on using two narrow-band dye lasers.

Our velocity selection scheme has many advantages over mechanical velocity selectors[3]. It has no mechanical vibration associated with it. Mechanical vibrations in our chamber may make cavity locking impossible. Moreover, it produces continuous atomic beam. Also, our scheme does not require any major mechanical construction in the microlaser chamber.

4.1- Two-laser velocity selection scheme

The concept behind our two-laser velocity selection scheme is simple. The first laser beam is used to pump all atoms into a metastable state while the second laser beam is used to repump atoms with a specific velocity back to the ground state. The Doppler shift is exploited to access all atoms by the first laser beam and a specific group of atoms by the second laser beam. An atom with velocity v sees the laser frequency shifted by an amount given by

$$\nu_{\text{atom}} = \nu_{\text{laser}} + \frac{v}{\lambda} \cos \theta, \quad (1)$$

where ν_{atom} is the frequency of the laser in the atom reference frame, ν_{laser} is the frequency in the lab reference frame, λ is the wavelength of the laser and θ is the angle between the laser beam and atom velocity vector. So if the angle between the laser and the atomic beam is 90° , the Doppler shift is zero and the laser interacts with all atoms irrespective of their velocity. On the other hand, if the angle is not 90° , only atoms with velocity such that the right hand side of Eq. (1) is equal to the atomic resonance frequency interact with the laser beam. Figure 1 explains this concept and shows the populations of barium ground state and metastable state at different stages of the velocity selection scheme. After the second laser, we have atoms with a narrow velocity distribution in the ground state and the rest of atoms are in the metastable state. Atoms in the metastable state do not interact with the microlaser cavity mode.

Figure 2 shows the barium atomic levels relevant to the velocity selection scheme[4]. The pump laser drives the $6s^2 \ ^1S_0 - 6s6p \ ^1P_1$ transition. The $6s6p \ ^1P_1$ state may decay back to the ground state or to the metastable states with branching ratio of 293 to 1. The lifetime of the $6s6p \ ^1P_1$ state is 8.4 nsec. The $6s6p \ ^1P_1$ state decays mainly to two metastable states, $6s5d \ ^1D_2$ and $6s5d \ ^3D_2$. Lifetimes of the $6s5d \ ^1D_2$ and $6s5d \ ^3D_2$ metastable states are about 0.2 sec. The repump laser drives the $6s5d \ ^1D_2 - 5d6p \ ^1P_1$ transition. About 26% of atoms are lost in the $6s5d \ ^3D_2$ metastable state. The $5d6p \ ^1P_1$ state decays to the ground state and to the $5d^2 \ ^1D_2$ metastable state. Another 3% of the atoms are lost in this metastable state.

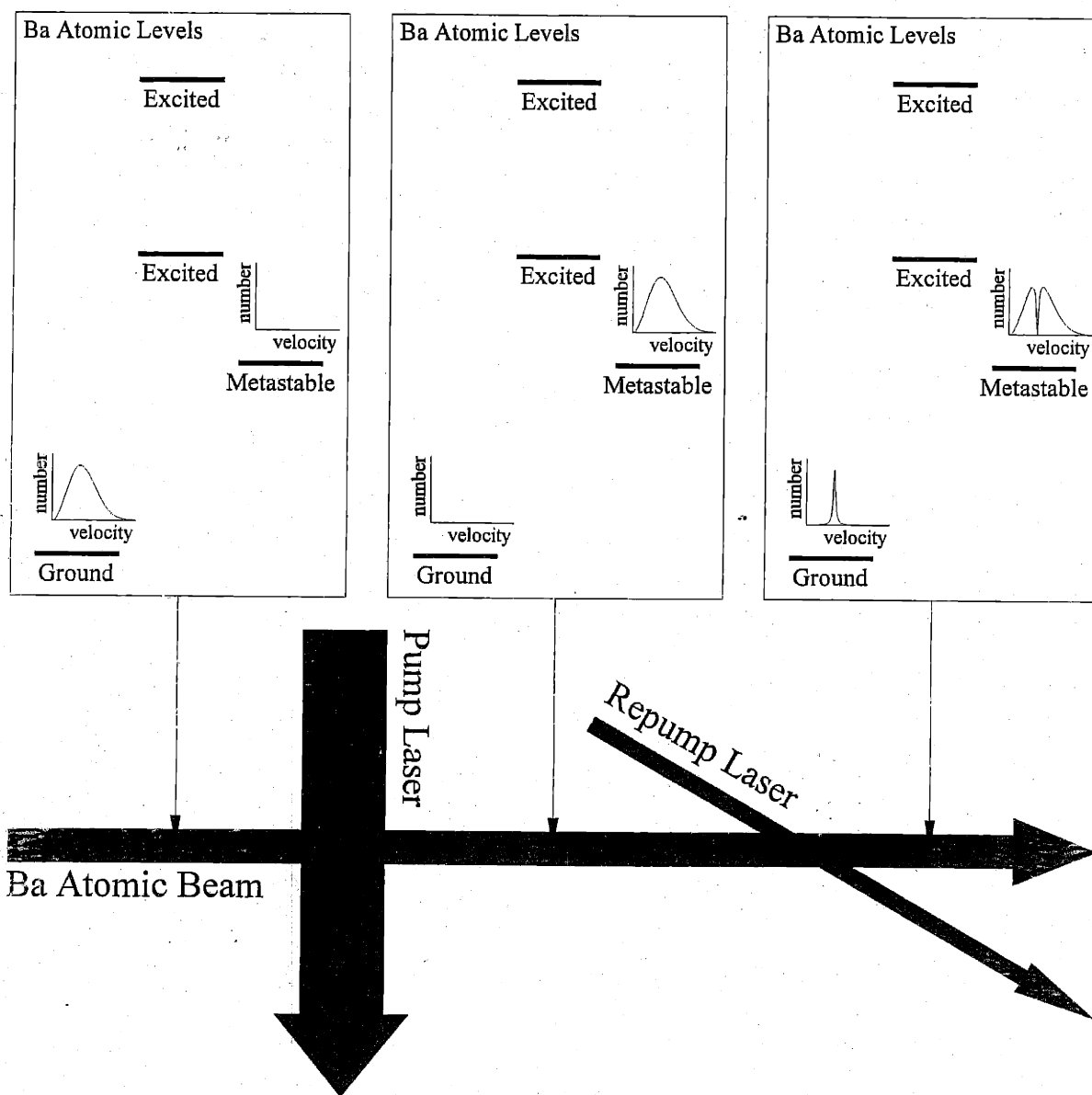


Figure 1. Arrangement of the pump and the repump lasers with respect to the atomic beam. Shown in the boxes, populations of the ground state and the metastable state at different positions of the atomic beam.

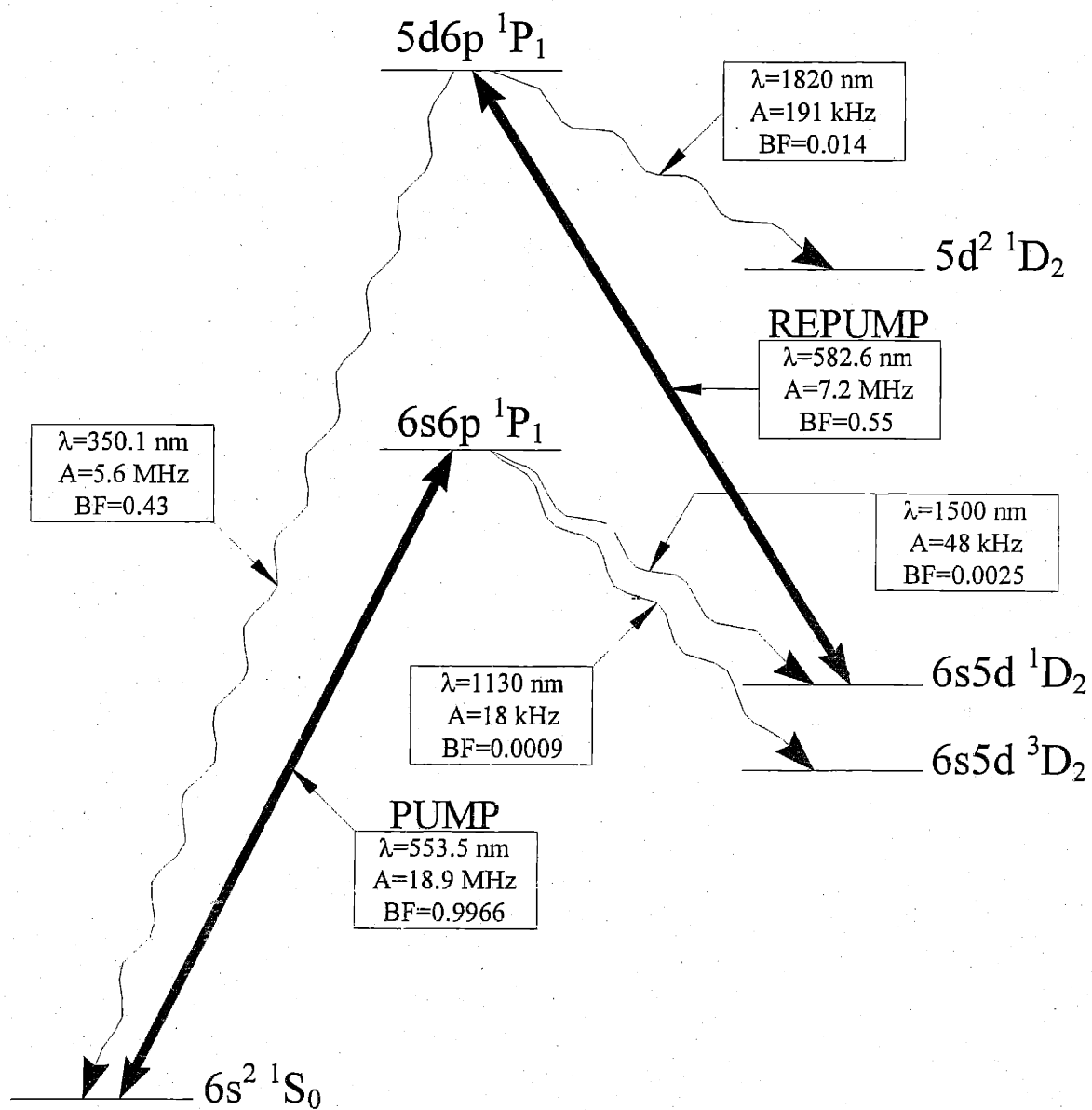


Figure 2. Relevant Ba atomic levels used in the velocity selection scheme. λ is the wavelength, A is the transition probability and BF is the branching fraction of the upper level.

To estimate widths and intensities of the pump and repump lasers, we use a simplified model of the barium atom. In this model we ignore the fact that barium atom has sublevels. Also, we use the rate-equation formulism instead the optical Bloch equation. The rate equations are simpler and should be quite accurate for our experimental parameters. When the coherence between the atom and the laser beam is ignored, the optical Bloch equations reduce to the rate equations. In our estimations, we can ignore the coherence between the atom and the laser beam because, in the pumping stage, we are interested in interaction times much larger than the lifetime of the excited state and, in the repumping stage, we are interested in repump laser intensities much smaller than the saturation intensity of the repump transition.

4.1.1- Pumping stage predictions

The population probability of different states as a function of the interaction time with the pump laser beam can be calculated from the following rate equations [5]:

$$\frac{d}{dt} n_{ep} = \frac{1}{2\tau_{gp}} \frac{I_p}{I_{sp}} (n_{gp} - n_{ep}) - \frac{n_{ep}}{\tau_p}, \quad (2-a)$$

$$\frac{d}{dt} n_{gp} = \frac{1}{2\tau_{gp}} \frac{I_p}{I_{sp}} (-n_{gp} + n_{ep}) + \frac{n_{ep}}{\tau_{gp}}; \quad (2-b)$$

$$\frac{d}{dt} n_{mp} = -\frac{n_{mp}}{\tau_{mp}}, \quad (2-c)$$

where n_{ep} , n_{gp} and n_{mp} are the population probability of the excited state $6s6p \ ^1P_1$, the population probability of the ground state $6s^2 \ ^1S_0$ and the population probability of the metastable states $6s5d \ ^1D_2$ and $6s5d \ ^3D_2$ respectively. $1/\tau_{gp}$ and $1/\tau_{mp}$ are the transition rate of the excited state to the ground state and to the metastable state respectively. $1/\tau_{gp} = 2\pi * 18.9 * 10^6 \text{ sec}^{-1}$ or $\tau_{gp} = 8.4 \text{ nsec}$ and $1/\tau_{mp} = 2\pi * (48+18) * 10^3 \text{ sec}^{-1}$ or $\tau_{mp} = 2.4 \ \mu\text{sec}$. $1/\tau_p = 1/\tau_{gp} + 1/\tau_{mp}$. The intensity of the pump laser beam is I_p and the saturation intensity of the $6s^2 \ ^1S_0 - 6s6p \ ^1P_1$ transition is I_{sp} . When $I_p = 2 I_{sp}$ the stimulated emission is equal to the spontaneous emission. I_{sp} is given by

$$I_{sp} = \frac{\pi hc}{3\lambda^3 \tau_{gp}} = 14.6 \text{ mW/cm}^2. \quad (3)$$

On the right hand sides of Eqs. (2-a) and (2-b), the first term is the stimulated absorption rate, the second term is the stimulated emission rate, and the last term is the spontaneous emission decay rate. In Eq. (2-c), the term in the right-hand side is the spontaneous emission decay rate.

The coupled equations in (2) can be solved analytically. For the initial condition $n_g(0)=1$, $n_{ep}(0) = 0$ and $n_m(0) = 0$, the solution is given by,

$$n_{ep}(t) = \frac{S_p}{2\tau_{gp}} \frac{1}{\alpha p_+ - \alpha p_-} (e^{\alpha p_+ t} - e^{\alpha p_- t}), \quad (4-a)$$

$$n_{mp}(t) = \frac{S_p}{2\tau_{gp} \tau_{mp}} \frac{1}{\alpha p_+ - \alpha p_-} \left(\frac{e^{\alpha p_+ t}}{\alpha p_+} - \frac{e^{\alpha p_- t}}{\alpha p_-} \right) + 1, \quad (4-b)$$

$$n_{gp}(t) = 1 - n_{ep}(t) - n_m(t), \quad (4-c)$$

where

$$\alpha p_{\pm} = -\frac{1}{2} \left(\frac{S_p}{\tau_{gp}} + \frac{1}{\tau_p} \right) \pm \frac{1}{2} \sqrt{\left(\frac{S_p}{\tau_{gp}} + \frac{1}{\tau_p} \right)^2 - 2 \frac{S_p}{\tau_{gp} \tau_{mp}}}, \text{ and} \quad (5)$$

$$S_p = \frac{I_p}{I_{sp}}. \quad (6)$$

Since $\tau_{gp} \cong \tau_p$ and $\tau_{mp} \gg \tau_{gp}$, for $S_p \gg 1$ the set of Eqs in (4) reduces to

$$n_{ep}(t) \cong \frac{1}{2} \left\{ \exp\left(-\frac{1}{2\tau_{mp}} t\right) - \exp\left(-\frac{S_p}{\tau_{gp}} t\right) \right\}, \quad (7-a)$$

$$n_{mp}(t) \cong 1 - \exp\left(-\frac{1}{2\tau_{mp}} t\right), \quad (7-b)$$

$$n_{gp}(t) \cong \frac{1}{2} \left\{ \exp\left(-\frac{1}{2\tau_{mp}} t\right) + \exp\left(-\frac{S_p}{\tau_{gp}} t\right) \right\}, \quad (7-c)$$

It may be noticed that the population probability of the metastable state, $n_m(t)$ increases with the characteristic time $2\tau_{mp}$, not τ_{mp} . This reflects the fact that, because of stimulated emission, the population of the excited state is at most equal to the population of the ground state. Thus, for a very high intense laser beam, only half of the atoms are available in the excited state at any time. Consequently, the characteristic time for moving atoms from the ground state to the metastable state is double the time for an atom to decay from the excited state to the metastable state. For $t > \tau_{gp}$, the second term in Eqs. (7-a) and (7-c) is negligible compared with the first term and both $n_{gp}(t)$ and $n_{ep}(t)$ decay with time constant of $2\tau_{mp}$. Also, Eq. (7-b), which is correct for high laser intensity, does not depend on the laser intensity. This shows that, beyond some high laser intensity value, higher laser intensity is not necessary and does not help in pumping atoms to the metastable state. Instead one needs longer interaction time to pump more atoms to the metastable state.

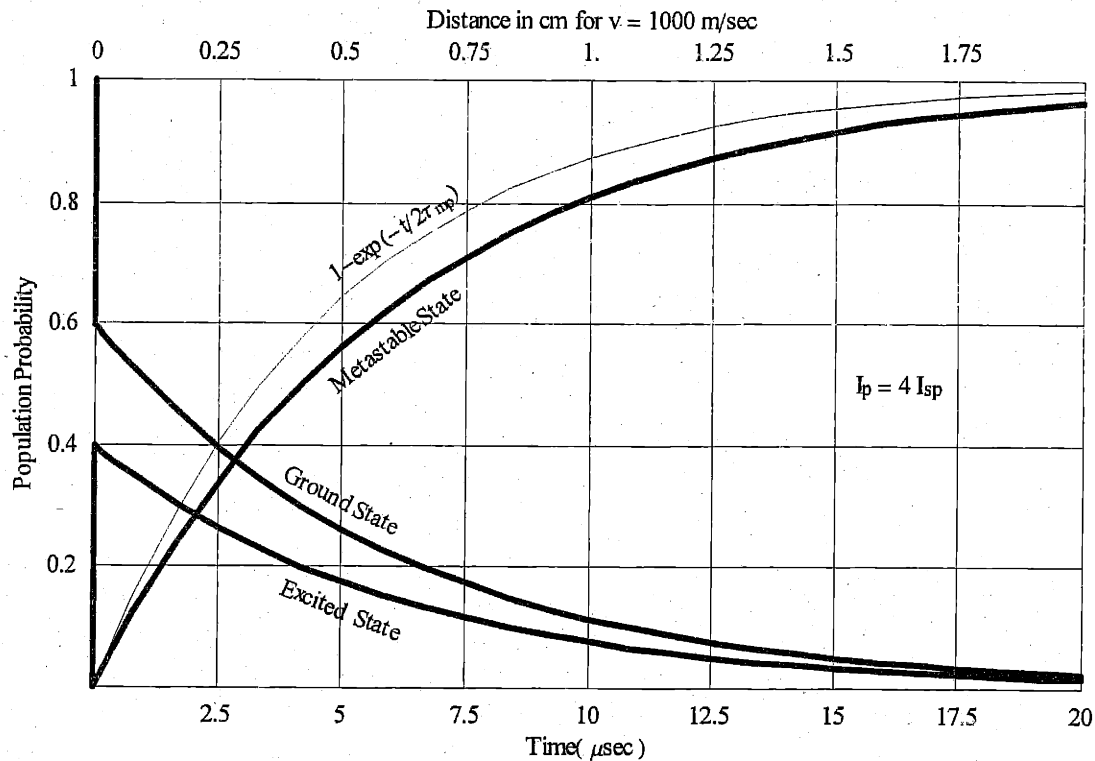


Figure 3. Prediction of Eq. (4) for $I_p = 4 I_{sp}$

Figure 3 shows the prediction of Eq. (4) for laser intensity equals to 4 times the saturation intensity of the $6s^2\ ^1S_0 - 6s6p\ ^1P_1$ transition. Also it shows the maximum pumping to the metastable state that may be achieved with infinite laser intensity; $1 - \exp(-t/2\tau_{mp})$. The upper x-axis shows the distance, in cm, for atoms with speed of 1000 m/sec. Since the most probable speed of our effusive atomic beam is about 400 m/sec, more than 99.5% of the atoms in our atomic beam have speed less than 1000 m/sec. Thus, laser beam with width of about 2 cm should be enough to pump most of the atoms into the metastable state.

4.1.2- Repumping stage predictions

The rate equations for the repump stage are given by

$$\frac{d}{dt} n_{er} = \frac{1}{2\tau_{mr}} \frac{I_r}{I_{sr}} \frac{1}{1 + \left(\frac{2\Delta}{\tau_{mr}}\right)^2} (n_{mr} - n_{er}) - \frac{n_{er}}{\tau_r}, \quad (8-a)$$

$$\frac{d}{dt} n_{mr} = \frac{1}{2\tau_{mp}} \frac{I_r}{I_{sr}} \frac{1}{1 + \left(\frac{2\Delta}{\tau_{mr}}\right)^2} (-n_{mr} + n_{er}) + \frac{n_{er}}{\tau_{mr}}, \quad (8-b)$$

$$\frac{d}{dt} n_{gr} = -\frac{n_{er}}{\tau_{gr}}, \quad (8-b)$$

where n_{er} , n_{gr} and n_{mr} are the population probability of the excited state $5d6p\ ^1P_1$, the population probability of the ground state $6s^2\ ^1S_0$ and the population probability of the metastable states $6s5d\ ^1D_2$, respectively. $1/\tau_{gr}$ and $1/\tau_{mr}$ are the transition rate of the excited state to the ground state and to the metastable state respectively. $1/\tau_{gr} = 2\pi * 5.6 * 10^6\ \text{sec}^{-1}$ or $\tau_{gr} = 28.4\ \text{nsec}$ and $1/\tau_{mr} = 2\pi * 7.2 * 10^6\ \text{sec}^{-1}$ or $\tau_{mp} = 22.1\ \text{nsec}$. $1/\tau_r = 1/\tau_{gr} + 1/\tau_{mr}$. $\Delta = \omega_l - \omega_{em}$ is the detuning between the laser frequency ω_l and the atomic transition frequency ω_{em} . The repump laser intensity is I_r and the saturation intensity of the $6s5d\ ^1D_2 - 5d6p\ ^1P_1$ transition is I_{sr} .

$$I_{sr} = \frac{\pi h c}{3 \lambda^3 \tau_{mr}} = 4.8 \text{ mW/cm}^2. \quad (9)$$

We want to study Eq. (8) to guide us in choosing the interaction length and the repump laser intensity, which produce a reasonable efficient repumping and a narrow velocity distribution.

A numerical example and analytical analysis of Eq. (8) are presented to demonstrate and establish the following fact: for a repump laser intensity much lower than the saturation intensity of the repump transition, the resulting velocity distribution depends only on the product of the laser intensity and the interaction length. Or, from experimental point of view, two different interaction lengths produce similar velocity-selected distribution when the laser intensity is adjusted to give similar repumping efficiency for the most probable velocity.

Figure 4 shows our simulations. It presents the initial population of the metastable state, which is assumed to have effusive-atomic-beam velocity distribution, and the resulting population repumped to the ground state. The repump laser is tuned to the most probable velocity and it is at 45 degrees with respect to the barium atomic beam. Narrower velocity distributions can be obtained by using smaller angles. Two different interaction lengths 10 mm and 1.0 mm are shown in Figure 4. The repump laser intensity is adjusted such that 90% of atoms with the most probable velocity are repumped to the ground state. For the 10 mm interaction length, the laser intensity is adjusted to $0.009 I_s = 0.04 \text{ mW/cm}^2$, while for the 1.0 mm interaction length, the laser intensity is adjusted to $0.095 I_s = 0.45 \text{ mW/cm}^2$. The distributions resulting from these two interaction lengths are almost overlapped, as shown by the continuous lines, and the difference between them is hard to see on the figure. The dashed line is a Lorentzian fit to the velocity-selected distribution. It has FWHM of about 13 % of that of the original effusive atomic beam velocity distribution. It may be noticed that atoms with slower velocities are repumped more than those with higher velocities. This is because the slower atoms spend more time in the laser beam than the faster ones.

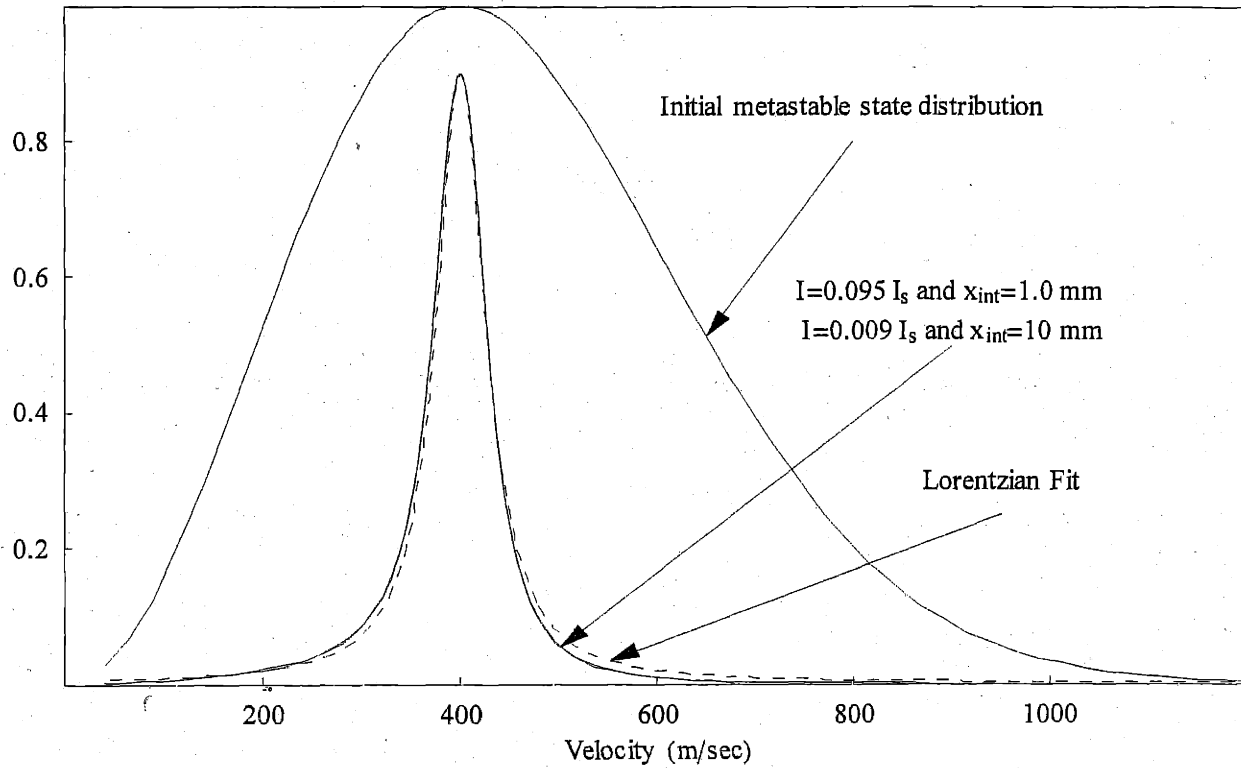


Figure 4. Velocity distributions for atoms initially in metastable state and atoms repumped to the ground state with a laser at 45° with the atomic beam and tuned to the most probable velocity of the initial distribution. The laser intensity and the interaction time are adjusted such that 90% of atoms with the most probable velocity are repumped to ground state.

Next, it is shown analytically that, for $I \ll I_s$, similar velocity distributions are obtained by making the product of the repump laser intensity and the interaction distance the same.

For the initial condition $n_{mr}(0) = 1$, $n_{er}(0) = 0$ and $n_{gr}(0) = 0$, the ground-state population is given by

$$n_{gr}(t) = \frac{S_r}{2\tau_{mr}\tau_{gr}} \frac{1}{\alpha_{r+} - \alpha_{r-}} \left(\frac{e^{\alpha_{r+}t}}{\alpha_{r+}} - \frac{e^{\alpha_{r-}t}}{\alpha_{r-}} \right) + 1, \quad (10)$$

where

$$\alpha_{r\pm} = -\frac{1}{2} \left(\frac{S_r}{\tau_{mr}} + \frac{1}{\tau_r} \right) \pm \frac{1}{2} \sqrt{\left(\frac{S_r}{\tau_{mr}} + \frac{1}{\tau_r} \right)^2 - 2 \frac{S_p}{\tau_{mr}} \frac{1}{\tau_{gr}}}, \quad \text{and} \quad (11)$$

$$S_r = \frac{I_r}{I_{sr}} \frac{1}{1 + \left(\frac{2\Delta}{\tau_{mr}}\right)^2}. \quad (12)$$

Since $\tau_{mr} \cong \tau_{gr} \cong \tau_r$, for $I_r/I_{sr} \ll 1$ (or $S_r \ll 1$), Eq. (11) is approximated by

$$\alpha r_+ \cong -\frac{S_r}{\tau_{mr}} \frac{\tau_{gr}}{\tau_r}, \text{ and} \quad (13)$$

$$\alpha r_+ \cong -\frac{1}{\tau_r}. \quad (14)$$

So, for $I_r/I_{sr} \ll 1$, Eq. (11) becomes

$$n_{gr}(t) \cong 1 - \exp\left[-\frac{I_r}{2I_{sr}} \frac{1}{4\Delta^2 \tau_{mr}^2 + 1} \frac{\tau_r}{\tau_{gr} \tau_{mr}} t\right]. \quad (15)$$

Thus, the population of the ground state depends on the product of the laser intensity and the interaction time. The resulting ground state distribution after the interaction length of x_{int} is given by

$$f(v) = C v^2 \text{Exp}\left[-\frac{v^2}{v_0^2}\right] \left\{1 - \exp\left[-\frac{I_r}{2I_{sr}} \frac{1}{4\left(\frac{v-v_0}{\lambda} \cos\theta\right)^2 \tau_{mr}^2 + 1} \frac{\tau_r}{\tau_{gr} \tau_{mr}} \frac{x_{int}}{v}\right]\right\}, \quad (16)$$

where C is a normalization constant and v_0 is the most probable velocity in the original velocity distribution. If the repump efficiency is not close to 100%, the velocity distribution in Eq. (16) is approximately Lorentzian as shown, for example, in Figure 4. The full width at half maximum of this distribution can be found numerically by setting

$$\frac{1}{2} f(v_0) = f(v_{hm}), \quad (17)$$

where v_{hm} is the velocity at which the height of the distribution is half of the maximum height. This equation cannot be solved analytically. Figure 5 shows the width of the velocity distribution as a function of the repump efficiency

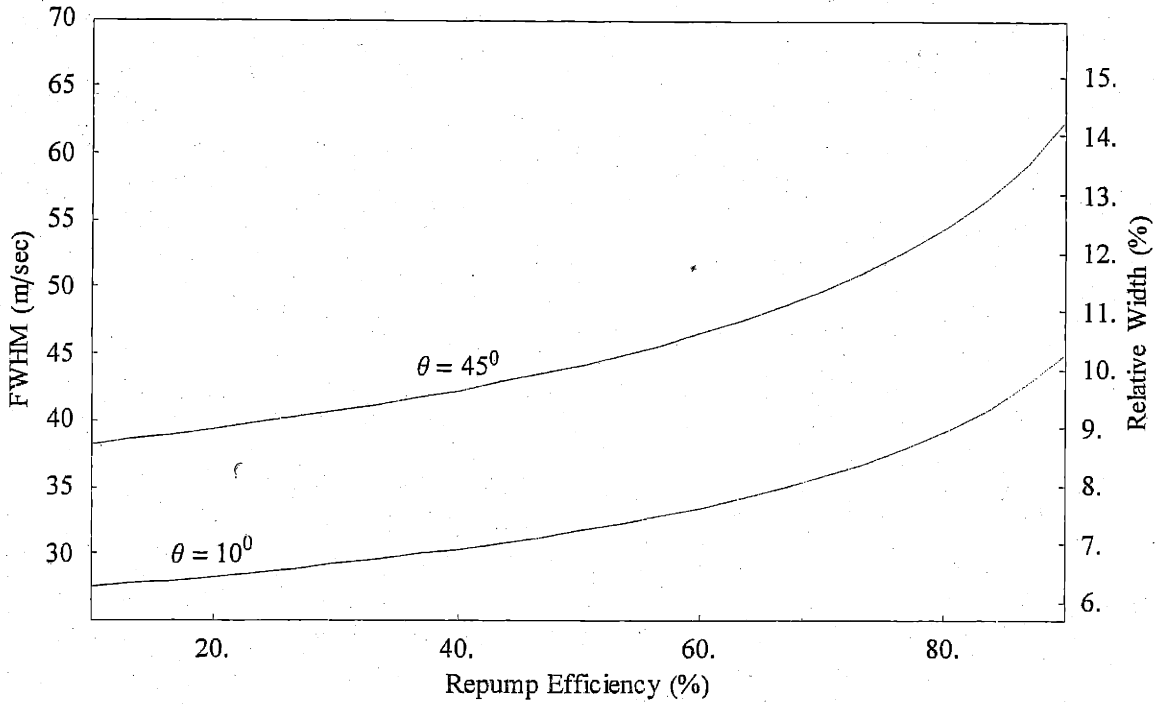


Figure 5. The full width at half maximum of the velocity distribution of Eq (16) as a function of the repump efficiency of atoms with the most probable velocity is shown for two different angles. The right y-axis is the percentage ratio between the width of the repumped velocity distribution and the width of the original effusive beam velocity distribution. The most probable velocity is 380 m/sec.

For a very low repump efficiency, the width of the velocity distribution can be derived from Eq. (1).

$$\delta v = \frac{\lambda}{\cos(\theta)} \delta \Delta$$

$$FWHM = \frac{\lambda}{\cos(\theta)} \Gamma_m, \quad (18)$$

where the spread in frequency $\delta \Delta$ is equated with the line width of the $6s5d \ ^1D_2 - 5d6p \ ^1P_1$ transition Γ_m .

In the analysis of the velocity selection scheme we ignored the effect of sublevels. This may cause the repumping process to be less efficient and the final velocity spread to be wider.

4.2- Experiment

We use three dye lasers to study our velocity selection scheme. One laser is used for pumping atoms to the metastable state, another is used to repump atoms back to the ground state and the third laser is used to probe the resulting velocity distribution. All lasers are pumped with one Ar-Ion laser Coherent Innova 100.

The pump laser is a ring dye laser Coherent CR-699-21. R110 dye is used to produce a wavelength of 553 nm. The laser has a typical output of about 500 mW when it is pumped with 6 W of Ar-Ion laser beam. It has jitter of less than 1 MHz RMS at 10 kHz bandwidth and a long-term drift of about 100 MHz/hour[8].

Both the repump and the probe lasers are a standing-wave dye lasers Coherent CR-599-21. R110 dye is used in the probe laser to produce a wavelength of 553 nm, while R6G dye is used in the repump laser to produce a wavelength of 583 nm. Each laser produce about 20 mW when each is pumped with 3 W Ar-Ion laser beam. Both lasers have frequency jitter and drift similar to the pump laser[8].

4.2.1- Pumping stage

Figure 6 shows the experimental setup for studying the pumping stage. A laser beam from the 699 dye laser is expanded by two cylindrical lenses ($f = -0.64$ cm and $f = 10.0$ cm) into a beam about 1.8 cm wide, and then is sent perpendicularly to the atomic beam. This laser is tuned to the $6s^2\ ^1S_0 - 6s6p\ ^1P_1$ transition. Its intensity is about $60\text{ mW/cm}^2 = 4 I_s$. To eliminate any contributions from other barium isotopes, the probe is also sent perpendicular to the atomic beam. The probe is about 2.5 mm in diameter and it has intensity of about $0.2\text{ mW/cm}^2 = 0.014$

I₃. The probe scans 390 MHz around the $6s^2\ ^1S_0-6s6p\ ^1P_1$ transition in 2.5 sec. The distance between the pump region and the probe region is about 5 cm. The fluorescence from the probe area is imaged by a lens ($f = 0.5\ \text{m}$) into a fiber optics bundle to a Hamamatsu R1635-02 PMT. The probe collection port is shielded well such that scattering from the laser beams and the fluorescence in the pump area is much smaller than the probe signal. A Stanford Research Systems preamplifier SR440 and counter SR400 are used to amplify and count pulses from the PMT. The counts on the counter are transfer to a computer by an RS232 interface and stored there.

Figure 7 shows the experimental result for the pumping stage. The upper experimental scan shows the probe signal when the pump laser is blocked. The fluorescence from ^{138}Ba isotope along with the fluorescence from other barium isotopes can be observed. In our oven, we use barium metal, which has the natural abundance of barium isotopes. The natural abundance of the ^{138}Ba isotope is 71.7%. The ^{137}Ba isotope contributes 11.2 % of the natural barium metal and its resonance fluorescence is 65 MHz away from that of the ^{138}Ba isotope. The ^{134}Ba , ^{135}Ba and ^{136}Ba isotopes have natural abundance of 2.4%, 6.6% and 7.9% respectively. These isotopes are 140MHz, 105MHz and 125 MHz away from that of the ^{138}Ba isotope, respectively. The lower scan in Figure 7 shows the probe signal when the pump is allowed to pump atoms to the metastable states. About 98% of the ^{138}Ba isotope is pumped to the metastable states, which is in agreement with the prediction of Eq.(7)(See Figure 3).

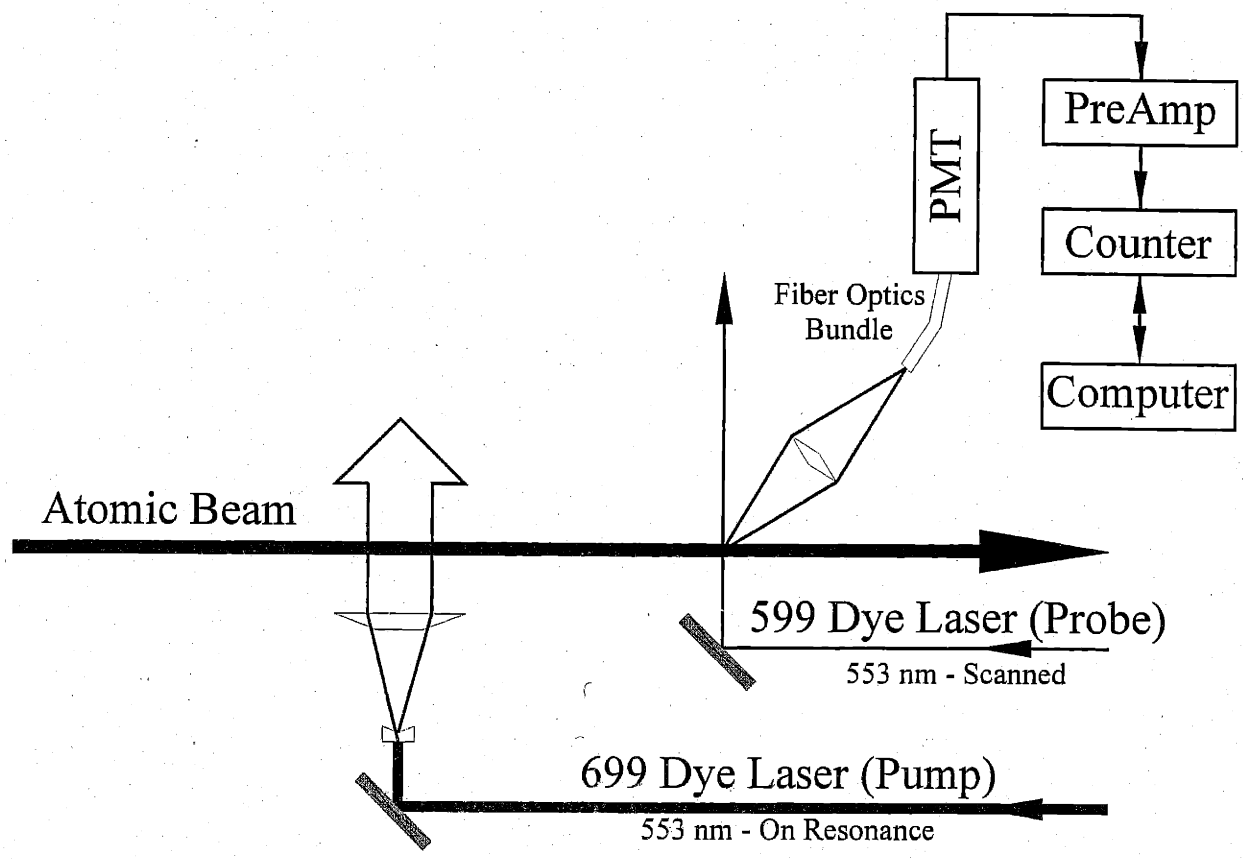


Figure 6. Experimental setup used to study the effectiveness of the pumping stage.

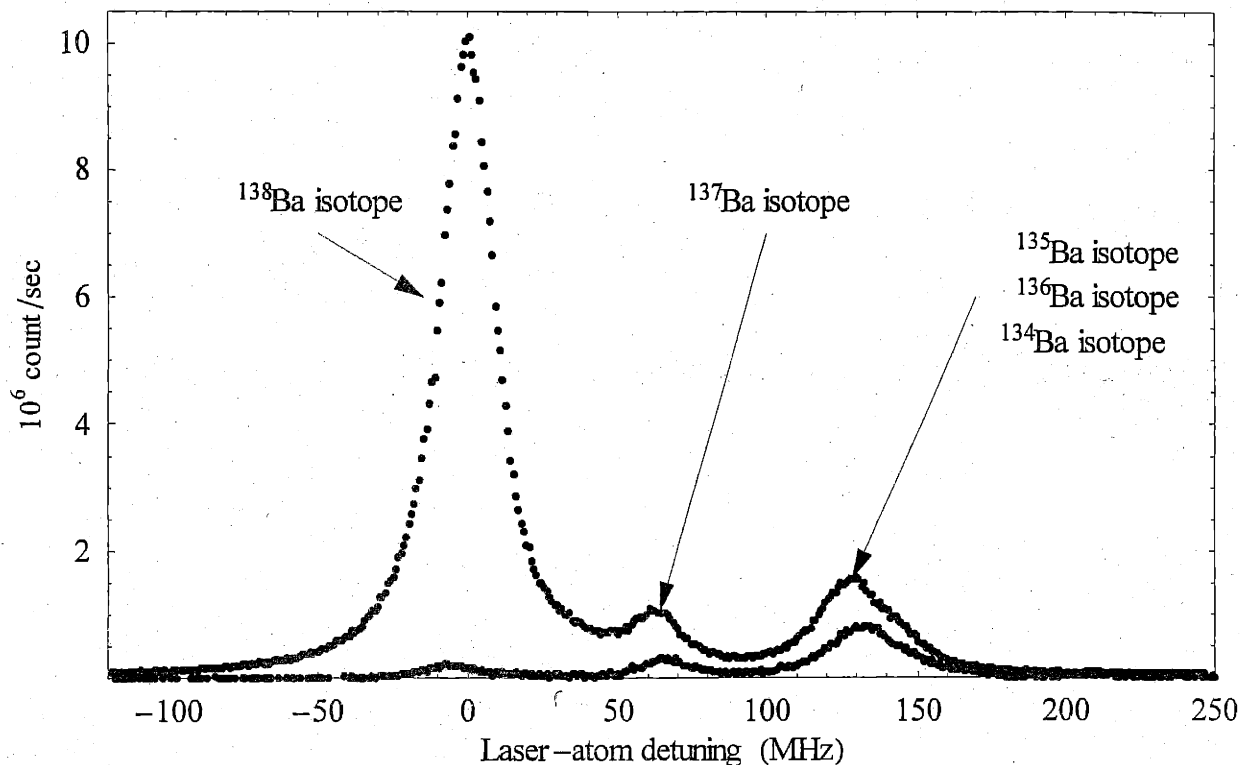


Figure 7. Pumping of barium to the metastable state by a 1.8 cm wide and $4 I_s$ intense laser beam.

4.2.2- Finding 583 nm Resonance

Before the velocity selection experiment, all our dye lasers were tuned to the 553 nm transition. We have chosen one of them to be the repump laser and have changed its dye to R6G. This repump laser has to be tuned to the $6s5d \ ^1D_2 - 5d6p \ ^1P_1$ transition. This might be accomplished by measuring its wavelength with a calibrated wave meter. Instead, we tuned the laser using a simple technique described below. Figure 8 shows the experimental set up to tune the repump laser. The 699 dye laser is used to pump barium atoms to the metastable states and also to probe them down stream. The repump laser is sent between the pump and the probe beams. If the repump laser is not in resonance with the $6s5d \ ^1D_2 - 5d6p \ ^1P_1$ transition, the signal in the probe region will be almost zero otherwise we should have a huge signal there.

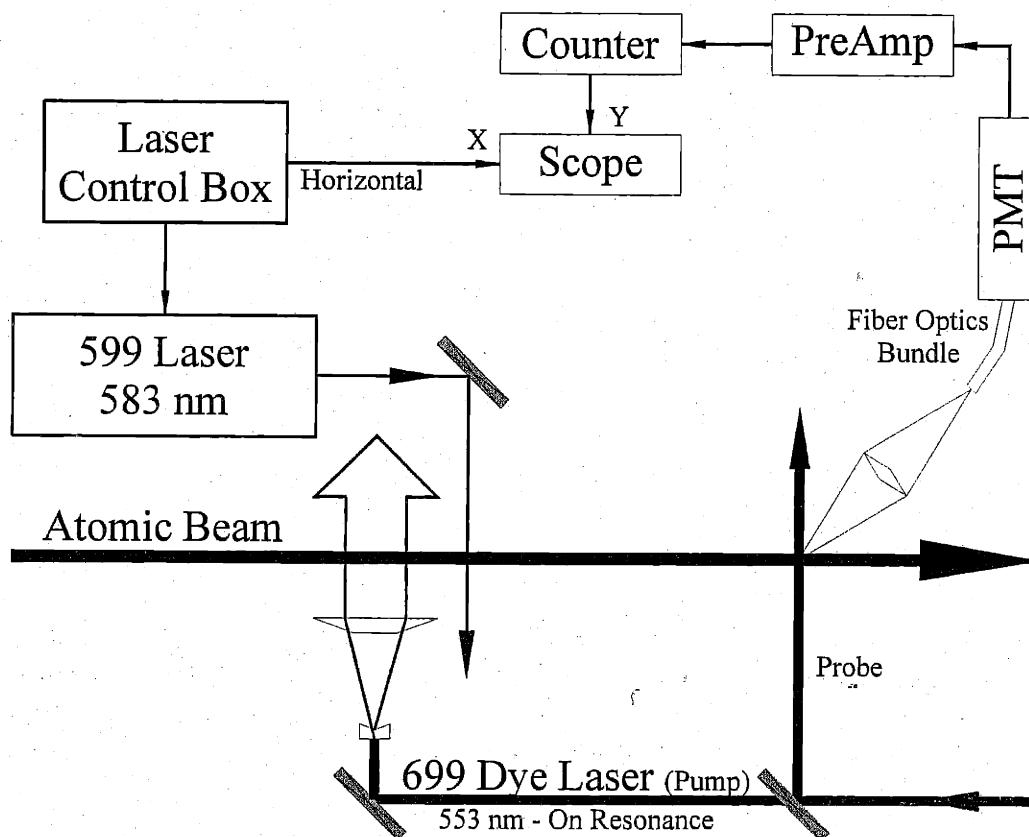


Figure 8. Experimental setup to tune the repump laser to the $6s5d\ ^1D_2 - 5d6p\ ^1P_1$ transition.

We force the repump laser to have broadband oscillation by taking its internal cavity assembly (ICA) out of the laser cavity. Now, the birefringence filter limits the laser oscillation frequency to about 20 GHz band. Actually, because of gain competition, the laser oscillates at any time in just one single mode but because of mechanical vibrations in the laser cavity, the laser is jumping randomly between many single modes lying within the band allowed by the birefringence filter[6]. There are about 70 single modes each is separated by 283 MHz. Thus this trick provides us with an intense narrow spectral laser beam sampling a huge range of frequency.

We scan the birefringence filter until a flickering in the probe signal is observed. This means that we are less than 20 GHz away from the $6s5d\ ^1D_2 - 5d6p\ ^1P_1$ transition. We place the ICA back into the laser cavity and manually scan the laser by 10 GHz to find the steady probe

signal. Sometimes we may need to hop the laser by the thin etalon offset knob in the laser control box to find the resonance.

4.2.3- Repumping stage

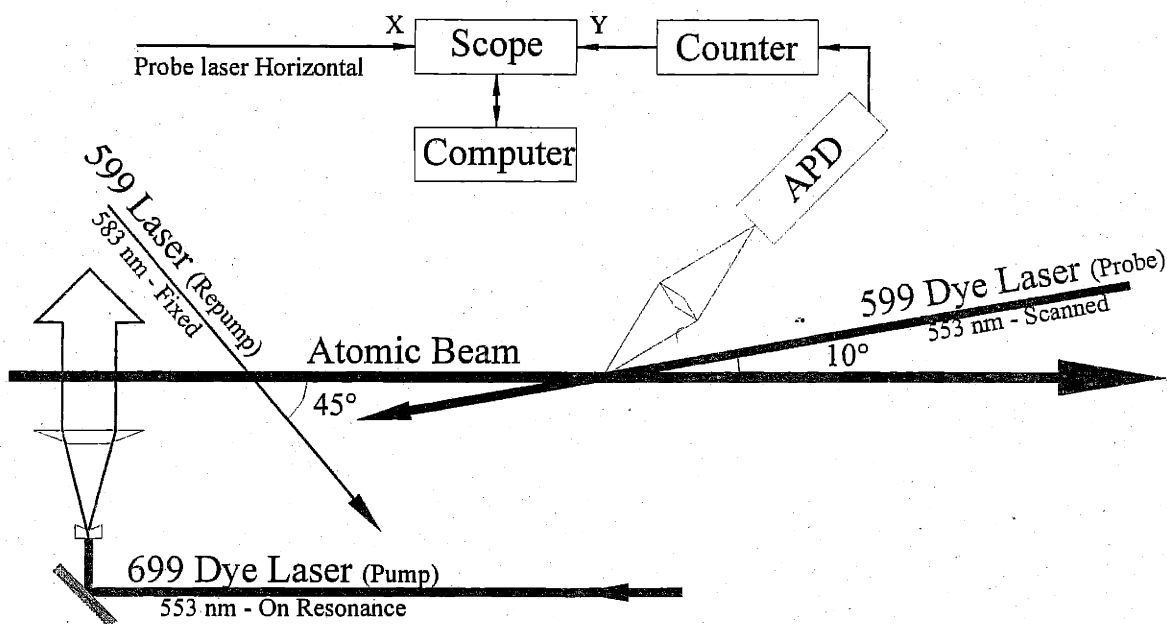


Figure 9. Experimental setup to monitor the two-laser velocity selection scheme.

Figure 9 depicts the experimental setup for our velocity scheme. Figure 10 shows the probe signal when the repump laser beam is blocked. The upper distribution is when the pump is blocked. This distribution includes contributions from different barium isotopes. The lower distribution is when the pump is allowed to pump the atoms to the metastable states. We use the same pump laser intensity and interaction length as in Figure 7. Thus the lower distribution is mainly contributions from barium isotopes other than ^{138}Ba isotope. This lower distribution will be used to subtract the contribution from barium isotopes other than ^{138}Ba isotope. For example, the original ^{138}Ba velocity distribution can be obtained by subtracting the lower distribution from

the upper one. This is the upper distribution shown in Figure 12. The solid line going through this distribution is a Maxwell-Boltzmann distribution fit.

$$f(v) = v^2 e^{-\left(\frac{v}{381}\right)^2} \quad (19)$$

The most probable velocity is 381 m/sec. The most probable velocity is related to the oven temperature by

$$T = \frac{1}{2} m v_0^2 \frac{1}{k_B}, \quad (20)$$

where T is the oven temperature in the absolute temperature scale, m is ^{138}Ba atom mass, v_0 is the most probable velocity and k_B is the Boltzmann constant. The most probable velocity of 381 m/s, thus, corresponds to oven temperature of 940°C .

The x-axis in figure 10 is converted to velocity using Eq. (1). The angle between the atomic beam and the probe beam, θ , is 10° . The frequency of the probe laser that corresponds to zero velocity is found from fitting the distribution to Eq. (19).

This experiment is done with the microlaser atomic beam. An avalanche photodiode (APD), EG&G C30902S-TC, originally aligned to monitor the density of barium atoms in the microlaser cavity, is used to detect the probe signal. The APD has saturation count rate of about 300×10^3 count/sec[7]. We have to keep the signal size much smaller than this value to avoid saturation.

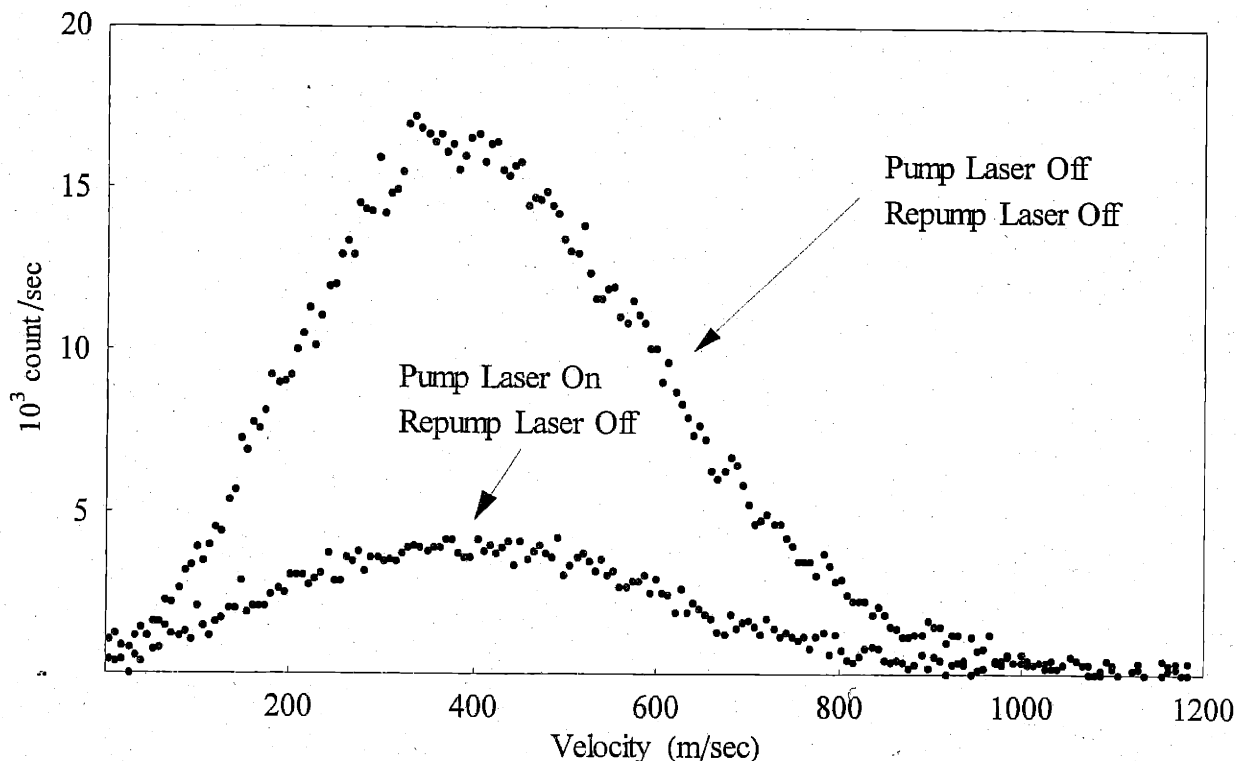


Figure 10. The probe signal when the repump laser is off. The lower trace is mainly contribution from barium isotopes other than ^{138}Ba isotope.

Figure 11 shows probe signal when both the pump laser and the repump laser are on. Now the repump laser repumps ^{138}Ba atoms with specific velocities back to ground state. We can see in this figure the sharp velocity peak from ^{138}Ba atoms on top of the broad background, which mainly from barium isotopes other than ^{138}Ba isotope. When the lower distribution in Figure 10 is subtracted from the distribution in Figure 11, we obtain the velocity distribution of the selected ^{138}Ba atoms. The result of this subtraction is shown as the sharp distribution in Figure 12. The continuous line through this distribution is a Lorentzian fit. The ratio between the width of the velocity-selected distribution and the original distribution is about 12 %. The ratio of the heights of these the two distributions is about 55 %. The middle curve shown in Figure 12 represents the distribution of the $6s5d\ ^1D_2$ metastable state before the repump laser. This is obtained from the upper distribution by assuming that $9/(9+25) = 0.26$ of atoms go to the $6s5d\ ^3D_2$ metastable state, which is not accessible by our laser. The efficiency of the repump process can be found by comparing the heights of the velocity selected distribution and the $6s5d\ ^1D_2$ metastable state distribution. This ratio is 75%.

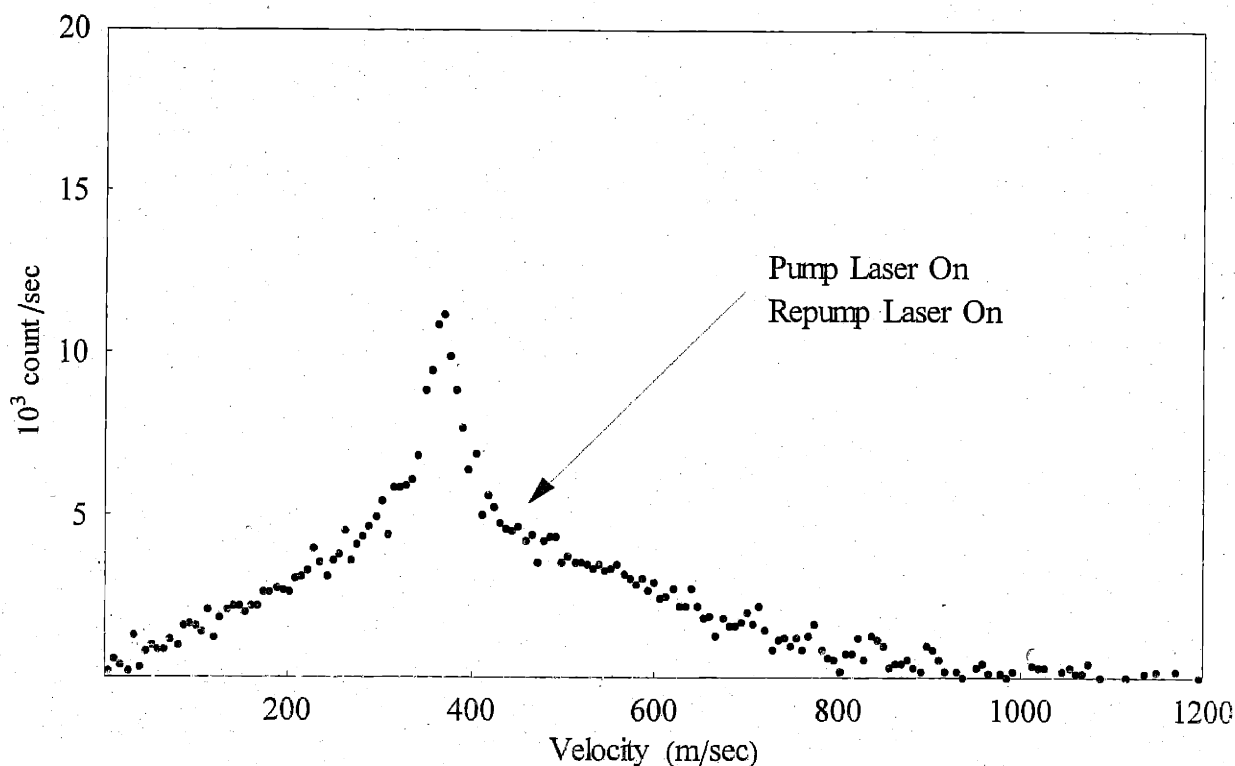


Figure 11. The probe signal when both the pump laser and the repump laser are on. The broad distribution is from barium isotopes other than ^{138}Ba isotope. The sharp distribution is the ^{138}Ba atoms repumped back to the ground state by the repump laser.

Figure 13 shows relative width between the velocity-selected distribution and the original velocity distribution of ^{138}Ba atoms as a function of the efficiency. Two types of efficiency are shown: Total efficiency and repump efficiency. The total efficiency is the ratio between the height of velocity-selected distribution and the height of the original velocity distribution while the repump efficiency is the ratio between the height of velocity-selected distribution and the height of the distribution of atoms in the $6s5d\ ^1D_2$ metastable state before the repump laser. The interaction length between the repump laser and the atomic beam, x_{int} , is about 10 mm and the repump laser intensity, I_r , is adjusted to obtain the desired efficiency. It is verified experimentally that, as indicated by Eq. (16), for $I_r \ll I_{sr}$, similar velocity distributions are obtained for similar values of the product $I_r x_{\text{int}}$. The solid curve in Figure 13 is a fit using Eq. (16). In Eq. (16), the product $I_r x_{\text{int}}$ is varied to obtain the required efficiency and the FWHM of the velocity distribution is found numerically. The experimental values and the calculated

values agree with each other except for high repump efficiencies. This may be attributed to the simplicity of our model, which ignores the sublevel structure of the barium atomic states.

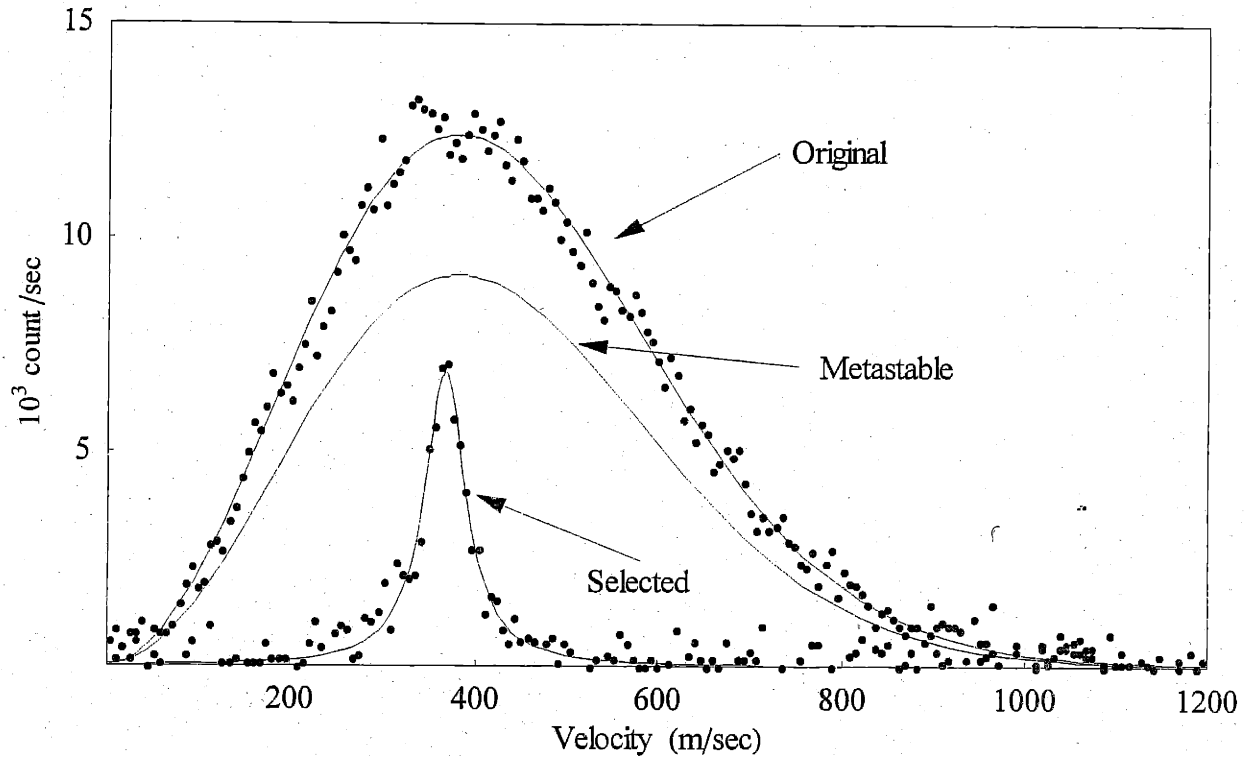


Figure 12. The upper distribution is the initial ^{138}Ba atoms distribution. The solid line going through it is a Maxwell-Boltzmann distribution fit. This distribution is obtained by subtracting the lower distribution from the upper distribution in Figure 11. The lower sharp distribution is the ground state ^{138}Ba atoms selected by the repump laser. The fit through this distribution is Lorentzian. This distribution is obtained by subtraction the lower distribution in Figure 10 from the distribution in Figure 11. The middle curve represents the distribution of the $6s5d\ ^1D_2$ metastable state before the repump laser.

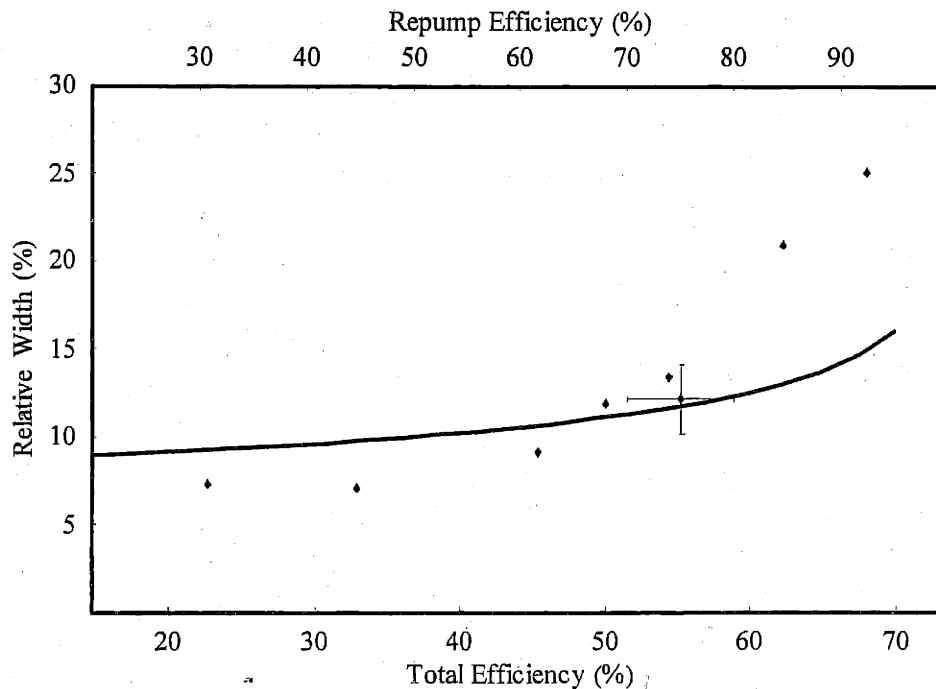


Figure 13. Relative width between the velocity-selected distribution and the original velocity distribution of ^{138}Ba atoms as a function of the efficiency. The total efficiency is measured with respect to the original velocity distribution while the repump efficiency is measured with respect to the distribution of atoms in the $6s5d\ ^1D_2$ metastable state before the repump laser. The solid curve is a fit using Eq. (16) with $v_0 = 380$ m/sec and $\theta = 45^\circ$.

4.3- Laser long-term drift stabilization:

Dye lasers from Coherent Company have long-term frequency drift of about 100 MHz/hour [8]. This drift rate is quite large when compared with typical time for collecting one data point for the degree of the second-order coherence function, which is about 20 minutes. During this time, dye lasers drift by amounts much larger than the line width of the states used in velocity selection scheme. To be able to use our velocity selection scheme effectively, we need to get rid of this long-term drift. We accomplish this task by locking the two lasers to barium atomic transitions.

Figure 14 shows a block diagram of the scheme we used to lock both the pump and repump lasers. Because of space limitation we are not able to use the microlaser chamber to lock the lasers, instead a separate chamber and oven are dedicated for this purpose. The design

of the locking oven is similar to that of the microlaser oven, which is discussed in Chapter 3. In front of the oven there are two apertures to produce two atomic beams. One atomic beam is used to lock the pump laser while the other is used to lock the repump laser.

The long-term drift of the 699 dye laser (the pump laser) is eliminated by locking it to the $6s^2 \ ^1S_0 - 6s6p \ ^1P_1$ transition (the pump transition). A local oscillator of a lock-in amplifier dithers the frequency of the pump dye laser and the fluorescence intensity from the pump transition is detected by a photodiode, which sends its signal back to the input of the lock-in amplifier. The output of the lock-in amplifier is proportional the DC component of multiplication of the input signal and the local oscillator. The output of the lock-in amplifier is integrated and added to the local oscillator and is fed back to the external frequency control of the laser to correct its frequency and to maintain it on resonance.

Figure 15 illustrates how the output of the lock-in amplifier changes with the central value of the dithered laser frequency. When the laser is on resonance the output of the lock-in amplifier is zero while it is negative when the laser is above resonance and positive when the laser is below the resonance. This provides negative feedback to the laser frequency and maintains it always on resonance.

The DC levels in Figure 15 may be anticipated by comparing values of the detector signal during the first half and during the second half of the local oscillator cycle. When the laser is on resonance, the detector signal during the positive half of the local oscillator cycle is similar to that during the negative half. Thus the average value of the multiplication of the detector signal and the local oscillator signal is zero. When the laser is above resonance, the value of the detector signal during the positive half of the local oscillator cycle is lower than that during the negative half cycle. This produces negative average value for the multiplication of the detector signal and the local oscillator. The opposite is true when the laser is below resonance.

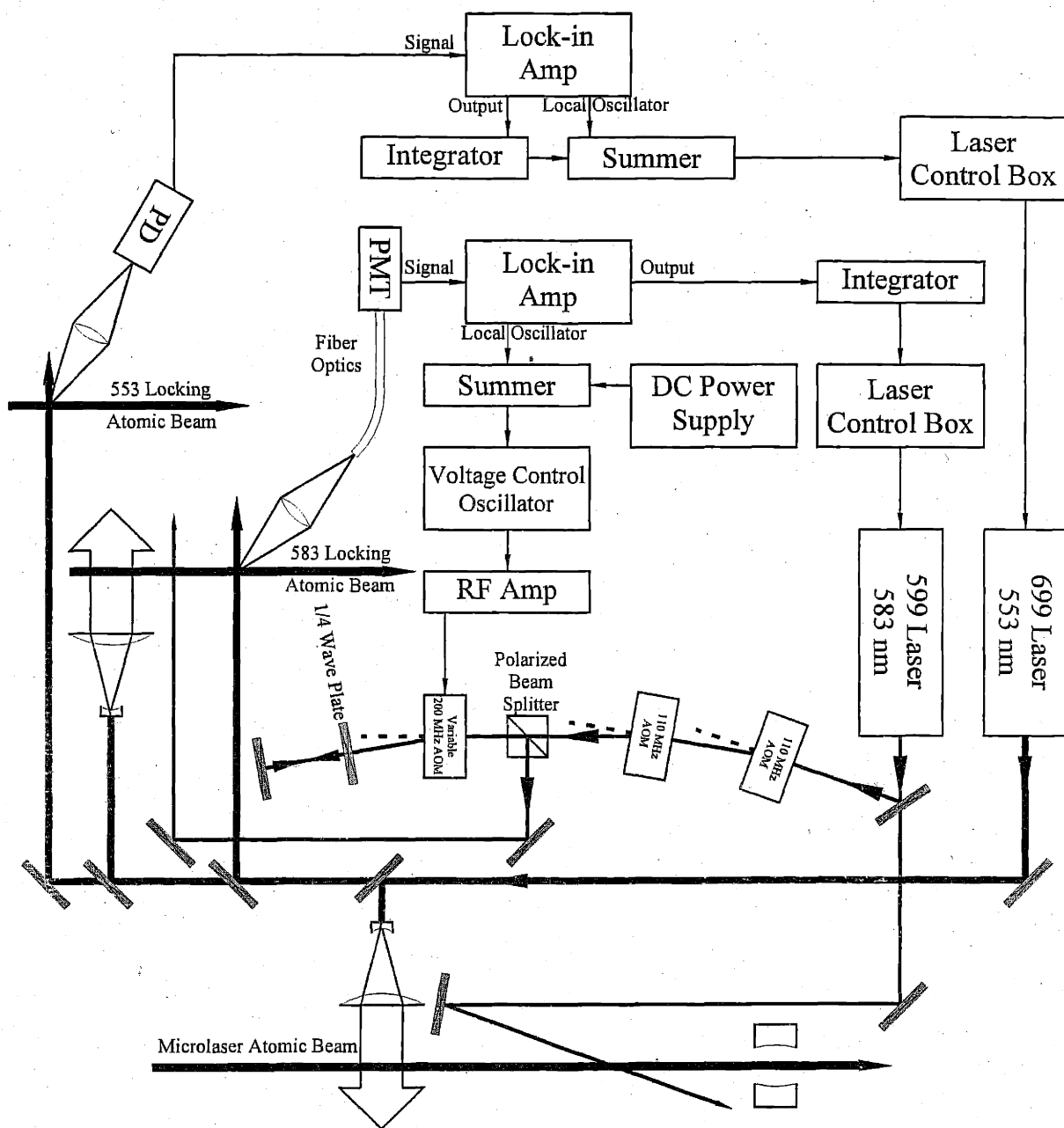
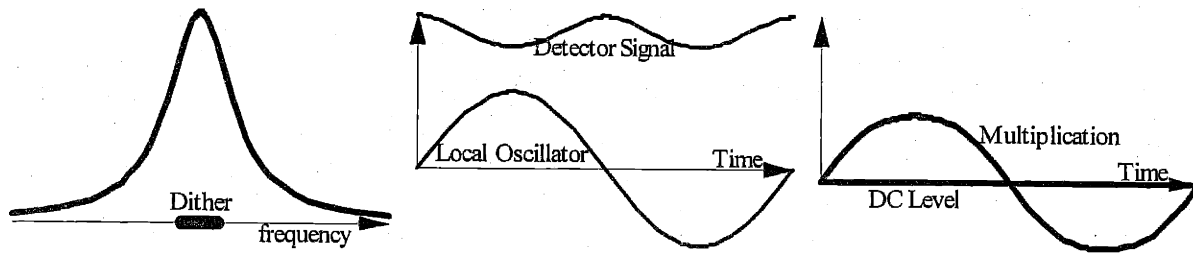
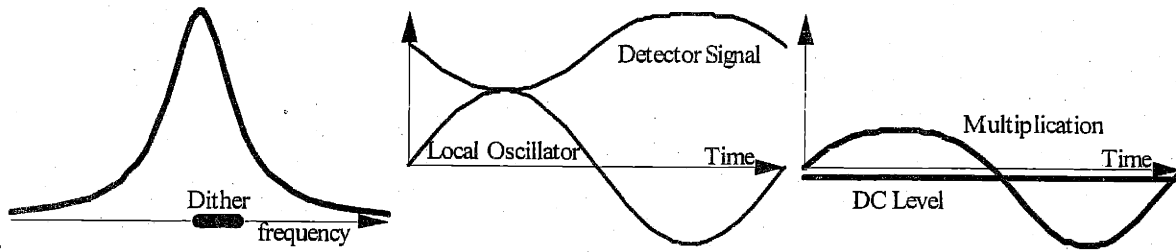


Figure 14. Block diagram for log-term drift stabilization of the pump laser, the 699 dye laser, and the repump laser, the 599 dye laser.

(a) On resonance



(b) Above Resonance.



(c) Below resonance.

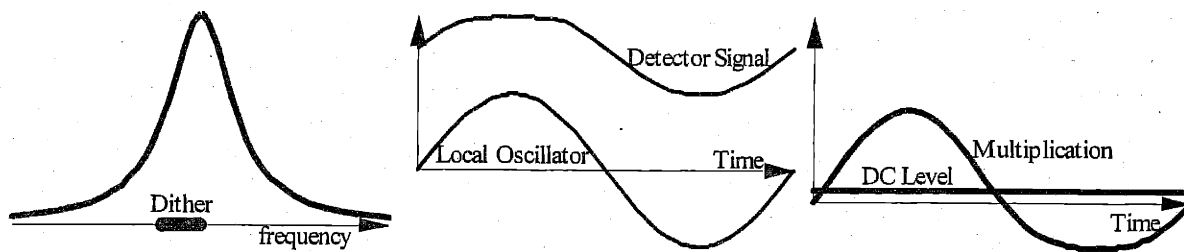


Figure 15. Illustration of relationship between the lock-in amplifier output and the position of the central value of dithered laser frequency. The plot on the left represents the detector signal when the laser is scanned through the atomic transition. The small thick line on the frequency axis represents the laser dither value that produces the two plots on the right.

Our lock-in amplifier is from Princeton Applied Research model number 121 and our photodiode is from ThorLabs model number det110. The laser dithering amplitude is about 0.5 MHz with dithering frequency of order of 100 Hz. The laser beam, with this small dithering, is sent directly to the microlaser atomic beam to pump atoms into the metastable state. The dither in laser frequency has almost no effect on the pumping process because of two reasons. First, the dither amplitude is much smaller than the power-broadened pumping transition line width. Typically we use $I \sim 10 I_s$ and thus the power-broaden line width is $19MHz\sqrt{1+10} = 36.5MHz$. Second, as mentioned previously, after some high intensity value, higher intensity does not help in pumping more atoms and hence small change in the very high intense laser power has almost no effect.

For the 599 laser (the repump laser), the laser itself and the laser beam going to the microlaser chamber are not dithered. Instead, an acousto-optic modulator (AOM) is used to dither the beam going to the locking chamber. Two beams from the 699 laser, which is now locked to the pumping transition, are sent to the 583 nm locking atomic beam. One beam is expanded and used to pump atoms to the metastable state and the other is used to probe atoms down stream after the repump laser beam. To augment the signal size at the probe area, the repump laser is sent perpendicular to the atomic beam. When the repump laser is scanned through the repump transition, the fluorescence in the probe region scans a Lorentzian profile with a FWHM of about 7.2 MHz (the repump transition FWHM) provided that the repump intensity is low. Thus, dithering the frequency of the repump locking laser beam modulates the intensity of fluorescence in the probe area. This fluorescence modulation may be used to stabilize the repump laser in almost a similar manner as the pump laser is stabilized.

The fact that the repump locking laser beam is perpendicular to the atomic beam means the Doppler shift for this laser beam is zero. So we need to introduce a frequency shift between this perpendicular laser beam and the repump tilted laser beam in the microlaser chamber so that we may be able to repump atoms with the most probable velocity. We obtained a shift of $620 \pm 80MHz$ by using three AOMs as follows: we shift the locking repump laser beam twice by two 110MHz fixed-frequency AOMs then we shift it by double-passing it through $200 \pm 40MHz$ variable-frequency AOM. As Figure 14 shows, to pick up the laser beam coming

out of the double-passed AOM, a $\frac{1}{4}$ wave plate changes the polarization of the laser beam by 90 degrees and then a polarized beam splitter picks it up and sends it to the locking chamber.

A voltage control oscillator (VCO), Mini-Circuits model ZOS-400, produces radio frequency oscillation, which is amplified by a radio frequency amplifier, Mini-Circuits model ZHL-2-8 to appropriate level to drive the double-passed AOM. A local oscillator of a lock-in amplifier, Stanford Research Systems SR510, dithers the frequency of the VCO and a variable DC power supply changes its central frequency. Because the variable-frequency AOM is double-passed, the direction of the output laser beam does not change (to the first order) by changing the beam frequency. The repump locking laser beam is dithered by amplitude of about 0.5 MHz and dithering frequency of order of 100 Hz.

A Hamamatsu PMT R1635-02 detects the fluorescence in the probe region. Its current is fed to the input of the lock-in amplifier whose output is integrated and then fed back to the external frequency control of the repump laser to maintain the laser frequency with respect to the repump transition.

By this long-term frequency drift stabilization technique, the two dye lasers are able to provide a stable velocity-selected atomic beam for several hours .

4.4- References

-
- [1] C. Weiquan, C. Houxin, L. Fusheng, S. Wei, S. Shundi and W. Yuzhu, Chin. Phys. Lett. **12**, 269 (1995).
 - [2] W. D. Phillips, J. Prodan and H. Metcalf. J. Opt. Soc. Am. B, **2**, 1751(1985).
 - [3] M. E. Donovan, M. Sc. Thesis, Massachusetts Institute of Technology, June 1990.
 - [4] S. Niggli and M. Huber, Phys. Rev. A **35** 2908(1987).
 - [5] O. Svelto, Principles of Lasers, Second Edition, p59, Plenum Press 1986.
 - [6] W. Demtroeder, Laser Spectroscopy Basic Concepts and Instrumentation, Second Edition, p225, Springer 1998.
 - [7] K. An, Ph.D. Thesis, Massachusetts Institute of Technology, 1995.

[8] Coherent Manuals for 699-21 and 599-21 dye lasers.

Chapter

5 Multi-Stop Time-to-Digital Converter

5.1- Introduction

In this chapter, a new design for a multi-stop time to digital converter (MSTDC) is described. This MSTDC is used to measure the degree of the second-order coherence $g^{(2)}(\tau)$ function. The design is conceptually simple and it is easily and inexpensively implemented. Our implemented MSTDC has a resolution of 20 nsec and a range of up to 0.6 msec. This resolution should be enough for measuring $g^{(2)}(\tau)$ for our microlaser, which has typical correlation time of about 1 μ sec. This correlation time is obtained from applying the single-atom microlaser theory to our system [1] and is demonstrated experimentally..

The degree of the second-order coherence $g^{(2)}(\tau)$ is defined as the normalized joint probability for measuring two photons separated by time τ . This joint probability is normalized such that for uncorrelated photons it has a value of 1.

Experimentally, one way to measure $g^{(2)}(\tau)$ is to use a photoelectron pulse to start a time interval T and then measure within T . Then, T is digitized into many small time bins such that when the arrival time of a photon lies within a time bin, the count in that bin is incremented by one. This process of starting an interval time T and measuring the arrival times of subsequent photons is repeated until each time bin has good statistics. Assuming that the interval T is much larger than the correlation time between two photons, the resulting count distribution is normalized by dividing the distribution by the average counts in the bins near the end of T .

In one T interval, more than one photon might be detected. It is important not to just register the first photon and ignore all other photons as it is the case when a simple time to digital

converter unit is used. This will not produce the $g^{(2)}(\tau)$ distribution but rather it produces the two-successive photon distribution $P_{01}(\tau)$. These two distributions are quite different when the counts rate is high but they are proportional to each other in the limit of zero light intensity.[2]. For example, as Figure 1 shows, for a light source with a Poisson statistics, $g^{(2)}(\tau)$ is straight horizontal line while $P_{01}(\tau)$ is an exponential decay function with a decay time proportional to the light source intensity. Thus, while the shape of $g^{(2)}(\tau)$ is only a function of the intrinsic propriety of the light source, $P_{01}(\tau)$ shape depends on the intrinsic propriety of the light source as well as its intensity.[3].

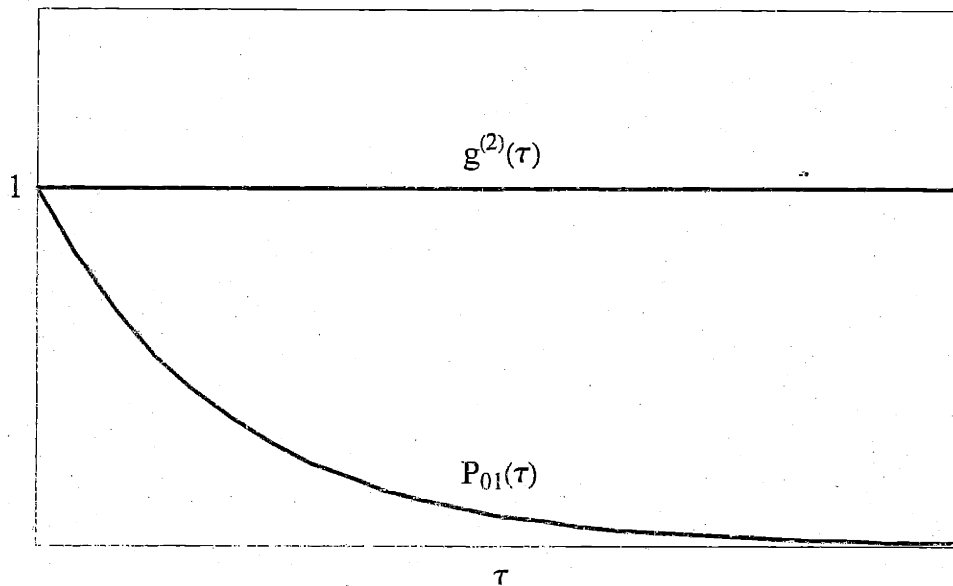


Figure 1. Difference between two distributions. One is obtained by using a one-stop time to digital converter ($P_{01}(\tau)$), and the other is obtained by using a multi-stop time to digital converter ($g^{(2)}(\tau)$).

Our MSTDC has the capability to measure all stop photons as long as each of them is separated by more than 20 nsec from the others. For example if the MSTDC range is set to 20 μ sec, then it can detect up to 1000 photons after the start photon.

Theoretically, one can use only one fast detector to measure $g^{(2)}(\tau)$. Both the start and stop photons come from the same detector. Another approach is to use two different detectors,

one to start and the other to stop. So, shall we design our MSTDC for one-detector configuration or two-detector configuration?

The principal problem with one-detector configuration is that afterpulses may distort the $g^{(2)}(\tau)$ measurement. In real detectors some pulses are generated not from real photons but rather they are spurious pulses associated with the real photon pulses. These spurious pulses are called afterpulses and they occur after the real photon pulses with a certain probability within a specific time range. Their origin, for example in the PMT's, is the residual gases inside the PMTs. These gases can be ionized by the accelerated electrons. Afterpulses are generated when these ions strike the photocathode or earlier stages of dynodes of the PMTs. Afterpulses cannot be electronically discriminated because their heights are comparable or larger than the real pulses.[4].

Figure 2 shows afterpulse distribution from our PMT Hamamatsu R943-02. The probability for an afterpulsing to occur is about 0.14% within a time range of about $1\mu\text{sec}$ [5].

The afterpulses associated with the start pulses, called start afterpulses, might severely distort $g^{(2)}(\tau)$ measurements, especially when the count rate is low. For every start pulse, there is a chance of having an afterpulse within a specific time range. This chance is independent of photon count rate. On the other hand, the probability of detecting a stop photon over the same time range is proportional to the count rate and, for low enough count rates, this probability might be comparable with that of detecting the start afterpulses. Thus, over this time range we have two comparable contributions: One from the start afterpulses and the other from the real photon pulses. Beyond this range we have only contributions from the photon stop pulses.

Contributions from afterpulses associated with the stop pulses, called stop afterpulses, to the $g^{(2)}(\tau)$ measurement are not detrimental as those from the start afterpulses. They occur over all time range and their relative contributions are equal to their probability to occur, for example in our PMT it is about 0.1%. As a numerical example, the rate of detecting two real photons signals, one at time zero and the other within a time width $0.2\mu\text{sec}$ is given by $(5 \times 10^3) (5 \times 10^3) (0.2 \times 10^{-6}) = 5\text{ cps}$. Here we assume that the detector detects a count rate of $5 \times 10^3\text{ cps}$ from a

light source with a Poisson statistics and the probability of an afterpulse to occur within 0.2 μsec of a real pulse is 0.1%. This is comparable to count rate from start afterpulses, which is $(5 \times 10^3) (0.001) = 5$ counts per second. The contribution from stop afterpulses is given by $(5 \times 10^3) (0.2 \times 10^{-6}) (0.001) = 0.005$ counts per sec.

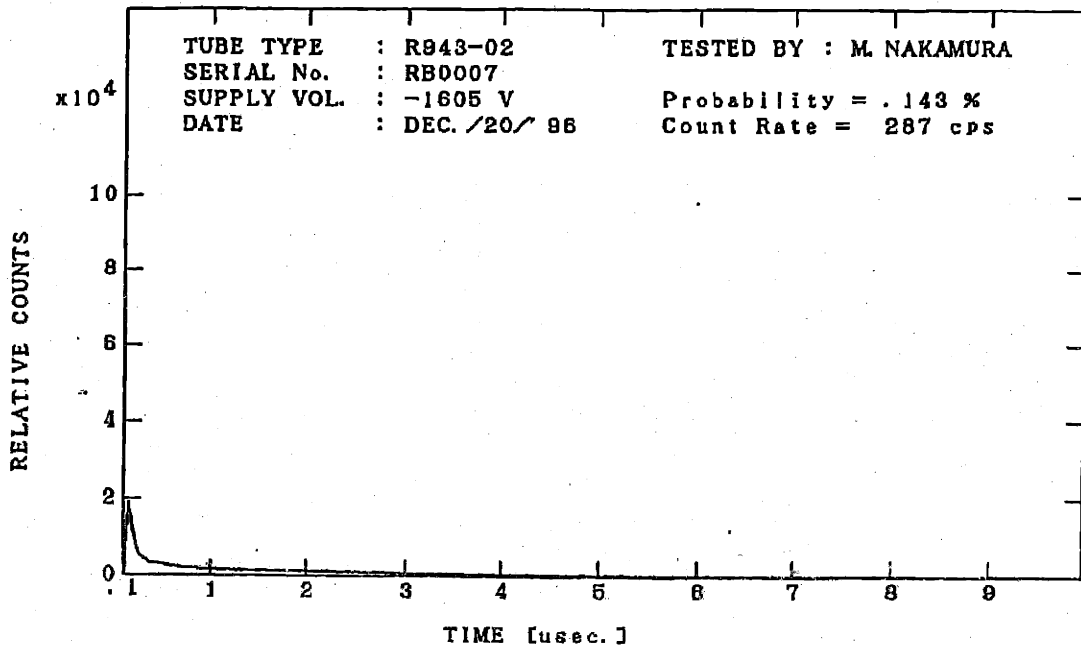


Figure 2. Afterpulse distribution for our PMT Hamamatusu R943-02.

When another detector is used to start, no start after pulses are used as a stop pulse and the bad effect associated with the start afterpulses is eliminated. The only contribution from the start detector afterpulses is to start the MSTDC. But the probability of this to occur is equal to the probability of afterpulsing which very small. So we design our MSTDC for a two detector configuration.

Figure 3 shows two measurements of the $g^{(2)}(\tau)$: the first is obtained using the one-detector configuration and the other using two-detector configuration. The predicted $g^{(2)}(\tau)$ is just a horizontal straight line. The start-afterpulse distortion is clear on the one-detector configuration.

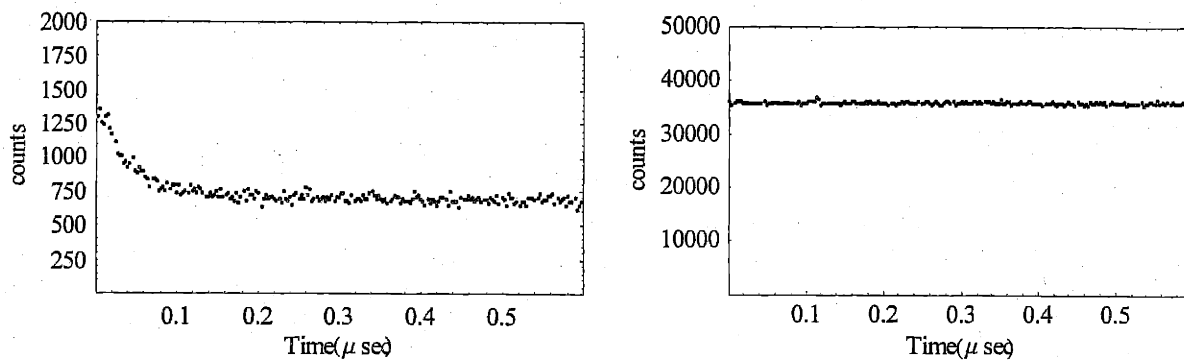


Figure 3. Start afterpulse correlation is clear in the one-detector configuration (left plot) while it is absent in the two-detector configuration.

5.2- MSTDC overview

The basic idea of our MSTDC design is to start a binary counter by a pulse from the start detector. When the stop detector detects a photon, the count on the counter is registered on a memory. When a predetermined time range is reached the counter is stopped and reset to zero, waiting for another start pulse. The registered arrival times in the memory are transferred to a computer, and a histogram of the degree of the second-order coherence is built up.

Figure 4 shows a block diagram of our MSTDC. A pulse from the start detector is sent to a smart switch, which enable a 16-bit counter. The counter is incremented for every pulse from a 50 MHz clock; that is every 20 nsec. The Clock synchronizes the counter to both the stop signal synchronizer and the smart switch. A signal from the stop detector should request the memory to read the counter. But it cannot do this at any time. This is because at some instances the counter is updating its contents, and reading during these instances leads to wrong results. This is avoided by using the synchronizer. The job of the synchronizer is to delay the stop pulses slightly, on average 10 nsec, to avoid those instances when the counter is updating its contents. When the counter reaches its predetermined time limit, a signal is sent from the counter to the switch. The switch then stops the counter and reset it to zero. Another pulse from the start detector starts the counter again. We use first in first out (FIFO) memory for which the first number written into memory is the first number read out of the memory. The binary numbers, stored in the memory, represent the arrival times of the stop signals relative to a start signal in

units of the clock period: 20 nsec. An interface card reads these binary numbers from the memory to a computer where they are processed to produce $g^{(2)}(\tau)$.

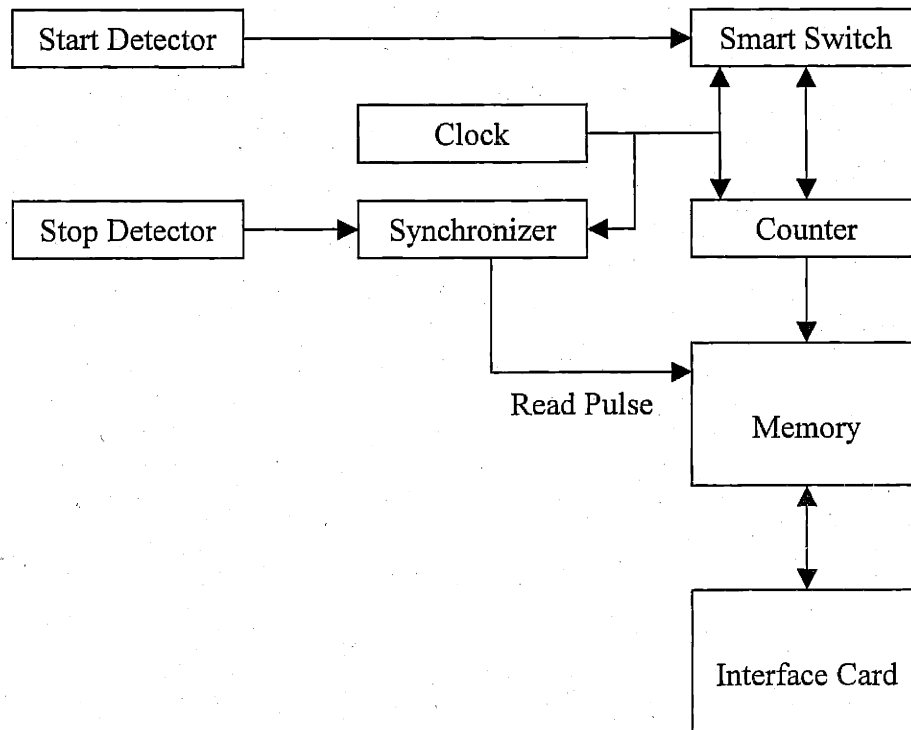


Figure 4. Block digaram of our multi-stop time to digital converter.

5.3- MSTDC details

Except for the FIFO memory, we use 74F logic family (F stands for fast), which was introduced by Fairchild Semiconductor Company in 1979. This family is a TTL logic family with 0 (Low) level defined as a voltage below 0.8 V and 1 (High) level defined as a voltage above 2.0 V. When an input port is not connected, the level is assumed to be High. In general 74F logic family can operate at frequency as high as 100 MHz.[6]

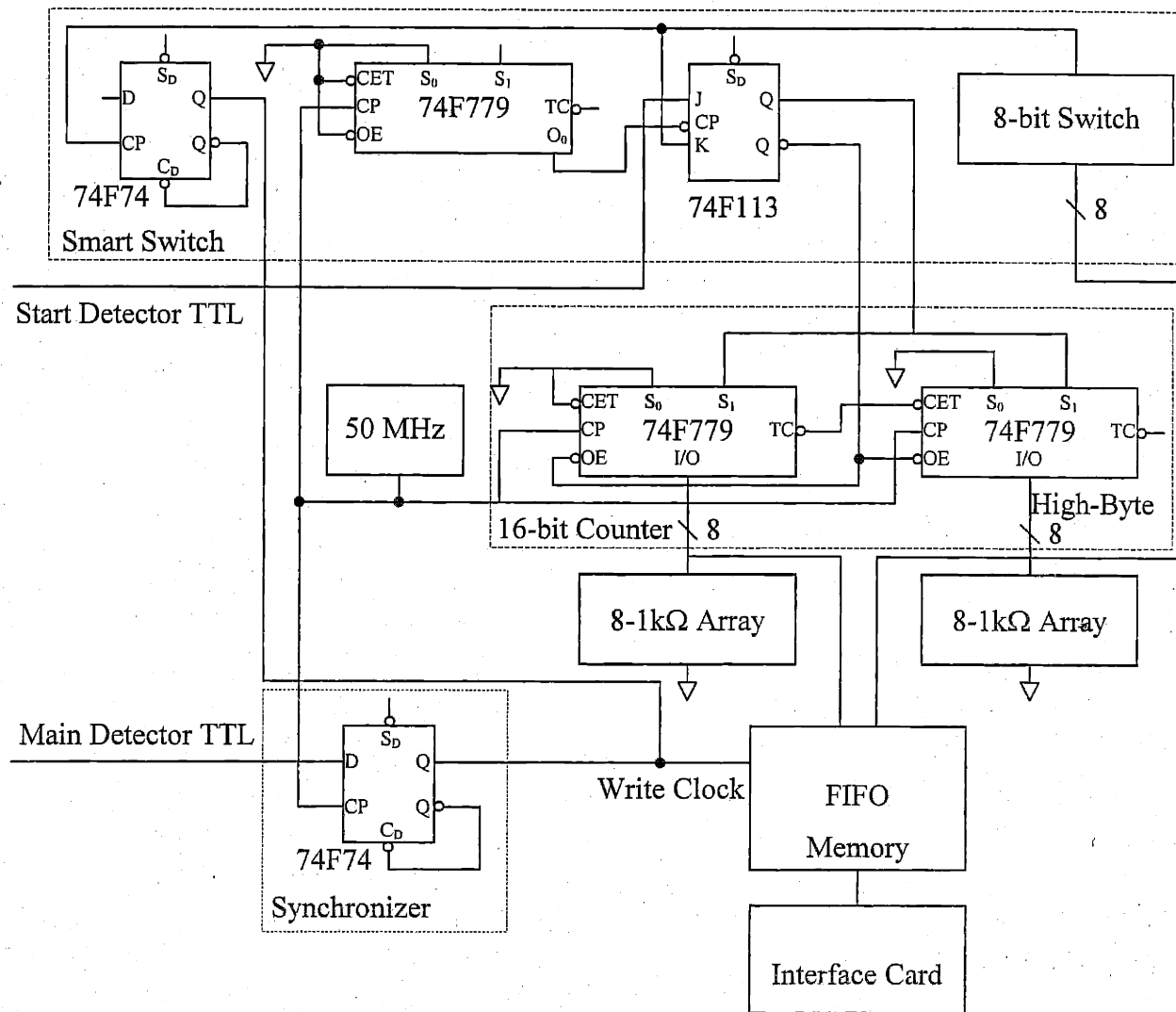


Figure 5. Circuit Diagram of our MSTDC.

Figure 5 shows a circuit diagram of our MSTDC. In what follows, a detailed description of each component of our MSTDC is discussed. Appendix C shows the circuit layouts used to manufacture both sides of the printed circuit board of the MSTDC and NIM to TTL circuits.

5.3.1- Clock

We use a 50 MHz clock from Epson Electronics America, Inc part number SG-615PCV-50.000MC2. It has stability ± 100 part per million. Its output can deliver current up to 4 mA. It drives one D flip flop which consumes up to 0.6 mA and three 8-bit counters each of which

consumes up to 0.2 mA. Figure 6 shows the connection diagram for the clock. The output of the clock is disabled when its OE input is grounded and it is enabled when it is not connected.[7]

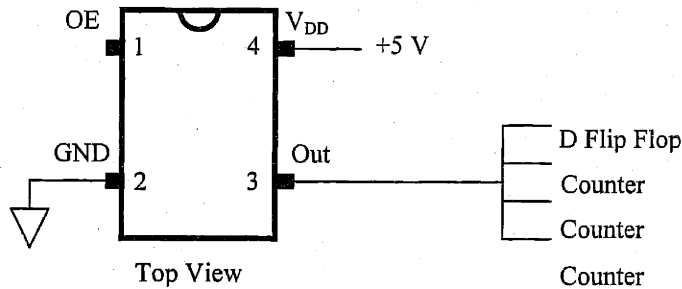


Figure 6. Connection diagram for the 50 MHz clock.

5.3.2- Synchronizer


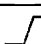
Signals from stop detector need to order the FIFO memory to read the counter. The job of the synchronizer is to make sure that these signals are not ordering the FIFO memory to read while the counter is updating its counts. It does its job by delaying some of the stop signals by an average of 10 nsec.

We use one of the two flip-flops in the 74F74PC chip as our synchronizer. The truth table for 74F74 is shown in Table 1. The 74F74 is a positive edge-triggered flip-flop. Information at the Input D is transferred to the Output Q on the positive edge of the clock pulse. After the clock pulse threshold voltage has been passed, the data input is locked out and information present will not be transferred to the outputs until the next rising edge of the clock pulse. To transfer the input level correctly to the output during the clock positive edge, the input level must not change during the setup and hold times. The setup time is the time just before and the hold time is the time just after the clock rising-edge threshold. For 74F74, the setup time is about 3 nsec and the hold time is about 1 nsec. Unpredictable output level is resulted when this condition is not met. \bar{Q} is a complimentary output which always has the opposite logic level of the Q level. At any

time, setting Set Input \overline{S}_D level to low, forces the Q level to high while setting the Clear Input \overline{C}_D level to low, forces the Q level to low.[8]

A connection diagram for the synchronizer is shown in Figure 7. The flip-flop is connected such that it produces a pulse instead of constant high level signal when it is triggered while the input level is high. This is accomplished by using the following trick: the Complimentary Output \overline{Q} is connected to the Clear Input \overline{C}_D . When the input level is low and the flip-flop is triggered, the Output Q becomes low and \overline{Q} becomes high. High level on the Clear Input \overline{C}_D does nothing and Q remains low. On the other hand, when the flip-flop is triggered while the input level is high, Q becomes high and \overline{Q} becomes low. But low signal on the Clear Input \overline{C}_D forces the Output Q back to the low level. Since \overline{Q} or the Clear Input \overline{C}_D is high now, Q remains there until the flip-flop is triggered again. It takes about 5 nsec for a low signal on the Clear Input \overline{C}_D to force the Q output back to low. Thus a pulse of width 5 nsec is produced after a fixed time from the rising edge of the clock. Figure 8 show a pulse from our synchronizer.

Table 1. Truth table for 74F74 flip-flop. X means immaterial and lower case letters h and l mean high or low for a set time prior and hold time after the low-to-high clock transition. Q_0 and \overline{Q}_0 are the values before the low-to-high clock transition.

Inputs				Outputs	
\overline{S}_D	\overline{C}_D	CP	D	Q	\overline{Q}
L	H	X	X	H	L
H	L	X	X	L	H
L	L	X	X	H	H
H	H		h	H	L
H	H		l	L	H
H	H	L	X	Q_0	\overline{Q}_0

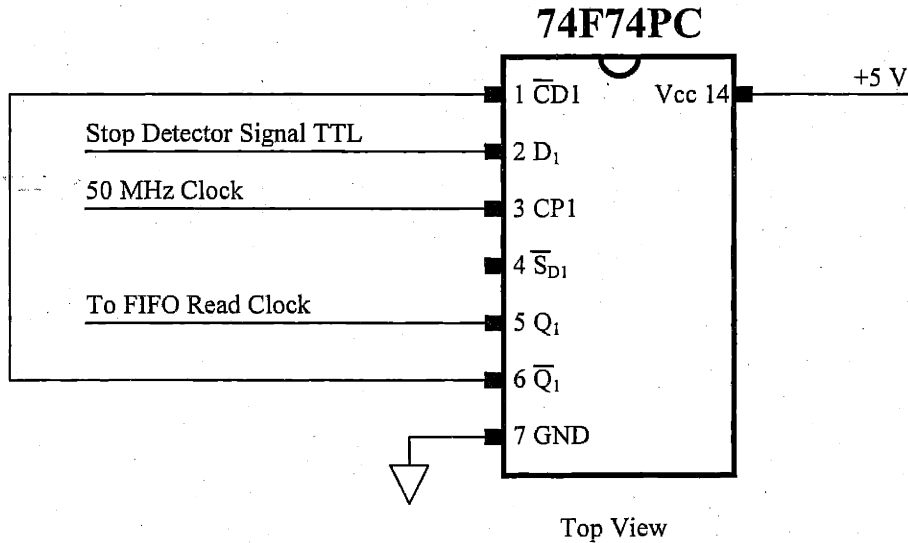


Figure 7. Connection diagram for the synchronizer.

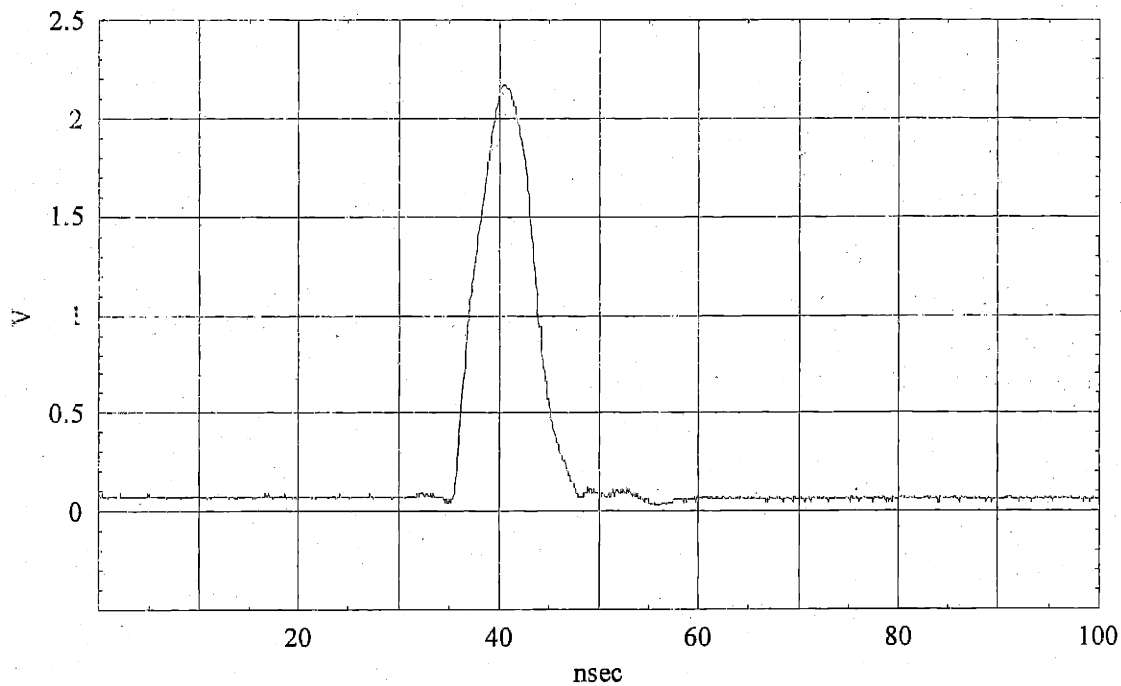


Figure 8. A pulse from the synchronizer.

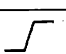
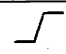

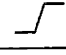
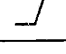
A signal from the stop detector, which may arrive any time at the synchronizer, is shaped such that its width is about 18 nsec slightly smaller than the clock period. This makes its chance to meet a clock positive rising edge large and its chance to meet two successive clock positive

rising edges zero. Thus signal from the stop detector at most produces one pulse at the output of the synchronizer. Some pulses are not sampled by the flip-flop and are lost because they change their level during the setup or hold times. The fraction of the lost pulses is equal to the ratio of the setup and hold times to the clock period. This is about 20%.

5.3.3- Counters

Since there is no 16-bit counter in the 74F logic family, two 8-bit counters 74F779 are connected together to produce a 16-bit counter. Each individual counter can operate at speed as fast as 105 MHz but when two counters are connected together their maximum speed becomes about 60 MHz. This is why a 50-MHz clock is chosen to drive our MSDTC. A third 8-bit counter is used to produce test pulses as well as to double the clock period to drive the smart switch (a JK flip-flop). Table 1 presents the function table for the 74F779 counter and Figure 9 shows the connection diagram for the three counters.

Table 2. Function table for the 74F779 counter. X means immaterial.

S ₁	S ₀	$\overline{\text{CET}}$	$\overline{\text{OE}}$	CP	Function
X	X	X	H	X	I/O ₀ to I/O ₇ in High Z
X	X	X	L	X	Flip-flop output appear on I/O lines
L	L	X	H		Parallel load all flip-flops
Not LL		H	X		Hold ($\overline{\text{TC}}$ held high)
H	H	X	X		Hold
H	L	L	X		Count up
L	H	L	X		Count down

The counter that provides the first eight least significant digits is called the low-byte counter while the other counter is called the high-byte counter. When the Q output of the JK flip-flop becomes high, for both counters, the select input one (S₁) becomes high and the output enable input ($\overline{\text{OE}}$) becomes low. This enables every rising edge of the clock to increment the

low-byte counter because its count trickle input (\overline{CET}) is always low. The high-byte counter is not incremented by the clock unless its \overline{CET} input is low. This happens when the terminal count output (\overline{TC}) of the low-byte counter becomes low. The \overline{TC} output becomes low when the counter reaches its limits (all its bits are high).

The reason that two connected counters cannot operate at speed as high as the speed of a single counter is the following. When the clock increments the low-byte counter to its limit, low signal appears on its \overline{TC} output about 10 nsec from the triggering edge of the clock. To increment the high-byte counter by the next clock rising edge, this low signal should appear on its \overline{CET} input for about 7 nsec (Set time for \overline{CET} to clock). Thus we need at least a clock period of about 17 nsec (59 MHz) to operate connected counters correctly.

The outputs of both counters are connected directly to the data inputs of the FIFO memory. In addition, the outputs of the high-byte counter are connected to 8-bit switch. The purpose of this switch is to choose which bit of the high-byte counter is used to stop both counters. This bit determines the range of the MSDTC. The output of the switch is connected to the K input of the JK flip-flop. When this chosen bit is high, the Q of the JK flip-flop is forced to low. This in effect stops the counters and loads them with the voltages available on their output/input ports. Since these input/output ports are connected to the ground through 1-k Ω resistors, they are loaded with zeros and they are rest. The value of 1 k Ω is chosen low enough so that the characteristic decay time of the effective resistor-capacitor circuit formed by the counter output/input port and the 1 k Ω resistor is much smaller than the clock period. Also the value of the resistor should not be so small that it drains a lot of current from the counters and disable them from delivering high enough voltage for the high level logic. The maximum allowable current per output/input port is 20 mA. This put a lower limit on the resistor of $2.0V/20mA=100\Omega$. [9]

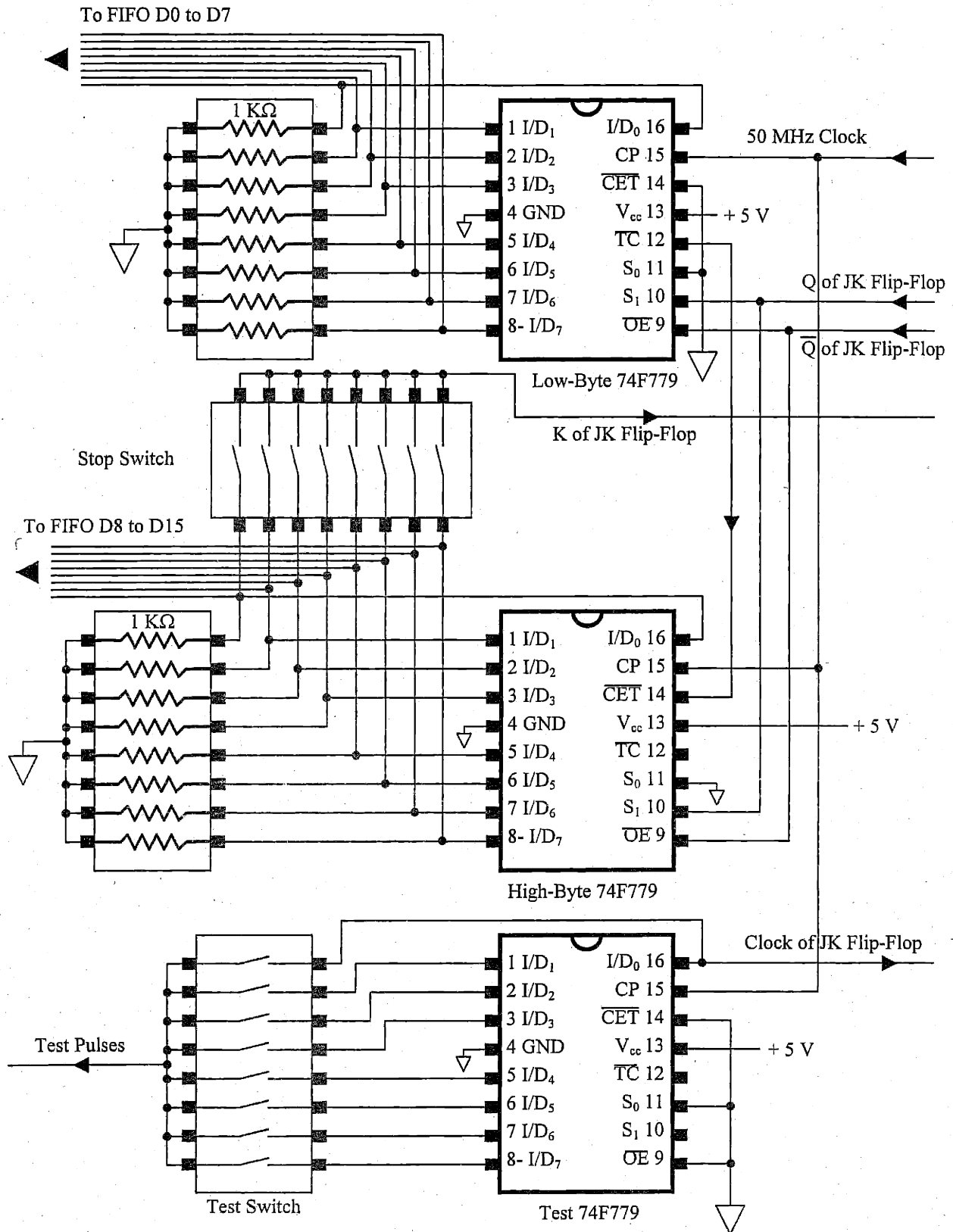


Figure 9. Connection diagram for the 79F779 counters

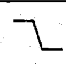
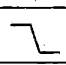
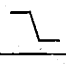

5.3.4- Smart switch

The purpose of the smart switch is to start the low-byte and high-byte counters by a start pulse from the start detector and to stop them when a preset time is reached. Also, it sends a pulse to the FIFO memory read clock to order the FIFO memory to write the contents of the counters before they are reset. The counters are read even when there is no stop pulse during the preset time range. This reading is used as a tag to indicate that a start pulse is received and the end of the time range is reached.

Our smart switch consists of a JK flip-flop 74F113 and a D-type flip-flop 74F74. Its connection diagram is shown in Figure 11 and the truth table of the JK flip-flop is presented in Table 3. The 74F113 JK flip-flop is a negative-edge triggered flip-flop. In another words, it is triggered when its clock goes from high to low logic levels.

Here is how the JK flip-flop works. As long as the Q output of the JK flip-flop is low, both counters are halted and reset. Regardless of the status of the K input, a pulse from the start detector, received on the J input during a falling edge of the clock, changes the Q output from low to high. After that, the Q output does not go low except when K input goes high. That is, after the first starting pulse and while the K input is low, subsequent starting pulses do not affect the status of the JK flip-flop.

Table 3. Truth table for 74F113 flip-flop. X means immaterial and lower case letters h and l mean high or low for a set time prior and hold time after the high-to-low clock transition. Q_0 and \bar{Q}_0 are the values before the high-to-low clock transition.

Inputs				Outputs	
\bar{S}_D	\bar{CP}	J	K	Q	\bar{Q}
L	X	X	X	H	L
H		h	h	\bar{Q}_0	Q_0
H		l	h	L	H
H		h	l	H	L
H		l	l	Q_0	\bar{Q}_0

The D-type flip-flop is used to generate a pulse from the stop bit as follows. The stop bit is connected to the clock input of the D flip-flop. Since the D input is not connected, it is always high. When the stop bit goes from low to high it triggers the D flip-flop and a pulse is produced in similar manner as a pulse is generated in the synchronizer.[10]

The JK flip-flop is not clocked by the main clock of the MSDTC, but instead it is clocked by the D_0 of the test counter, which has double the period of the main clock. The reason for this arrangement is that a JK flip-flop clock period of 20 nsec does not stop the counters as shown on the left side of Figure 10. The stop-bit goes high after a propagation time of about 5 nsec from the rising edge of the counters clock. The JK flip-flop clock is shifted such that there is just enough set time of about 4 nsec for the JK flip-flop to read high on its K input. The Q output goes low after a propagation time of about 4 nsec. The remaining time before the next rising edge of the counters clock is about 7 nsec. This is smaller than the required set time for the S_1 inputs and thus the counters do not recognize S_1 low and it does not stop. The next falling edge of the JK flip-flop clock toggles its Q output to high and thus the S_1 inputs is again high during the next rising edge of the counter clock.. This brings us back to a situation similar to that during the first falling edge of the JK flip-Flop clock. On the other hand, when the JK flip-flop clock period is 40 nsec, as show on the right side of Figure 10, , the third rising edge of the counters clock comes before the second falling edge of the JK flip-flop clock. Therefore, S_1 remains low during this rising edge and the counters are halted and loaded with zeros.

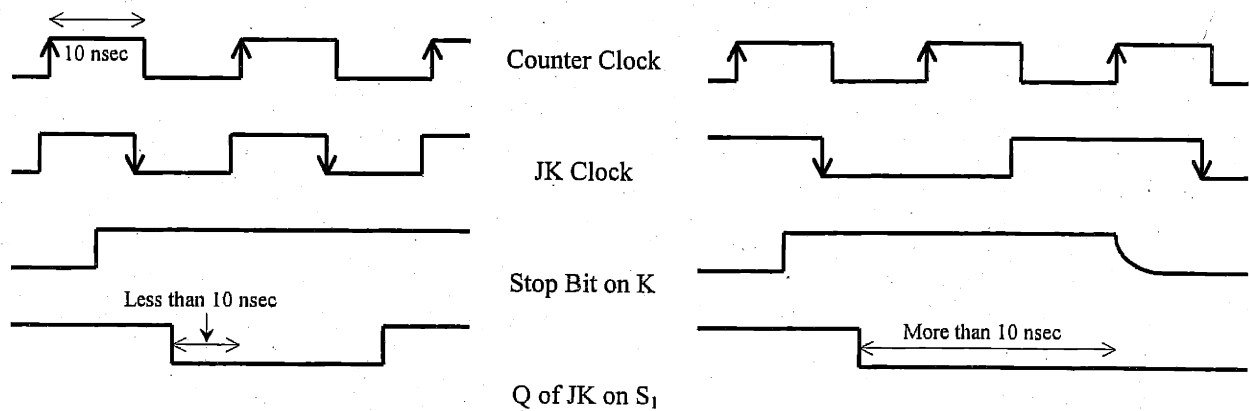


Figure 10. On the left, the counters do not stop when the period of the JK flip-flop clock is 20 nsec, while, on the right, they stop when a clock period of 40 nsec is used. Here the J input of the JK flip-flop is assumed always high.

The efficiency and resolution of the MSDTC depend on the width of the starting pulses as well as the width of the stopping pulses. The efficiency is determined by the fraction of the pulses detected by the start and stop detectors that are used in producing the $g^{(2)}(\tau)$ distribution. Wider pulses have better chance to be sampled by the synchronizer or the JK flip-flop and therefore the efficiency is higher for wider pulses. The resolution is determined by the width of each bin in the $g^{(2)}(\tau)$ distribution which is the sum of the width of the start pulse and the width of the stop pulse. Thus, wider pulses have poorer resolution. In our measurements, we shape the starting and stopping pulses such that their widths are just smaller than the JK flip-flop and the synchronizer clock periods, respectively. The reason for losing some of these pulses is that they change their logic levels during the set time and hold time. Therefore, the fraction of pulses that are lost can be found from ratio of the set time plus the hold time to the clock periods. The set and hold time for the JK flip flop is about 4 nsec and that for the synchronizer is about 5 nsec. Therefore 10% of starting pulses are lost and 20% of stopping pulses are lost. The width of each bin in the $g^{(2)}(\tau)$ distribution is about 60 nsec.

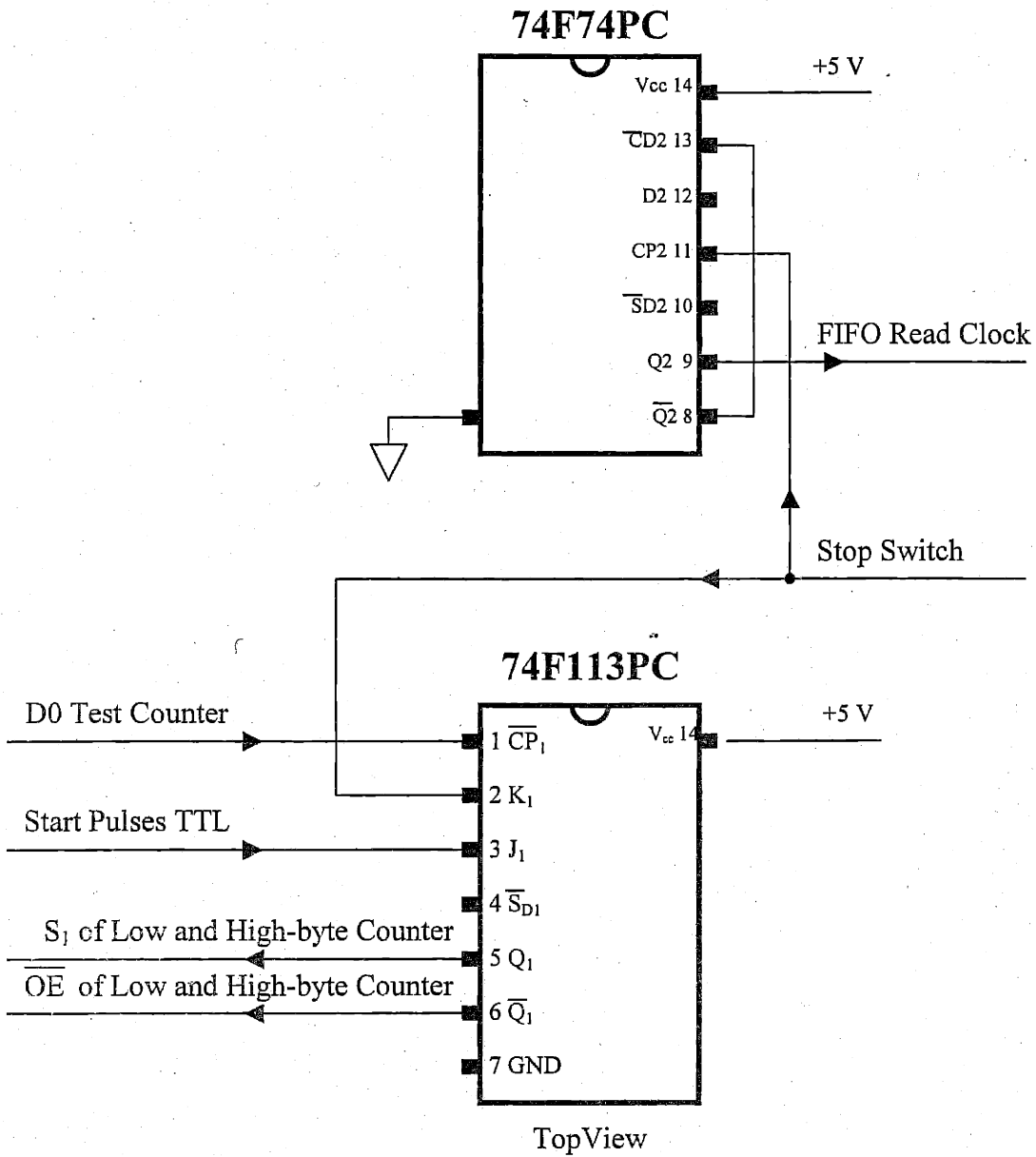


Figure 11. Connection diagram for the smart switch

5.3.5- FIFO memory

Our FIFO memory is from Integrated Device Technology, Inc. model number IDT72V2113L7.5. The connection diagram for this memory is shown in Figure 12.

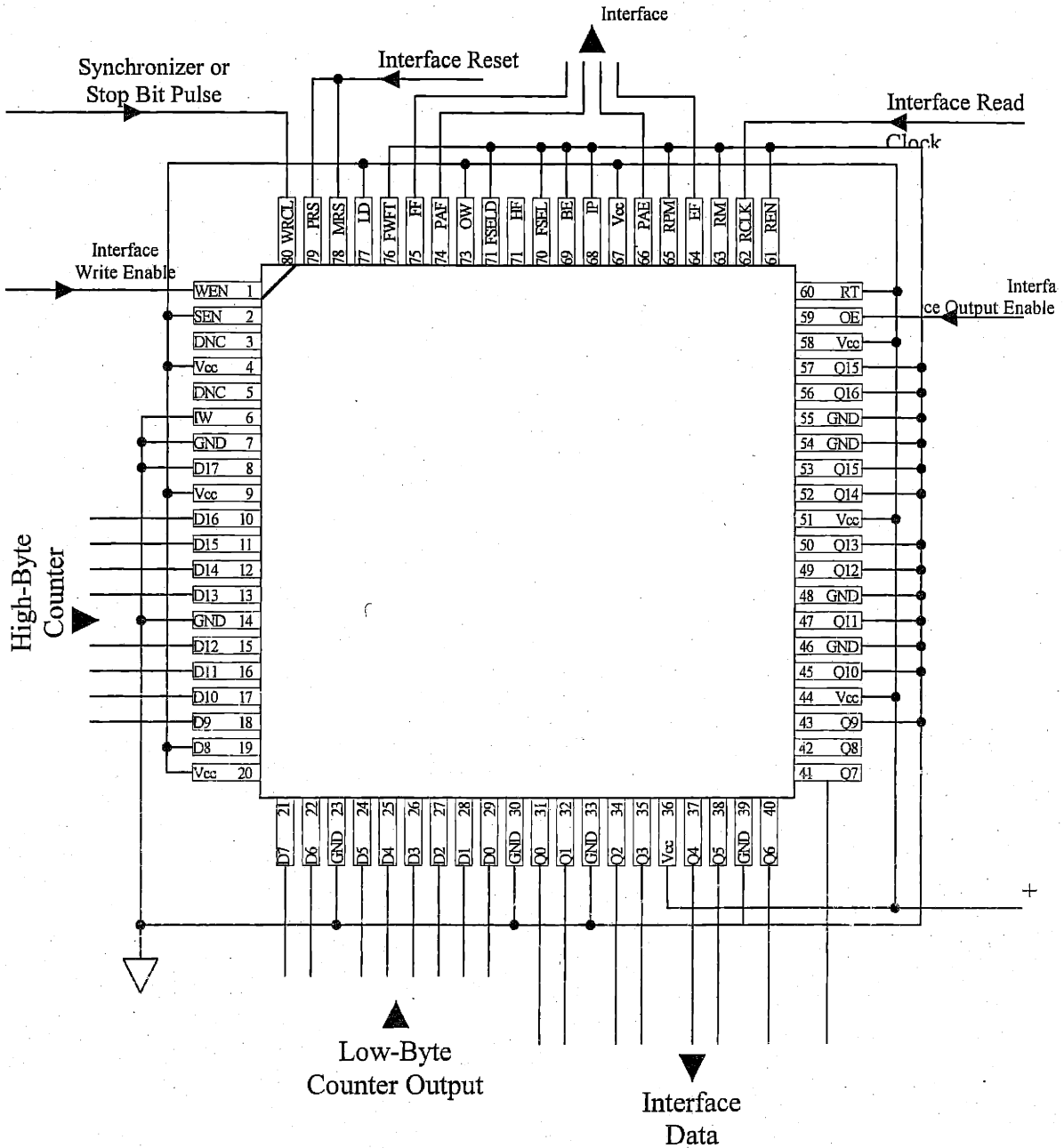


Figure 12. Connection diagram for the FIFO memory.

Data can be written to the IDT72V2113L7.5 or read from it with speed as high as 133 MHz. The read clock (RCLK) input can be clocked independently from the write clock (WCLK) input and thus data can be written to or read from it simultaneously. A low logic level on its write enable ($\overline{\text{WEN}}$) input enables the rising edge of its WCLK to write data available on its

input data bus. Although a low logic level on its read enable ($\overline{\text{REN}}$) input enables the rising edge of its RCLK to read data from it, data is not available on its output data bus unless the output enable $\overline{\text{OE}}$ pin is asserted low. In our MSDTC, the $\overline{\text{REN}}$ input is always low and the interface card generates the $\overline{\text{OE}}$, as well as the RCLK. The synchronizer or the smart switch generates the WCLK while the interface card controls the $\overline{\text{WEN}}$ input.

The IDT72V2113L7.5 input data bus and its output data bus can be configured to be 9-bit or 18-bit long. In our MSDTC, we configure the input data bus to be 18-bit long while its output data bus to be 9-bit long. We do not use the 9th and 18th bit in the input data bus nor do we use the 9th bit in the output data bus. With this configuration the IDT72V2113L7.5 can store up to 262144 numbers each of which has 18 bits. Since the big-endian pin is grounded, the big-endian operation is selected. Thus, for the 16-bit numbers stored in the memory, the high significant byte is read before the low significant byte.

A low logic level on the master reset ($\overline{\text{MRS}}$) input clears entire FIFO memory contents. The interface card controls this input. The FIFO is configured to operate on the first word fall through mode (FWFT). In this mode, three transitions of the RCLK are needed to read the first byte written to an empty FIFO. All subsequent bytes need only one RCLK transition.

The IDT72V2113L7.5 has five flags pins to indicate its memory usage. A low logic level from the empty flag ($\overline{\text{EF}}$) pin indicates that there is no data in the memory while a low logic level on the full flag ($\overline{\text{FF}}$) pin implies that there is no more space left for more data. The logic level on half-full flag ($\overline{\text{HF}}$) goes low when half of the capacity is used. The programmable almost empty flag ($\overline{\text{PAE}}$) indicates how many data read while the programmable almost full flag ($\overline{\text{PAF}}$) indicates how many data needed to full the memory. In our MSDTC $\overline{\text{PAE}}$ and $\overline{\text{PAF}}$ are programmed to indicate that are 1023 data points read and 1023 data points left, respectively.[11]

5.3.6- Synchronization

To write correctly the data on the counters to the FIFO memory, they should not change their logic levels during a set time of 2.5 nsec before and a hold time of 0.5 nsec after the rising edge of the FIFO write clock WCLK. The WCLK is generated by two kinds of pulses: pulses from the synchronizer, which are produced from the stopping pulses, and pulses from the D-type flip flop of the smart switch, which are produced, from the stop bit. Two coaxial cables of type RG174/U and of length 1.70 m and 0.24 m are used to delay pulses from the synchronizer and from the smart switch, respectively. The RG174/U coaxial cable has an impedance of 50Ω and one meter of it provides a delay of 5 nsec.[12] Synchronizing the WRCK with one bit of the counter should synchronize it with other bits since the 74F779 counter is a synchronous counter and all its bits change at the same time. Figure 13 shows the timing between a WCLK pulse and the D_0 output of the low-byte counter.

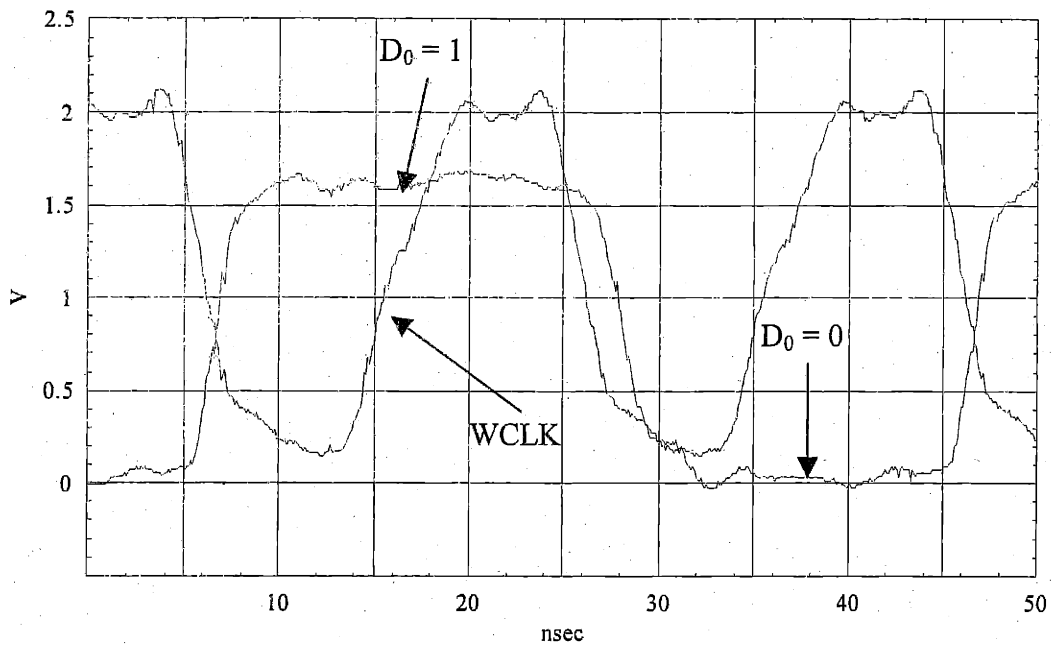


Figure 13. Timing of the WCLK of the FIFO memory with respect to the D_0 output of the low-byte counter.

5.4- NIM to TTL

We use the constant fraction discriminator CFD Stanford TC454 to shape the pulses from the start and stop detectors. The outputs of the CFD produce fast NIM logic. On a $50\ \Omega$ resistor, a low fast NIM logic level is between $-0.05\ \text{V}$ and $+0.05\ \text{V}$ and a high level logic is between $-0.9\ \text{V}$ and $-0.7\ \text{V}$. [13] We use the quad MECL-to-TTL translator MC10H125 from Motorola [14] to translate the fast NIM logic levels to TTL levels. The connection diagram for the MC10H125 chip is shown in Figure 14. The MC10H125 chip is quite fast and its propagation delay is about $2.5\ \text{nsec}$. It has four translators and each translator has two inputs: one is inverting (the one with a bar on) and the other is non-inverting. To produce the TTL levels, a translator compares its two inputs. A high TTL level is produced when the inverting input voltage is lower than the non-inverting input voltage while a low TTL level is produced for the opposite case. We set the non-inverting input at $-0.4\ \text{V}$ and connect the output of the CFD to the inverting input.

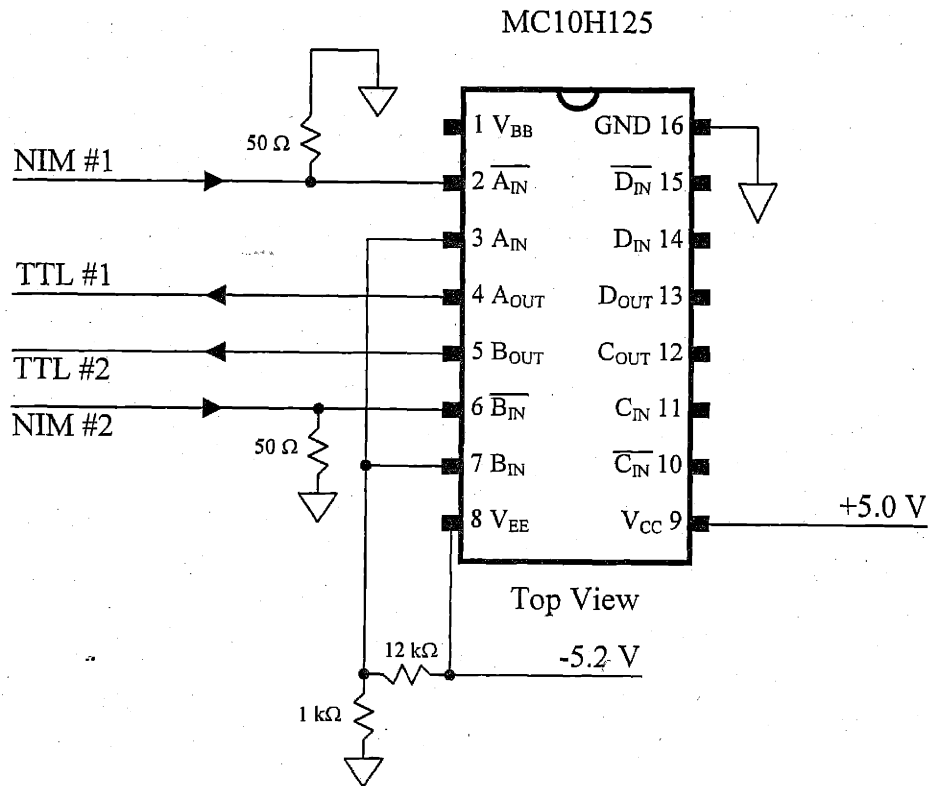


Figure 14. Connection diagram for the Quad MECL-to-TTL translator.

5.5- Interface card

Our interface card is built to do three main tasks. First, it reads one byte at a time, called the data byte, from the FIFO memory data. It also provides the necessary read clock signal as well as the output enable signal for the FIFO memory. Second, through the status byte, it reads the status of the FIFO memory flags and status of the. The stop acquisition bit switch is a manual switch which is turned on when the $g^{(2)}(\tau)$ apparatus is ready for data collection. Third, using the control byte, it controls cavity-locking process; it controls the process of writing the counters contents to the FIFO memory and it resets the FIFO memory.

We build our interface on a PC ISA bus. It can read or write one byte per 1 μ sec. Figure 15 shows a circuit diagram for the interface card and Table 4 shows pins assignment of its 25-pin subminiature D-connector.

Table 4. Pins assignment of the 25-pin subminiature D-connector of the interface card.

#	Byte Name		Description	#	Byte Name		Description
1	Status Byte	D2	BNC - Not Used	14	Status Byte	D3	BNC- stop acquisition
2	Status Byte	D4	FIFO FF flag	15	Status Byte	D5	FIFO PEF flag
3	Status Byte	D6	FIFO PAE flag	16	Status Byte	D7	FIFO EE flag
4	Control Byte	Q0	BNC - AOM B	17	Control Byte	Q1	BNC - AOM A
5	Control Byte	Q2	BNC - Cavity Lock	18	Control Byte	Q3	BNC - Not Used
6	Control Byte	Q4	BNC - Not Used	19	Control Byte	Q5	BNC - Not Used
7	Control Byte	Q6	FIFO WEN	20	Control Byte	Q7	FIFO MRS
8	Ground			21	FIFO OE		FIFO Output Enable
9	FIFO RCLK		FFIO Read Clock	22	Data Byte	D7	8/ 16 bit
10	Data Byte	D6	7 / 15 bit	23	Data Byte	D5	6/ 14 bit
11	Data Byte	D4	5 / 13 bit	24	Data Byte	D3	4 / 12 bit
12	Data Byte	D2	3 / 11 bit	25	Data Byte	D2	2 / 10 bit
13	Data Byte	D0	1 / 9 bit				

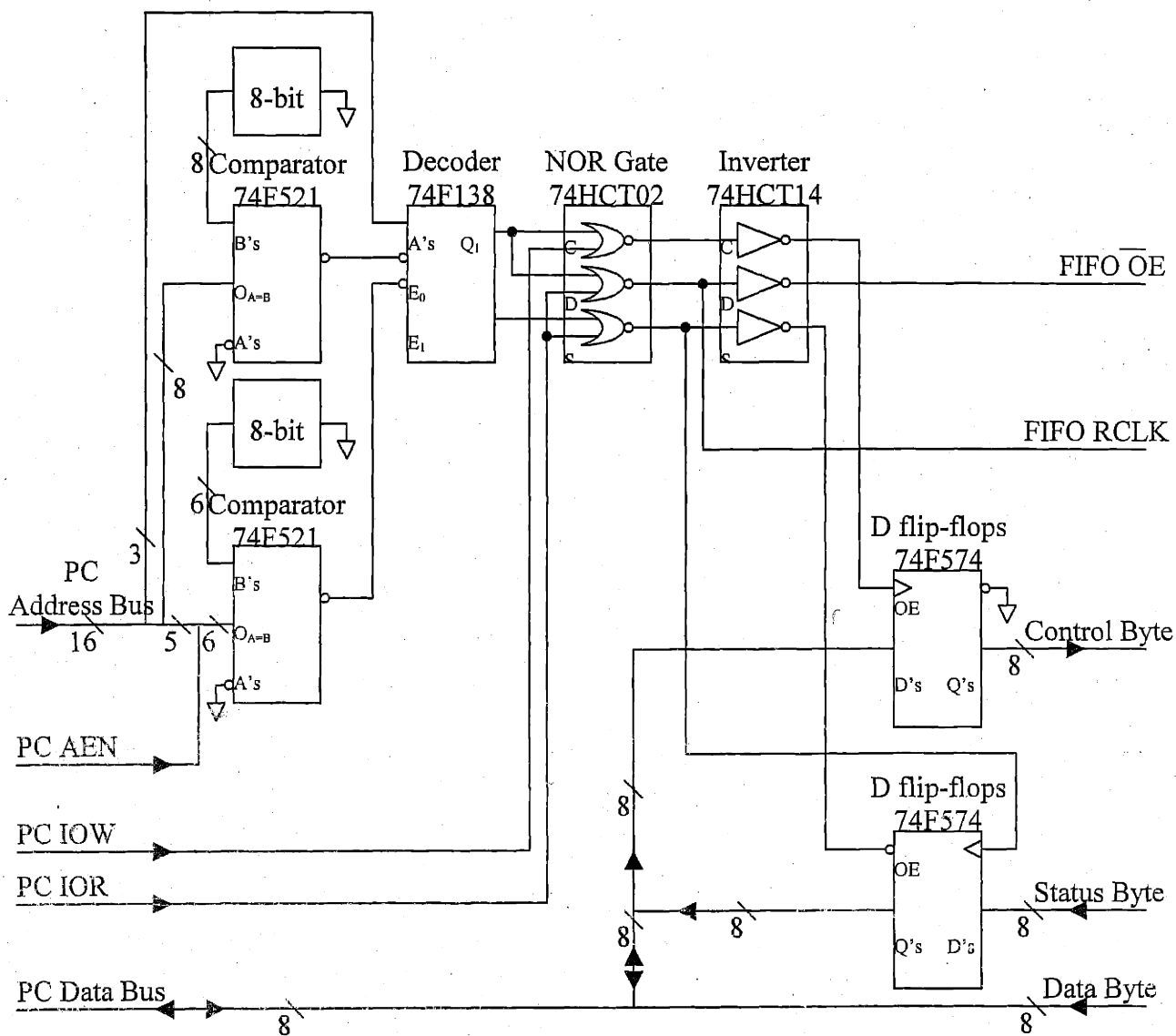


Figure 15. Circuit diagram for the interface card.

When the PC wants to read a byte from an ISA interface card, the PC pulls its address enable (AEN) signal low and sends the 16-bit address of the card on its address bus for a period of about 900 nsec. As shown in Figure 16, after 92 nsec from the beginning of the 900nsec period, it pulls its input output read (IOR) signal low for about 630 nsec. On the rising edge of the IOR signal, the data on the PC data bus is latched to the PC memory. This data should not change their levels for about 50 nsec prior to the rising edge of the IOR signal. Similarly, when a PC wants to write a byte to its data bus, it pulls its AEN signal low and sends the desire address

on its address bus for period of about 900 nsec. After 92 nsec from the beginning of the 900nsec period, it pulls its input output write (IOW) signal low for about 630 nsec. The data is available on the data bus for about 516 nsec before and 135 nsec after the rising edge of the IOW signal.[15]

Our interface card uses two different addresses. The first address is used to read the data byte and to write the control byte. This address is called data/control address. The second address, which is called the status address, is used to read the status byte. Two 8-bit identity comparators 74F521 chips and one 1-of-8 decoder/demultiplexer 74F138 chip (will be called the decoder) are used to identify these two addresses. The 74F521 compares its 8 A's input with its 8 B's inputs and it produces low logic level on its output $O_{A=B}$ when both A's and B's inputs are equal. 13 address signals A3 to A15 of the address bus as well as AEN signal are connected to the A's input of these two identity comparator chips. The B's inputs are connected to two 8-bit switches through which the most significant 13-bit of the desired address can be chosen. Because any unconnected input in the 75F logic family is treated as a high logic level, when a switch is off the corresponding B input is high. The two outputs of the identity comparator chips are connected to the two active low enable inputs of the decoder chip: \bar{E}_0 and \bar{E}_1 . The remaining three address signals A0 to A2 are connected to the three A's inputs of the decoder. The decoder is active when both its input enable \bar{E}_0 and \bar{E}_1 are low and its third input enable E_2 is high. When the decoder is active, it produces a low logic level on one of its eight outputs that corresponds to the value of the three-bit binary number applied to its A's inputs. Otherwise all its outputs are high. We choose address 921 (0000 0011 1001 1001) for the data/control address and address 924 (0000 0011 1001 1100) for the status address. So when the AEN signal is low, the data/control address on the data bus causes the Q_1 of the decoder to go low while the status address causes the Q_4 output to go low. The propagation delay through the comparator is about 7 nsec while it is about 6 nsec for the decoder.

When the PC wants to read a byte from the FIFO memory data, it pulls Q_1 signal of the decoder low then it pulls the IOR signal low. This causes the output of the NOR gate D in the 74HCT02 chip to go high. NOR gate is always low except when both of its inputs are low. The transition of the NOR gate D from low to high is used to trigger the FIFO read clock. The output

of the NOR gate D is inverted by the inverter chip 74HCT14 and its low output is used to enable the FIFO to put the byte on the PC data bus where the PC latches it to its memory during the rising edge of the IOR signal. The timing for reading a byte from the FIFO memory to the PC memory is shown in Figure 16.

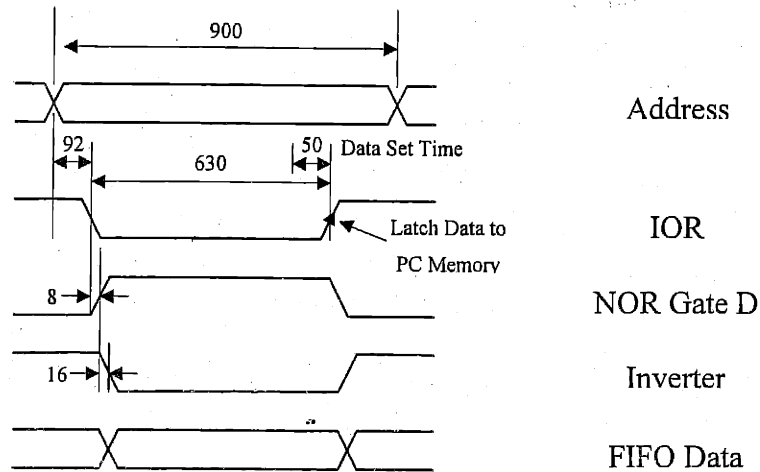


Figure 16. Timing for reading a byte from the FIFO memory to the PC memory. Numbers are in unit of nsec.

The NOR gate S plays similar rule in reading the status byte as the NOR gate D in reading the data byte. The output of the NOR gate S clocks an octal D-type flip-flop 74F574 chip while the output of the inverter S enables the Q's output of the 74F574 chip to appear on the data bus. The 74F574 chip has eight independent flip-flops driven by one clock. The propagation time from the rising edge of the clock to the Q's output is about 5 nsec. Q's outputs appear on the data bus after about 6 nsec from the time of applying a low logic level on the 74F574 chip output enable \overline{OE} input.

For writing the control byte, the output of the inverter C, which follows the logic levels of the IOW pulse with a delay of about 24 nsec, is used to trigger another octal D-type flip-flop 74F574 chip. Thus the data, which is available on the PC data bus for about 516 nsec before and 135 nsec after the rising edge of the IOW signal, is latched to the 74F574 chip.

The circuit layouts used to manufacture both sides of the printed circuit board of the interface card are shown in Appendix C.

5.6- MSTDC Tests

Our MSTDC has been tested by sequences of electrical pulses, as well as photoelectron pulses produced from a quasi-thermal light source.

In testing with electrical pulses, the J input of the JK flip-flop is disconnected. Since any disconnected input in the 74F logic family is treated as having high logic level, the first falling edge of the JK flip-flop clock switches the smart switch on and allows the counters to count. When the stop bit from the counters is high, the Q output of JK flip-flop clock toggles to low and thus the counters are switched off and are cleared before the next falling edge of the JK flip-flop starts them again.

On the TTL input of the stop detector, we use different electrical pulse distributions. The first distribution we use is a sequence of pulses separated by a time which is equal to the period of the main clock, 20 nsec. Computer reads from the FIFO memory, as expected, sequences of consecutive integer numbers from 0 to $2^{8+n}+2$ with a zero separates each sequence. Here n is the number of high-byte counter bit used as the stop bit. The extra two numbers corresponds to time the smart switch needs to stop the counters. This happens when the JK flip-flop clock on the right hand side of Figure 9 has slightly more delay with respect to counter clock so that rising edges of the counter clock elapses before the counters are stop. These consecutive pulses are produced simply by disconnecting the input of the synchronizer. Another pulses sequences are produced by feeding the test switch output (see Figure 8) to the input of the synchronizer. For example when the second bit of the test counter, I/O₁, is chosen, sequences of four pulses separated by 20 nsec followed by no pulses for 80 nsec are produced. The computer reads from the FIFO memory sequences of numbers from 0 to $2^{8+n}+2$ but now it reads four consecutive numbers and misses the next four consecutive numbers and so on as follows 0, 1, 2, 3, 8, 9, 10, 11, 16, 17, 18, 19.... It always reads the stop number that is 2^{8+n} . It is important to

do the last test because there is small overlap between consecutive pulses and this may change slightly their trigger time for an isolated pulse.

We also test our MSTDC by measuring $g^{(2)}(\tau)$ function from a quasi-thermal light source. We produce such a light source by focusing a He-Ne laser beam onto a rotating ground glass plate. [16] The correlation time is roughly equal to the time for a point on the ground glass disc to pass one diameter of the He-Ne beam. $g^{(2)}(\tau)$ function should have Gaussian form with $g^{(2)}(\tau=0) = 2$. The result of such test is shown in Figure 17. This measurement also shows that different parts of our $g^{(2)}(\tau)$ apparatus are working together.

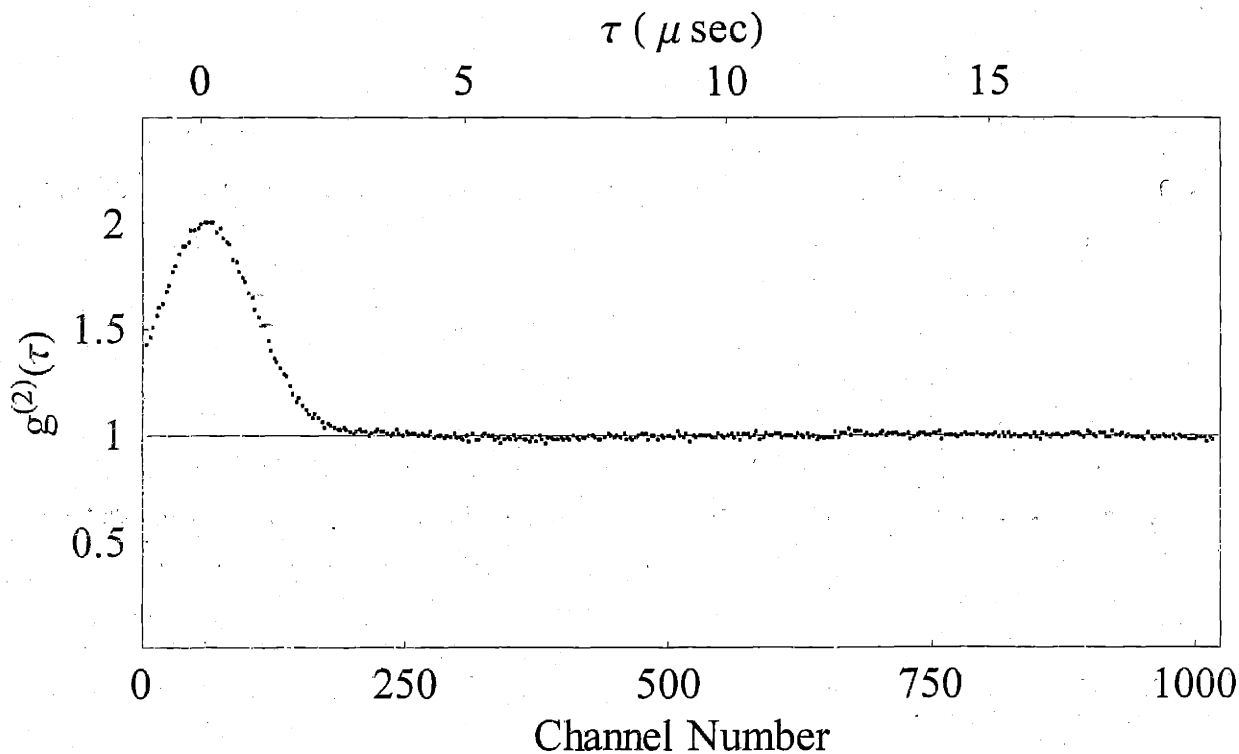


Figure 17. $g^{(2)}(\tau)$ measurement of quasi-thermal light.

5.7- References

- [1] T. Quang, Phys. Rev. A 46,682(1992), S. A. Kumar and G. S. Agarwal, Phys. Rev. A **50**, 680(1994)
- [2] F. Davidson and L. Mandel, Journal of Applied Physics **39**,62(1968)
- [3] L. Mandel and E. Wolf, Optical Coherence and Quantum Optics, Ch 14, 1st Edition, 1995, Cambridge University Press.
- [4] Hamamatsu Photonics K.K., Photomultiplier Tubes Construction and Operating Characteristics Connections to External Circuits, 1998.
- [5] Private communication with Hamamatsu.
- [6] P. Horowitz and W. Hill, The Art of Electronics, Ch, 9, 2nd Edition, 1989, Cambridge University Press.
- [7] Epson Electronics America, Inc, SOJ High frequency Crystal Oscillator Sg-615 Series Data Sheet,
- [8] Fairchild Semiconductor, 74F74 Dual D-Type Positive Edge-Triggered Flip-Flop Data Sheet, 1999.
- [9] Fairchild Semiconductor, 74F779 8-Bit Bidirectional Binary counter with 3-State Output Data Sheet, 1999 and private communication with Fairchild Semiconductor engineers.
- [10] Fairchild Semiconductor, 74F113 Dual JK Negative Edge-Triggered Flip-Flop Data Sheet, 1999.
- [11] Integrated Device Technology, Inc., 3.3 Volt High-Density Supersync II Narrow Bus FIFO Data Sheet, Dec. 1998.
- [12] J. Moore, C. Davis and M. Coplan, Building Scientific Apparatus a Practical Guide to Design and Construction. P373, 2nd Edition, 1989, Addison-Wesley Publishing Company, Inc.
- [[13]] J. Moore, C. Davis and M. Coplan, Building Scientific Apparatus a Practical Guide to Design and Construction. P448, 2nd Edition, 1989, Addison-Wesley Publishing Company, Inc.

-
- [14] Motorola, Inc. Quad MECL-to-TTL Translator Semiconductor Technical Data, Rev. 6, 1996.
- [15] P. Horowitz and W. Hill, The Art of Electronics, Ch, 10, 2nd Edition, 1989, Cambridge University Press.
- [16] W. Martienssen and E. Speller, Am. J. Phys. **32** 919(1964). F. T. Arecchi, Phys. Rev. Lett. **15**,912(1965)

Chapter

6 Results

In this chapter, we first present results from the adiabatic pumping process and describe the experiment by which the pump position is determined. Then, before we discuss the data that relate the number of photons and the number of atoms inside the cavity mode, we present the procedure by which the atomic number is determined from the resonance fluorescence measurements. Afterwards, we discuss our measurements of the average number of photons in the cavity mode, $\langle n \rangle$, as a function of the average number of atom in the cavity, $\langle N \rangle$. Finally, we present the $g^{(2)}(t)$ function measurements.

6.1- Pumping process

As discussed earlier in Chapter 2, when atoms are sent slightly away from the focus of the Gaussian pump beam, they may be inverted adiabatically. Beyond some level of pump intensity, this process is almost independent of the pump intensity, and it is almost independent of the atomic velocities. Indeed, we discovered this powerful process accidentally. At the beginning we were not aware of the possibility of inverting atoms adiabatically. We found this behavior during our trials to determine the pump power that produces a π -pulse for atoms with the most probable velocity in our effusive atomic beam. Since the π -pulse condition depends on the atomic velocity, not all atoms in our effusive atomic beam will be fully inverted to the excited state. According to our simulation, a laser beam whose intensity is adjusted to produce a π -pulse for the most probable velocity leaves about 30% of atoms in the effusive atomic beam in ground state. Furthermore, the simulation anticipates that the fraction of atoms left in the ground state oscillates as a function of the laser intensity with the first minimum occurring at the pump intensity that corresponds to π -pulse for atoms with the most probable velocity. To our surprise, our experiment found that less than 10% of atoms remained in the ground state. In addition, as

a function of the pump intensity, the fraction of atoms left in the ground state decreased monotonically to less than 10% and stays there regardless of the strength pump intensity; we observed no oscillation in the fraction of atoms left in the ground state. After many diagnostic experiments and simulations, we recognized that our observation cannot be explained by simple nonadiabatic pumping process. Rather, because our pump is slightly out of focus, the atoms experience frequency chirp and they are adiabatically inverted.

Figure 1 shows the 553-nm fluorescence of ^{138}Ba atoms inside the cavity mode as a function of pump laser power. The 553-nm fluorescence indicates the total number of atoms in the ground state. This includes the atoms not excited by the pump beam, as well as the atoms decay from the excited state during the traveling time in the 553-nm laser beam. Over $50\ \mu\text{m}$, about 3% of atoms decay to the ground state and about 5% decay to the metastable states (See Figure 2 in chapter 3). The 553-nm laser beam is aligned to the cavity mode by using the Ti:sapphire cavity probe beam. When the Ti:sapphire cavity probe beam is aligned to the cavity mode, transmission from $\text{TEM}_{0,0}$ is maximum. The size of the 553-nm laser beam is made approximately the same as that of the Ti:sapphire cavity probe beam, and is sent parallel to it. Then the Ti:sapphire cavity probe beam is blocked. Each point in Figure 1 is a result of 30-sec exposure to the CDD camera. The 699-dye laser, which produces the 553-nm laser beam, is locked to the $6s^2\ ^1\text{S}_0 \leftrightarrow 6s6p\ ^1\text{P}_1$ atomic transition using another atomic beam. In the experiment, the pump laser power is chosen slightly higher than the power at which the fraction of the ground state atoms starts to level off to its minimum value. This makes the pumping process insensitive to power fluctuation or drift of the pump laser beam. Very high pump power works fine, but it increases the pump scattering into the cavity mode which, in turn, increases the background of the microlaser output.

We also studied the effect of the pumping process on the velocity distribution of the ground state atoms. A 553-nm laser beam was sent into the cavity mode behind the pump beam almost counter-propagating to the atomic beam (See Figure 2). The fluorescence was observed by an avalanche photodiode located along the cavity axis. The velocity distribution of the ground-state atoms in the cavity mode was obtained from their fluorescence when the dye laser is scanned around the 553-nm resonance. When the pump laser was allowed to pump atoms, we

observed no structure in the velocity distribution of the atoms remaining in the ground state. This is a good indication that our pumping process was adiabatic since the nonadiabatic pumping process is velocity dependent (See Section 2.7).

Fluorescence in the Cavity

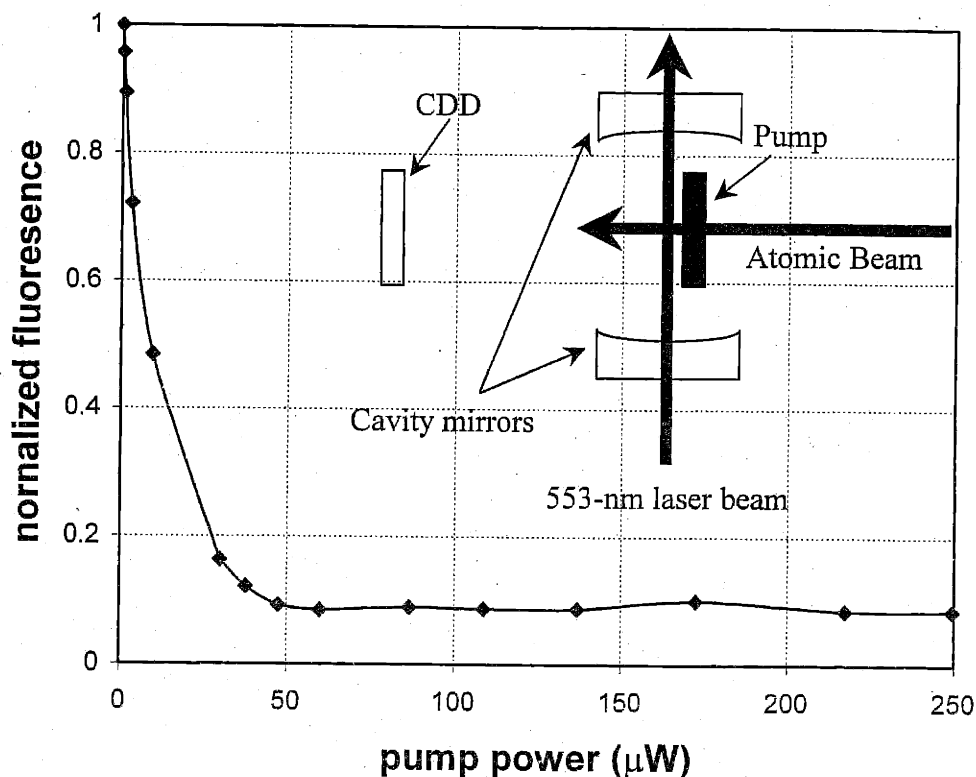


Figure 1. 553-nm fluorescence from ^{138}Ba atoms inside the cavity mode as a function of pump laser power.

The position of the pump beam with respect to the cavity mode is found as follows. The 553-nm laser beam is sent through the cavity mode and the intensity of the 553-nm fluorescence is observed as a function of the pump beam position. Figure 3 shows the normalized fluorescence as a function of the pump beam position. The pump beam is moved through the 553-nm laser beam in a direction opposite to the atomic beam direction. When the pump beam is completely behind the 553-nm laser beam (relative to the oven), maximum fluorescence is observed since no atoms in the cavity mode were pumped. When the pump beam starts to overlap with the 553-nm laser beam, the fluorescence decreases because some of the atoms are

shelved by the pump beam into the $6p\ ^3P_1$ excited state and they are no longer in resonance with 553-nm laser beam. The decrease in the fluorescence continues until the pump beam starts to move out in front of the 553-nm laser beam. Then the fluorescence starts to increase as the pump is moved away from the 553-nm laser beam. This increase is observed because some atoms that have shelved by the pump beam into the excited state have enough time to decay back to the ground state. For initial alignment, the position of the pump beam is chosen in front of the cavity mode at the point where the fluorescence starts to increase. Final adjustment of the position of the pump is accomplished by maximizing the output of the microlaser.

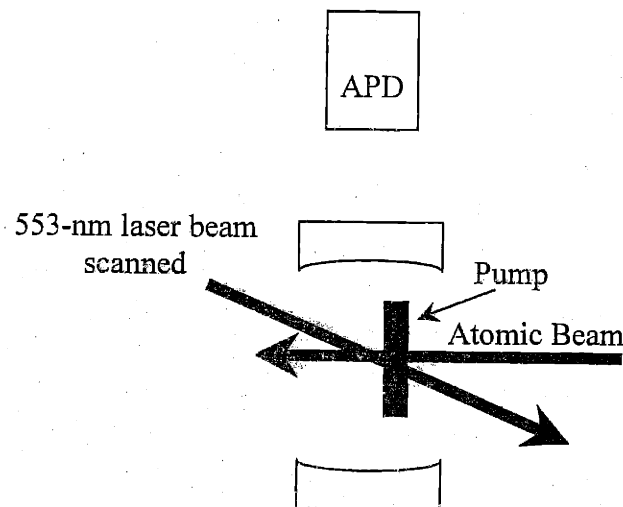


Figure 2. Beams arrangements to study the effect of the pumping process on the atomic beam velocity distribution.

6.2- Atomic number and photon number calibration

Fluorescence measurements are used to determine the number of atoms inside the cavity mode. A beam from the 699 dye laser, which is locked to the $6s^2\ ^1S_0 \leftrightarrow 6s6p\ ^1P_1$ atomic transition, is sent along the cavity axis and the CDD camera looking from the side of the cavity is used to measure the fluorescence from the atomic beam. The counts on the CDD camera C are related to the atomic density ρ by the following relation:

$$C = [\int d^3r \rho(r)R(r)][F_{\Omega}\eta T]t, \quad (1)$$

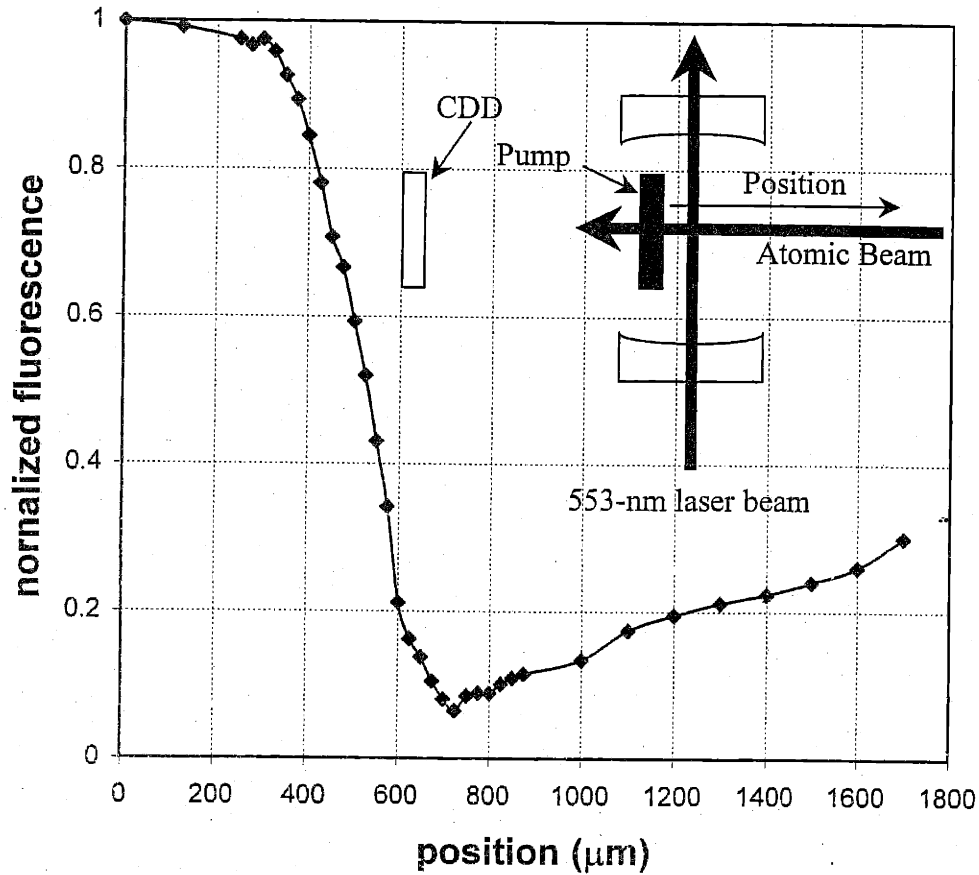


Figure 3. Fluorescence in the cavity as the pump moved through the cavity mode.

where r is the position the cavity mode, $R(r)$ is the emission rate of photons per atom at r , F_{Ω} is the fraction of the fluorescence power emitted by one atom into the solid angle subtended by the CDD camera, η is the detection efficiency of the CDD camera, T is the transmission from the atom-laser region to the CDD camera, and t is the collection time.

Since we use a very thin slit just in front of the cavity mode to define the atomic beam, it is a very good approximation to assume that the atomic density in the cavity mode is independent of the position in the cavity mode, and the integration in Eq. (1) can be written as

$$\int d^3r \rho(r)R(r) = \rho A \int_{-\infty}^{\infty} dx R(x). \quad (2)$$

Here A is the area of the slit and x is the coordinate along the atomic beam direction. We also use the fact that the slit width is much smaller than the radius of 553-nm probe beam to make the approximation that the emission rate $R(r)$ depends only on the x coordinate.

We need to define a volume to be able to extract the number of atoms from the atomic density. Along x , the Gaussian cavity mode does not have well-defined boundaries but according to microlaser theory, this mode is equivalent to a top-hat mode whose width is given by $\sqrt{\pi}w_c$, where w_c is mode waist of the cavity mode. Our volume will have the width of this top-hat mode and a cross-section area A of the slit. When we speak about the number of atoms in the cavity mode $\langle N \rangle$, we mean the number of atom in a volume given by $A\sqrt{\pi}w_c$. Similarly the number of atoms in the 553-nm probe laser N_p is the number of atoms in a volume defined by $A\sqrt{\pi}w_p$, where w_p is the radius of the 553-nm beam in the cavity. $\langle N \rangle$ and N_p are related by

$$\rho = \frac{\langle N \rangle}{A\sqrt{\pi}w_c} = \frac{N_p}{A\sqrt{\pi}w_p}. \quad (3)$$

Using the above equations, the number of atoms in the cavity mode can be found from

$$\langle N \rangle = \frac{w_c}{w_p} \frac{C}{\bar{R}tF_\Omega \eta T}, \quad (4)$$

where \bar{R} is given by

$$\bar{R} = \int_{-\infty}^{\infty} dx \frac{1}{\sqrt{\pi w_p}} R(x) = \int_{-\infty}^{\infty} dx \frac{1}{\sqrt{\pi w_p}} \frac{\Gamma_g}{2} \frac{\frac{p}{p_s} e^{-2(\frac{x}{w_p})^2}}{1 + \frac{p}{p_s} e^{-2(\frac{x}{w_p})^2}} \quad (5)$$

Here Γ_g is the decay rate of the $6s6p \ ^1P_1$ state into the ground state which is $2\pi \cdot 18.9 \cdot 10^6 \text{ sec}^{-1}$, and p is the power of the 553-nm probe laser beam and p_s is the saturation power of the atomic transition.

The p_s and w_p are found experimentally from fluorescence measurements taken when the CDD camera is looking from the top of the cavity. (See Figure 4.) The saturation power p_s may be found from measuring the integrated counts of the CDD camera along the axis of the probe laser, C_a , as a function of the probe laser power. As Figure 5 shows, these measurements fit well a saturation function which is given by

$$C_a = a \frac{\frac{p}{p_s}}{1 + \frac{p}{p_s}} = 11.14 \times 10^3 \frac{\frac{p(\mu\text{W})}{11.2}}{1 + \frac{p(\mu\text{W})}{11.2}} \quad (6)$$

In the calibration measurements we use a probe laser power of about $10 \mu\text{W}$.

The CDD integrated counts along the probe laser direction may be used to find the intensity profile of the probe laser in the cavity. We need to account for the saturation effect introduced by the fact that the probe laser has a Gaussian intensity profile and its total power is comparable to the saturation power. This can be done by inverting Eq. (6). Figure 6 shows the saturation-corrected CDD integrated counts, along with the uncorrected integrated CDD counts. A Gaussian function fits the corrected counts well.

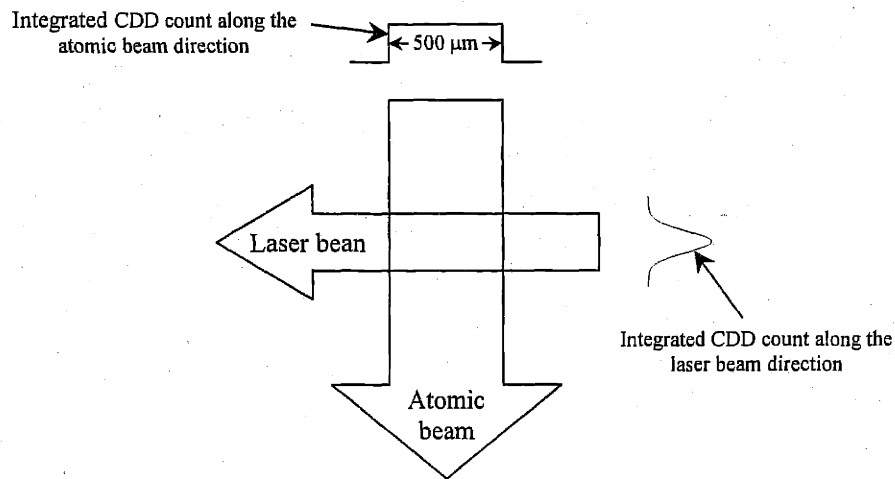


Figure 4. In measuring the saturation power p_s and the radius of the probe laser beam, the CDD camera is looking from the top.

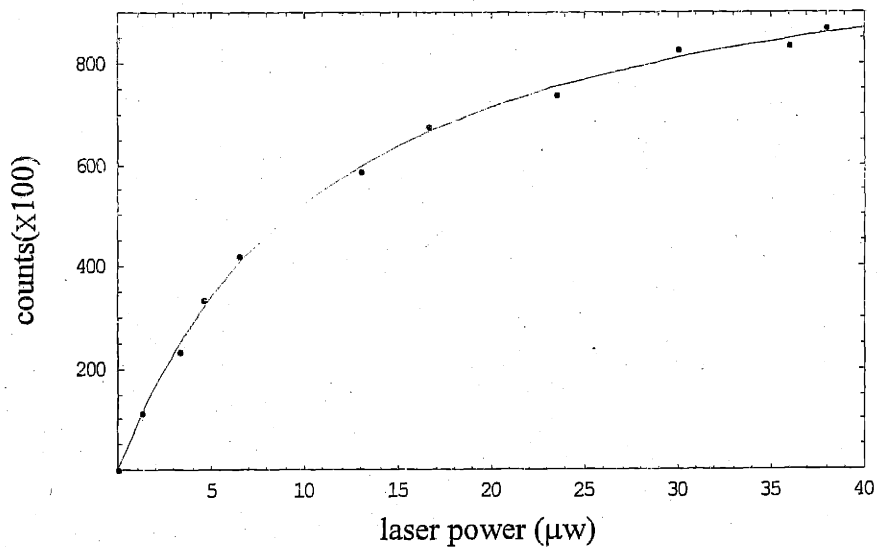


Figure 5. The saturation power is obtained from fitting the measurements of the counts along the axis of the 553-nm laser beam as a function of its power.

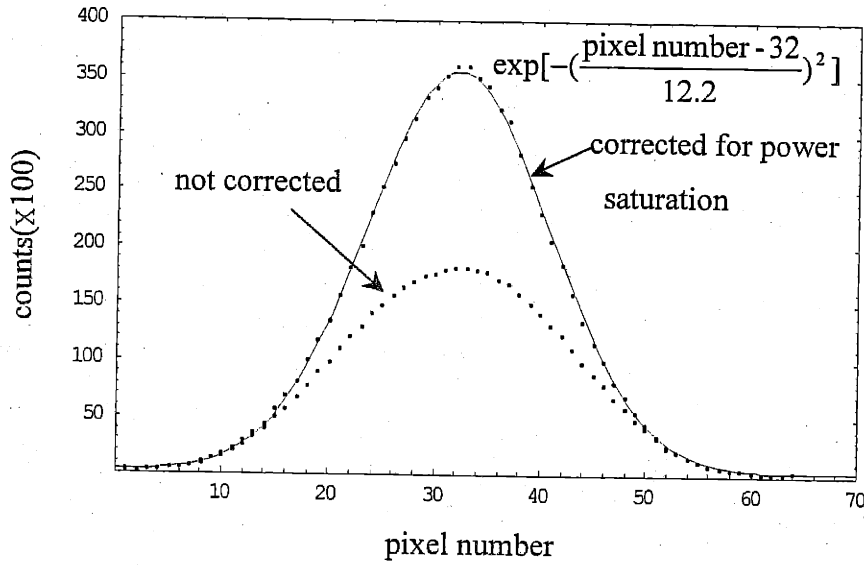


Figure 6. The radius of the probe beam w_p is obtained from fluorescence measurements when the CDD camera is looking from the top.

The curve of the CDD integrated counts along the atomic beam has a top-hat shape with width given by the length of the thin slit, which is $500 \mu\text{m}$. This is used to calibrate the size of a pixel to the actual size of the image. Each pixel corresponds to $8.33 \mu\text{m}$. Also, the sharpness of the top-hat shape is used to estimate the aberration introduced by the optics between the atom-beam region and the CDD camera. This aberration can be represented by a Gaussian function given by $\text{Exp}[-(\frac{\text{pixel number}}{3.2})^2]$. The Gaussian shape in Figure 6 is a convolution of this aberration Gaussian function and the actual Gaussian shape of the laser beam. This leads to

$$w_p = 8.33\sqrt{2}\sqrt{12.2^2 - 3.2^2} = 139 \mu\text{m}.$$

Using the cavity geometry, the mode waist of the cavity is calculated to be $42 \mu\text{m}$. The collection efficiency of the CDD camera η is given by

$$\eta = \frac{\text{Quantum Efficiency}}{\text{Gain Index}} = \frac{0.35}{5.6} = 0.0625. \quad (7)$$

Here the gain index is the number of photoelectrons that produce one count on the CDD pixel. The fluorescence is transmitted to the CDD camera through a vacuum chamber window, a

composite lens, a filter and an objective lens. The transmission through the chamber window is assumed to be $(0.96)^2$. The transmission through the composite lens and the filter is measured to be 0.25 and though the objective lens to be 0.97. Thus, the total transmission T is estimated to be 0.22.

The flux of photons emitted by a barium atom has a dipole emission pattern which is proportional to $[\sin(\theta)]^2$, where θ is the angle between the polarization vector of the probe laser and the observation direction. We adjust the probe laser polarization vector such that the CDD camera receives maximum flux ($\theta = 90^\circ$). The power emitted by an atom into the solid angle Ω is proportional to $\int_{\Omega} \sin^2(\theta) d\Omega'$ and the fraction of power emitted into the solid angle suspended by the CDD camera Ω_{CDD} is given by

$$F_{\Omega} = \frac{\int_{\Omega_{\text{CDD}}} \sin^2(\theta) d\Omega'}{\int_{\text{All}} \sin^2(\theta) d\Omega'} \approx \frac{\Omega_{\text{CDD}}}{2\pi \int_0^{\pi} d\theta \sin^3(\theta)} = \frac{\Omega_{\text{CDD}}}{\frac{2}{3} 4\pi}. \quad (8)$$

In replacing the integration in the numerator by Ω_{CDD} , we use the fact that over the CDD, θ does not deviate a lot from 90° . The Ω_{CDD} is defined by the composite lens which has a diameter of 1" and is located 20 cm from the fluorescence source.

$$\Omega_{\text{CDD}} = \frac{\pi(0.5 * 2.54)^2}{20^2} = .019 \text{ sr}. \quad (9)$$

We use a collection time of 30 sec to measure the number of atoms in the cavity $\langle N \rangle$. From the above discussion, $\langle N \rangle$ is related to the integrated count on the CDD camera by

$$\langle N \rangle = 19 \text{ atoms} / 10^6 \text{ counts}. \quad (10)$$

In addition to estimating $\langle N \rangle$, we need to estimate the number of photons inside the cavity $\langle n \rangle$ from the count rate on the PMT n_{det} using the following relation

$$n_{\text{det}} = \frac{\langle n \rangle}{2} \Gamma_c \frac{T_c}{T_c + L_c} T_d \eta_p. \quad (11)$$

$\langle n \rangle$ is divided by two because half of the photons leak from one of the cavity mirrors. Γ_c is the cavity decay rate, which is $1.2 \times 10^6 \text{ sec}^{-1}$ for a cavity finesse of one million. T_d and L_d are the transmission and loss of the cavity mirror, respectively. T_d is measured to be typically 0.5×10^{-6} and L_d to be typically 3×10^{-6} . η_p is the quantum efficiency of the PMT, which is 0.12. T_d is the transmission through the optics between the cavity and the PMT. In transporting the output of the microlaser to the PMT, we use six coated mirrors, three coated lenses with transmission, an AOM, a beam splitter, a coated vacuum chamber window and uncoated mirror. T_d is found to be 0.6. Thus the average number of photons inside the cavity mode can be related to the count rate on the PMT by the following relation

$$\langle n \rangle = 0.16 \text{ photons} / (10^3 \text{ count per sec on the PMT}). \quad (12)$$

The systematic error in finding $\langle N \rangle$ from the CCD counts is estimated to be 15% and the systematic error in extracting $\langle n \rangle$ from the PMT is estimated to be 20%. None of these errors are shown in the following plots.

6.3- Microlaser average number of photons measurements

The emission of the microlaser is measured as a function of the average number of atoms in the cavity mode. Two configurations are studied and compared to the microlaser theory. Since the flux from our velocity selection scheme is too low, thermal atomic beams are used for both configurations. In the standing-wave configuration, the atomic beam and the cavity mode are perpendicular while in the traveling-wave configuration they are not. In these two configurations the experimental parameters are quite different. This provides a nice test of the microlaser theory over a wide range of experimental conditions. In the standing-wave configuration, the atoms experience a huge variation in the coupling constant strengths; an atom may experience a coupling constant strength as small as zero when it passes through the

standing-wave node and as large as g_0 when it passes through the antinode. Furthermore, the atoms have a wide atom-cavity interaction-time distribution. On the other hand, in the traveling-wave configuration, the atom-cavity coupling has a uniform strength and the atoms have a weak velocity selectivity provided by the Doppler shifts.

Figure 7 shows a typical output of the traveling-wave microlaser as a function of the atom-cavity detuning. The cavity is tuned by a slow ramp on its high voltage. The standing-wave-cavity mode is equivalent to two traveling waves moving in opposite directions. Because of the Doppler shift, atoms can not resonate with both of these two traveling waves at the same time. In this figure, each of the big peaks is the consequence of the atomic interaction with one of these two traveling waves. The small peaks are the transmission from the sidebands of the 791-nm cavity probe beam, which are separated by 49.2 MHz and are used to calibrate the time axis. Here, the main transmission of the probe beam is blocked. The atomic tilt angle can be estimated from the frequency difference between the microlaser output peaks. These peaks occur when atoms with the most probable velocity $v_0 \approx 370$ m/sec are in resonance with the cavity mode. This leads to a tilt angle of 10 mrad.

A typical output of the standing wave microlaser is shown in Figure 8. For the standing wave configuration the atomic beam should be aligned to be perpendicular to the cavity mode. The atomic beam alignment is achieved by moving the atomic oven such that the frequency width of the microlaser peak is minimum. The full width at half maximum of the microlaser output is about 3 MHz, which is consistent with broadening caused by the short atomic transit time through the cavity mode.

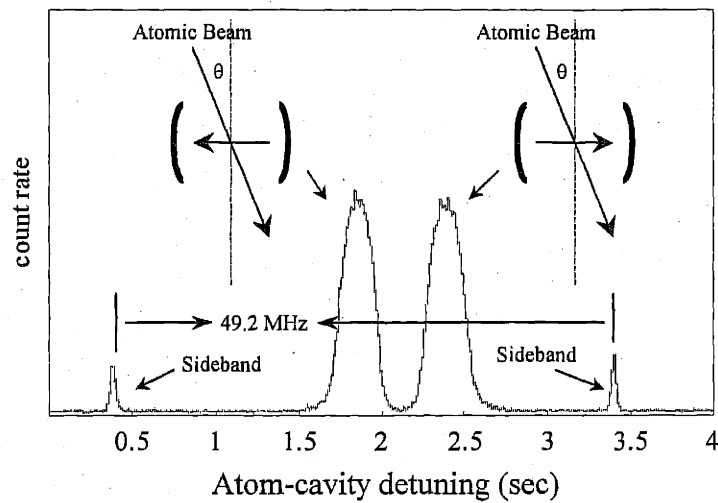


Figure 7. Typical output of the traveling-wave microlaser as a function of the atom-cavity detuning.

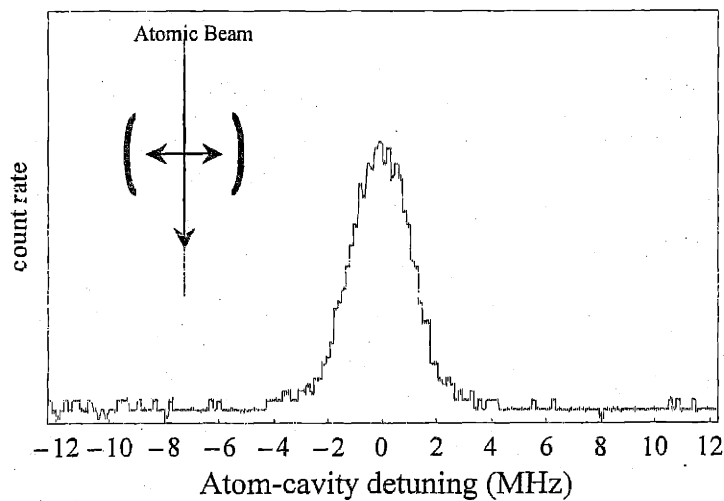


Figure 8. Typical output of the standing-wave microlaser as a function of the atom-cavity detuning.

Figure 9 presents the average number of photons $\langle n \rangle$ as a function of the average number of atoms in the cavity mode for the traveling-wave configuration. The average number of photons, $\langle n \rangle$, is obtained from the PMT count rates of one traveling-wave peak. The data points fit well to the microlaser theory predictions. In the microlaser theory, the gain per atom

term is averaged over the velocity distribution of an effusive atomic beam and over the variation of the coupling constant along the thin slit width. (See Chapter 2 for more details). In our fit we use the following experimental parameters: finesse = 1 million, most probable velocity = 370m/sec and cavity length = 1.1 mm. To fit the data, the theory values for $\langle N \rangle$ and $\langle n \rangle$ are multiplied by 0.92 and 1.12, respectively. This scaling is within our experimental accuracy in extracting $\langle N \rangle$ and $\langle n \rangle$ from fluorescence measurement and from the PMT count rates, and it will be used consistently for the other data.

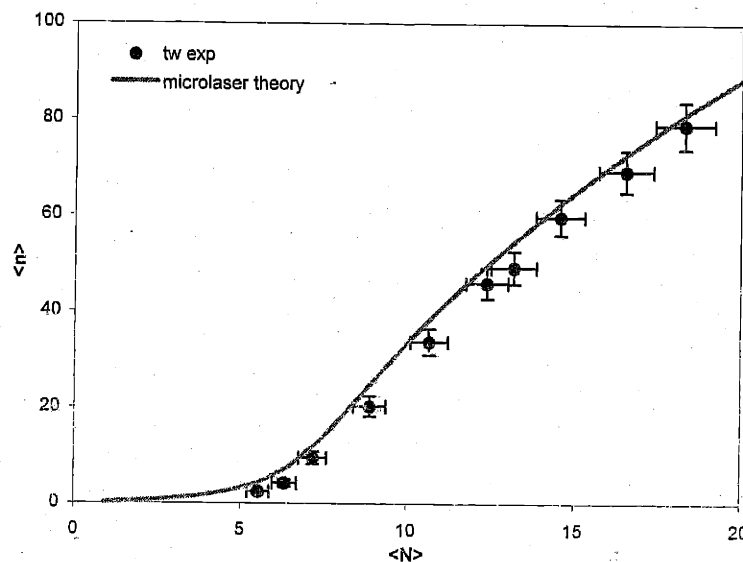


Figure 9. The average number of photons, $\langle n \rangle$, as a function of the average number of atoms, $\langle N \rangle$, for the traveling-wave configuration.

Similarly, Figure 10 shows that the experimental data of $\langle n \rangle$ versus $\langle N \rangle$ for the standing-wave configuration fits well the microlaser theory calculations. The gain per atom term in the microlaser theory is averaged over the atomic velocity distribution, the standing-wave coupling constant strengths along the cavity mode axis, and the variation in the coupling strength along the width of the thin slit.

Figure 11 compares $\langle n \rangle$ versus $\langle N \rangle$ for the standing-wave microlaser and the traveling-wave microlaser. For the standing-wave case, the microlaser threshold occurs at smaller number of atoms. This is because, on average, the coupling constant strength is larger in

the standing-wave case. Moreover, all the atoms are in resonance with cavity mode. On the other hand, photon number increases much faster in the traveling-wave microlaser. This difference in the two configurations is a consequence of the difference between the shapes of the gain curves in both cases. This difference is also obvious in the measurements of the intensity correlation time.

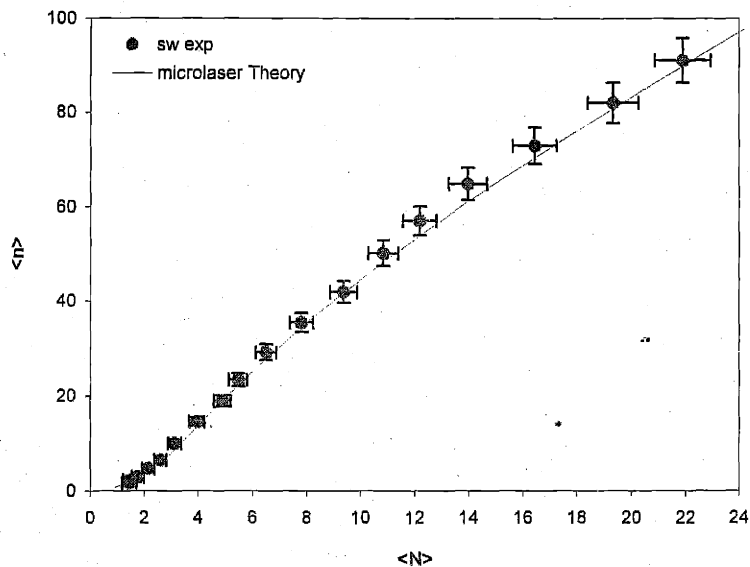


Figure 10. The average number of photons $\langle n \rangle$ as a function of the average number of atoms $\langle N \rangle$ for the standing-wave configuration.

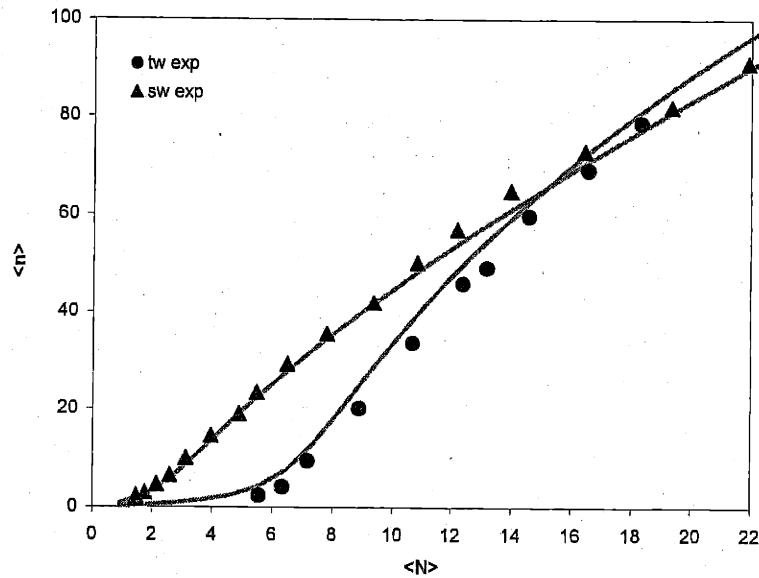


Figure 11. Comparison between the standing-wave and the traveling-wave microlasers.

6.4- The degree of the second-order coherence

A typical measurement of the degree of the second order-coherence function $g^{(2)}(\tau)$ is shown in Figure 12. It takes about one hour to collect such a measurement. The actual collection is typically 1000 sec and the rest of the time is spent in preparing the system: locking the cavity, waiting for the oven temperature to be stabilized and measuring the atomic density. The degree of the second-order coherence function is obtained from the raw counts in the multi-stop time-to-digital converter (MSTDC) in two steps. First, the contribution from the background signals is subtracted. Second, the corrected raw data is normalized by dividing each bin count by the average count in the bins where the $g^{(2)}(\tau)$ levels down and becomes parallel to the time axis. For these bins τ is much larger than the intensity correlation time.

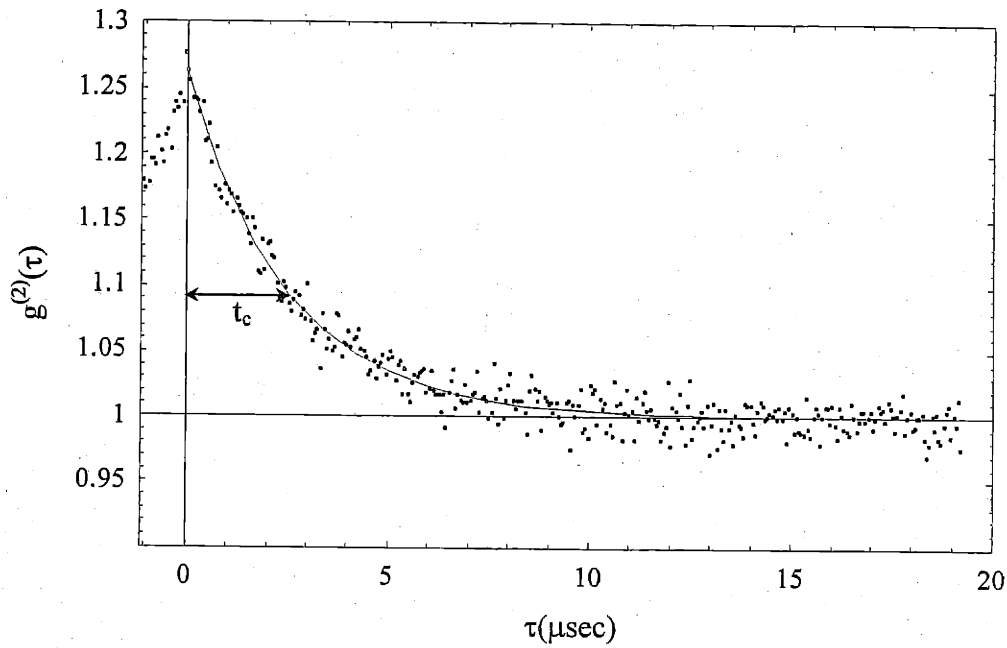


Figure 12. A typical measurement of the degree of second-order coherence function. Data fits an exponential function very well.

The main source of the background signal is the scattering from the pump beam of the microlaser. The contribution of the background counts to the microlaser $g^{(2)}(\tau)$ measurements can be accounted for as follows. The raw count in a MSTDC bin i is given by

$$c[i] = \alpha \langle (n_{ps}(i\Delta t) + n_{pb}(i\Delta t))(n_{as}(0) + n_{ab}(0)) \rangle. \quad (13)$$

Here α is a proportionality constant. The two terms enclosed in the first set of parentheses are the instantaneous count rates from the PMT at relative time $i\Delta t$, where Δt is the time width of the bin. The first term $n_{ps}(i\Delta t)$ is the contribution from the microlaser signal while the other term $n_{pb}(i\Delta t)$ is the contribution from the background. Similarly, the two terms enclosed in the second set of parentheses are the instantaneous count rate from the APD at relative time zero, with the first term $n_{as}(0)$ corresponding to the microlaser signal and the second term $n_{ab}(0)$ corresponding to the background. Since the background photons are not correlated to each other nor are they correlated to the microlaser photons, Eq. (13) can be written as

$$c[i] = \alpha \langle n_{ps}(i\Delta t)n_{as}(0) \rangle + \alpha \{ \langle n_{ps} \rangle \langle n_{ab} \rangle + \langle n_{as} \rangle \langle n_{pb} \rangle + \langle n_{pb} \rangle \langle n_{ab} \rangle \},$$

$$\equiv c_m[i] + c_b. \quad (14)$$

Here $c_m[i]$ is the contribution from only the microlaser signal while the second term c_b , which is independent of i , is the contribution due to the presence of the background. For times much larger than the microlaser intensity correlation time, Eq(14) can be written as

$$c[\infty] = \alpha \langle n_{ps} \rangle \langle n_{as} \rangle + c_b, \quad (15)$$

where $c[\infty]$ corresponds to bin numbers where the time is much larger than the intensity correlation time of the microlaser. Using Eq(14) and Eq(15), one can find the contribution due to the microlaser signal to be

$$c_m[i] = c[i] - c[\infty] \frac{\langle n_{ps} \rangle \langle n_{ab} \rangle + \langle n_{as} \rangle \langle n_{pb} \rangle + \langle n_{pb} \rangle \langle n_{ab} \rangle}{\langle n_{ps} \rangle \langle n_{as} \rangle + \langle n_{ps} \rangle \langle n_{ab} \rangle + \langle n_{as} \rangle \langle n_{pb} \rangle + \langle n_{pb} \rangle \langle n_{ab} \rangle},$$

or

$$c_m[i] = c[i] + c[\infty] \left(1 - \frac{\langle n_{ps} \rangle \langle n_{as} \rangle}{\langle n_p \rangle \langle n_a \rangle}\right), \quad (16)$$

where n_p and n_a are the total count rates from the PMT and APD, respectively. For $c[\infty]$ value, we use the average value of many bins that corresponds to times much larger than t_c . The correction due to the background is small. The biggest correction occurs when the microlaser signal is the smallest. In the following $g^{(2)}(\tau)$ measurements the smallest microlaser signal is 20 k cps on the PMT and 11 k cps on the APD. Typically the background signal is 6 k cps on the PMT and 3 k cps on the APD. This leads to a correction of 5%.

Figure 13 shows the value of the degree of the second-order coherence at time at $\tau = 0$, $g^{(2)}(0)$ for the traveling-wave microlaser as a function of the average number of the atoms in the cavity mode $\langle N \rangle$. The data is fitted to the microlaser theory with appropriate averaging over the gain term, as done previously in fitting the average number of photons inside the cavity mode. As

expected, at threshold, as a function of $\langle N \rangle$, $g^{(2)}(0)$ starts near 2 and decreases monotonically to 1. Similar behavior is observed for the standing-wave microlaser, as shown in Figure 14. The width of the photon number distribution can be extracted from $g^{(2)}(0)$ measurements using the following relation:

$$Q = (g^{(2)}(0) - 1) \langle n \rangle. \quad (17)$$

Here Q as defined previously is $Q \equiv \frac{\langle n^2 \rangle - \langle n \rangle^2}{\langle n \rangle} - 1$. As Figure 15 indicates, the width of the photon number distribution in the traveling-wave case can be as wide as twice that of a Poisson distribution. Maximum Q occurs for $\langle n \rangle \approx 34$. Thus, if the photon distribution were Poissonian, its width would be $2\sqrt{34} \approx 12$. For the standing-wave case, Figure 16, the maximum width of the photon number distribution is about $\sqrt{2.5} = 1.6$ of a Poisson distribution. This occurs for $\langle n \rangle \approx 6$. The difference in Q values in both cases may be understood by considering the steepness of the $\langle n \rangle$ versus $\langle N \rangle$ curve. One source of fluctuations is the number of atoms in the cavity. Since the atoms are injected randomly into the cavity mode, their number distribution is a Poisson distribution and its width is given by $2\sqrt{\langle N \rangle}$. From this width and the slope of the $\langle n \rangle$ versus $\langle N \rangle$ curve we can find the size of the photon number fluctuation due to atom fluctuations. Where the slope of the curve is maximum, the relative size of the photon number fluctuations is the highest. Since the traveling-wave microlaser output as a function of $\langle N \rangle$ is steeper than the standing-wave one, its Q value is larger.

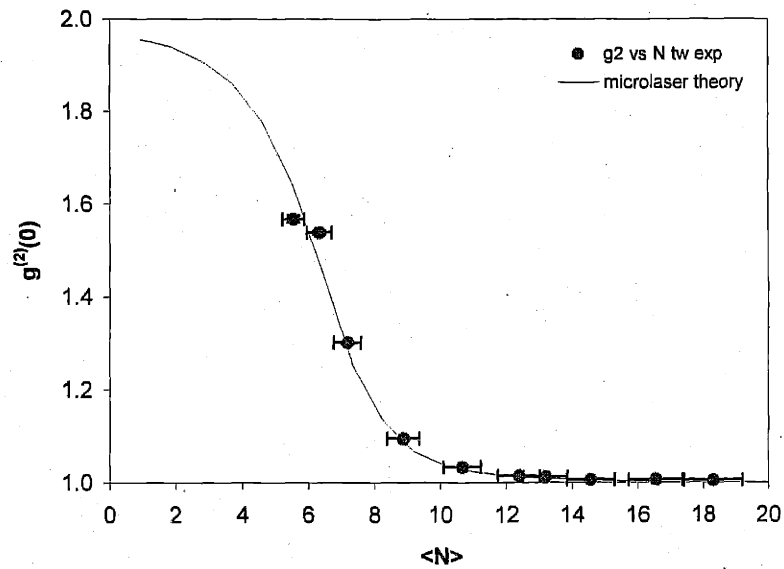


Figure 13. $g^{(2)}(0)$ as a function of the average number of atoms inside the cavity mode $\langle N \rangle$ for the traveling-wave case.

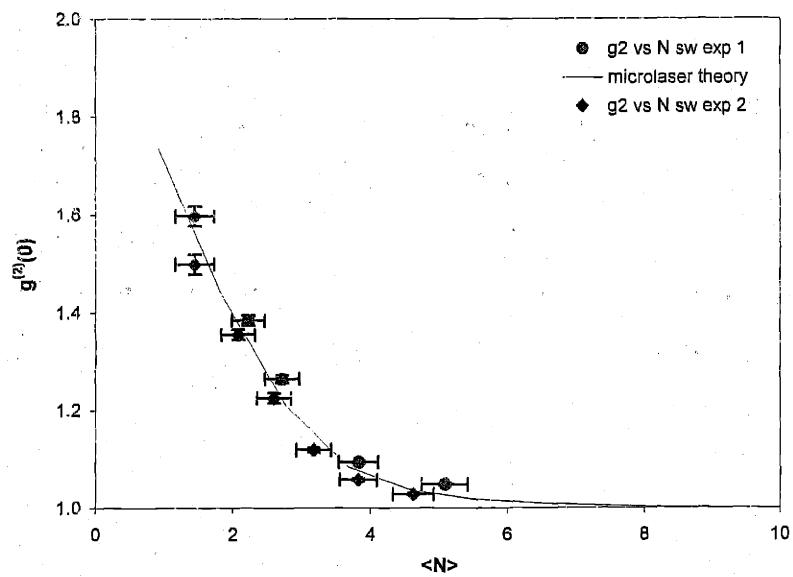


Figure 14. $g^{(2)}(0)$ for the standing-wave configuration as a function of the average number of atoms inside the cavity mode $\langle N \rangle$.

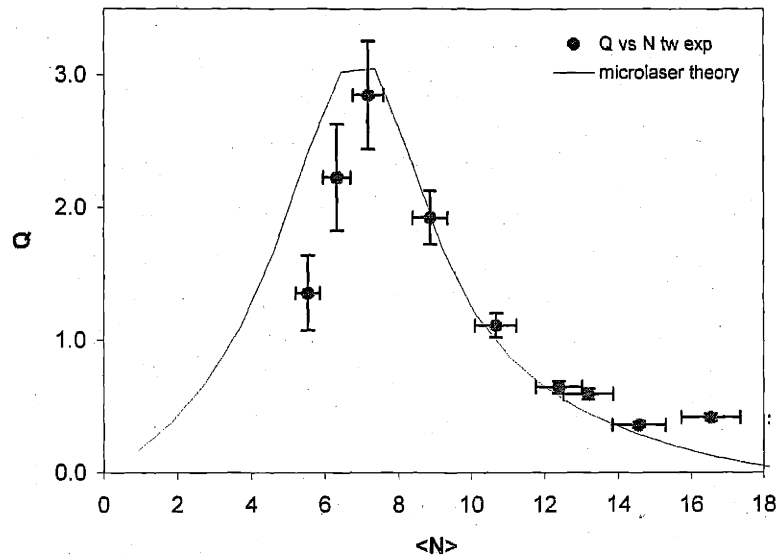


Figure 15. The normalized variance Q as a function of the average number of atoms inside the cavity mode $\langle N \rangle$ for the traveling-wave case

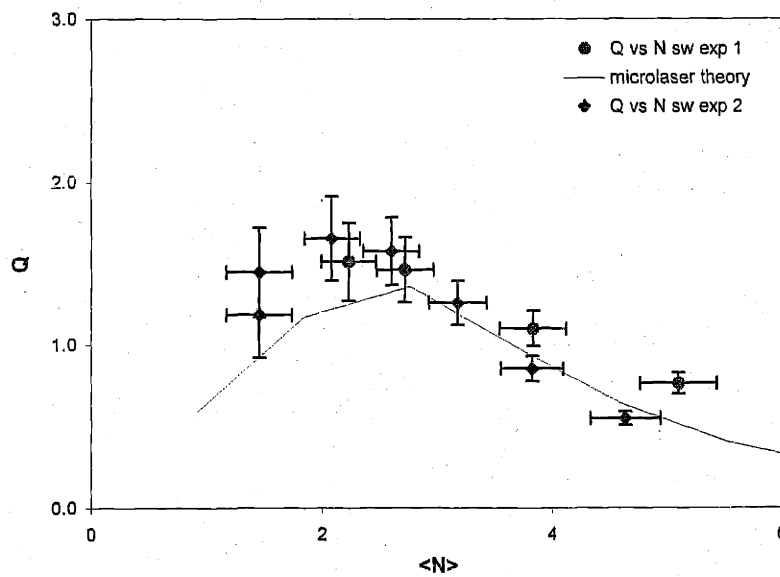


Figure 16. For the standing-wave microlaser, the Q parameter is shown as a function of the average number of atoms inside the cavity mode $\langle N \rangle$.

All our $g^{(2)}(\tau)$ measurements fits very well an exponential function which is given by $g^{(2)}(\tau) = (g^{(2)}(0) - 1)e^{-\tau/t_c} + 1$. The intensity correlation time t_c is defined as the time at which the exponential part of the $g^{(2)}(\tau)$ function decays to $1/e$ of its value at $\tau=0$. As was shown using the rate-equation model, the size of t_c reveals the difference between the slope of the gain and the loss terms. Figure 17 and Figure 18 present the measurements and the fits of t_c as a function of $\langle N \rangle$ for the traveling-wave and standing-wave cases, respectively. In Figure 19, t_c for both cases are shown on the same plot. Here the $\langle N \rangle$ -axis is adjusted so that t_c curves for the both cases peak at the same $\langle N \rangle$. In general, t_c for the traveling wave-configuration is larger than that for the standing wave. Larger values of t_c indicate that the system has slower response to disturbances caused by fluctuations of the atom number or photon number inside the microlaser. In other words, the traveling-wave system has a longer memory.

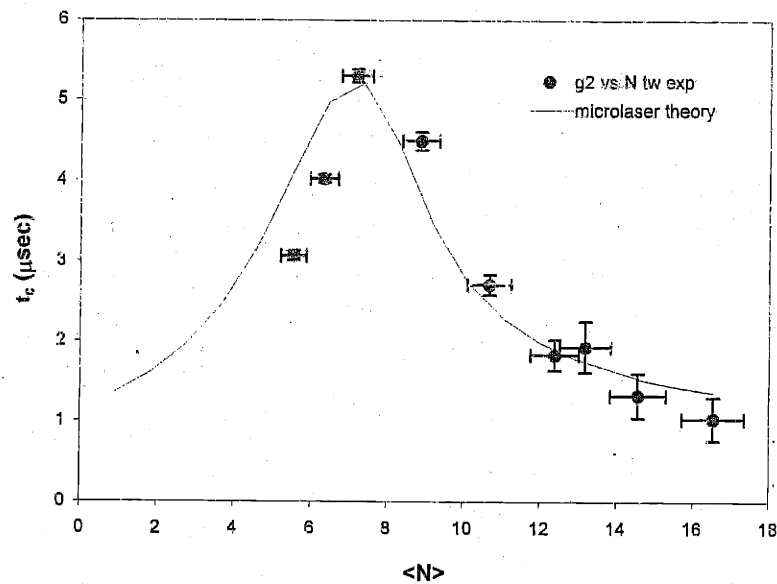


Figure 17. The intensity correlation time t_c for the traveling-wave configuration as a function of the average number of atoms inside the cavity mode $\langle N \rangle$.

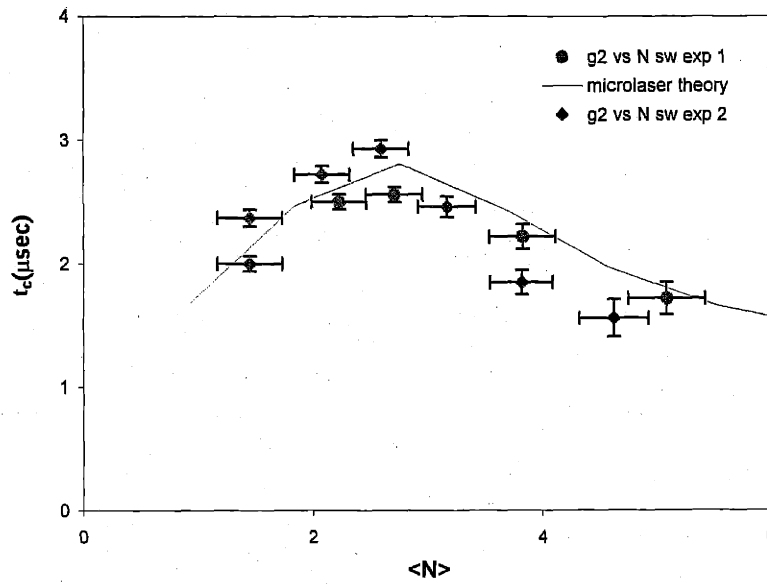


Figure 18. The intensity correlation time t_c as a function of the average number of atoms inside the cavity mode $\langle N \rangle$ for the standing-wave microlaser.

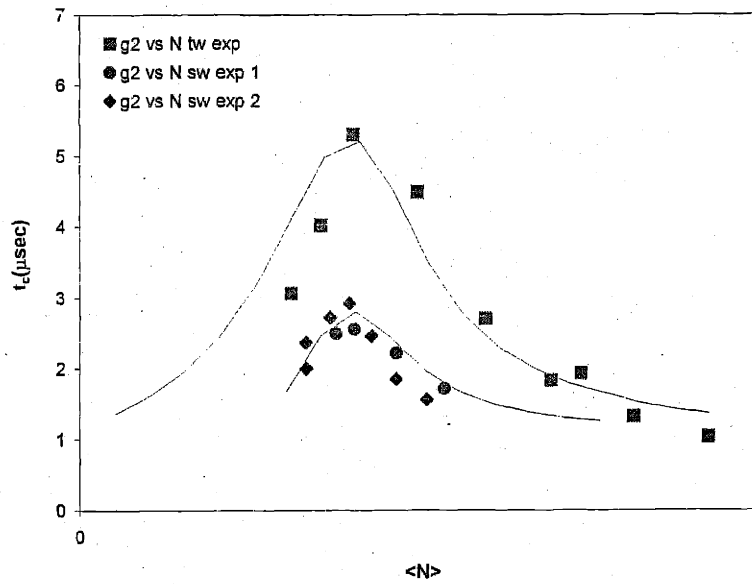


Figure 19. The intensity correlation time t_c for both configurations. The $\langle N \rangle$ axis is adjusted so that both curves peak at the same $\langle N \rangle$.

Chapter

7 Conclusions and future improvements

We have studied experimentally the output and the degree of second-order coherence function of the microlaser. With an effusive atomic beam, two microlaser configurations have been explored, namely, traveling-wave and standing-wave configurations. Although our microlaser has up to 20 atoms in its cavity mode, we have found that these measurements agree well with the single-atom microlaser theory. This observation is also supported by the quantum trajectory simulation (QTS) of up to five atoms inside the cavity mode. At our regime of operation, QTS indicates that the single-atom microlaser theory is applicable to our many-atom microlaser since we have $\Gamma_{c, \text{int}} \ll 1$. The behavior of our microlaser can be understood by using a simple physical picture based on the rate-equation formalism. We can attribute the difference between the behavior of the two configurations to the difference in their gain curves.

Measuring $g^{(2)}(0)$ less than one is an indication of a sub-Poisson statistics. The microlaser is expected to have this kind of photon statistics beyond the threshold regime. With our effusive atomic beam, it is difficult to reach the region where the microlaser statistics becomes sub-Poissonian. To observe this interesting non-classical behavior, we need to improve either the flux of our atomic beam or the finesse of our cavity. We have put a lot of effort into improving both of these two crucial parameters. In addition, we have improved the uniformity of the atom-cavity coupling constant, which makes it easier, with a high flux narrow-velocity atomic beam, to observe this non-classical behavior.

Collaborating with Research Electro Optic, Inc. we spent about one and a half years trying to improve the reflectivity of our mirrors but success was not our partner in this journey. Higher cavity finesse makes it easier to observe sub-Poisson statistics. For example, if the cavity finesse is an order of magnitude higher than what we have now, the $g^{(2)}(0)$ is at about 3 % below 1 which is fairly easy to observe over relatively short collection time.

Recently we have succeeded in developing a supersonic atomic beam with a huge atomic flux that should take us well beyond the threshold. In addition to studying photon statistics well beyond the threshold regime, this high flux atomic beam will enable us to study many aspects of the microlaser we were not able to reach before such as photon number stabilization and the sharp jumps expected in the photons number. We do not need to use a velocity selection scheme since the velocity distribution of this atomic beam is already narrow. The narrow velocity distribution enables us to use the nonadiabatic pumping process more efficiently. We can study more systematically the effect of partially pumped atoms on the performance of the microlaser.

The average velocity of this atomic beam is more than double than that of the effusive atomic beam. This means that the average number of photons produced by this atomic beam is typically more than four times than that form the effusive atomic beam. More photons in the cavity makes it more difficult to observe $g^{(2)}(0) < 1$, even when the photon-number distribution is strongly squeezed ($Q \cong -1$). According to the microlaser theory, for this supersonic atomic beam, $g^{(2)}(0)$ is at most 0.1% below 1. But with higher count rates and longer collection times, we may able to achieve good statistics that enables us to observe this small effect.

Appendix

A Calculations of P_n and $g^{(2)}(\tau)$

The following is a list of a Mathematica program to calculate the photon number distribution and the degree of the second-order coherence function for the microlaser.

```

$TextStyle = {FontFamily -> "Times", FontSize -> 14};
$RecursionLimit = 10000;
<< Graphics`Graphics`;
<< Statistics`NonlinearFit`

```

In qts, detuning is in $\frac{m\text{th} \cdot \theta}{\lambda}$ units for travelling wave and zero detuning occurs at 1.

Micromasercalculation: See mmaserTheory ExperPara.nb

Γ_c in Hz

g_0 in Hz

v_1 = atom velocity for which cavity decays during transversing the cavity

v_2 = atom velocity for which one oscillation occurs during transversing the cavity

v_3 = atom velocity for which atom decays during transversing the cavity

■ Initialization for our experiment

$$nb = 0.00; n = .; F = 1.0 \cdot 10^6; \lambda = 791 \cdot 10^{-9};$$

$$L = 1.1 \cdot 10^{-3}; r_0 = .1; \Gamma_a = 50 \cdot 10^3; c = 3 \cdot 10^8;$$

$$z_0 = \sqrt{\frac{r_0 L}{2}}; f_{sr} = \frac{c}{2 L};$$

$$w_0 = \sqrt{\frac{\lambda z_0}{\pi}};$$

$$\tilde{\epsilon} = \frac{3}{4} \left(\frac{\lambda}{\pi w_0} \right)^2;$$

$$\Gamma_c = \frac{f_{sr}}{F};$$

$$v_1 = 2 \pi \Gamma_c \sqrt{\pi} w_0;$$

$$v_3 = 2 \pi \Gamma_a \sqrt{\pi} w_0;$$

■ Theory of microscopic maser (PRA Oct 86)

■ Monovelocity and uniform coupling

$$g_0 = \frac{1}{2} \sqrt{\frac{2}{\pi} f_{sr} f_{ra}} ;$$

$$v_2 = 2 \pi g_0 \frac{w_0}{\sqrt{\pi}} ;$$

$$x_{\beta}[k, v, N_{atom}, \Delta_{Over2g}] :=$$

$$x_{\beta}[k, v, N_{atom}, \Delta_{Over2g}] =$$

$$\frac{1}{k + (1 + nb)} \left(nb + k + N_{atom} \frac{v}{v_1} * \frac{k}{\Delta_{Over2g}^2 + k} \left(\sin \left[\sqrt{\Delta_{Over2g}^2 + k} \frac{\pi v_2}{v} \right] \right)^2 \right) ;$$

■ Standing wave with mono velocity

$$g_0 = \frac{1}{1} \sqrt{\frac{2}{\pi} f_{sr} f_{ra}} ;$$

$$v_2 = 2 \pi g_0 \frac{w_0}{\sqrt{\pi}} ;$$

$$x_{\beta}[k, v, N_{atom}, \Delta_{Over2g}] := \frac{1}{k} \frac{N_{atom}}{v_1} v \frac{1}{2} \left(1 - \text{BesselJ}[0, 2 \sqrt{k} \frac{\pi v_2}{v}] \right) ;$$

■ zero till uniform coupling with velocity distribution

$$g_0 = \frac{1}{1} \sqrt{\frac{2}{\pi} f_{sr} f_{ra}} ;$$

$$v_2 = 2 \pi g_0 \frac{w_0}{\sqrt{\pi}} ;$$

$$\text{ave}_{\beta}[k, v] :=$$

$$\text{ave}_{\beta}[k, v] = \text{NIntegrate} \left[v v \frac{4}{v \sqrt{\pi}} \left(\frac{v v}{v} \right)^2 \text{Exp} \left[- \left(\frac{v v}{v} \right)^2 \right] \left(\sin \left[\sqrt{k} \frac{\pi v_2}{v v} \right] \right)^2 , \right.$$

$$\left. \{v v, 20., 1300.\} \right] ;$$

$$x_{\beta}[k, v, N_{atom}, \Delta_{Over2g}] := \frac{1}{k} \frac{N_{atom}}{v_1} \text{ave}_{\beta}[k, v] ;$$

■ Standing wave with velocity distribution

```

g0 = 1 / 1 * sqrt(2 / pi * fsr fra) ;
v2 = 2 * pi * g0 * w0 / sqrt(pi) ;
aveβ[k_, v_] :=
  NIntegrate[vv * 4 / (v * sqrt(pi)) * (vv/v)^2 * Exp[-(vv/v)^2] * .5 * (1 - BesselJ[0, 2 * sqrt(k) * pi * v2 / vv]) ,
    {vv, 20., 1300.}] ;
xβ[k_, v_, Natom_, ΔOver2g_] := 1 / k * Natom / v1 * aveβ[k, v] ;

```

■ Standing wave with velocity distribution and gaussian mode along y

```

g0 = 1 / 1 * sqrt(2 / pi * fsr fra) ;
v2 = 2 * pi * g0 * w0 / sqrt(pi) ;
w = 25 * 10^-6 ;
aveβ[k_, v_] :=
  aveβ[k, v] =
  NIntegrate[1 / w * vv * 4 / (v * sqrt(pi)) * (vv/v)^2 * Exp[-(vv/v)^2] * .5 *
    (1 - BesselJ[0, 2 * sqrt(k) * pi * v2 / vv * Exp[-(y/w0)^2]]) , {y, -w/2., w/2.}, {vv, 20., 1300.},
  PrecisionGoal -> 4] ;
xβ[k_, v_, Natom_, ΔOver2g_] := 1 / k * Natom / v1 * aveβ[k, v] ;

```

■ Traveling wave with velocity distribution

$$g_0 = \frac{1}{2} \sqrt{\frac{2}{\pi} f_{sr} f_{ra}} ;$$

$$v_2 = 2 \pi g_0 \frac{w_0}{\sqrt{\pi}} ;$$

$$\theta = 10 \cdot 10^{-3} ;$$

$$d_{\text{Over}2g}[v_w, v] := 2 \pi \frac{v_w - v}{\lambda} \text{Sin}[\theta] \frac{1}{2 (2 \pi g_0)} ;$$

$$\text{ave}\beta[k, v, \Delta_{\text{Over}2g}] :=$$

$$\text{ave}\beta[k, v, \Delta_{\text{Over}2g}] =$$

$$\text{NIntegrate}\left[\frac{4}{v \sqrt{\pi}} \left(\frac{v_w}{v} \right)^2 \text{Exp}\left[-\left(\frac{v_w}{v}\right)^2\right] \frac{k}{(d_{\text{Over}2g}[v_w, v] + \Delta_{\text{Over}2g})^2 + k} \right. \\ \left. \left(\text{Sin}\left[\sqrt{(d_{\text{Over}2g}[v_w, v] + \Delta_{\text{Over}2g})^2 + k} \frac{\pi v_2}{v_w}}\right]\right)^2, \{v_w, 20., 1300.\} \right] ;$$

$$x\beta[k, v, \text{Natom}, \Delta_{\text{Over}2g}] := \frac{1}{k} \frac{\text{Natom}}{v_1} \text{ave}\beta[k, v, \Delta_{\text{Over}2g}] ;$$

■ Traveling wave with velocity distribution and gaussian mode along y

$$g_0 = \frac{1}{2} \sqrt{\frac{2}{\pi} f_{sr} f_{ra}} ;$$

$$v_2 = 2 \pi g_0 \frac{w_0}{\sqrt{\pi}} ;$$

$$w = 25 \cdot 10^{-6} ;$$

$$\theta = 10 \cdot 10^{-3} ;$$

$$d_{\text{Over}2g}[v_w, v, y] := d_{\text{Over}2g}[v_w, v, y] = 2 \pi \frac{v_w - v}{\lambda} \text{Sin}[\theta] \frac{1}{2 (2 \pi g_0 \text{Exp}\left[-\left(\frac{y}{w_0}\right)^2\right])} ;$$

$$\text{ave}\beta[k, v, \Delta_{\text{Over}2g}] :=$$

$$\text{ave}\beta[k, v, \Delta_{\text{Over}2g}] =$$

$$\text{NIntegrate}\left[\frac{1}{w} \frac{4}{v \sqrt{\pi}} \left(\frac{v_w}{v} \right)^2 \text{Exp}\left[-\left(\frac{v_w}{v}\right)^2\right] \frac{1}{(d_{\text{Over}2g}[v_w, v, y] + \Delta_{\text{Over}2g})^2 + k} \right. \\ \left. \left(\text{Sin}\left[\sqrt{(d_{\text{Over}2g}[v_w, v, y] + \Delta_{\text{Over}2g})^2 + k} \frac{\pi v_2}{v_w} \text{Exp}\left[-\left(\frac{y}{w_0}\right)^2\right]}\right]\right)^2, \right. \\ \left. \{y, -w/2., w/2.\}, \{v_w, 20., 1300.\}, \text{PrecisionGoal} \rightarrow 4 \right] ;$$

$$x\beta[k, v, \text{Natom}, \Delta_{\text{Over}2g}] := \frac{\text{Natom}}{v_1} \text{ave}\beta[k, v, \Delta_{\text{Over}2g}] ;$$

▪ $P_n, n, n^2, Q, g^{(2)}(0)$

```

SumPkOverC[1, maxk_, v_, Natom_, ΔOver2g_] := 1.;
SumPkOverC[i_, maxk_, v_, Natom_, ΔOver2g_] :=
  SumPkOverC[i-1, maxk, v, Natom, ΔOver2g] * xβ[maxk+1-i, v, Natom, ΔOver2g] + 1;
KpkSumOverC[1, maxk_, v_, Natom_, ΔOver2g_] := 0.;
KpkSumOverC[i_, maxk_, v_, Natom_, ΔOver2g_] :=
  KpkSumOverC[i-1, maxk, v, Natom, ΔOver2g] * xβ[maxk+1-i, v, Natom, ΔOver2g] + maxk-i;

n[maxk_, v_, Natom_, ΔOver2g_] :=
  KpkSumOverC[maxk+2, maxk+2, v, Natom, ΔOver2g] /
  (SumPkOverC[maxk+1, maxk+1, v, Natom, ΔOver2g]);

p[n_, maxk_, v_, Natom_, ΔOver2g_] :=
  
$$\left( \prod_{k=1}^n xβ[k, v, Natom, ΔOver2g] \right) / (\text{SumPkOverC}[maxk+1, maxk+1, v, Natom, ΔOver2g]);$$


K2pkSumOverC[1, maxk_, v_, Natom_, ΔOver2g_] := 0.;
K2pkSumOverC[i_, maxk_, v_, Natom_, ΔOver2g_] :=
  K2pkSumOverC[i-1, maxk, v, Natom, ΔOver2g] * xβ[maxk+1-i, v, Natom, ΔOver2g] +
  (maxk-i)^2;

n2[maxk_, v_, Natom_, ΔOver2g_] :=
  K2pkSumOverC[maxk+2, maxk+2, v, Natom, ΔOver2g] /
  (SumPkOverC[maxk+1, maxk+1, v, Natom, ΔOver2g]);

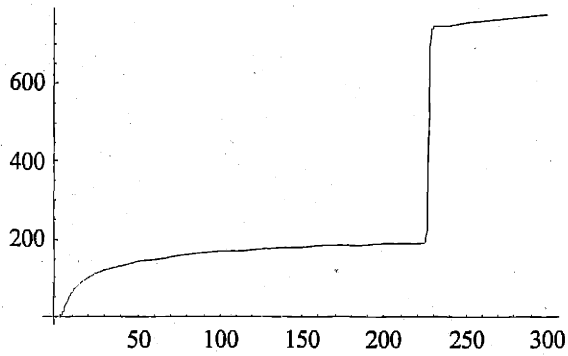
σ[maxk_, v_, Natom_, ΔOver2g_] :=
  
$$\sqrt{((n2[maxk, v, Natom, ΔOver2g] - (n[maxk, v, Natom, ΔOver2g])^2) / n[maxk, v, Natom, ΔOver2g])};$$


q[maxk_, v_, Natom_, ΔOver2g_] := (σ[maxk, v, Natom, ΔOver2g])^2 - 1;
g2[maxk_, v_, Natom_, ΔOver2g_] :=
  (n2[maxk, v, Natom, ΔOver2g] - n[maxk, v, Natom, ΔOver2g]) /
  (n[maxk, v, Natom, ΔOver2g])^2;

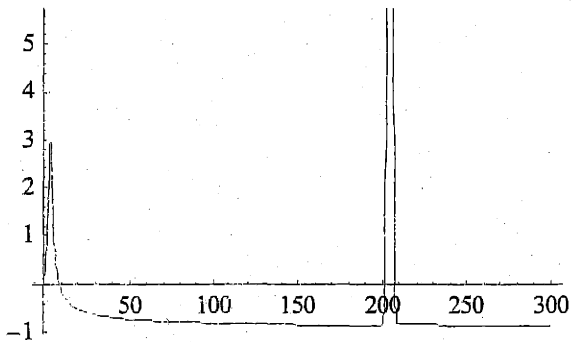
```

■ Calculating n, n^2, Q

```
pltn = Plot[n[950, 400, x, 0], {x, 0, 300}];
```



```
pltq = Plot[q[800, 360, x, 0], {x, 0, 300}, PlotPoints -> 200];
```



Solution; See Quang Paper

code notation → Quang notation

$x \rightarrow n$

$Q[y=x,x] \rightarrow Q_n$

$Q[y=x+1,x] \rightarrow Q_n^+$

$Q[y=x-1,x] \rightarrow Q_n^-$

$PP \rightarrow \vec{P}$ vector

$PPinit \rightarrow \vec{P}(0)$ vector

mQ = matrix of Q

mQEV eigen values of Q matrix

mQEFun eigenfunctiona od Q matrix

maxInP munber of terms to calculate P_n

maxInP munber of terms to calculate \vec{P}_n

minInPP = 0 to include all lower terms

One Peak

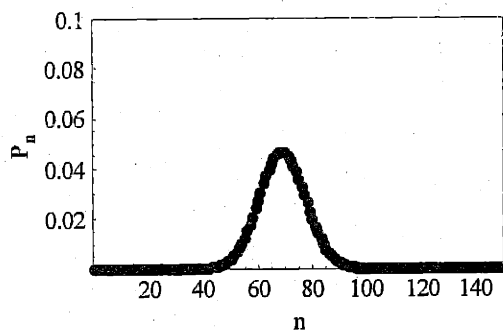
```
NumberOfatom = 19;  
velocity = 367;
```

```
maxInP = 150;  
maxInPP = 150;  
minInPP = 0;
```

```
x = .;  
Q[x_, y_] := Which[y == x + 1, 2 *  $\pi$  * rc (nb + 1) (x + 1), y == x,  
2 *  $\pi$  * rc (- x  $\beta$  [x + 1, velocity, NumberOfatom, 0] (x + 1) - (nb + 1) (x) - nb (x + 1)),  
y == x - 1,  
2 *  $\pi$  * rc (x  $\beta$  [x, velocity, NumberOfatom, 0] - (x) + nb * (x)), (y < x - 1) || (y > x + 1), 0];
```

```
i = .;  
Timing[1stPn = Table[p[i, maxInP, velocity, NumberOfatom, 0], {i, minInPP, maxInPP + 1}];]  
1st2 = Table[{minInPP + i - 1, 1stPn[[i]]}, {i, 1, Length[1stPn]}];  
pltPn = ListPlot[1st2, PlotRange -> {{minInPP, maxInPP}, {0, .1}},  
PlotStyle -> PointSize[.03], Frame -> True, FrameLabel -> {n, Pn},  
FrameTicks -> {Automatic, Automatic, {}, {}}];
```

{2.09 Second, Null}




```

MatrixForm[mQ = N[Array[Q, {maxInPP - (minInPP - 1), maxInPP - (minInPP - 1), minInPP}]];

mQEV = Eigenvalues[mQ];
MatrixForm[mQEFun = Transpose[Eigenvectors[mQ]]];
MatrixForm[PPinit = Table[(x + 1) * lstPn[[x + 1 - (minInPP - 1)]], {x, minInPP, maxInPP}]];
coefficient = Inverse[mQEFun].PPinit;
PP[t_] := mQEFun.(Exp[mQEV * t] * coefficient);
lstnumber = Table[minInPP + i - 1, {i, 1, Length[mQEV]}];
g2[t_] := 
$$\frac{\text{lstnumber} \cdot \text{PP}[t]}{n[\text{maxInP}, \text{velocity}, \text{NumberOfatom}, 0]^2};$$

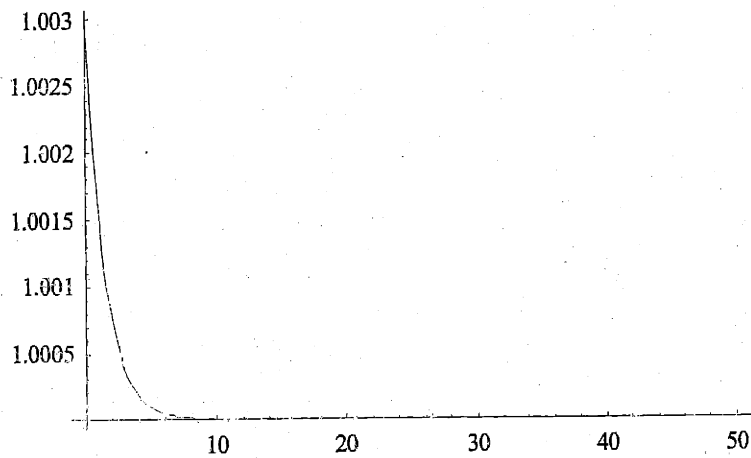

```

Tc vs N

```

pltfit = Plot[g2[10^(-6) t], {t, 0, 50}, PlotRange -> All, PlotStyle -> Thickness[.004]]

```



- Graphics -

```

lstfit = Table[{t, g2[10^(-6) t]}, {t, 0, 20, .05}];
lstpar = BestFitParameters /. NonlinearRegress[lstfit, a Exp[-t/b] + d, {t},
  {{a, g2[0] - 1}, {b, 1}, {d, 1}}];

```

```

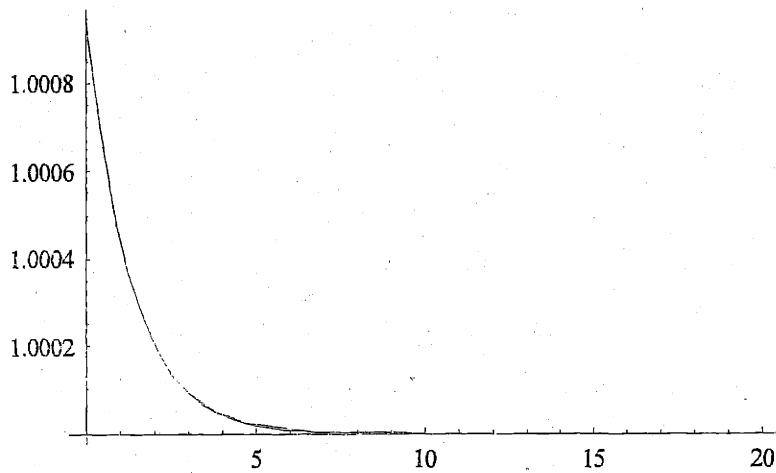
aa = a /. lstpar; bb = b /. lstpar; cc = c /. lstpar; dd = d /. lstpar;
Print["g2[0] = "<> ToString[g2[0]]]
Print["Tc = "<> ToString[bb] <> " microsec"]
Print["n = "<> ToString[n[maxInP, velocity, NumberOfatom, 0]]]
ff[t_] := aa Exp[-t/bb] + dd;
pltfit = Plot[{ff[t], g2[10^(-6) t]}, {t, 0, 20}, PlotRange -> All,
  PlotStyle -> Thickness[.004]]

```

g2[0] = 1.00094

Tc = 1.30492 microsec

n = 68.9087



- Graphics -

Appendix

B Controlling and data collecting program

The following is a list of a C program written for Windows 95 operating system to control the experiment and to collect the $g^{(2)}(\tau)$ data.

```
#include <windows.h>
#include "resource.h"
#include <commdlg.h>
#include <stdlib.h>
#include <math.h>

#define EDITED 1

#define FRAME_X0 40.
#define FRAME_Y0 60.
#define FRAME_WIDTH 720.
#define FRAME_HEIGHT 450
#define UNTITLED TEXT("(untitled)")
#define MAX_RANGE 256*256-1 //256*256-1
#define MAX_STOP_PULSES 800

/*****
// Functions *****/

LRESULT CALLBACK WndProc (HWND, UINT, WPARAM,LPARAM);
BOOL CALLBACK AboutDlgProc (HWND, UINT, WPARAM, LPARAM) ;

// function read status data. parameter is number of data to read
unsigned _int8 iRead_status(int) ;

// function to read FIFO. parameter is number of data to read
void iRead_FIFO(int) ;

// function write a byte to control experiment
void Write_data(_int8) ;

// function to draw on the screen
void DrawDataFixed(HWND hwnd);
void DrawDataChanged(HWND hwnd);

// function for initilaize file
```

```

void g2FileInitialize (HWND);

// function for save dialog box
BOOL g2FileSaveDlg(HWND, PTSTR, PTSTR);

// function to write g2 data to a file
BOOL g2FileWrite(PTSTR);

// initialize data in the g2 dialoge box
void initialize_dialog_variables(void);

// initialize data not in the dialoge box
// this is used when ok button is preesed in the dialog box
// to initialize data that may depends on the dialog box
void initialize_other_variables(void);
//*****
// global variables *****

struct g2_data_file
{
    SYSTEMTIME localTime;

    int    iLock_time;           // in unit of 2Byte read time ~ 2 microsec
    int    iUnlock_time;        // in unit of 2Byte read time ~ 2 microsec
    int    iBetween_time;       // in unit of 2Byte read time ~ 2 microsec
    int    iCollection_time_sec; // in sec
    int    iMTAC_range;         //in 5.2 microsec
// when first bit of second counter is used to stop counter
//iMTAC_range is 1 this corresponds to 260* 20 nsec

    float fNozzel_temp;
    float fCenter_temp;
    float fBack_temp;
    float fPressure;

    int iTi_laser_power;
    float fPump_OD;
    float fPump_position;
    float fA_beam_height;

    float fVel_Sel_pump_power;
    float fVel_Sel_pump_width;
    float fVel_Sel_repump_power;
    float fVel_Sel_AOM_110_volt;
    float fVel_Sel_AOM_200_volt;

    float fPMT_B_count_time;
    float fPMT_B_count_range;
    float fPMT_B_volt;

    float fPMT_S_B_count time;
    float fPMT_S_B_count_range;
    float fPMT_S_B_volt;

    float fAPD_B_count_time;
    float fAPD_B_count_range;

```

```

float fAPD_B_volt;

float fAPD_S_B_count_time;
float fAPD_S_B_count_range;
float fAPD_S_B_volt;

float fPMT_high_voltage;
int iPMT_preampl;
float fPMT_disc_level;
float fPMT_CFD_level;
float fPMT_CFD_width;

float fAPD_high_voltage;
float fAPD_CFD_level;
float fAPD_CFD_width;

float fLock_circuit_x_gain;
float fLock_circuit_y_gain;

int iLock_AOM_configuration;

float fLock_AOM_voltage;
float fB_field_current;

ULONG ulCount_in_Bin[MAX_RANGE];

};
typedef struct g2_data_file structData;
typedef structData * pstructData;

structData file_data;
pstructData pfile_data;

ULONG ulOld_count_in_Bin[MAX_RANGE]; // used to erase old bin count in the screen
int bin_temp[MAX_STOP_PULSES]; // used to eliminate data which are not between
// two end of range pulses
int iBin_temp_index=0;
int iEnd_range_bin; // corresponds to pulse counter sends to stop jk

ULONG ulStart_time_msec; //in milisec
ULONG ulElapsed_time_msec; //in milisec
ULONG ulElapsed_time_msec_temp; //in milisec
ULONG ulElapsed_before_stop_bit_on; //in milisec
ULONG ulCollection_time_msec; //in milisec

BOOL bStop_bit = 0;
BOOL bClock_on = 0;
BOOL bFirst_data_flag; // used to elminate first pulses before end range flage

int reference_bin; // bin used to normalized data
int iNumber_of_bins;

_int16 iReadStatusAddress=924; //to read other data
_int16 iReadFIFOWriteAddress=921; //to read FIFO data or Write data
static int cxClient,cyClient;

```

```

unsigned_int8 a_up=2;           // a means aom after the cavity
unsigned_int8 b_up=1;           // b means aom before the cavity
unsigned_int8 c_up=4;           // c means cavity intgrator
unsigned_int8 wen_up=64;        // wen means write enable for FIFO
unsigned_int8 reset_up=128;     // reset means reset FIFO; reset when this bit is down
unsigned_int8 write_byte=0;     // byte written to the output
unsigned_int8 status_byte;      // byte written to the output
static OPENFILENAME ofn;        // used to save data

TCHAR szAppName[]=TEXT("g2");

//*****
int WINAPI WinMain (HINSTANCE hInstance, HINSTANCE hPrevInstance, PSTR szCmdLine, int iCmdShow)
{
    HWND          hwnd;
    MSG           msg;
    WNDCLASS      wndclass;

    wndclass.style          = CS_HREDRAW | CS_VREDRAW;
    wndclass.lpfWndProc     = WndProc;
    wndclass.cbClsExtra     = 0;
    wndclass.cbWndExtra     = 0;
    wndclass.hInstance     = hInstance;
    wndclass.hIcon          = LoadIcon(NULL,IDI_APPLICATION);
    wndclass.hCursor       = LoadCursor(NULL,IDC_ARROW);
    wndclass.hbrBackground = (HBRUSH) GetStockObject (WHITE_BRUSH) ;
    wndclass.lpszMenuName  = szAppName;
    wndclass.lpszClassName = szAppName;

    if (!RegisterClass (&wndclass))
    {
        MessageBox(NULL,TEXT("wrong windows version"), szAppName,MB_ICONERROR);
        return 0;
    }

    hwnd = CreateWindow (
        szAppName,
        TEXT("g2 version 1"),
        WS_OVERLAPPEDWINDOW,
        0, // CW_USEDEFAULT, // initial x position
        0, // CW_USEDEFAULT, // initial y position
        790, // CW_USEDEFAULT, // initial x size
        580, // CW_USEDEFAULT, // initial y size
        NULL,
        NULL,
        hInstance,
        NULL);

    ShowWindow (hwnd, iCmdShow);
    UpdateWindow (hwnd);

    while(TRUE)
    { //1
        if(PeekMessage (&msg,NULL,0,0,PM_REMOVE))
        { //2

```

```

        if(msg.message == WM_QUIT)
            break;
        TranslateMessage (&msg);
        DispatchMessage (&msg);

    } // 2
    else
    { // 3
        // the two AOM are alternating
        if(file_data.iLock_AOM_configuration==0)
            { // 4
                status_byte=iRead_status(1) & 8;

                // ckeck stop bit D3
                if(status_byte == 0)
                    bStop_bit = 0;
                else
                    bStop_bit = 1;

                if((bStop_bit == 1) && (ulCollection_time_msec > ulElapsed_time_msec))
                { // 5
                    if(bClock_on == 0 )
                    { // 6
                        bClock_on = 1;
                        ulStart_time_msec = GetTickCount();
                        ulElapsed_time_msec = 0;
                        ulElapsed_time_msec_temp = 0;
                    } // 6
                    bFirst_data_flag = 1;

                    // reset FIFO
                    write_byte = c_up + a_up + wen_up;
                    Write_data(write_byte);

                    // iT5
                    write_byte = c_up + a_up + reset_up;
                    Write_data(write_byte);
                    iRead_status(file_data.iUnlock_time); // this is just to take time

                    // stop writing to FIFO
                    write_byte = c_up + a_up + wen_up + reset_up;
                    Write_data(write_byte);

                    // iT1
                    write_byte = c_up + a_up + wen_up + reset_up;
                    Write_data(write_byte);
                    iRead_FIFO(file_data.iBetween_time);

                    // iT2
                    write_byte = c_up + wen_up + reset_up;
                    Write_data(write_byte);
                    iRead_FIFO(file_data.iBetween_time);

                    // iT3
                    write_byte = c_up + b_up + wen_up + reset_up;
                    Write_data(write_byte);
                    iRead_FIFO(file_data.iBetween_time);
                }
            }
        }
    }
}

```

```

// iT4
write_byte = b_up + wen_up + reset_up;
Write_data(write_byte);
iRead_FIFO(file_data.iLock_time);

// iT3
write_byte = c_up + b_up + wen_up + reset_up;
Write_data(write_byte);
iRead_FIFO(file_data.iBetween_time);

// iT2
write_byte = c_up + wen_up + reset_up;
Write_data(write_byte);
iRead_FIFO(file_data.iBetween_time);

// iT1
write_byte = c_up + a_up + wen_up + reset_up;
Write_data(write_byte);
iRead_FIFO(file_data.iBetween_time);

ulElapsed_time_msec = GetTickCount() - ulStart_time_msec + ulElapsed_before_stop_bit_on;

// draw every sec
if (ulElapsed_time_msec - ulElapsed_time_msec_temp > 1000)
{ // 7
    ulElapsed_time_msec_temp = ulElapsed_time_msec;
    DrawDataChanged(hwnd);
} // 7

} // 5
else
{ // 8
    if (bClock_on == 1)
    { // 9
        bClock_on = 0;
        ulElapsed_before_stop_bit_on = ulElapsed_time_msec;
    } // 9

// iT5
write_byte = c_up + a_up + reset_up;
Write_data(write_byte);
iRead_status(file_data.iUnlock_time); // this is just to take time

// iT1
write_byte = c_up + a_up + wen_up + reset_up;
Write_data(write_byte);
iRead_status(file_data.iBetween_time);

// iT2
write_byte = c_up + wen_up + reset_up;
Write_data(write_byte);
iRead_status(file_data.iBetween_time);

// iT3
write_byte = c_up + b_up + wen_up + reset_up;
Write_data(write_byte);

```



```

        iRead_status(file_data.iBetween_time);

        // iT4
        write_byte = b_up + wen_up + reset_up;
        Write_data(write_byte);
        iRead_status(file_data.iLock_time);

        // iT3
        write_byte = c_up + b_up + wen_up + reset_up;
        Write_data(write_byte);
        iRead_status(file_data.iBetween_time);

        // iT2
        write_byte = c_up + wen_up + reset_up;
        Write_data(write_byte);
        iRead_status(file_data.iBetween_time);

        // iT1
        write_byte = c_up + a_up + wen_up + reset_up;
        Write_data(write_byte);
        iRead_status(file_data.iBetween_time);
    } // 8 -
} // 4

    // AOM before on and AOM after is off nd cavity is locked
if(file_data.iLock_AOM_configuration==1)
    {
        write_byte = b_up + wen_up + reset_up;
        Write_data(write_byte);
    }

// AOM before off and AOM after is on
if(file_data.iLock_AOM_configuration==2)
    {
        write_byte = a_up + wen_up + reset_up;
        Write_data(write_byte);
    }

// both AOMs on
if(file_data.iLock_AOM_configuration==3)
    {
        write_byte = a_up + b_up + wen_up + reset_up;
        Write_data(write_byte);
    }
} // 3 else of if(PeekMessage ..
} // 1 while(TRUE)
return msg.wParam;
}
/*****
void OkMessage (HWND hwnd, TCHAR * szMessage, TCHAR * szTitleName)
{
    TCHAR szBuffer[64 + MAX_PATH];
    wsprintf (szBuffer, szMessage, szTitleName[0] ? szTitleName : UNTITLED);
    MessageBox (hwnd, szBuffer, szAppName, MB_OK | MB_ICONEXCLAMATION);
}

```

```

/*****
void DoCaption (HWND hwnd, TCHAR * szTitleName)
{
    TCHAR szCaption[64 + MAX_PATH];
    wsprintf (szCaption, TEXT ("%s - %s"), szAppName, szTitleName[0] ? szTitleName : UNTITLED);
    SetWindowText (hwnd, szCaption);
}
/*****
short AskAboutSave (HWND hwnd, TCHAR * szTitleName)
{
    TCHAR szBuffer[64 + MAX_PATH];
    int    iReturn;

    wsprintf (szBuffer, TEXT ("Save current changes in %s?"),
        szTitleName[0] ? szTitleName : UNTITLED);

    iReturn = MessageBox (hwnd, szBuffer, szAppName, MB_YESNOCANCEL | MB_ICONQUESTION);

    if (iReturn == IDYES)
        if (!SendMessage (hwnd, WM_COMMAND, IDM_FILE_SAVE, 0))
            iReturn = IDCANCEL;
    return iReturn;
}
/*****
void g2FileInitialize (HWND hwnd)
{
    static TCHAR szFilter[] = TEXT ("Text Files (*.TXT)\0*.txt\0") \
        TEXT ("ASCII Files (*.ASC)\0*.asc\0") \ TEXT ("All Files (*.*)\0*. *\0\0");

    ofn.lStructSize = sizeof (OPENFILENAME);
    ofn.hwndOwner = hwnd;
    ofn.hInstance = NULL;
    ofn.lpstrFilter = szFilter;
    ofn.lpstrCustomFilter = NULL;
    ofn.nMaxCustFilter = 0;
    ofn.nFilterIndex = 0;
    ofn.lpstrFile = NULL; // Set in Open and Close functions
    ofn.nMaxFile = MAX_PATH;
    ofn.lpstrFileTitle = NULL; // Set in Open and Close functions
    ofn.nMaxFileTitle = MAX_PATH;
    ofn.lpstrInitialDir = NULL;
    ofn.lpstrTitle = NULL;
    ofn.Flags = 0; // Set in Open and Close functions
    ofn.nFileOffset = 0;
    ofn.nFileExtension = 0;
    ofn.lpstrDefExt = TEXT ("txt");
    ofn.lCustData = 0L;
    ofn.lpfnHook = NULL;
    ofn.lpTemplateName = NULL;
}
/*****
BOOL g2FileSaveDlg (HWND hwnd, PTSTR pstrFileName, PTSTR pstrTitleName)
{
    ofn.hwndOwner = hwnd;
    ofn.lpstrFile = pstrFileName;
    ofn.lpstrFileTitle = pstrTitleName;
}

```

```

    ofn.Flags      = OFN_OVERWRITEPROMPT ;
    return GetSaveFileName (&ofn) ;
}
//*****
BOOL g2FileWrite (PTSTR pstrFileName)
{
    DWORD      dwBytesWritten ;
    HANDLE     hFile ;
    int        iLength;
    PTSTR      pstrBuffer ;

    // Open the file, creating it if necessary
    if (INVALID_HANDLE_VALUE ==
(hFile = CreateFile (pstrFileName, GENERIC_WRITE, 0, NULL, CREATE_ALWAYS, 0, NULL)))
        return FALSE ;

    // allocatememory for data
    pfile_data = (pstructData)malloc ( sizeof (structData)) ;
    if (!pfile_data)
    {
        CloseHandle (hFile) ;
        return FALSE ;
    }

    *pfile_data=file_data;

    WriteFile (hFile, pfile_data,sizeof (structData) , &dwBytesWritten, NULL) ;

    if ((sizeof (structData)) != (int) dwBytesWritten)
    {
        CloseHandle (hFile) ;
        free (pfile_data) ;
        return FALSE ;
    }

    CloseHandle (hFile) ;
    free (pfile_data) ;

    return TRUE ;
}
//*****
LRESULT CALLBACK WndProc (HWND hwnd, UINT message, WPARAM wParam,LPARAM lParam)
{
    static HINSTANCE hInst ;
    static TCHAR    szFileName[MAX_PATH], szTitleName[MAX_PATH] ;
    HDC             hdc;
    PAINTSTRUCT     ps;
    HMENU           hMenu;
    int             i,j,k;                // index to initilaize old_data

    switch (message)
    {
    case WM_CREATE:
        hInst = ((LPCREATESTRUCT) lParam) -> hInstance ;
        g2FileInitialize (hwnd) ;
        initialize_dialog_variables();

```

```
szFileName[0] = '\0';  
szTitleName[0] = '\0';
```

```
SendMessage(hwnd, WM_COMMAND, IDM_FILE_EXPPAR, 0);
```

```
return 0;
```

```
case WM_SIZE:
```

```
cxClient = LOWORD(IParam);  
cyClient = HIWORD(IParam);  
return 0;
```

```
case WM_COMMAND:
```

```
hMenu = GetMenu(hwnd);  
switch (LOWORD(wParam))  
{
```

```
    // Messages from File menu
```

```
case IDM_FILE_SAVE:
```

```
    if (szFileName[0])
```

```
    {  
        if (g2FileWrite(szFileName))
```

```
        {  
            return 1;
```

```
        }  
        else
```

```
        {  
            OkMessage (hwnd, TEXT ("Could not write file %s"), szTitleName);  
            return 0;
```

```
        }  
    }
```

```
if (g2FileSaveDlg (hwnd, szFileName, szTitleName))
```

```
{  
    DoCaption (hwnd, szTitleName);
```

```
    if (g2FileWrite (szFileName))
```

```
    {  
        return 1;
```

```
    }  
    else
```

```
    {  
        OkMessage (hwnd, TEXT ("Could not write file %s"), szTitleName);  
        return 0;
```

```
    }  
}
```

```
return 0;
```

```
case IDM_FILE_EXPPAR :
```

```
    DialogBox (hInst, TEXT ("g2"), hwnd, AboutDlgProc);  
    return 0;
```

```
case IDM_FILE_QUIT:
```

```
    SendMessage (hwnd, WM_CLOSE, 0, 0);  
    return 0;
```

```

    }

    break;

    case WM_CLOSE:
        if (IDCANCEL != AskAboutSave (hwnd, szTitleName))
            DestroyWindow (hwnd);
        return 0;

    case WM_PAINT:
        hdc = BeginPaint (hwnd, &ps);
        EndPaint (hwnd,&ps);
        DrawDataFixed(hwnd);
        DrawDataChanged(hwnd);
        return 0;

    case WM_DESTROY:
        PostQuitMessage (0);
        return 0;
    }
    return DefWindowProc(hwnd,message,wParam,lParam);
}
}
/*****
BOOL CALLBACK AboutDlgProc (HWND hDlg, UINT message, WPARAM wParam, LPARAM lParam)
{
    HWND hwndCombo;           // for combo box
    TCHAR CounterRange[ ]="321"; // for combo box
    TCHAR Buffer[10];          // to convert from float to text

    switch (message)
    {
    case WM_INITDIALOG:
        // TIME
        SetDlgItemInt(hDlg,IDC_EDIT_LOC_TIM,file_data.iLock_time,FALSE);
        SetDlgItemInt(hDlg,IDC_EDIT_UNL_TIM,file_data.iUnlock_time,FALSE);
        SetDlgItemInt(hDlg,IDC_EDIT_BET_TIM,file_data.iBetween_time,FALSE);
        SetDlgItemInt(hDlg,IDC_EDIT_COL_TIM,file_data.iCollection_time_sec,FALSE);
        SetDlgItemInt(hDlg,IDC_EDIT_TAC_RAN,file_data.iMTAC_range,FALSE);

        // OVEN
        _gcvt((file_data.fNozzel_temp),5, Buffer);
        SetDlgItemText(hDlg,IDC_EDIT_NOZ_TEM, Buffer);
        _gcvt((file_data.fCenter_temp),5, Buffer);
        SetDlgItemText(hDlg,IDC_EDIT_CEN_TEM, Buffer);
        _gcvt((file_data.fBack_temp),5, Buffer);
        SetDlgItemText(hDlg,IDC_EDIT_BAC_TEM, Buffer);
        _gcvt((file_data.fPressure),5, Buffer);
        SetDlgItemText(hDlg,IDC_EDIT_PRESSURE, Buffer);

        // PUMP BEAM
        SetDlgItemInt(hDlg,IDC_EDIT_TI_POW,file_data.iTi_laser_power,FALSE);
        _gcvt((file_data.fPump_OD),5, Buffer);
        SetDlgItemText(hDlg,IDC_EDIT_PUM_OD, Buffer);
        _gcvt((file_data.fPump_position),5, Buffer);
        SetDlgItemText(hDlg,IDC_EDIT_PUM_POS, Buffer);
        _gcvt((file_data.fA_beam_height),5, Buffer);

```

```

SetDlgItemText(hDlg, IDC_EDIT_A_BEI_HEI, Buffer);

// Velocity Selection
_gcvt((file_data.fVel_Sel_pump_power),5, Buffer);
SetDlgItemText(hDlg, IDC_EDIT_PUM_POW, Buffer);
_gcvt((file_data.fVel_Sel_pump_width),5, Buffer);
SetDlgItemText(hDlg, IDC_EDIT_PUM_WID, Buffer);
_gcvt((file_data.fVel_Sel_repump_power),5, Buffer);
SetDlgItemText(hDlg, IDC_EDIT_REP_POW, Buffer);
_gcvt((file_data.fVel_Sel_AOM_110_volt),5, Buffer);
SetDlgItemText(hDlg, IDC_EDIT_110_AOM_V, Buffer);
_gcvt((file_data.fVel_Sel_AOM_200_volt),5, Buffer);
SetDlgItemText(hDlg, IDC_EDIT_200_AOM_V, Buffer);

// PMT Background
_gcvt((file_data.fPMT_B_count_time),5, Buffer);
SetDlgItemText(hDlg, IDC_EDIT_PMT_B_COU_TIM, Buffer);

// initialize Combo Box PMT Background
hwndCombo = GetDlgItem(hDlg, IDC_COMBO_PMT_B);
SendMessage(hwndCombo, CB_ADDSTRING, 0, "321");
SendMessage(hwndCombo, CB_ADDSTRING, 0, "432");
SendMessage(hwndCombo, CB_ADDSTRING, 0, "543");
SendMessage(hwndCombo, CB_SETCURSEL, 0, 0);
_gcvt((file_data.fPMT_B_volt),5, Buffer);
SetDlgItemText(hDlg, IDC_EDIT_PMT_B_COU_V, Buffer);

//PMT Signal and Background
_gcvt((file_data.fPMT_S_B_count_time),5, Buffer);
SetDlgItemText(hDlg, IDC_EDIT_PMT_S_B_COU_TIM, Buffer);

// initialize Combo Box PMT Signal and Background
hwndCombo = GetDlgItem(hDlg, IDC_COMBO_PMT_S_B);
SendMessage(hwndCombo, CB_ADDSTRING, 0, "321");
SendMessage(hwndCombo, CB_ADDSTRING, 0, "432");
SendMessage(hwndCombo, CB_ADDSTRING, 0, "543");
SendMessage(hwndCombo, CB_SETCURSEL, 0, 0);
_gcvt((file_data.fPMT_S_B_volt),5, Buffer);
SetDlgItemText(hDlg, IDC_EDIT_PMT_S_B_COU_V, Buffer);

//APD Background
_gcvt((file_data.fAPD_B_count_time),5, Buffer);
SetDlgItemText(hDlg, IDC_EDIT_APD_B_COU_TIM, Buffer);

// initialize Combo Box PMT Background
hwndCombo = GetDlgItem(hDlg, IDC_COMBO_APD_B);
SendMessage(hwndCombo, CB_ADDSTRING, 0, "321");
SendMessage(hwndCombo, CB_ADDSTRING, 0, "432");
SendMessage(hwndCombo, CB_ADDSTRING, 0, "543");
SendMessage(hwndCombo, CB_SETCURSEL, 0, 0);
_gcvt((file_data.fAPD_B_volt),5, Buffer);
SetDlgItemText(hDlg, IDC_EDIT_APD_B_COU_V, Buffer);

//APD Signal and Background
_gcvt((file_data.fAPD_S_B_count_time),5, Buffer);
SetDlgItemText(hDlg, IDC_EDIT_APD_S_B_COU_TIM, Buffer);

```

```

// initialize Combo Box APD Signal and Background
hwndCombo = GetDlgItem(hDlg, IDC_COMBO_APD_S_B);
SendMessage (hwndCombo, CB_ADDSTRING, 0, "321");
SendMessage (hwndCombo, CB_ADDSTRING, 0, "432");
SendMessage (hwndCombo, CB_ADDSTRING, 0, "543");
SendMessage (hwndCombo, CB_SETCURSEL, 0, 0);
_gcvt((file_data.fAPD_S_B_volt), 5, Buffer);
SetDlgItemText(hDlg, IDC_EDIT_APD_S_B_COU_V, Buffer);

// PMT
_gcvt((file_data.fPMT_high_voltage), 5, Buffer);
SetDlgItemText(hDlg, IDC_EDIT_PMT_HIG_V, Buffer);
SetDlgItemInt(hDlg, IDC_EDIT_PMT_PRE_AMP, file_data.iPMT_preampl, FALSE);
_gcvt((file_data.fPMT_disc_level), 5, Buffer);
SetDlgItemText(hDlg, IDC_EDIT_PMT_DIS_LEV, Buffer);
_gcvt((file_data.fPMT_CFD_level), 5, Buffer);
SetDlgItemText(hDlg, IDC_EDIT_PMT_CFD_LEV, Buffer);
_gcvt((file_data.fPMT_CFD_width), 5, Buffer);
SetDlgItemText(hDlg, IDC_EDIT_PMT_CFD_WID, Buffer);

// APD
_gcvt((file_data.fAPD_high_voltage), 5, Buffer);
SetDlgItemText(hDlg, IDC_EDIT_APD_HIG_V, Buffer);
_gcvt((file_data.fAPD_CFD_level), 5, Buffer);
SetDlgItemText(hDlg, IDC_EDIT_APD_CFD_LEV, Buffer);
_gcvt((file_data.fAPD_CFD_width), 5, Buffer);
SetDlgItemText(hDlg, IDC_EDIT_APD_CFD_WID, Buffer);

// Lock Circuit
_gcvt((file_data.fLock_circuit_x_gain), 5, Buffer);
SetDlgItemText(hDlg, IDC_EDIT_LOC_X_GAI, Buffer);
_gcvt((file_data.fLock_circuit_y_gain), 5, Buffer);
SetDlgItemText(hDlg, IDC_EDIT_LOC_Y_GAI, Buffer);

// Lock Voltage
_gcvt((file_data.fLock_AOM_voltage), 5, Buffer);
SetDlgItemText(hDlg, IDC_EDIT_LOC_AOM_V, Buffer);

// B field
_gcvt((file_data.fB_field_current), 5, Buffer);
SetDlgItemText(hDlg, IDC_EDIT_B_CUR, Buffer);

// locking AOM configuration
hwndCombo = GetDlgItem(hDlg, IDC_COMBO_LOC_AOM_CON);
SendMessage (hwndCombo, CB_ADDSTRING, 0, "Alternating");
SendMessage (hwndCombo, CB_ADDSTRING, 0, "Before ON - after OFF");
SendMessage (hwndCombo, CB_ADDSTRING, 0, "Before OFF - after ON");
SendMessage (hwndCombo, CB_ADDSTRING, 0, "Both ON");
SendMessage (hwndCombo, CB_SETCURSEL, 0, 0);

return TRUE ;

case WM_COMMAND:
    switch (LOWORD (wParam))
    {

```

```

// TIME
case IDC_EDIT_LOC_TIM:
    file_data.iLock_time = GetDlgItemInt(hDlg, IDC_EDIT_LOC_TIM, NULL, FALSE);
    return TRUE;

case IDC_EDIT_UNL_TIM:
    file_data.iUnlock_time = GetDlgItemInt(hDlg, IDC_EDIT_UNL_TIM, NULL, FALSE);
    return TRUE;

case IDC_EDIT_BET_TIM:
    file_data.iBetween_time = GetDlgItemInt(hDlg, IDC_EDIT_BET_TIM, NULL, FALSE);
    return TRUE;

case IDC_EDIT_COL_TIM:
    file_data.iCollection_time_sec = GetDlgItemInt(hDlg, IDC_EDIT_COL_TIM, NULL, FALSE);
    ulCollection_time_msec = 1000 * file_data.iCollection_time_sec;
    return TRUE;

case IDC_EDIT_TAC_RAN:
    file_data.iMTAC_range = GetDlgItemInt(hDlg, IDC_EDIT_TAC_RAN, NULL, FALSE);
    return TRUE;

// OVEN

case IDC_EDIT_NOZ_TEM:
    GetDlgItemText(hDlg, IDC_EDIT_NOZ_TEM, Buffer, 10);
    file_data.fNozzel_temp = atof(Buffer);
    return TRUE;

case IDC_EDIT_CEN_TEM:
    GetDlgItemText(hDlg, IDC_EDIT_CEN_TEM, Buffer, 10);
    file_data.fCenter_temp = atof(Buffer);
    return TRUE;

case IDC_EDIT_BAC_TEM:
    GetDlgItemText(hDlg, IDC_EDIT_BAC_TEM, Buffer, 10);
    file_data.fBack_temp = atof(Buffer);
    return TRUE;

case IDC_EDIT_PRESSURE:
    GetDlgItemText(hDlg, IDC_EDIT_PRESSURE, Buffer, 10);
    file_data.fPressure = atof(Buffer);
    return TRUE;
    // Pi pulse

case IDC_EDIT_TI_POW:
    file_data.iTi_laser_power = GetDlgItemInt(hDlg, IDC_EDIT_TI_POW, NULL, FALSE);
    return TRUE;

case IDC_EDIT_PUM_OD:
    GetDlgItemText(hDlg, IDC_EDIT_PUM_OD, Buffer, 10);
    file_data.fPump_OD = atof(Buffer);
    return TRUE;

case IDC_EDIT_PUM_POS:
    GetDlgItemText(hDlg, IDC_EDIT_PUM_POS, Buffer, 10);

```



```

        file_data.fPump_position = atof(Buffer);
        return TRUE;

    case IDC_EDIT_A_BEA_HEI:
        GetDlgItemText(hDlg, IDC_EDIT_A_BEA_HEI, Buffer, 10);
        file_data.fA_beam_height = atof(Buffer);
        return TRUE;

// Velocity Selection
    case IDC_EDIT_PUM_POW:
        GetDlgItemText(hDlg, IDC_EDIT_PUM_POW, Buffer, 10);
        file_data.fVel_Sel_pump_power = atof(Buffer);
        return TRUE;

    case IDC_EDIT_PUM_WID:
        GetDlgItemText(hDlg, IDC_EDIT_PUM_WID, Buffer, 10);
        file_data.fVel_Sel_pump_width = atof(Buffer);
        return TRUE;

    case IDC_EDIT_REP_POW:
        GetDlgItemText(hDlg, IDC_EDIT_REP_POW, Buffer, 10);
        file_data.fVel_Sel_repump_power = atof(Buffer);
        return TRUE;

    case IDC_EDIT_110_AOM_V:
        GetDlgItemText(hDlg, IDC_EDIT_110_AOM_V, Buffer, 10);
        file_data.fVel_Sel_AOM_110_volt = atof(Buffer);
        return TRUE;

    case IDC_EDIT_200_AOM_V:
        GetDlgItemText(hDlg, IDC_EDIT_200_AOM_V, Buffer, 10);
        file_data.fVel_Sel_AOM_200_volt = atof(Buffer);
        return TRUE;

// PMT Background
    case IDC_EDIT_PMT_B_COU_TIM:
        GetDlgItemText(hDlg, IDC_EDIT_PMT_B_COU_TIM, Buffer, 10);
        file_data.fPMT_B_count_time = atof(Buffer);
        return TRUE;

    case IDC_COMBO_PMT_B:
        hwndCombo = GetDlgItem(hDlg, IDC_COMBO_PMT_B);
        file_data.fPMT_B_count_range = SendMessage(hwndCombo, CB_GETCURSEL, 0, 0);
        return TRUE;

    case IDC_EDIT_PMT_B_COU_V:
        GetDlgItemText(hDlg, IDC_EDIT_PMT_B_COU_V, Buffer, 10);
        file_data.fPMT_B_volt = atof(Buffer);
        return TRUE;

//PMT Signal and Background
    case IDC_EDIT_PMT_S_B_COU_TIM:
        GetDlgItemText(hDlg, IDC_EDIT_PMT_S_B_COU_TIM, Buffer, 10);
        file_data.fPMT_S_B_count_time = atof(Buffer);
        return TRUE;

```

```

        case IDC_COMBO_PMT_S_B:
            hwndCombo = GetDlgItem(hDlg, IDC_COMBO_PMT_S_B);
            file_data.fPMT_S_B_count_range = SendMessage(hwndCombo, CB_GETCURSEL, 0, 0);
            return TRUE;

        case IDC_EDIT_PMT_S_B_COU_V:
            GetDlgItemText(hDlg, IDC_EDIT_PMT_S_B_COU_V, Buffer, 10);
            file_data.fPMT_S_B_volt = atof(Buffer);
            return TRUE;

//APD Background
        case IDC_EDIT_APD_B_COU_TIM:
            GetDlgItemText(hDlg, IDC_EDIT_APD_B_COU_TIM, Buffer, 10);
            file_data.fAPD_B_count_time = atof(Buffer);
            return TRUE;

        case IDC_COMBO_APD_B:
            hwndCombo = GetDlgItem(hDlg, IDC_COMBO_APD_B);
            file_data.fAPD_B_count_range = SendMessage(hwndCombo, CB_GETCURSEL, 0, 0);
            return TRUE;

        case IDC_EDIT_APD_B_COU_V:
            GetDlgItemText(hDlg, IDC_EDIT_APD_B_COU_V, Buffer, 10);
            file_data.fAPD_B_volt = atof(Buffer);
            return TRUE;

//APD Signal and Background
        case IDC_EDIT_APD_S_B_COU_TIM:
            GetDlgItemText(hDlg, IDC_EDIT_APD_S_B_COU_TIM, Buffer, 10);
            file_data.fAPD_S_B_count_time = atof(Buffer);
            return TRUE;

        case IDC_COMBO_APD_S_B:
            hwndCombo = GetDlgItem(hDlg, IDC_COMBO_APD_S_B);
            file_data.fAPD_S_B_count_range = SendMessage(hwndCombo, CB_GETCURSEL, 0, 0);
            return TRUE;

        case IDC_EDIT_APD_S_B_COU_V:
            GetDlgItemText(hDlg, IDC_EDIT_APD_S_B_COU_V, Buffer, 10);
            file_data.fAPD_S_B_volt = atof(Buffer);
            return TRUE;

//PMT
        case IDC_EDIT_PMT_HIG_V:
            GetDlgItemText(hDlg, IDC_EDIT_PMT_HIG_V, Buffer, 10);
            file_data.fPMT_high_voltage = atof(Buffer);
            return TRUE;

        case IDC_EDIT_PMT_PRE_AMP:
            file_data.iPMT_preamp1 = GetDlgItemInt(hDlg, IDC_EDIT_PMT_PRE_AMP, NULL, FALSE);
            return TRUE;

        case IDC_EDIT_PMT_DIS_LEV:
            GetDlgItemText(hDlg, IDC_EDIT_PMT_DIS_LEV, Buffer, 10);
            file_data.fPMT_disc_level = atof(Buffer);
            return TRUE;

```

```

case IDC_EDIT_PMT_CFD_LEV:
    GetDlgItemText(hDlg, IDC_EDIT_PMT_CFD_LEV, Buffer, 10);
    file_data.fPMT_CFD_level = atof(Buffer);
    return TRUE;

case IDC_EDIT_PMT_CFD_WID:
    GetDlgItemText(hDlg, IDC_EDIT_PMT_CFD_WID, Buffer, 10);
    file_data.fPMT_CFD_width = atof(Buffer);
    return TRUE;

// APD
case IDC_EDIT_APD_HIG_V:
    GetDlgItemText(hDlg, IDC_EDIT_APD_HIG_V, Buffer, 10);
    file_data.fAPD_high_voltage = atof(Buffer);
    return TRUE;

case IDC_EDIT_APD_CFD_LEV:
    GetDlgItemText(hDlg, IDC_EDIT_APD_CFD_LEV, Buffer, 10);
    file_data.fAPD_CFD_level = atof(Buffer);
    return TRUE;

case IDC_EDIT_APD_CFD_WID:
    GetDlgItemText(hDlg, IDC_EDIT_APD_CFD_WID, Buffer, 10);
    file_data.fAPD_CFD_width = atof(Buffer);
    return TRUE;

// Lock Circuit
case IDC_EDIT_LOC_X_GAI:
    GetDlgItemText(hDlg, IDC_EDIT_LOC_X_GAI, Buffer, 10);
    file_data.fLock_circuit_x_gain = atof(Buffer);
    return TRUE;

case IDC_EDIT_LOC_Y_GAI:
    GetDlgItemText(hDlg, IDC_EDIT_LOC_Y_GAI, Buffer, 10);
    file_data.fLock_circuit_y_gain = atof(Buffer);
    return TRUE;

// Lock Voltage
case IDC_EDIT_LOC_AOM_V:
    GetDlgItemText(hDlg, IDC_EDIT_LOC_AOM_V, Buffer, 10);
    file_data.fLock_AOM_voltage = atof(Buffer);
    return TRUE;

// B field
case IDC_EDIT_B_CUR:
    GetDlgItemText(hDlg, IDC_EDIT_B_CUR, Buffer, 10);
    file_data.fB_field_current = atof(Buffer);
    return TRUE;

// locking AOM configuration
case IDC_COMBO_LOC_AOM_CON:
    hwndCombo = GetDlgItem(hDlg, IDC_COMBO_LOC_AOM_CON);
    file_data.iLock_AOM_configuration = SendMessage(hwndCombo, CB_GETCURSEL, 0, 0);
    return TRUE;

```

```

        case IDOK:
            EndDialog (hDlg, 0);
            initialize_other_variables();
            return TRUE;
        }
    }
    break;
}
return FALSE;
}
}
//*****
void initialize_dialog_variables(void)
{
    file_data.iLock_time      = 100000;
    file_data.iUnlock_time   = 100000;
    file_data.iBetween_time  = 1000;
    file_data.iCollection_time_sec = 2000;
    file_data.iMTAC_range    = 4;

    file_data.fNozzel_temp   = 0.;
    file_data.fCenter_temp   = 0.;
    file_data.fBack_temp     = 0.;
    file_data.fPressure      = 0.1;

    file_data.iTi_laser_power = 380;
    file_data.fPump_OD        = 0.04;
    file_data.fPump_position  = 0;
    file_data.fA_beam_height = 0.;

    file_data.fVel_Sel_pump_power = 0;
    file_data.fVel_Sel_pump_width = 0;
    file_data.fVel_Sel_repump_power = 0;
    file_data.fVel_Sel_AOM_110_volt = 0;
    file_data.fVel_Sel_AOM_200_volt = 0;

    file_data.fPMT_B_count_time = 0.01;
    file_data.fPMT_B_count_range = 0;
    file_data.fPMT_B_volt = 0;

    file_data.fPMT_S_B_count_time = 0.01;
    file_data.fPMT_S_B_count_range = 0;
    file_data.fPMT_S_B_volt = 0;

    file_data.fAPD_B_count_time = 0.01;
    file_data.fAPD_B_count_range = 0;
    file_data.fAPD_B_volt = 0;

    file_data.fAPD_S_B_count_time = 0.01;
    file_data.fAPD_S_B_count_range = 0;
    file_data.fAPD_S_B_volt = 0;

    file_data.fPMT_high_voltage = 1800.;
    file_data.iPMT_preamp1 = 100;
    file_data.fPMT_disc_level = .110;
    file_data.fPMT_CFD_level = 2.5;
    file_data.fPMT_CFD_width = 18.;
}

```

```

file_data.fAPD_high_voltage      = 166;
file_data.fAPD_CFD_level        = 2.5;
file_data.fAPD_CFD_width        = 36;

file_data.fLock_circuit_x_gain   = 8;
file_data.fLock_circuit_y_gain   = 7;

// nomal =0; before on and after off = 1;
// before off and after on 2; both on 3;
file_data.iLock_AOM_configuration = 0;

file_data.fLock_AOM_voltage      = 8.2;
file_data.fB_field_current       = 4.2 ;
}
/*****
void initialize_other_variables(void)
{
    int i;

    GetLocalTime(&(file_data.localTime));
    reference_bin = (260-20)*file_data.iMTAC_range ;
    iNumber_of_bins = 260*file_data.iMTAC_range ;
    ulCollection_time_msec = 1000*(file_data.iCollection_time_sec);

    // set bin count to zero
    for(i=0;i<iNumber_of_bins;i++)
    {
        file_data.ulCount_in_Bin[i]=1;
        ulOld_count_in_Bin[i]=1;
    }

    iEnd_range_bin = 256*file_data.iMTAC_range;

    // set bin count to zero
    for(i=0;i<MAX_STOP_PULSES;i++)
        bin_temp[i]=0;

    file_data.ulCount_in_Bin[reference_bin] =1;
    ulOld_count_in_Bin[reference_bin] =1;

    bStop_bit      = 0;
    bClock_on      = 0;
}
/*****
void DrawDataFixed (HWND hwnd)
{
    HDC hdc;
    int i;
    int x,y,y_old;
    int iLength ;
    TCHAR szBuffer [50] ;
    hdc = GetDC(hwnd);

    iLength = wsprintf (szBuffer, TEXT ("collection time =      sec"));
    TextOut (hdc, FRAME_X0, 10, szBuffer, iLength);
}

```

```

iLength = wsprintf (szBuffer, TEXT ("elapsed time      =          sec"));
TextOut (hdc, FRAME_X0, 25, szBuffer, iLength);

iLength = wsprintf (szBuffer, TEXT ("count in ref. bin  ="));
TextOut (hdc, FRAME_X0, 40, szBuffer, iLength);

iLength = wsprintf (szBuffer, TEXT ("Oven Temp Nozzel  ="));
TextOut (hdc, FRAME_X0+FRAME_WIDTH/2.0, 10, szBuffer, iLength);

iLength = wsprintf (szBuffer, TEXT ("Oven Temp Center  ="));
TextOut (hdc, FRAME_X0+FRAME_WIDTH/2.0, 25, szBuffer, iLength);

iLength = wsprintf (szBuffer, TEXT ("Oven Temp Back   ="));
TextOut (hdc, FRAME_X0+FRAME_WIDTH/2.0, 40, szBuffer, iLength);

SelectObject(hdc,GetStockObject(NULL_BRUSH));

Rectangle(hdc,FRAME_X0,FRAME_Y0,
          FRAME_X0+FRAME_WIDTH+1,FRAME_Y0+FRAME_HEIGHT+1);

ReleaseDC (hwnd,hdc);
}
//*****
void DrawDataChanged (HWND hwnd)
{
    HDC hdc;
    HPEN hpen;
    int i;
    int x,y,y_old;
    int iLength ;//test
    TCHAR szBuffer [50];

    hdc = GetDC(hwnd);

    iLength = wsprintf (szBuffer, TEXT ("      "));
    TextOut (hdc, 170, 40, szBuffer, iLength);

    iLength = sprintf (szBuffer, TEXT ("%d"),file_data.iCollection_time_sec);
    TextOut (hdc, 180, 10, szBuffer, iLength);

    iLength = sprintf (szBuffer, TEXT ("%5.f"),ulElapsed_time_msec/1000.);
    TextOut (hdc, 180, 25, szBuffer, iLength);

    // write data[REFERENCE_BIN] on screen
    iLength = sprintf (szBuffer, TEXT ("%d "),file_data.ulCount_in_Bin[reference_bin]);
    TextOut (hdc, 180, 40, szBuffer, iLength);

    iLength = sprintf (szBuffer, TEXT ("%5.1f"),file_data.fNozzel_temp);
    TextOut (hdc, 560, 10, szBuffer, iLength);

    iLength = sprintf (szBuffer, TEXT ("%5.1f"),file_data.fCenter_temp);
    TextOut (hdc, 560, 25, szBuffer, iLength);

    iLength = sprintf (szBuffer, TEXT ("%5.1f"),file_data.fBack_temp);

```

```

TextOut (hdc, 560, 40, szBuffer, iLength) ;

iLength = sprintf (szBuffer, TEXT ("%5.1f"),260.*20./1000.*file_data.iMTAC_range) ;
TextOut (hdc, 715, 510, szBuffer, iLength) ;

Rectangle(hdc,FRAME_X0,FRAME_Y0,
          FRAME_X0+FRAME_WIDTH,FRAME_Y0+FRAME_HEIGHT+1);

hpen = CreatePen(PS_DOT,1,BLACK_PEN);
SelectObject(hdc,hpen);
MoveToEx(hdc,FRAME_X0,FRAME_Y0+FRAME_HEIGHT/2,NULL);
LineTo(hdc,FRAME_X0+FRAME_WIDTH,FRAME_Y0+FRAME_HEIGHT/2);

DeleteObject(hpen);
// plot count in bins

for(i=0;i<=iNumber_of_bins;i++)
{
    x=(int)(FRAME_X0+(FRAME_WIDTH*((float)i/iNumber_of_bins)));
// use iRange instead of RANGE when you divide
    // y_old to erase old data
    y_old =FRAME_Y0+FRAME_HEIGHT*(1-
    .5*(float)ulOld_count_in_Bin[i]/(float)ulOld_count_in_Bin[reference_bin]);
    // data[reference_bin] @ 0.5 of frame height
    y =FRAME_Y0+FRAME_HEIGHT*(1-
    0.5*(float)file_data.ulCount_in_Bin[i]/(float)file_data.ulCount_in_Bin[reference_bin]);

    SetPixel(hdc,x,y_old,RGB(255,255,255));
    SetPixel(hdc,x,y,RGB(255,0,0));
    ulOld_count_in_Bin[i]=file_data.ulCount_in_Bin[i];
}
}
//*****
unsigned _int8 iRead_status(int num_to_read)
{
    int i;          // index
    unsigned _int8 dataTemp;

    for(i=0;i<=num_to_read;i++)
    {
        __asm mov dx,iReadStatusAddress
        __asm in al, dx
        __asm mov dataTemp,al

        __asm in al, dx
        __asm mov dataTemp,al
    }
    return dataTemp;
}
//*****
void iRead_FIFO(int num_to_read)
{
    int i,j;          // index
    unsigned _int8 data_hi_byte=0 ;
    unsigned _int8 data_low_byte=0 ;
    unsigned _int16 dataTemp=0 ;

```

```

for(i=0;i<=num_to_read;i++)
{
    __asm mov dx,iReadFIFOWriteAddress
    __asm in al,dx
    __asm mov data_hi_byte,al
    __asm in al,dx
    __asm mov data_low_byte,al

    dataTemp = 256*data_hi_byte + data_low_byte;
    if(bFirst_data_flag==0)
    {
        if(dataTemp==iEnd_range_bin)
        {
            bin_temp[iBin_temp_index] = dataTemp;
            ++ iBin_temp_index;
            for(j=0;j< iBin_temp_index;++j)
            {
                ++ file_data.ulCount_in_Bin[bin_temp[j]];
                bin_temp[j]=0;
            }
            iBin_temp_index = 0;
        }
        else
        {
            bin_temp[iBin_temp_index] = dataTemp;
            ++ iBin_temp_index;
            if(iBin_temp_index == MAX_STOP_PULSES)
                iBin_temp_index = 0;
        }
    }
    if(bFirst_data_flag==1)
    {
        if(dataTemp==iEnd_range_bin)
            bFirst_data_flag=FALSE;
        iBin_temp_index = 0;
    }
}
}
//*****
void Write_data(int8 data)
{
    __asm mov al,data
    __asm mov dx,iReadFIFOWriteAddress
    __asm out dx,al
}

```


Appendix

C PCB boards for the MSDTDC

Plots used to manufacture both sides of the printed circuit boards (PCBs) of the MSDTDC and the interface card.

Keys for Symbols in Figure 1:

IC1	Quad MECL-to-TTL translator MC10H125
IC2	8-Bit Bidirectional Binary Counter 74F779PC
IC3	Dual D-Type Flip-Flop 74F74
IC4	50 MHz Clock SG-615PCV-50.000MC2
IC5	Dual JK Negative Edge Triggered Flip-Flop 74F113PC
IC6	FIFO memory IDT72V2113L7.5
S	8-bit Switch
R1	500 Ω potentiometer
R2	120 Ω
R3	50 Ω
R4	1 k Ω
R5	12 k Ω
R6	8-1 k Ω isolated resistor array
R7	100 Ω
C1	0.1 μ F
C2	1 μ F
C3	10 μ F
B1	BNC TTL #2 output
B2	BNC TTL #1 output
B3	BNC NIM #2 input

B4	BNC NIM #1 input	
B5	BNC Not Used	
B6	BNC Not Used	
B7	BNC test pulses	
B8	BNC Not Used	
B9	BNC 5 V power supply	
B10	BNC cavity lock	Control Byte Q2
B11	BNC AOM A (after the cavity)	Control byte Q1
B12	BNC AOM B (before the cavity)	Control byte Q0
B13	BNC stop acquisition	Status Byte D3
B14	BNC not used	Status Byte D2
B15	BNC Stop TTL pulses	
B16	BNC Stop bit pulse to FIFO WCLK	
B17	BNC Stop pulses to FIFO WCLK	
B18	BNC Start TTL pulses	
B19	BNC FIFO WCLK	
B20	- 15 Power Supply	
B21	+15 Power Supply	
V1	Negative Voltage Regulator LM337	
V2	Positive Voltage Regulator LM350	
D	25-pin subminiature D-connector	

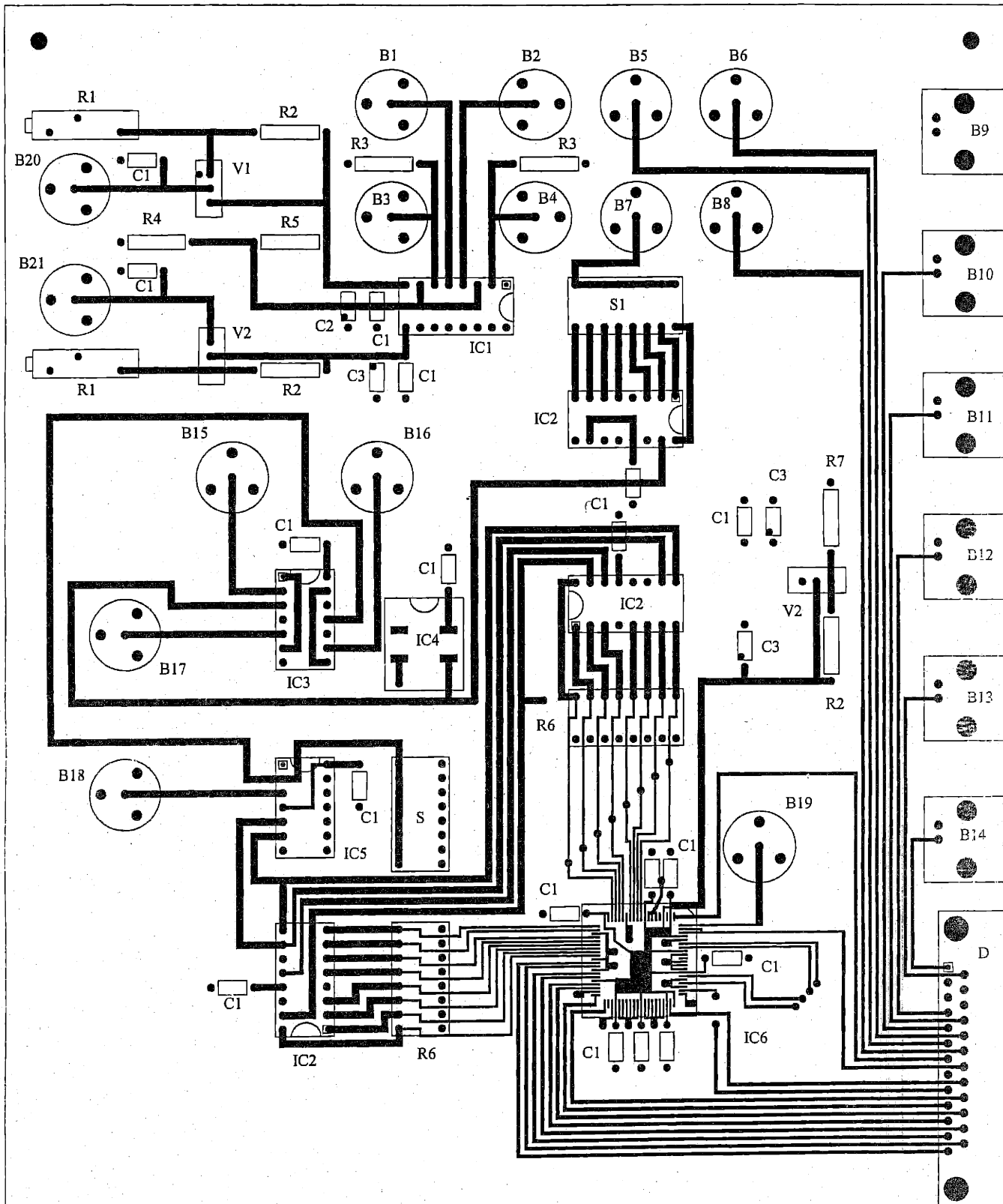


Figure 1. Top side of the PCB plot for the MSTDC and NIM to TTL circuits. Scale

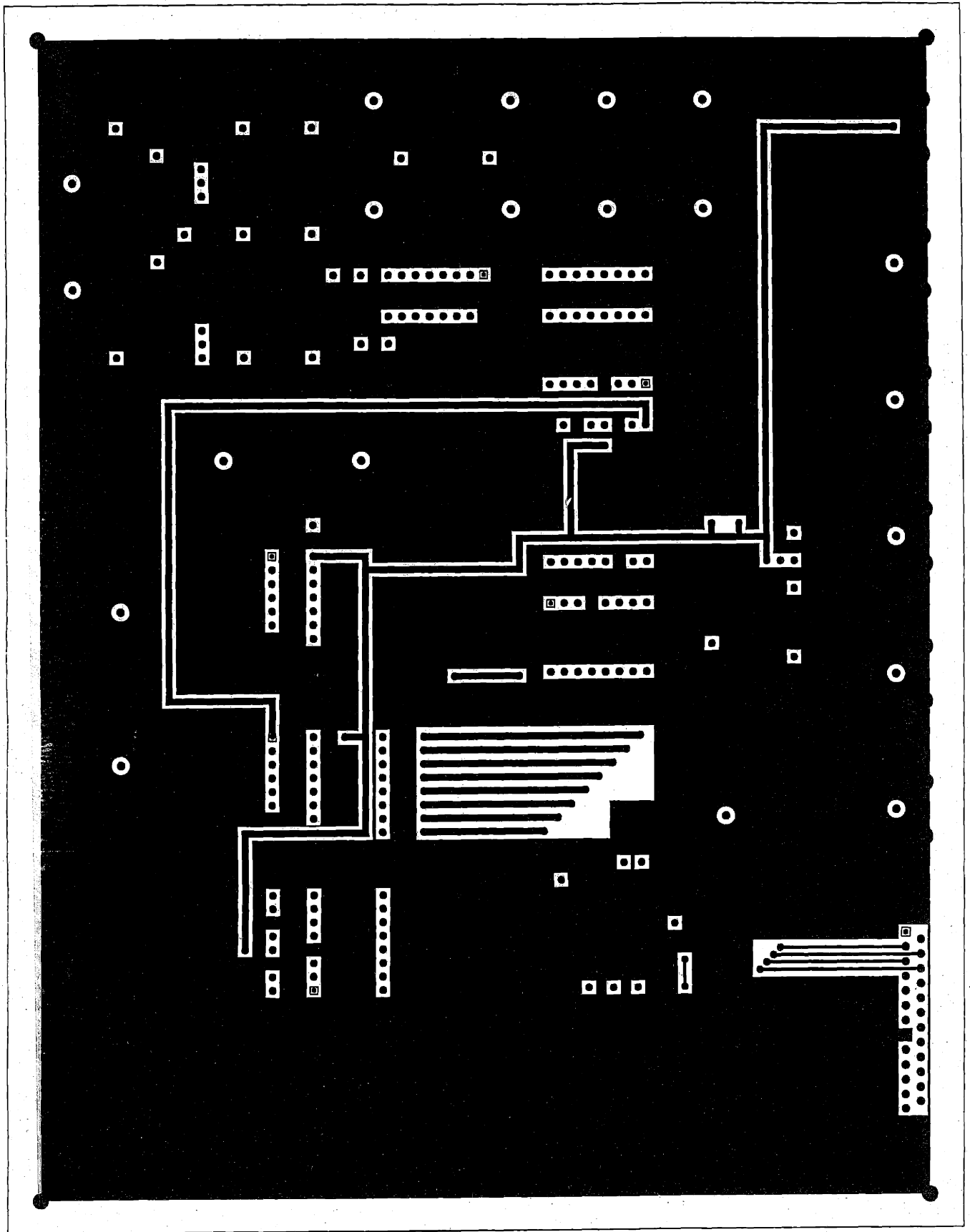
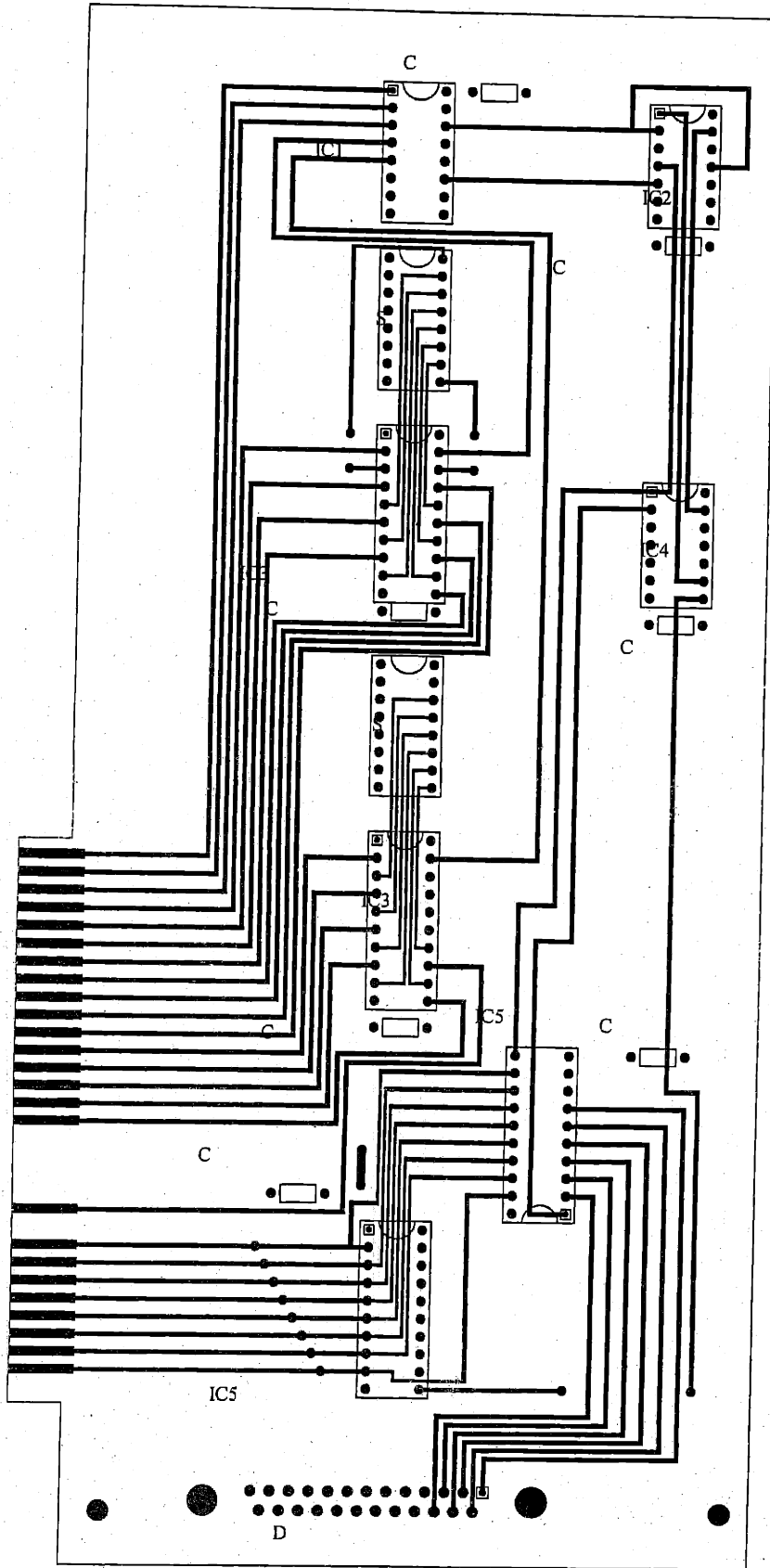


Figure 2. Bottom side of the PCB plot for the MSTDC and NIM to TTL circuits. Scale 1:1.



- Keys for Symbols in Figure 3
- IC1 Decoder 74F138PC
 - IC2 NOR Gates 74 HCT02PC
 - IC3 Identity Comparator 74F21
 - IC4 Inverting Schmitt Trigger 74HCT14
 - IC5 Octal D-type Flip-Flop 74F574PC
 - S 8-bit Switch
 - C 0.1 μ F
 - D 25-pin subminiature D-connector

Figure 3. Top side of the interface card circuit (Side A). Scale 1:1.

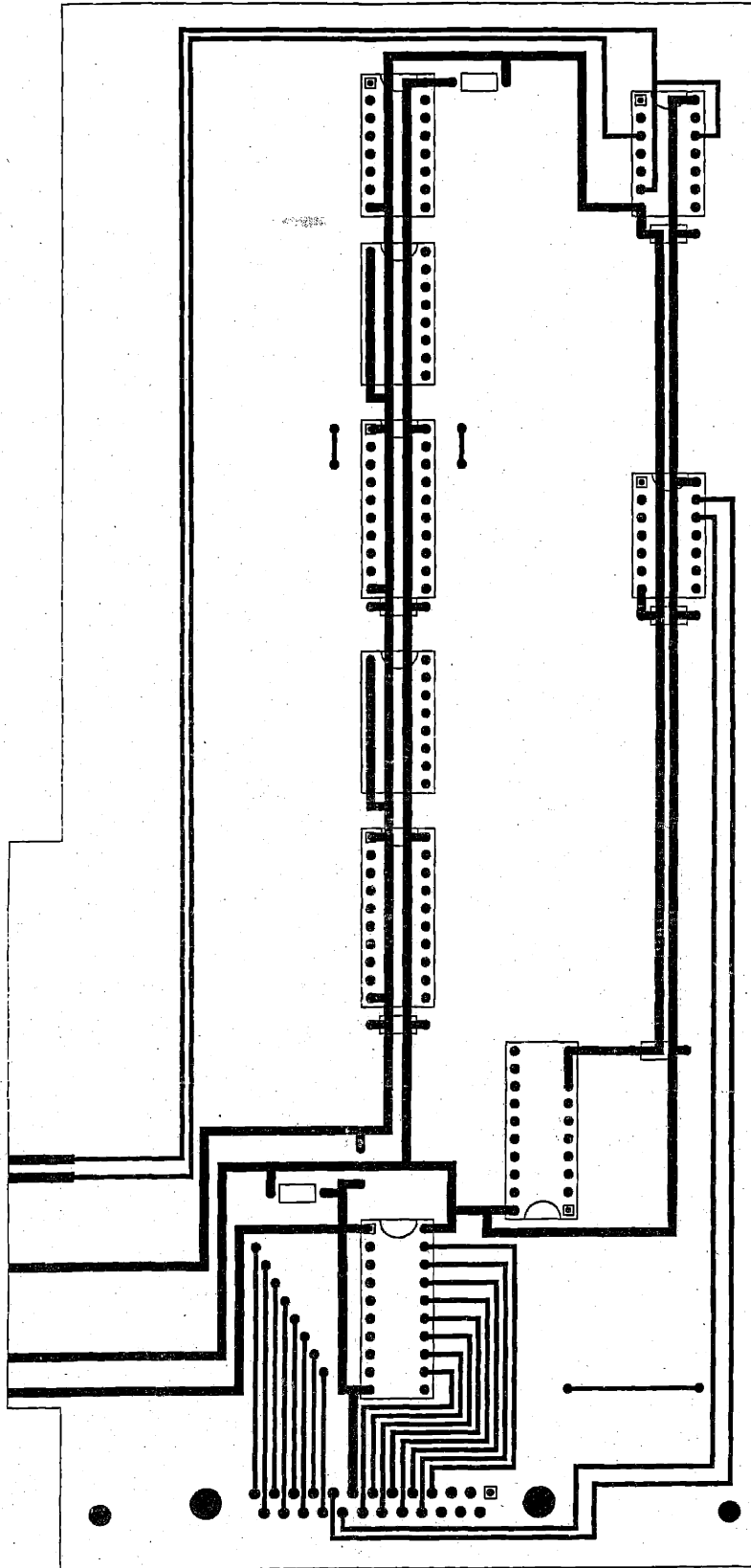


Figure 3. Bottom side of the interface card circuit(Side B). Scale 1:1.